PLASMONIC ENHANCEMENT OF ULTRAVIOLET FLUORESCENCE

by

Xiaojin Jiao

A dissertation submitted to the faculty of
The University of Utah
in partial fulfillment of the requirements for the degree of

Doctor of Philosophy

Department of Electrical and Computer Engineering

The University of Utah

May 2015

The University of Utah Graduate School

STATEMENT OF DISSERTATION APPROVAL

The dissertation of **Xiaojin Jiao**

has been approved by the following supervisory committee members:

Steven Blair, Chair		**01/26/2015** Date Approved
Ajay Nahata, Member		**01/21/2015** Date Approved
Rajesh Menon, Member		**01/12/2015** Date Approved
Jennifer Shumaker-Parry, Member		**01/12/2015** Date Approved
Sivaraman Guruswamy, Member		**01/12/2015** Date Approved

and by **Gianluca Lazzi**, Chair/Dean of the Department/College/School of **Electrical and Computer Engineering** and by David B. Kieda, Dean of The Graduate School.

ABSTRACT

Plasmonics relates to the interaction between electromagnetic radiation and conduction electrons at metallic interfaces or in metallic nanostructures. Surface plasmons are collective electron oscillations at a metal surface, which can be manipulated by shape, texture and material composition. Plasmonic applications cover a broad spectrum from visible to near infrared, including biosensing, nanolithography, spectroscopy, optoelectronics, photovoltaics and so on. However, there remains a gap in this activity in the ultraviolet (UV, < 400 nm), where significant opportunity exists for both fundamental and application research. Motivating factors in the study of UV Plasmonics are the direct access to biomolecular resonances and native fluorescence, resonant Raman scattering interactions, and the potential for exerting control over photochemical reactions. This dissertation aims to fill in the gap of Plasmonics in the UV with efforts of design, fabrication and characterization of aluminium (Al) and magnesium (Mg) nanostructures for the application of label-free bimolecular detection via native UV fluorescence.

The first contribution of this dissertation addresses the design of Al nanostructures in the context of UV fluorescence enhancement. A design method that combines analytical analysis with numerical simulation has been developed. Performance of three canonical plasmonic structures - the dipole antenna, bullseye nanoaperture and nanoaperture array - has been compared. The optimal geometrical parameters have been determined. A novel design of a compound bullseye structure has been proposed and numerically analyzed for the purpose of compensating for the large Stokes shift typical of UV fluorescence.

Second, UV lifetime modification of diffusing molecules by Al nanoapertures has been experimentally demonstrated for the first time. Lifetime reductions of $\sim 3.5\times$ have been observed for the high quantum yield (QY) laser dye p-terphenyl in a 60 nm diameter aperture with 50 nm undercut. Furthermore, quantum-yield-dependence of lifetime reduction has been experimentally demonstrated for the first time. Lifetime reduction as a function of aperture size and native quantum yield has been accurately predicted by simulation. Simulation further predicts greater net fluorescence enhancement for tryptophan compared to p-terphenyl. In order to increase fluorescence enhancement, the "poor" molecules and

structures with proper undercuts are required.

Third, UV lifetime modification by Mg nanoapertures has been experimentally demonstrated for the first time. Lifetime reductions of $\sim$13$\times$ have been observed for the laser dye p-terphenyl with high QY in a 50 nm diameter aperture with 125 nm undercut. In addition, extraordinary optical transmission of Mg nanohole arrays in the UV has been measured for the first time. By using Al as a reference, the feasibility of applying Mg in the UV plasmonic applications has been evaluated both numerically and experimentally.

Finally, this work has established a methodology for the study of plasmonic enhancement of UV fluorescence, including design method, thin-film characterization, nanofabrication with focus ion beam milling, and fluorescence measurement. It has paved the way for more extensive research on UV fluorescence enhancement.

To my wife, Xia,
and daughter, Sophia.

CONTENTS

LIST OF TABLES

ACKNOWLEDGMENTS

I would like to take this opportunity to thank my wife, Xia, who has always been supportive and helpful in taking tough decisions, especially while pursuing my second PhD. Her love and understanding have motivated me to persevere through difficult times and to always perform at my best. I would also like to thank my daughter, Sophia, for being such a delightful angel in my life.

I would like to thank my advisor, Dr. Steve Blair, for his constant guidance, encouragement and cooperation. His keen insight and profound knowledge in this area has been key in helping me solve many research problems.

My committee members, Dr. Ajay Nahata, Dr. Rajesh Menon, Dr. Jennifer S. Shumaker-Parry and Dr. Sivaraman Guruswamy, have been cooperative and helpful during my qualifying exam, proposal defense and dissertation defense. They have also provided me with guidance regarding research and study, which has helped me move forward with my PhD research.

Special thanks to Dr. Yunshan Wang, Dr. Eric Peterson and Mr. Kanagasundar Appusamy for their tremendous help with this dissertation work. Without their contributions, I could not have acquired most of the results presented in this dissertation. Many thanks to Precious Cantu for her generous help in reviewing the grammar and punctuation of my dissertation

I also want to thank my friends, Jingqi, Miguel, Mohit, Peng, Shuchang and Xiaowen. The time I spent with them at the University of Utah is and will always be one of the most precious memory in my life.

This work was accomplished by gracious funding from the Materials Research Science and Engineering Center (MRSEC grant DMR–1121252) at the University of Utah.

CHAPTER 1

INTRODUCTION

Plasmonic enhancement of UV fluorescence has led to the most promising application of Plasmonics in the ultraviolet: label-free detection with native UV fluorescence. The research in the UV, however, is still underdeveloped compared with the study of fluorescence enhancement in the visible range. In this chapter, the background and motivation of this dissertation work will be introduced by generally summarizing basics and applications of Plasmonics, more specifically by reviewing the motivation, challenges and research status of UV Plasmonics.

1.1 Research in Plasmonics

1.1.1 Basics of Plasmonics

Plasmonics studies the interaction between electromagnetic radiation and conduction electrons at metallic interfaces or in metallic nanostructures [1]. This interaction is described by surface plasmon polaritons (SPPs), which are surface electromagnetic modes only existing at metal/dielectric interfaces. Its dispersion relation can be described by [1]:

$$k_x = \frac{\omega}{C}\sqrt{\frac{\epsilon_m \epsilon_d}{\epsilon_m + \epsilon_d}} = k_0\sqrt{\frac{\epsilon_m \epsilon_d}{\epsilon_m + \epsilon_d}} \tag{1.1}$$

where ω is the angular frequency, k_x the SPP's wave vector along the interface, C the speed of light in free space, k_0 the wave vector of light in free space, and ϵ_m and ϵ_d the dielectric constants or permittivities of metal and dielectric. The dispersion relations of SPPs, bulk plasmon and light are shown in Figure 1.1 (a). We can see that SPP's wave vector is always larger than that of light (k_0), which means SPPs can not be directly excited with light due to the phase mismatch. Specifically designed nanostructures are required to compensate this mismatch, such as Kretschmann and Otto configurations, nano-tip, gratings and nanoparticles shown in Figure 1.1 (b). Furthermore, the wave vector along the direction vertical to propagation is always imaginary due to the relation of $k_z = \sqrt{k_0^2 - k_x^2}$, which means the field exponentially decays vertically as shown in Figure 1.1 (c). Therefore,

SPPs are highly localized 2D surface waves propagating along the interface. This surface feature is also called plasmonic localization, one important feature of SPPs. Let's imagine that the 2D metal surface supporting SPPs is folded into a 3D nanosphere; SPPs can only propagate around the spherical surface due to the plasmonic localization. When the sphere size is smaller than the light wavelength, SPPs become localized surface plasmons (LSPs). The unique property of LSPs is that the LSP resonance (LSPR) can be tuned by adjusting the size and shape of the particle without changing the material. Furthermore, plasmonic localization squeezes the energy of conventional light or an electromagnetic wave in 3D space into a 2D surface wave, so the field intensity is effectively enhanced at the interface. This phenomenon is called plasmonic enhancement. Plasmonic localization and enhancement are two unique features of SPPs. All plasmonic applications that have been proposed and studied rely on either one or both of them. For example, plasmon-enhanced spectroscopy and sensing have been hot topics [2]. Plasmonic enhancement introduces a strongly enhanced electric field, which is highly sensitive to changes in the local environment. At the same time, plasmonic localization confines the working volume down to the scale of wavelength. Combining both features makes it feasible to achieve single molecule analysis with relatively high concentration [3, 4].

Plasmonic enhancement (PE) is usually described as the ratio of electric field intensity with and without plasmonic structure. Considering a three-layer structure with a metal film sitting atop a substrate and covered by another dielectric (for example air), we can derive the PE of SPPs (PE_{SPP}) at the metal/covering interface as [5]

$$PE_{SPP} = \frac{1}{\epsilon_c}\frac{2|\epsilon'_m|^2}{\epsilon''_m}\frac{a}{1+|\epsilon'_m|} \tag{1.2}$$

where $a^2 = |\epsilon'_m|(\epsilon_s - 1) - \epsilon_s$, ϵ'_m and ϵ''_m are the real and imaginary parts of permittivity of metal, ϵ_s and ϵ_c are the permittivities of substrate and covering material.

For LSPs, the situation is more complicated, because PE is also determined by the size and shape of the nanoparticles, besides the dielectric constants. If we consider the simplest structure, a nanosphere with a diameter much smaller than wavelength, LSPR can be analytically analyzed under the dipole approximation. The PE of LSPs (PE_{LSP}) can be described by [6]

$$PE_{LSP} = |1 + \frac{2(\epsilon_m - \epsilon_d)}{2\epsilon_d + \epsilon_m}| \approx \frac{-3\epsilon'_m}{\epsilon''_m} \tag{1.3}$$

The latter expression only holds when the nanosphere is under resonance, i.e. $\epsilon_m = -2\epsilon_d$.

Plasmonic localization (PL) can be described by the decay length of electric field along the direction vertical to the surface, which is the distance at which the amplitude of electric field falls to $1/e$. For SPPs, PL_{SPP} can be described by

$$PL_{SPP} = \frac{1}{k_z''} = |\frac{1}{\sqrt{k_d^2 - k_x^2}}|'' \tag{1.4}$$

where k_z'' is the imaginary part of the wave vector along the normal direction of the surface, and k_d is the wave vector of light inside dielectric. k_x can be solved from Equation 1.1.

For PL of LSPs, we also consider the case of a tiny nanosphere. PL_{LSP} can be derived from electric field expression in [6]

$$PL_{LSP} = (\frac{4R^3(\epsilon_d - \epsilon_m)}{2\epsilon_d + \epsilon_m})^{\frac{1}{3}} \tag{1.5}$$

where R is the diameter of the nanosphere. It is clear that PL_{LSP} is proportional to the size of the nanosphere, which implies that PL can be tuned by adjusting the size of the nanosphere. In order to describe the difference between SPPs and LSPs, we calculate PE and PL by considering two practical cases: Aluminum (Al) film atop a glass substrate and covered by water, and an Al nanosphere with radius of 20 nm surrounded by water. The wavelength is 270 nm corresponding to the absorption peak of the biomolecule used in our experiment. So $\epsilon_m = -10.36941 + i1.44545$, $\epsilon_d = \epsilon_c = 1.914$, and $\epsilon_s = 2.244$. The PE and PL are calculated as

$$PE_{SPP} = 22 \qquad PE_{LSP} = 5\ (22) \qquad PL_{SPP} = 66\ nm \qquad PL_{LSP} = 38\ nm$$

One can see that SPPs have a stronger plasmonic enhancement (22) compared to LSP (5), which is due to the fact that the nanosphere is not under the resonant condition. PE_{LSP} becomes comparable (22) if under the resonance. On the other hand, PL_{LSP} is smaller, and can further decrease with nanosphere size. Therefore, with comparable PE and adjustable PL, LSPs are more preferred for the applications of plasmon-enhanced single-molecule analysis [3].

1.1.2 Overview of Application Research in Plasmonics

Research on SPPs can be traced back to the study of small particles by Mie at the beginning of the 90s [7]. Many studies have been done on SPPs but were limited to the fundamental study due to the limitation of nanofabrication techniques [5]. In 1998, Ebbesen et al. observed the extraordinary optical transmission (EOT) of silver nanohole arrays [8], which triggered the resurgence of this area with the help of the advance of nanofabrication

and numerical simulation. Extensive theoretical and experimental research on EOT [9, 10] has built the solid knowledge base for the exploding development of plasmonic applications. A new term, "Plasmonics", has been proposed [11], and the subfield of modern optics has been formed. With the advancing research on Plasmonics, the focus has been switched from fundamental to application, which has already demonstrated the huge potentials of Plasmonics for many important applications.

1.1.2.1 Applications Based on Plasmonic Enhancement

Utilizing the effect of plasmonic enhancement, Plasmonics can be applied to dramatically improve the sensitivity of spectroscopy [2] and biosensors [3, 4]. Furthermore, the subwavelength feature of plasmonic devices makes it relatively straightforward to integrate those devices into microfluidic chips for use in next-generation lab-on-chip techniques. Plasmonic enhancement has also been used to improve the efficiency of photovoltaic devices [12]. With different plasmonic geometries for light guiding and concentration, an optically thick but physically thin photovoltaic absorber can be formed. Plasmonic enhancement has provided a new strategy of design and optimization of thin-film photovoltaic devices.

1.1.2.2 Applications Based on Plasmonic Localization

Plasmonic localization can effectively confine the field around the metal surface, which means the confinement of the field is not limited by the diffraction limit, but by the physical size of metallic structures. By achieving structures with extremely small features, the field can be highly confined. Based on that, various plasmonic geometries have been proposed and experimentally demonstrated to fulfill highly compact SPP waveguide [13]. A SPP waveguide is capable of the manipulation of light in nanoscale regions with dynamic and active light controlling functionalities. It can also serve as a coupling component to deliver light energy to nanoscale optical and electronic devices [14, 15]. Furthermore, the metal nature of plasmonic structures is compatible with existing integrated electrical circuits, which makes it possible to merge photonics and electronics at nanoscale dimensions [16]. In addition, the effective wavelength of SPPs is always smaller than that of light, which relaxes the limitations on any applications governed by the diffract limit. Super-resolution imaging with SPPs has become another hot area in Plasmonics [17, 18]. Plasmonic nanolithography has proven to be a promising candidate for next-generation photolithography [19].

1.1.3 Selected Topics Related to Dissertation Work

Due to the fact that application research in Plasmonics is exponentially growing, it is impossible for one to cover all of the aspects. So only a brief overview has been given in the previous section. In this section, a more detailed introduction will be given on two selected topics related to this dissertation work.

1.1.3.1 Figure of Merit and Plasmonic Materials

Research in Plasmonics has reached a stage where ohmic losses of metals have become serious issues impairing the device performance. Searching for better plasmonic materials is an ongoing effort that has attracted more and more attention [20–25].

A materials response to an applied electromagnetic wave is described by its dielectric constant or permittivity, $\epsilon(\omega) = \epsilon'(\omega) + \epsilon''(\omega)$, in which the real part, $\epsilon'(\omega)$, describes the polarization strength induced by the external electric field, and the imaginary part, $\epsilon''(\omega)$, describes the material loss. Metals possess complex dielectric constants due to ohmic losses in the optical region, which mainly come from two different mechanisms. Free-electron losses are due to electron-electron scattering, electron-phonon scattering and lattice-defects or grain-boundary scattering. Bound-electron losses are due to interband transitions, which occur when bound electrons jump to higher energy levels caused by absorption of incident photons.

It should be noted that considering only the imaginary part of permittivity is not sufficient for the performance comparison of various materials used in different applications. Optical absorption can be described as $P_{abs} = \frac{1}{2}\omega\epsilon''(\omega)|E|^2$ [26]. This equation implies that the optical absorption is also affected by electric-field intensity, which is determined by the real part of permittivity, $\epsilon'(\omega)$. Therefore, researchers have proposed the concept of the figure of merit (FOM), which is a function of both ϵ' and ϵ'', to determine which material performs better [20,21]. Various applications have different $FOMs$, which are defined as [21]

$$FOM_{LSP} = \frac{-\epsilon_r}{\epsilon_i} \tag{1.6}$$

$$FOM_{SPP} = \frac{\epsilon'_m(\omega) + \epsilon_d(\omega)}{\epsilon'_m(\omega)\epsilon_d(\omega)} \frac{\epsilon'_m(\omega)^2}{\epsilon''_m(\omega)} \approx \frac{\epsilon'_m(\omega)^2}{\epsilon''_m(\omega)} \tag{1.7}$$

$$FOM_{TO} = \frac{1}{\epsilon''} \tag{1.8}$$

$$FOM_{SL} = \frac{-\ln(\frac{\epsilon''}{2})}{2\pi} \tag{1.9}$$

where ϵ_m and ϵ_d are permittivities of metal and dielectric. FOM_{LSP} describes the plasmonic enhancement of a nanosphere, which is the same as Equation 1.3 under the res-

onant condition. FOM_{SPP} is meant for SPP waveguide instead of SPP enhancement, and $FOM_{SPP} \approx \frac{\epsilon'_m(\omega)^2}{\epsilon''_m(\omega)}$ when $\epsilon'_m \gg \epsilon_d$. If SPP-enhanced applications are considered, Equation 1.2 should be used as FOM. Using $FOMs$, researchers have started to evaluate materials for different plasmonic applications. Blaber et al. has given an extensive review of metals and alloys [20]. Besides the conventional plasmonic materials (gold and silver), alkali metals have been evaluated, which have even better performance, but are difficult to work with. Metal alloys have the advantage of tuning the dielectric constant by adjusting the composition. Oxides and nitrides have also been proposed as alternative plasmonic materials [23]. They have advantages of ease of preparation and tunability with processing conditions, but are only metallic in red and near-infrared. Based on the FOM, they are more suitable for applications of transformation optics due to small real and imaginary parts of dielectric constant. In addition, heavily doped semiconductors and graphenes are possible plasmonic materials for infra-red and THz range [21, 24, 27]. Furthermore, researchers have proposed graphenes as protective layers for copper and silver plasmonic structures [28]. Recently, transition metal nitrides, specifically titanium nitride, have been proposed as refractory plasmonic materials [29, 30]. Refractory materials are defined as those with a high melting point and chemical stability at temperatures above 2000 °C. Titanium nitride has comparable plasmonic response compared with gold, but its superior properties, such as high temperature durability, chemical stability, corrosion resistance, low cost and mechanical hardness, make it the perfect candidate for applications in a harsh environment, such as heat-assisted magnetic recording and plasmon-assisted chemical vapor deposition.

1.1.3.2 Study of Plasmon-Enhanced Fluorescence at Single Molecule Level

Fluorescence-based spectroscopy is considered to be the primary research tool in biochemistry and biophysics [31]. The issues of fluorescent molecules are low intensities and photostability. One strategy can enhance the spontaneous emission by tailoring the electromagnetic environment around the molecule [32, 33]. The photonic mode density of environment has been revealed to be the important role in this phenomenon [34]. SPPs are the unique photonic modes in metallic structures. Extensive theoretical and experimental research on the interaction of an oscillating dipole with metallic structures has been carried out [35]. Surface-plasmon-enhanced fluorescence (SPEF) or metal-enhanced fluorescence (MEF) [36, 37] has been proven as a promising means to improve the fluorescence signal. Considering the relevance to this dissertation work, only the research of fluorescence enhancement at the single molecule level will be reviewed here. Fluorescence enhancement

of a single molecule started to gain interests after the observation of metal-tip-enhanced fluorescence [38] and nanoparticle-enhanced Raman scattering [39]. In 2003, nanoaperture as the platform, so-called zero-mode waveguide (ZMW), for single molecule analysis has been demonstrated for the first time [40]. Single-molecule fluorescence enhanced by Al nanoapertures [41] and gold nanoparticles [42] has been demonstrated later. Since then, a series of experimental studies on nanoapertures have been published from Wenger's group [43–48]. A systematic method of single-molecule analysis has been established, which combines lifetime measurement and fluorescence correlated spectroscopy (FCS) to distinguish the respective contributions from excitation and emission enhancement. The main advantage of the nanoaperture is that its sufficient small physical volume allows the single molecule to be isolated for optical analysis at high concentration. It has found many applications such as real-time imaging of protein-protein interaction, real-time observation of enzymatic activity, membrane-bound diffusion etc. [49] In addition, many other plasmonic structures have also been studied for SPEF, including bullseye [50, 51], bowtie antenna [52], bowtie aperture [53], nanoshell [54], nano-gap formed by particles [55], disk-coupled dots-on-pillar antenna array [56], plasmonic nanocavity [57, 58] etc.

1.2 UV Plasmonics

Compared with the explosive development of Plasmonics in the visible and near infrared, Still little attention has been paid to the ultraviolet (UV, < 400 nm). In this section, the motivation of UV Plasmonics is introduced. The challenges in this area are discussed from the perspectives of materials choice, nanofabrication and characterization. Both the background on understanding relevant discussion and efforts to address the issues are summarized. Finally, a brief review of UV plasmonic applications is given.

1.2.1 Motivations

Study of UV Plasmonics is motivated by several promising applications. Fluorescence-based spectroscopy is considered to be the primary research tool in biochemistry and biophysics [31]. Important biomolecules such as peptides, proteins and amino acids contain residues that absorb the light and emit native fluorescence in the UV (220-280 nm). Label-free detection with native fluorescence of biomolecules not only inherits the advantages of fluorescence-based techniques, but also decreases the complexity of sample preparation and data analysis by avoiding the fluorescent labels. However, those molecules have relatively low fluorescence quantum efficiencies and molar extinction coefficients [59], so achieving significant enhancement via plasmonic structures could be a key enabling factor for these

techniques.

Raman spectroscopy is another common technique for assessing molecular motion and fingerprinting by vibrational measurement [60]. Its application is limited by the weak signal of spontaneous Raman scattering. UV resonance Raman scattering results in approximately a 10^5 increase in cross-section as compared to the nonresonant case [61]. Therefore, surface/tip-enhanced Raman scattering in the UV can be very promising with 2-fold enhancement provided by both UV resonant Raman scattering and UV plasmonic structures.

UV light itself is useful in a wide range of applications such as purification of liquids and gases by sterilization, photocatalytic action with titanium oxide and photolithography. UV plasmonic enhancement can improve many UV-based applications, such as improvement of the efficiency of UV light sources and detectors, increase in the photocatalytic yield and rate, control of the photochemical reactions on a scale commensurate with the molecules themselves and with increased reaction rates, and so on.

1.2.2 Challenges

Plasmonic research routinely includes design, fabrication and characterization of metallic nanostructures, which require collaborative efforts from disciplines of science and engineering. In the ultraviolet, it becomes a more challenging task with new issues emerging. In this section, the challenges in the research of UV Plasmonics will be discussed from the perspectives of material choice, nanofabrication and characterization. We also summarize the approaches to address these issues.

1.2.2.1 Materials Choice

Material loss becomes a more serious problem in the UV, because conventional plasmonic materials, such as gold and silver, suffer from the influence of interband transitions near the blue part of the spectrum. Here, we chose several materials being metallic ($\epsilon' < 0$) in the UV range. The figures of merit of these materials are plotted in Figure 1.2. The material data are extracted from the Palik handbook [62]. Figure 1.2 (a) and (c) present the FOM_{LSP} and FOM_{SPP} versus wavelength according to the definitions in Equations 1.6 and 1.7. It should be noted that FOM_{LSP} assumes the nanosphere is always under resonance, i.e., $\epsilon'_m = -2\epsilon_d$. However, it is not always true for metals in the UV, so the so-called general FOM_{LSP} is also plotted in Figure 1.2 (b), which is calculated by the definition of PE_{LSP} in Equation 1.3. FOM_{LSP} can be derived from it when $\epsilon'_m = -2\epsilon_d$. In addition, FOM_{SPP} actually evaluates the performance of SPP waveguide by calculating the ratio

of real and imaginary parts of the SPP wave vector, so PE_{SPP} of Equation 1.2 is used as $PEFOM_{SPP}$ for the applications based on SPP PE, which is plotted in Figure 1.2 (d). To calculate general FOM_{LSP} and $PEFOM_{SPP}$, we consider a practical case close to our experiment: Al film/nanosphere with 20 nm radius is covered/surrounded by water. Al film is supported by a glass substrate. The plots of FOM_{LSP} and general FOM_{LSP} show an obvious difference. Mg and Ag have peaks at 260 nm and 400 nm in the plot of the general FOM_{LSP}, respectively, at which they have the similar values to FOM_{LSP} because the condition of $\epsilon'_m = -2\epsilon_d$ is satisfied. In addition, the best three metals shown by FOM_{LSP} in Figure 1.2 (a) are: Mg, Al and In, while those shown by general FOM_{LSP} in Figure 1.2 (b) are: Mg, In and Sn. Because the general FOM_{LSP} considers the case closer to the practical, we will use it to survey UV plasmonic materials later. The plots of FOM_{SPP} and $PEFOM_{SPP}$ do not show a big difference, except that Al is better than Mg at wavelengths shorter than 320 nm when considering $PEFOM_{SPP}$ in Figure 1.2 (d), instead of 400 nm for FOM_{SPP} in Figure 1.2 (c). In the following, we will survey the possible UV plasmonic materials based on Figure 1.2 (b), extensive review by Blaber et al. [20] and other published works.

Considering the general FOM_{LSP} in Figure 1.2 (b), one can see that alkali metal, magnesium (Mg), has the largest FOM_{LSP} due to the fact that it is around the resonance in the UV. But the issue with Mg is that it can keep growing an oxide layer of MgOH under a humid environment, even though it also forms a self-protective MgO layer of 20 to 50 nm [63]. So Mg can be a practical candidate if the humidity of the environment is controlled. Appusamy et al. have studied the influence of film thickness on optical constants of Mg thin-film [64]. By comparing the FOM_{LSP} of Mg and Al, they showed that 910 nm thick Mg film on glass substrate has the best plasmonic property, which is superior or comparable to Al in the UV. However, 910 nm film is too thick to be used for the nanofabrication of UV plasmonic structures. Recently, their new study has demonstrated a method to improve the plasmonic property of 100 nm thick Mg film by using a 10 nm Al seed layer [65]. Their research makes it possible to fabricate UV plasmonic structure from Mg thin film for the following experimental study, which will be discussed in detail in Chapter 5.

Silver (Ag) has the second largest FOM_{LSP} at 400 nm due to the plasmonic resonance. Its capability in UV has been demonstrated by the study of intrinsic fluorescence enhancement of DNA with Ag islands around 350 nm [66]. Later, Ag islands were also used to enhance the native fluorescence of tryptophan by 2–3 times, and the possibility of label-free

detection has been discussed [67]. But Ag's working range is limited down to 320nm where interband transitions happen. Also it degrades relatively quickly and has a large thickness threshold for uniform continuous films, which is around 12-23 nm [21].

It is unexpected that indium (In) and tin (Sn) outperforms Aluminum (Al) according to general FOM_{LSP}, although they are much worse according to FOM_{LSP}. Recently, Kumamoto et al. have demonstrated that indium-coated substrate can generate $11\times$ higher Raman signal when excited at 266 nm [68]. There is still no experimental study on Sn, besides theoretical works. Furthermore, taking into account the fact that Al is inexpensive, relatively easy to work with and chemically stable, Al is still by far the dominant plasmonic material for UV Plasmonics [69–96, 96–111]. It is also the main material being studied in this dissertation work. Being a group 13 metal as Al, Gallium (Ga) has maximal FOM_{LSP} of 3.7 at 155 nm [20]. Its potential as an UV plasmonic material has been experimentally demonstrated [112]. In this work, hemispherical Ga naoparticles deposited on a sapphire substrate have been used as a plasmonic substrate to achieve local Raman enhancement factors $> 10^7$ with excitation at 325 nm wavelength.

Other pure metals that have been experimentally studied are platinum (Pt) and zinc (Zn). Even though the value of general FOM_{LSP} of Pt is not impressive in the UV ($\sim$ 1), significant enhancement up to 20-fold of intrinsic fluorescence of nucleic acid around 340 nm by Pt nanoaprticles has been observed [113]. Zn should be a decent UV metal with maximal FOM_{LSP} of 3.59 at 344 nm [20]. Experimental study has demonstrated that Zn nanoparticles can enhance the fluorescence by 5-fold near the UV edge [114].

Besides pure metals, alloys are another choice as low-loss plasmonic materials. Various alloys have been surveyed in the broad range of spectrum [20, 21]; however, there is only one possible candidate for UV Plasmonics according to the material properties: amorphous PdSi (Max. $FOM_{LSPR} \sim 16$ at 330 nm). Besides, research has been performed by other groups that have suggested more options. Al/Ag bimetallic nanoparticles have been used to achieve up to 10-fold of enhancement of intrinsic fluorescence of tryptophan [78]. By alloying Al and Ag, it is possible to achieve both the enhancement comparable to Ag and the working range similar to Al. Ga/Mg alloy has also been experimentally studied for the purpose of improving the tunability of plasmonic resonance [115]. Both metals are possible UV plasmonic materials in terms of FOM_{LSP}. Ga nanoparticles have the perfect thermal stability, while Mg has the better plasmonic response. It has been demonstrated that Ga/Mg nanoparticles have tunable plasmonic resonance with varying Mg content, and also better thermal stability. Recent study also shows that a special semiconductor material

$Bi_{1.5}Sb_{0.5}Te_{1.8}Se_{1.2}$, known as a topological insulator, is a possible plasmonic material in the blue-ultraviolet range [116]. The gratings with varied periods made from it can have plasmonic resonance from 350 to 550 nm.

In addition, theoretical research has also been carried out to compare the material. Mahdavi et al. simulated the net enhancement of UV fluorescence from a single tryptophan molecule placed inside a nanoaperture made from gold, silver and aluminum. It demonstrates that the aluminum nanoaperture provides the greatest fluorescence enhancement (10× net enhancement) [79]. Performance of poor metals (Al, Ga, In, Sn, Tl, Pb and Bi) has been studied by calculating near-field enhancement of single nanosphere and dimers made from them [96]. All of them, except Bi, generate more than 10^3 enhancements in the ultraviolet range, which is comparable to or higher than that of Ag and Au in the visible. The influence of geometry, substrate and oxidation on the plasmonic behaviors of various metal nanoparticles in the near- and far-field regimes has been numerically studied, and it proves that Mg, Al, Ga, In and Rh are possible candidates for the application of UV Plasmonics [101]. The optimal electric field enhancement of Al and In dimers has been calculated and compared with Au and Ag [108]. Their research demonstrates that Al and In dimers can give comparable enhancement to that of Au and Ag in the visible, which further confirms the potential of poor metals in UV plasmonic applications.

In summary, interband transitions in the UV range introduce large ohmic losses, which hinder the advancement of UV Plasmonics, and boost the research on finding better plasmonic materials. Research so far has proven that Al is a good candidate. Even though there are few other metals and alloys as possible alternatives, further experimental studies of nanostrcutures made from those materials are still required in order to validate their potentials in UV Plasmonics.

1.2.2.2 Nanofabrication

The extensive experimental studies rely on nanofabrication techniques, which used to be the biggest roadblock. Nowadays, advanced nanofabrication techniques have fueled the exploding development of Plasmonics. Various sophisticated methods have been developed, such as soft lithography [117], nanosphere lithography [118,119], nanoparticle synthesis [120] and so on. An extensive review of top-down nanofabrication techniques for Plasmonics can be found [121]. However, it is still a challenging task to consistently fabricate nanostructures with typical feature size around 50 nm. In addition, different metals need more consideration according to their material properties. For example, Al can form a layer of Al_2O_3, which introduces more difficulties into fabrication due to its high etching resistance. Recently,

a review of Al fabrication techniques has been published due to Al's popularity in UV Plasmonics [111]. Here, we will briefly review the techniques been applied in the study of UV Plasmonics [69–84, 86–96, 96–115] not limited to Al, with emphasis on top-down fabrication techniques.

Electron beam lithography (EBL) has been applied extensively to fabricate plasmonic structures [121]. However, it has not been used in UV Plasmonics very often [83, 87, 89, 91], due to the fact that research is still at the early stage and no complicated structures are required. EBL is a serial top-down lithography process in which a focused electron beam is scanned over a resist which modifies the solubility of the resist by cross-scission or cross-linking. The exposed parts of the polymer resist can then be selectively removed to transfer a pattern into the resist. Depending on what kind of patterns to be fabricated, different following procedures are applied. Dry etching will transfer the pattern from resist to the substrate, which is suitable for the fabrication of patterned metal film such as nanogrid [83]. Resist removal following metal deposition (liftoff) generates the complementary pattern on the substrate, which is suitable for the fabrication of metallic particle-like structures, such as Al nanodisks [87,92], Al bowtie antenna [89] and Al dipole antenna [91]. Typical EBL tools use 10−100 kV acceleration voltages, and thus the de Broglie wavelength of the electrons is below 1 $\mathring{A}$, which means diffraction-limited beam spot can be extremely small. Although the real resolution is determined by aberration of the electron-optical imaging system and the following patter-transferring procedures, EBL can still provide sufficient resolution to meet the needs of the fabrication tasks in UV Plasmonics.

Another important technique is focused ion beam (FIB) milling. Same as the EBL, the potential of this technique has not been fully exploited in UV Plasmonics. So far there are only two published works using it [82, 116]. Nanoslits were fabricated on semiconductor material, $Bi_{1.5}Sb_{0.5}Te_{1.8}Se_{1.2}$, with feature size down to 120 nm [116]. From the perspective of instrumentation, FIB has a similar configuration to E-beam, which is an instrument focusing and manipulating ion beam instead of e-beam. But from the perspective of processing, FIB milling offers a one-step writing process, which is more convenient compared with EBL that requires spin-coating, exposure, development and etching. Furthermore, it provides the ability to use a gas injection system (GIS) for the deposition of various materials, such as Au and Pt. It is also possible to enhance the FIB milling with GIS system, such as iodine-enhanced etching. In addition, FIB milling can introduce and accurately control the undercut at the metal/substrate interface, which has been theoretically proven to be helpful for specific applications, such as the fact that 60 nm undercut can enhance

the signal to noise ratio by 6 times for nanoaperture-assisted single molecule imaging [122]. Considering these advantages, we will use FIB milling as the main nanofabrication tool in this dissertation work. Al and Mg nanoapertures with feature size down to 50 nm will be fabricated. The details will be discussed in the following chapters [82].

EBL and FIB milling are powerful tools to fabricate patterns with accurate control of small features, but they are not suitable to directly mass produce large area nanostructures due to the serial nature of fabrication. Therefore, several techniques have been employed to prepare different structures with a large scale for plasmonic application in UV. Al thin films on a planar or curved surface can be deposited by thermal evaporation [69, 76, 84, 88, 93, 95, 98] or magnetron sputtering [73] or vacuum electron beam deposition [95]. Al island films can be prepared by thin-film evaporation at slow deposition rate [71, 77, 78], or rapid thermal annealing of a thin film deposited on a super-repellent substrate [103], or Al dewetting on a patterned substrate [102]. Al nanoparticles of 20 to 60 nm have been prepared with oblique angle deposition [106]. Al nanodisks, triangular particles, nano-voids and nanohole arrays have been prepared with nanosphere lithography [74, 75, 100, 104]. Free-standing Al hole arrays and Al nanoparticle arrays have been fabricated over large areas using extreme-UV interference lithography [70,94]. In addition, Hemispherical gallium particles can be deposited on the sapphire substrate with molecular beam epitaxy [112]. Zn and Pt thin-film with nanoparticulate surface were also prepared with thermal evaporation and sputtering [113, 114]. In summary, at the early stage of research in UV Plasmonics, only a few plasmonic structures have been fabricated and studied. EBL, FIB milling, and other large-area-fabrication techniques have been applied so far. Figure 1.3 summaries the typical structures that have been prepared.

1.2.2.3 Characterization Techniques

Characterization of near- and far-field properties help us understand light-matter interaction in metallic nanostructures, which builds the foundation for many novel plasmonic applications. Methods including ultraviolet-visible (UV-vis) spectroscopy, transmission measurement and surface plasmon resonance (SPR) measurement are popular techniques for far-field study. In addition, ultrafast time-resolved techniques have been applied to probe the fast dynamic interactions of SPPs with nano-emitters. On the other hand, near-field characterization of optical properties and physical quality of thin film and nanostructures is essential to unveil the deviation of practical structures from design, which is a crucial step for structure optimization. Far-field methods are characterization techniques to measure the scattering or extinction spectrum, transmission spectrum and reflectance

of nanostructures. Because the peak or dip of the spectrum corresponds to plasmonic resonance, it is usually applied to validate nanostructures' resonance in desired regions, UV for UV Plasmonics [66, 67, 70, 71, 74, 75, 87, 88, 92, 102–104]. Plasmon-enhanced fluorescence has been a hot area in Plasmonics as reviewed in the previous section. It is the same case in UV Plasmonics. Furthermore, fluorescence enhancement has also been a primary means to characterize the plasmonic enhancement [66, 67, 69, 71, 72, 77, 78, 98, 112–114]. Fluorescence-based time-resolved measurement is widely used because it contains more information than is available from the steady-state data. For example, it can measure the lifetime of a fluorescent molecule, which is a fingerprint of a molecule and highly sensitive to the local environment. By placing fluorescent molecules on top of or inside metallic nanostructures, researchers can characterize the near-field properties of metallic nanostructures by monitoring the change of lifetime [82]. It is a main technique being applied in this dissertation. Another category of far-field characterization techniques, ellipsometry and X-ray photoelectron spectroscopy (XPS), has been employed to fully characterize the oxidation of Al films and nanoparticles [92]. High-resolution near-field imaging techniques give straightforward information of near-field of metallic nanostructures. Scanning electron microscopy (SEM) has become the standard tool for almost every study on Plasmonics. Imaging with electrons make it possible to achieve images with super-resolution compared to optical ones due to the short de Broglie wavelength of the electrons (below 1 $\mathring{A}$). Cathodluminescence (CL) is a phenomenon in which light can be emitted from the excited atoms bombarded with high-energy electrons. CL imaging technique scans the sample with an electron beam and forms a high-resolution image by collecting CL. It is an emerging but powerful imaging technique that has been applied in Plasmonics, and recently it has been used to study the near-field pattern of aluminum nanoantennas. [91]

1.2.3 Overview of UV Plasmonic Applications

Although plasmonic applications have been pervasive in a broad range as reviewed in the previous section, there are still few applications reported in the UV range.

1.2.3.1 Surface-Plasmon-Enhanced UV Ffluorescence

Besides the signal enhancement and improvement of photostability of fluorescent molecules, surface-plasmon-enhanced fluorescence (SPEF) in the UV has its unique advantage. By enhancing the intrinsic or native UV fluorescence of biomolecules such as amino acids and DNA, it is possible to achieve label-free detection, which, the author believes, is the most promising application of UV Plasmonics. This application is the main motivation

of this dissertation work. Here, only an overview is given. The detailed summary will be presented in the following section. Lakowicz et al. reported the enhancement of intrinsic UV fluorescence from DNA by silver nanoparticles in 2001 for the first time [66]. However, the silver nanoparticles still have the resonance in the blue edge of visible, instead of UV. Later, the same group demonstrated the UV fluorescence emission from DNA excited by SPPs on Al thin-film through reverse Kretschmann configuration [69]. Ray et al. studied the UV-blue fluorescence of DNA enhanced by particulate Al films in 2007 [71]. By spin-coating 10 nm thick poly film with two probes on Al surfaces, the researchers observed an increase in fluorescence emission and a reduction in fluorescence lifetime. Figure 1.4 (a) demonstrates the change of Al island films with increase of thickness. Figure 1.4 (b) presents the enhancement of fluorescence of two probes (2-AP and 7-HC) versus Al film thickness. The 10-nm-thick Al film generates the highest enhancement up to 9× for 2-AP and 6× for 7-HC. Later, extensive numerical simulation further demonstrated that Al nanoparticles can be an efficient substrate for SPEF in the UV [77]. At the same time, the possibility of label-free detection of tryptophan residue in protein with Ag nanostructure was studied [67]. Recently, a new bimetallic (Ag/Al) nanostructure was proposed by the same group [78]. Up to 10x enhancement of UV fluorescence has been observed. Furthermore, numerical simulation demonstrated that bimetallic substrates composed of Ag and Al have a distinct advantage in the wavelength region that is important for the detection of intrinsic fluorescence of proteins. SPEF from smooth aluminum films spin-coated with fluorescent layers was also studied by deep-UV excitation of SPPs with Kretschmann structure [88, 98]. Al nanohole arrays have also been used to enhance the fluorescence enhancement of special molecule, $DBMBF_2$, by 3.8 times, which demonstrates for the first time that Al nanohole arrays can be an attractive structures for fluorescence enhancement applications in the UV. In addition, Yang et al. experimentally demonstrated UV SPEF with gallium nanoparticles, which provides another material choice [112]. Zn nanoparticles can enhance the fluorescence by 5-fold near the UV edge [114]. Significant enhancement up to 20-fold of intrinsic fluorescence of nucleic acid around 340 nm by Pt nanoparticles has been observed [113].

1.2.3.2 UV Surface/Tip-Enhanced Raman Spectroscopy

Surface-enhanced Raman spectroscopy (SERS) has been studied in 1980s even before the term "Plasmonics" appeared (2001) [2]. However, similar to SPEF in UV, research on SERS in UV is still at the early stage. The first UV SERS was observed for pyridine adsorbed on roughened rhodium and ruthenium electrodes with 325 nm excitation in 2003 [123].

And the first deep UV SERS was achieved from crystal violet on Al thin film excited at 244 nm in 2007 [73]. Raman excitation wavelength region below 250 nm is also more interesting because amino acids and proteins show an electronic resonance enhancement in this wavelength region. Compared with SPEF in UV, more Al nanostructures, in addition to Al thin-films, have been fabricated for SERS in UV. Al bowtie nanoantenna (shown in Figure 1.5 (a)) dramatically increased the signal of Raman spectra of benzene by 10^5 times at 258.8 nm excitation [89]. Al nanoparticle arrays (shown in Figure 1.5 (b)) coated with adenine molecules excited at 257.2 nm could detect Raman signal from less than 10 amol molecules, which proved that deep-UV SERS is an extremely sensitive tool for biomolecular detection [94]. Al nanovoids (shown in Figure 1.5 (c)) excited at 244 nm provides enhancement of about 6 orders of magnitude, and good reproducibility was also demonstrated [100].

Tip-enhanced Raman scattering (TERS) is a novel approach combining the sensitivity of SERS and the high-resolution of a scanning probe microscope. The first deep-UV tip-enhanced Raman scattering (TERS) was successfully achieved with an Al-coated silicon tip (shown in Figure 1.5 (d)) from crystal violet and adenine molecules excited at 266 nm in 2009 [76]. This work also demonstrated the possibility to achieve nanoscale analysis and imaging with deep-UV TERS. Recently, UV TERS imaging was accomplished with an Al tip illuminated by 355 nm laser, which gives both topography and Raman scattering of nanomaterials simultaneously with high spatial resolution [93].

1.2.3.3 Other Plasmonic Applications in the UV

UV detectors have many important applications, such as in situ temperature monitoring, ozone layer monitoring and instrument calibration for UV lithography. A LSP-enhanced metal-semiconductor-metal (MSM) UV photodetector with 30 nm Al nanoparticle arrays deposited in between MSM contacts has been proposed, and presents a 1.5x enhancement of quantum efficiency around 340 nm [87]. Deep-UV light-emitting diodes (LEDs) can be used for biological detection, water purification and optical catalysis. A SPP-enhanced deep-UV LED with 5-nm-think Al layer deposited on the surface presents 217% enhancement in peak photoluminescence (PL) intensity at 294 nm. The suppressed PL from LED with Al oxide further proves that the enhanced PL is attributed to the Al layer [95].

Deep ultraviolet light (224.3 nm) excitation of SPPs resonance with an Al film can enhance photoelectron emission by 9 times from the metal surface, because deep-UV SPP has higher energy than that of visible light [84]. Strong plasmonic enhancement in UV can also be used to accelerate the chemical reaction and thermal deposition in the nanoscale.

Al nanoapertures have been applied to photoactivate the surface coupling of biotinylated capture probe oligos [85]. Local thermal energy deposition can be enhanced and controlled with the photothermal effect of Al nanoparticles [97].

Above all, UV Plasmonics has some promising applications. However, the application research is still underdeveloped. Among those potential applications, plasmonic enhancement of UV fluorescence is the promising one due to its unique advantage of directly utilizing native fluorescence, and also due to the solid knowledge base that has been built in the visible range. This is the aiming application of this dissertation work, so the detailed background and the state of the art will be introduced in the following section.

1.3 Plasmonic Enhancement of UV Fluorescence

As mentioned before, by utilizing native UV fluorescence of biomolecules, such as protein and amino acids, it is possible to achieve label-free biomolecular detection. However, the native UV fluorescence needs to be effectively enhanced in order to generate the comparable signal as the dye molecules do in the visible. Plasmonic enhancement of metallic nanostructures has been proven as a promising means in the visible [2], but its feasibility still needs to be carefully examined in the UV.

1.3.1 Basics of Plasmon-Enhanced Fluorescence

Luminescence is the emission of light from any substance that has absorbed energy [35]. It can be described by a system of three energy levels shown in Figure 1.6—singlet ground state S_0, first excited singlet state S_1, and dark nonfluorescing, or first excited triplet state T_1. After the molecules absorb the light, they are excited from the ground state to the excited singlet state. The molecules can relax back to the ground state by emitting one kind of luminescence: fluorescence. They can also move to the triplet state through intersystem crossing, then the transition from triplet state to ground state is forbidden, which can still happen very slowly with emitting another kind of luminescence: phosphorescence. The difference between fluorescence and phosphorescence can be found from the lifetime. Lifetime (τ) is the average time the excited molecules spend before returning to the ground state. Lifetime of fluorescence is usually on the order of nanoseconds, while that of phosphorescence is typically milliseconds to seconds. The procedure of phosphorescence is so low compared with fluorescence that we can treat it as a procedure without emitting light.

Fluorescence and phosphorescence represent one channel of molecules' relaxation from excited state: radiative relaxation. Molecules can also return to the ground state without emitting any light, which is called nonradiative relaxation. Usually the rate constants are

used to describe how fast certain relaxation happens. $k_{tot} = k_{rad} + k_{nr}$, where k_{rad} and k_{nr} stand for the rate constants for radiative emission and nonradiative de-excitation from S_1 to S_0. k_{tot} is the rate constant of total emission including two channels, so according to the definition of lifetime

$$\tau = \frac{1}{k_{tot}}$$

Lifetime is the fingerprint of the molecule, and highly sensitive to the local environment, so the interaction of molecules with plasmonic structures can be effectively monitored by measuring the lifetime.

Quantum yield (ϕ) is the ratio of the number of photons emitted to the number absorbed by the molecule, which can be described as

$$\phi = \frac{k_{rad}}{k_{tot}} = \frac{k_{rad}}{k_{rad} + k_{nr}}$$

so it measures how efficient a molecule is in terms of fluorescence emitting, which is an important factor to be considered in the study of plasmonic enhancement of UV fluorescence.

In order to analyze the fluorescence enhancement of a single molecule, we need a way to describe the fluorescence emitted by a single molecule, which is defined as count rate per molecule (CRM). In steady state, CRM is given by [47, 48]

$$CRM = \kappa\phi\frac{\sigma I_e}{1 + I_e/I_s} \tag{1.10}$$

where κ is the light collection efficiency (combination of the optical system and radiation profile), σI_e the net excitation rate, σ the absorption cross-section and the saturation intensity $I_s = k_{tot}/[\sigma(1 + k_{isc}/k_d)]$, where k_{isc} and k_d are the rate constants for intersystem crossing to the triplet state and relaxation to the ground state, respectively.

Energy transfer between the molecule and the plasmonic structure is mediated through the radiative transition of the molecule (with the internal nonradiative rate k_{nr} unchanged). We denote k'_{rad} as the effective radiative rate of the structure and k'_{nr} as the dissipation rate of the structure, and define the parameter [47]

$$\zeta = \frac{k'_{rad} + k'_{nr}}{k_{rad}} \tag{1.11}$$

to represent the change in lifetime of a perfect dipole emitter (i.e., one with no internal resistive losses, with unity native QY ϕ_0). This factor can readily be obtained from simulation [52], and does not change with the particular value of k_{rad}. The Purcell factor

represents the reduction in lifetime of the molecule [32], i.e., change of total emission rate, and is defined as

$$f_{Purcell} = \frac{\tau}{\tau'} = \frac{k'_{rad} + k'_{nr} + k_{nr}}{k_{rad} + k_{nr}} = 1 + \phi_0(\zeta - 1) \tag{1.12}$$

Lifetime reduction is readily measurable, as described in Section 4.1 of Chapter 4. Note that $1/\tau$ is often referred to as the spontaneous emission rate, not to be confused with the radiative rate k_{rad}, and ϕ_0 is the native QY. The change in QY can then be expressed as

$$f_\phi = \frac{f_{rad}}{f_{Purcell}} \tag{1.13}$$

where $f_{rad} = k'_{rad}/k_{rad}$ is the ratio of the effective radiative rate with the influence of the plasmonic structure (k'_{rad}) and without the structure (k_{rad}).

It is clear from Equation 1.12 that the Purcell factor for a nonideal emitter depends on its native QY ϕ_0. Stated differently, two emitters with different native quantum yields will experience different Purcell factors within the same electromagnetic environment. For an emitter with low ϕ_0, k_{nr} dominates k_{rad}, and since the structure acts through k_{rad}, ζ must be large to effect a decrease in lifetime. For the same emitter, f_ϕ is roughly proportional to f_{rad}. In contrast, for a high ϕ_0 emitter, k_{rad} dominates k_{nr}, and lifetime reduction is roughly proportional to ζ . However, since $f_{rad} \leq \zeta$, then $f_\phi \lessapprox 1$. This is the origin of increased net fluorescence enhancement for molecules with low quantum yield [47, 52], and also leads to the practical conclusion that it takes a poor emitter in the first place in order to realize enhancement via f_ϕ .

The expression for CRM can be simplified under saturated ($I_e \gg I_s$) and unsaturated ($I_e \ll I_s$) conditions

$$CRM|_{I_e \gg I_s} \rightarrow \kappa k_{rad} \qquad \Rightarrow \qquad NE|_{I_e \gg I_s} \rightarrow f_\kappa f_{rad} \tag{1.14}$$

$$CRM|_{I_e \ll I_s} \rightarrow \kappa \phi \sigma I_e \qquad \Rightarrow \qquad NE|_{I_e \ll I_s} \rightarrow f_\kappa f_I \frac{f_{rad}}{f_{Purcell}} = f_\kappa f_I f_\phi, \tag{1.15}$$

where NE represents the net fluorescence enhancement in each limit, f_I is the excitation enhancement, and f_κ is the change in collection efficiency, which we set to unity throughout the paper in order to focus on change in effective radiative rate. From these two expressions, we know that net enhancement of fluorescence is mainly determined by excitation enhancement (f_I) and emission enhancement (f_{rad} and $f_{Purcell}$).

1.3.2 Native UV Fluorescence

Organic molecules have electronic resonances in the UV part of the spectrum. The advantages of UV-resonant molecular spectroscopy have been recognized for decades [61,

124], such as the use of UV resonant Raman scattering for structural conformational and kinetics studies. Biomolecules such as peptides and proteins contain residues that absorb in the UV (220-280 nm); the aromatic amino acids tryptophan, tyrosine and phenylalanine are fluorescence and Raman active. However, aromatic residues have relatively low fluorescence quantum efficiencies and molar extinction coefficients [59, 124], as do nucleic acid bases, so achieving significant enhancement via plasmonic structures [71] could be a key enabling factor in the label-free detection of proteins [67] or DNA molecules [66, 125].

Table 1.1 lists some relevant properties of UV active species for comparison against the common red dye label Cy-5. In fluorescence, the "brightness" of nucleic and amino acids, as defined by the product of absorption cross-section and quantum yield, is orders of magnitude smaller than Cy-5, making enhancement methods essential for practical label-free detection based upon native fluorescence. In addition, the Stokes shift, i.e., the wavelength difference between absorption and emission peaks, is typically larger for UV molecules. It implies that multiresonance of plasmonic structures are required in order to overlap both absorption and emission.

1.3.3 State of the Art

Plasmonic enhancement of UV fluorescence is the main topic of this dissertation work, so it is worth summarizing the state of the art of the research in this area based on the overview of the previous section. Then a detailed research plan can be made.

Table 1.2 presents the research status of experimental studies outlined in terms of species, excitation and emission wavelengths, plasmonic structures, fluorescence enhancement and lifetime reduction. The list is arranged in chronological order. One can see that only Al and Ga have been experimentally studied, which implies that more materials can be exploited based on the proposed materials reviewed in Section 1.2.2. Among them, Mg is the most possible candidate thanks to the work of Prof. Guruswamy's group. As discussed in Section 1.2.2, they have carried out extensive studies on material properties [64, 65], which give us the opportunity to further evaluate the potential of Mg for UV fluorescence enhancement. One can also see that only nanoparticles and hole arrays have been studied, so more designs can be investigated. Maximal fluorescence enhancement that has been published is 80, which is weaker compared with that of the visible range. It implies that there is more space for material and structure optimization. Furthermore, all of the fluorescence was measured from the thin-layer embedded with fluorescent molecules, which makes it difficult to analyze the enhancement of a single molecule. The diffusing molecules or molecules in solution have to be used for that purpose. At last, three works [71, 78, 113]

have demonstrated that different molecules have different fluorescence enhancement and lifetime reduction even if the plasmonic environment is the same. However, no further analysis has been performed to explain why.

In summary, there are still a great deal of unknown areas worth exploiting in the field of UV fluorescence enhancement. Based on the summary of the research status, we will choose Al and Mg as plasmonic materials, then design and fabricate nanostructures, and study the plasmonic enhancement of UV fluorescence of diffusing molecules.

1.4 Dissertation Outline

Aiming at filling the gap of Plasmonics in the UV, we chose the application of label-free biosensing with plasmon-enhanced UV fluorescence as the entry point. This dissertation research follows the work flow shown in Figure 1.7, including a loop of numerical design, thin-film characterization and nanofabrication, and UV fluorescence study. The experimental results obtained at the last step will be used to improve the previous steps. The rest of the dissertation will be organized into five chapters accordingly.

Chapter 2 will develop the design method, and present a performance analysis of three canonical plasmonic structures. In addition, a novel design of a compound bullseye structure will be proposed for the purpose of compensating for the large Stokes shift typical of UV fluorescence.

Chapter 3 will characterize Al thin-film properties in terms of dielectric constants, oxide layer thickness and oxidation percentage. Characterization methods and procedures will be developed and summarized. Several designed plasmonic structures will be fabricated with focused ion beam milling. The recipe of Al nanofabrication will be given. The detailed procedure of automatic slicing and imaging with duo-beam analysis for undercut measurement will be introduced as well.

Chapter 4 will present, in detail, the experimental study of lifetime reduction with Al nanoapertures. Our design method will be validated, so that further numerical analysis can be applied on the study of UV fluorescence enhancement of Al nanoapertures.

Chapter 5 will evaluate the feasibility of applying magnesium in the UV plasmonic applications. The UV lifetime reduction of Mg nanoapertures will be experimentally studied. Extensively numerical simulation will be performed to analyze the UV fluorescence enhancement of Mg nanoapertures. In addition, extraordinary optical transmission (EOT) of Mg nanohole arrays in the UV will be measured and compared with EOT of Al structures with the same parameters.

Chapter 6 will summarize the whole dissertation and propose the ideas for future work.

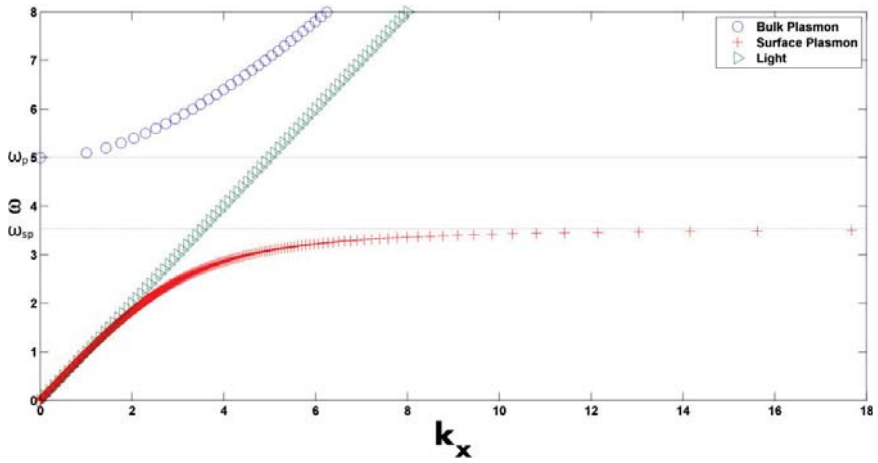

(a)

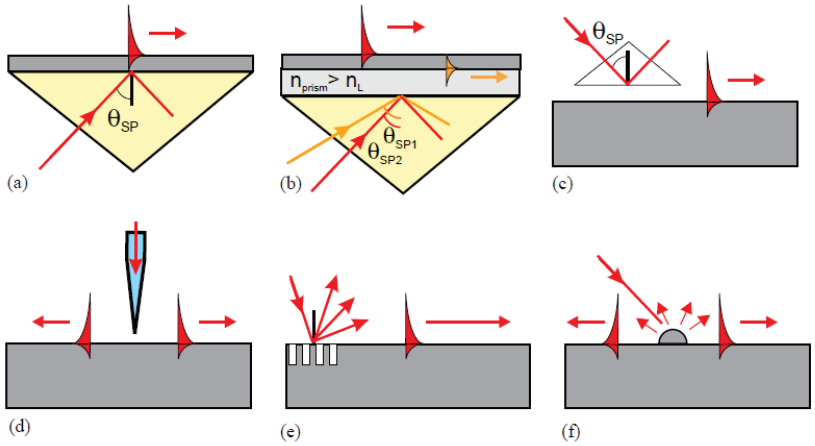

(b)

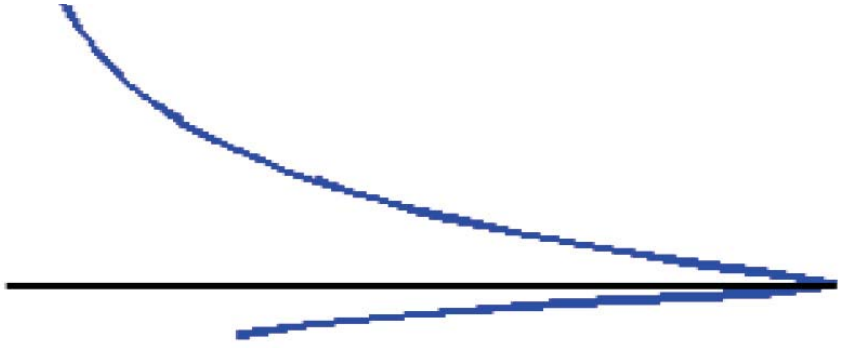

(c)

Figure 1.1. Diagrams of SPP properties: (a) dispersion relations of SPPs, bulk plasmon and light, (b) different strategies to excite SPPs (Reprinted from [126], Copyright (2005), with permission from Elsevier.) and (c) E-field intensity of SPPs across the interface.

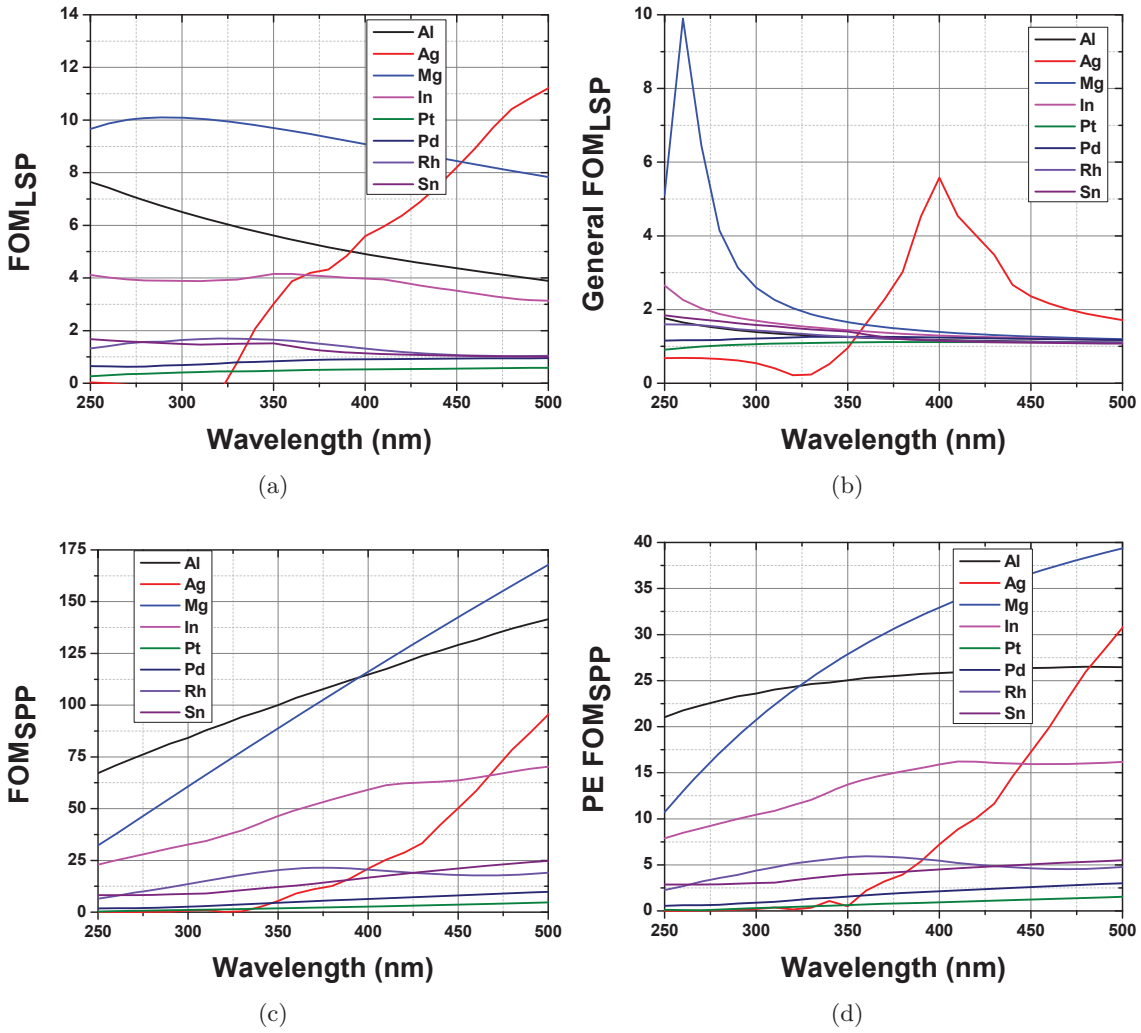

Figure 1.2. Figures of merit of possible UV plasmonic materials versus wavelength. (a) FOM_{LSP} (Equation 1.6 considering the resonant condition), (b) General FOM_{LSP} (Equation 1.3 considering both resonant and nonresonant conditions), (c) FOM_{SPP} (Equation 1.7 calculating ratio of the real and the imaginary parts of SPP wave vectors) and (d) $PEFOM_{SPP}$ (Equation 1.2). An Al film supported by a glass substrate and covered with water is considered for $PEFOM_{SPP}$. A 20 nm Al nanosphere surrounded with water is considered for general FOM_{LSP}.

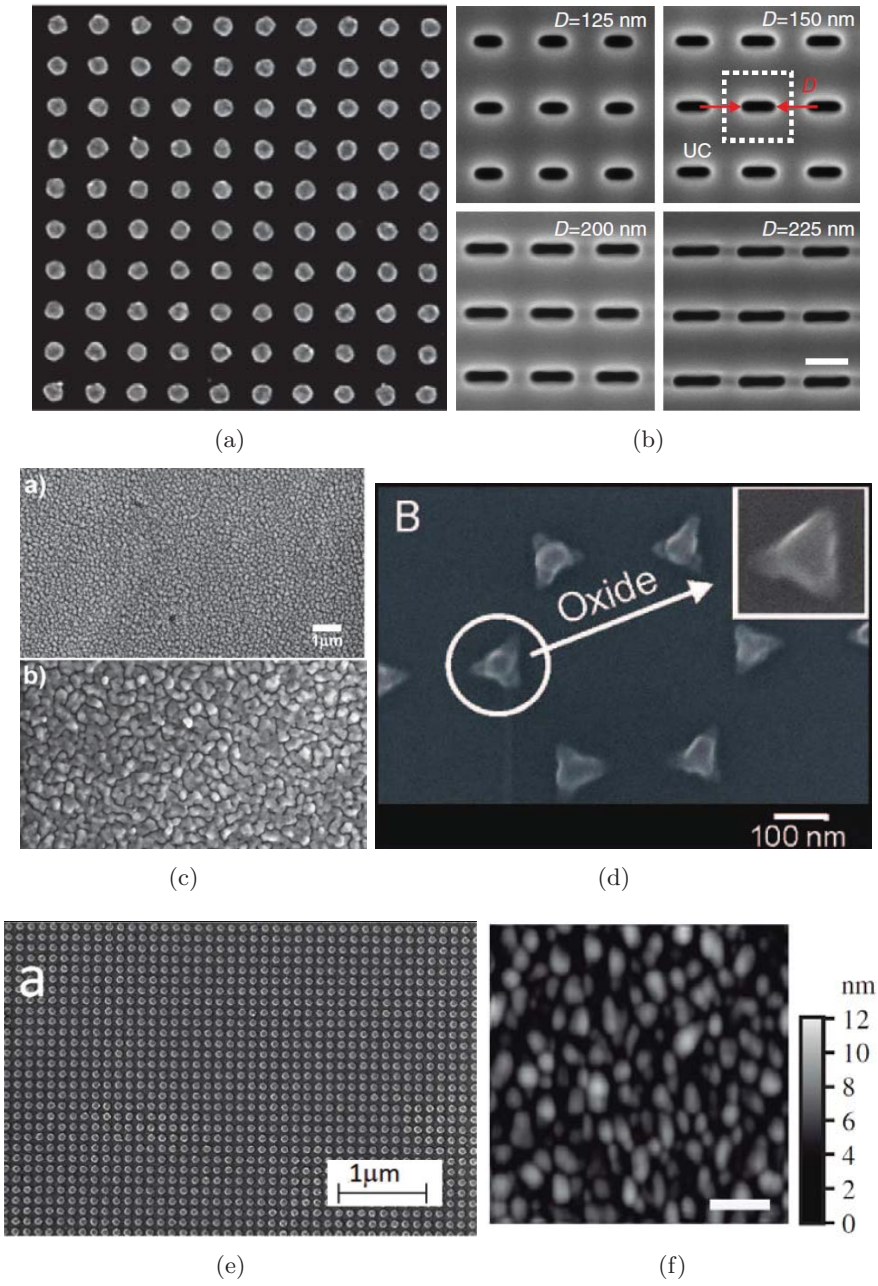

Figure 1.3. SEM images of (a) Al nanodisks (EBL). Scale bar is 100 nm. Reprinted from [87] by permission of IOP Publishing. (b) Nanoslits (FIB). Scale bar is 200 nm. Reprinted by permission from Macmillan Publishers Ltd: Nature Communications [116], copyright 2014. (c) Al thin-film (thermal evaporation). Adapted with permission from [71]. Copyright 2007 American Chemical Society. (d) Al nanotriangles (nanosphere lithography). Reprinted with permission from [75]. Copyright 2008 American Chemical Society. (e) Al nanoparticles (extreme UV interference lithography). Reprinted with permission from [94]. Copyright 2012 American Chemical Society. (f) Al nanoparticles (oblique angle deposition). Reprinted from [106] by permission of IOP Publishing.

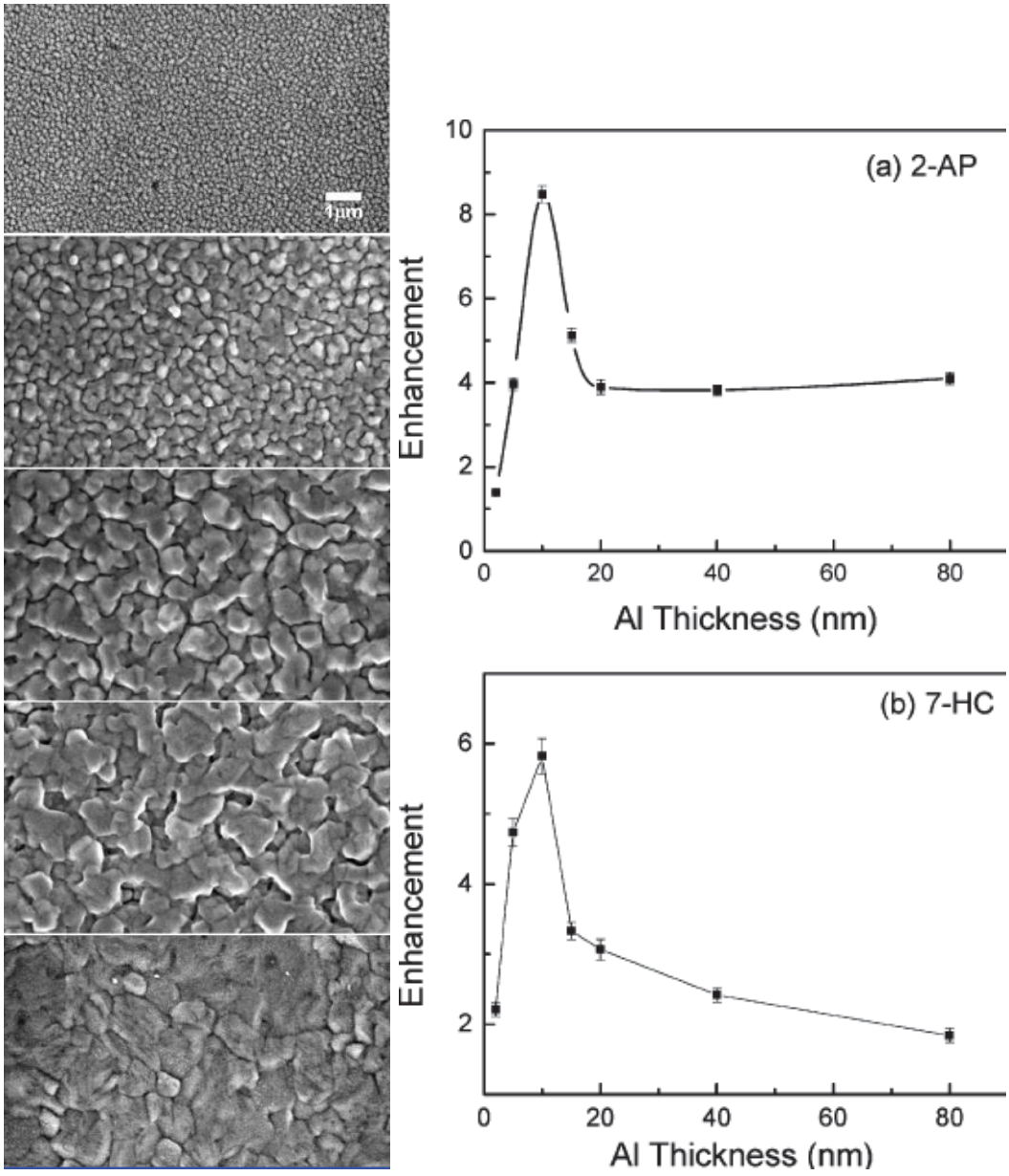

Figure 1.4. UV fluorescence enhanced by Al films. (a) SEM images of thermally evaporated Al films on quartz substrates with thicknesses increasing from top down. (b) Dependence of fluorescence intensity enhancement of 1-AP and 7-HC on AL film thickness. Reprinted with permission from [71]. Copyright 2007 American Chemical Society.

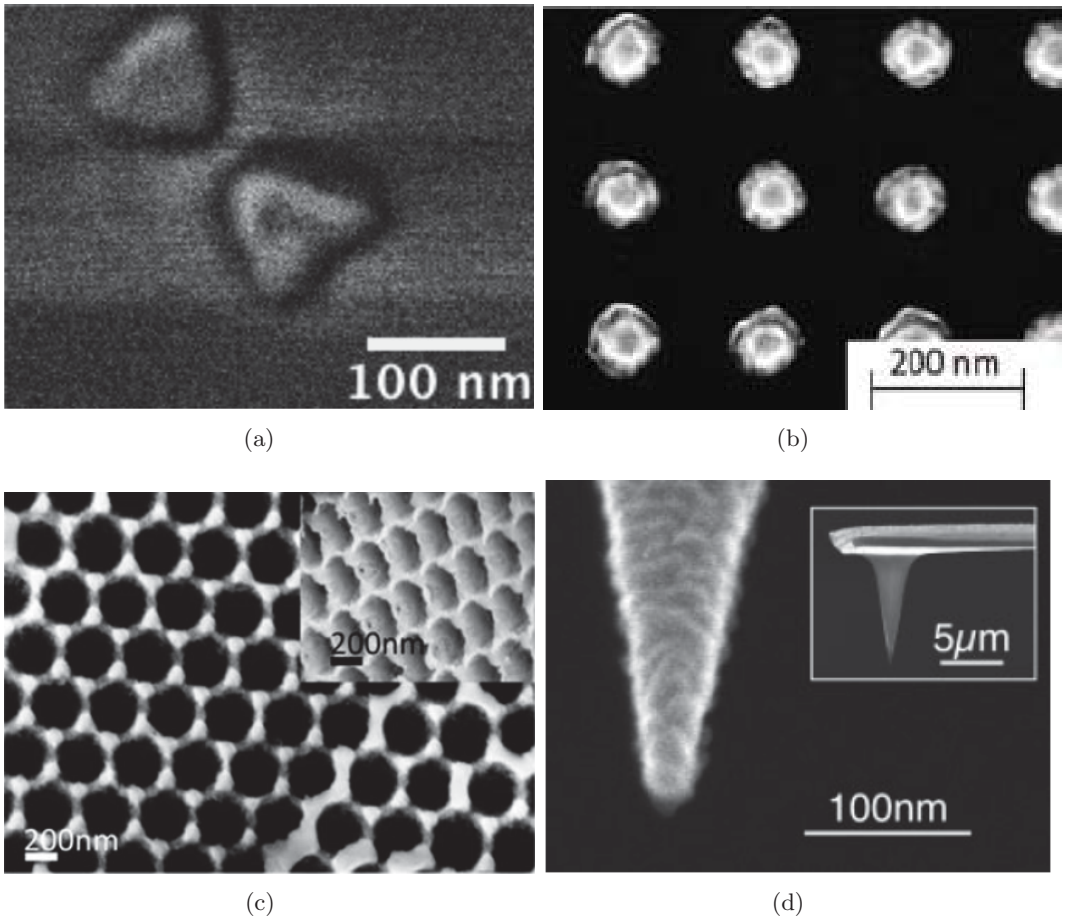

Figure 1.5. SEM images of (a) Al bowtie nanoantenna (Reprinted with permission from [89]. Copyright 2012, AIP Publishing LLC.), (b) Al nanoparticle arrays (Reprinted with permission from [94]. Copyright 2012 American Chemical Society.), (c) Al nanovoid arrays (Reprinted with permission from [100]. Copyright 2013 American Chemical Society.) and (d) silicon tip coated with 25-nm-thick Al (Reprint with permission from [76]. Copyright 2009 John Wiley & Sons Inc.) for application of surface/tip enhanced Raman spectroscopy.

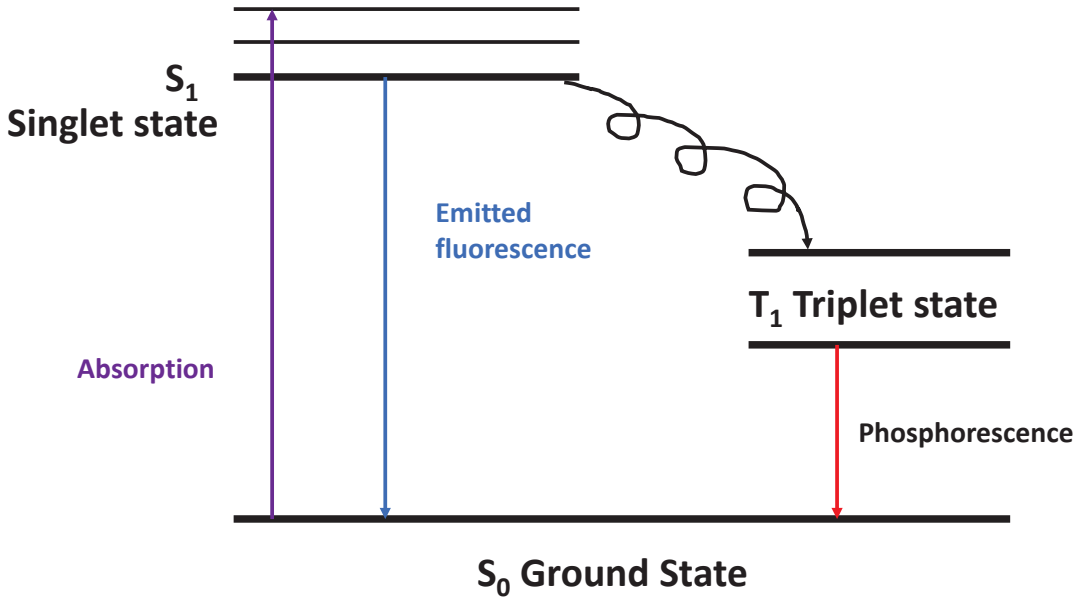

Figure 1.6. Diagram of system of three energy levels for luminescence.

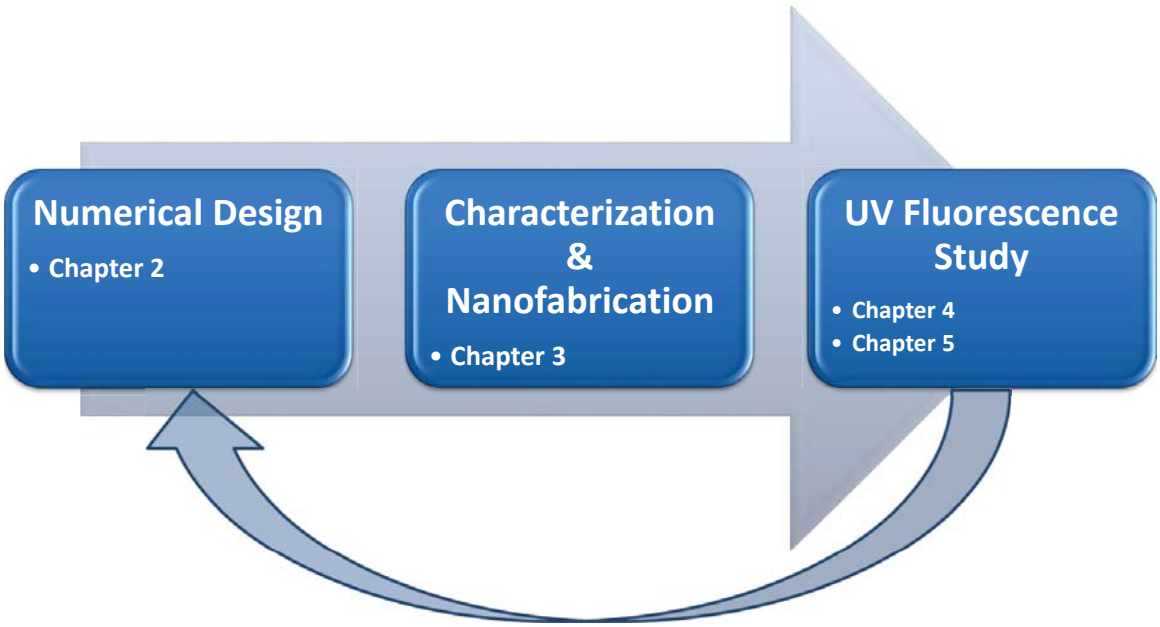

Figure 1.7. Work flow of this dissertation research.

Table 1.1. Photophysical properties of UV active species such as DNA and aromatic amino acids. Note that there is variation among the specific nucleic acids; only average values are reported. Here, δ is the photon absorption cross-section, ϕ_0 is the native quantum efficiency. Data for Cy-5, a common fluorescent label in the red, is shown for comparison.

Species	λ_{abs} (nm)	σ (cm^2)	$\lambda_{emit}(nm)$	ϕ_0
nucleic acid	260	2×10^{-17}	340	<0.1%
Tryptophan	225, 280	10^{-17}	340	13%
Tyrosine	230, 275	2×10^{-18}	300	14%
Cy-5	650	5×10^{-14}	670	28%

Table 1.2. Summary of research status of plasmonic enhancement of UV fluorescence.

Species	$\lambda_{ex}/\lambda_{em}$ (nm)	Structures ($\lambda_{resonance}$)	Fluorescence Enhancement	Lifetime Reduction	
DNA	287/340	Ag islands (∼420 nm)	80	3	[66]
Tryptophan	280/340	Ag islands (∼450 nm)	2	2	[67]
DNA	300/380	20 nm Al film (∼450 nm)	NA	1.2	[69]
2-AP 7-HC	300/370 300/450	<20 nm Al islands (Broad∼650 nm)	9 6	∼3.8 ∼2	[71]
7-HC	405/470	∼10 nm Zn islands (380 nm)	8	NA	[114]
Tryptophan	280/340	10 nm Al islands (∼450 nm)	14	6	[72]
Tryptophan	280/340	10 nm Al islands (∼450 nm)	11	2	[77]
NATA-tys NATA	280/340 280/340	10 nm Ag/Al islands (Broad∼620 nm)	10 2	∼3 ∼2.5	[78]
Nucleotides DNA	280/340 280/340	10 nm Pt islands (Broad∼225 nm)	20 5	∼3 ∼2.5	[113]
Water	204/450	21 nm Al film (NA)	2	NA	[88]
CdS QDs	266/380	18 nm Al film (NA)	18	NA	[98]
Crystal violet	325/590	∼70 nm Ga NPs (590 nm)	18	NA	[112]
$DBMBF_2$	385/590	Al hole arrays (440 nm)	3.8	NA	[104]

CHAPTER 2

DESIGN OF UV PLASMONIC STRUCTURES

Based on the three-level model of fluorescence emission discussed in Section 1.3.1, we will develop a design method by using finite difference time domain (FDTD) method to numerically calculate the enhancement factors involved in Equation 1.14 and 1.15, so that the influence of plasmonic structures on excitation and emission procedures of UV fluorescence can be fully analyzed. Using our design method, we will compare the performance of three plasmonic antenna structures for UV fluorescence enhancement [81]. Among the antenna performance metrics considered are the excitation enhancement (f_I) and quantum yield (QY) enhancement (f_ϕ), the product of which represents the net fluorescence enhancement (NE). With realistic structures in aluminum, we will predict the net enhancement of UV fluorescence. The advantage and disadvantage of different designs will be also discussed. For the purpose of compensation of large Stokes shift typical of UV fluorophores, we will also present and analyze a novel optical antenna structure (compound bullseye) in the form of a polarization multiplexed bullseye antenna with a central nanoaperture [80]. The resonance response for each polarization can be tailored to a specific wavelength separately. We will predict intra-aperture intensity enhancements at two independent resonance wavelengths spanning the UV-visible spectrum. The possibility of tuning enhancement amplitudes of two resonances by adjusting the aperture diameter will be also discussed.

2.1 Design Method

Electromagnetic modeling is a powerful and efficient tool for the design and optimization of plasmonic structures given the advancing of computing power of modern computers. The finite-difference time-domain (FDTD) method is a grid-based differential numerical modeling method. The temporal and physical spaces are divided into small meshes. The time-dependent Maxwell's equations (in partial differential form) are discretized using central-difference approximations on the meshing points. The electromagnetic problem can

be solved in a leapfrog manner: the electric field vector components in the space are solved at a given time step; then the magnetic field vector components in the same space are solved at the next time step; and the process is repeated over and over again until the field reaches steady-state. By utilizing FDTD method (Lumerical FDTD Solutions), we can accurately simulate the electromagnetic behaviors of plasmonic structures, which is an essential step of our design method.

In our design of structures for fluorescence enhancement, we always assume an epifluorescence configuration [51], which means the excitation and fluorescence collection are achieved from the same side (the substrate side). The plasmonic enhancement of fluorescence involves two contributions: excitation and emission, so two simulations are required for both procedures. Figure 2.1 shows the cross-section view of simulation models (nanoaperture) for excitation and emission calculations, respectively. In Figure 2.1 (a), a plane wave with unit amplitude (1 V/m) (purple arrow stands for direction; blue arrow stands for polarization) at wavelength corresponding to the molecular absorption peak is introduced inside the substrate, which normally illuminates the structures from the bottom. Average excitation enhancement is calculated by integrating the total intensity within a thin (usually 10 nm thick) monitor (yellow rectangles) covering the active region, and dividing by the integrated intensity within the same volume but in the absence of the metallic structures.

Figure 2.1 (b) shows the model for the emission calculations. The analysis of the FDTD results rely on the fact that, for an atomic dipole transition that can only occur through radiation, the quantum mechanical decay rate in an inhomogeneous environment can be related to the classical power radiated by the dipole in the same environment [127]. Specifically, we can relate every rate constant to the corresponding power, such as

$$\frac{k_{rad}}{k_{rad}+k_{nr}} = \frac{P_{rad}}{P_o}$$

where k_{rad} and k_{nr} are the rate constants for radiative emission and nonradiative de-excitation, P_{rad} and P_o the radiative and total emission power of a dipole inside a metallic structure. In our simulation, an electric dipole with unit amplitude (1 V/m) (only blue arrow stands for polarization) at wavelength corresponding to the molecular emission peak is positioned at the center of active region. The radiative emission is calculated as the transmission through monitors around the structure (two yellow lines in the top and bottom regions), while the total emission is calculated as the transmission through monitors around the dipole (small yellow box). Calculations are performed for x, y, and z dipole orientations, and the calculated enhancements are an average across these orientations.

It should be noted that the calculated total emission enhancement corresponds to ζ in Equation 1.11, which is equal to Purcell factor ($f_{Purcell}$) in Equation 1.12 when a perfect emitter with native QY $\phi_0 = 1$ is considered. Therefore, we need to used Equation 1.12 to convert a calculated Purcell factor (ζ) to a practical one corresponding to a specific molecule. In addition, more consideration needs to be given in order to simulate the practical case of fluorescence emission. In the practical case, the fluorescent molecule or dipole source in simulation cannot be localized only in the bottom 10 nm region as simulated in the numerical model. The Purcell factor and radiative enhancement measured in the experiment is a position-average over all contribution of molecules inside the active region (aperture for nanoaperture). In order to calculate those average values, the simulation need to be performed mainly as following three steps:

1. Perform simulations corresponding to different dipole positions inside the active region.

2. Calculate net enhancement for different dipole positions.

3. Calculate position-average Purcell factor/radiative enhancement as the weighted-average of Purcell factor/radiative enhancement with the net enhancement versus dipole position.

Using our design method, we can calculate excitation enhancement (f_I), radiative enhancement (f_{rad}) and total emission enhancement or Purcell factor ($f_{Purcell}$). Plugging those values into Equations 1.13, 1.15 and 1.14 discussed in Section 1.3.1, we can finally analyze QY enhancement and net enhancement of a specific molecule by any plasmonics structures. This method cannot only design and optimize the plasmonic structures for future fabrication, but also help to interpolate the experimental data of UV fluorescence study.

2.2 Plasmonic Structures Design for UV Fluorescence Enhancement

As the first step of UV fluorescence study, we evaluate the performance of three canonical plasmonic structures for UV fluorescence enhancement by using our design method. This work has been published in Optics Express [81].

2.2.1 Models

Three structures studied are depicted in Figure 2.2, including the plan views and cross-sections of (a) dipole antenna, (b) bullseye aperture and (c) aperture array. The structures

are assumed to be supported by a semi-infinite glass (SiO_2) substrate and covered by water. The active region, where the enhanced local field interacts with the fluorophore, is shown in the zoom-in image in Figure 2.2 extending just 10 nm above the glass substrate. Dielectric constants of aluminum, water and glass are incorporated via the dielectric constant obtained from handbook data [62].

Antisymmetric and symmetric boundaries are used in the FDTD simulation along the x and y directions according to the symmetry of the structure and the source, which reduces the calculation and memory overhead without sacrificing resolution. Perfectly matched layers (PML) are used on the other boundaries. The grid size is $1\times1\times1$ nm^3 for the dipole antenna and $2\times2\times$ 2 nm^3 for the bullseye and hole array. Here, The wavelengths of excitation and emission calculation correspond to one kind of amino acid, tryptophan, whose native quantum efficiency is $\phi_o = 13\%$ [124]. Tryptophan has maximum absorption near 266 nm and peak emission near 340 nm. It is noted that radiation only into the substrate is used in our calculations, which corresponds to a typical epifluorescence setup through a glass substrate [51], resulting in the change of an effective quantum efficiency. Thus, ϕ_o of tryptophan becomes 8% [79].

2.2.2 Dipole Antenna Design

There are four geometrical parameters determining the response of the dipole antenna, as shown in Figure 2.2. The arm length L defines the antenna resonance wavelength, while the gap distance G affects the coupling between the two arms. In our studies, we fix both thickness T and width W of each arm at 30 nm for simplicity, and vary gap size ($20\leq G \leq 50$ nm) and arm length ($20\leq L \leq 180$ nm).

Figure 2.3 shows the 2-D enhancement maps of six antenna performance metrics versus L and G. Peaks in both excitation and emission enhancement occur under resonance conditions determined by the arm length, whereas the gap size controls the level of enhancement. As expected, smaller gap size generates higher enhancement due to the stronger coupling between the arms. From the map of excitation enhancement in Figure 2.3(a), there are three resonances at the excitation wavelength, for arm lengths L=20 nm, 80 nm and 130 nm. The field intensity distributions (not shown) verify that these correspond to different resonance orders. Furthermore, peak enhancement increases with the arm length, which agrees with previous research [128], but it decreases at the fourth resonance (not shown here) due to the increase of material absorption. The highest excitation enhancement is $\sim$17 at the third resonance (when G=20 nm).

From the maps of emission enhancement in Figure 2.3(b), 2.3(c), 2.3(d) and 2.3(e),

the first and second peak values are at L=40 nm and 120 nm, which are shifted to longer arm length due to the longer emission wavelength of the dipole (340 nm compared to 266 nm). Comparing the peak enhancements at the two emission resonances, the Purcell factor is relatively unaffected by the arm length (maximum $f_{Purcell}$ is ∼11 when G=20 nm and L=40 nm), but the radiative enhancement factor (f_{rad}) has a lower peak value at the longer arm length. This behavior implies that the nonradiative emission increases with increase of the volume of metallic structure, which in turn gives the lower peak enhancement of QY at the longer arm, as shown in Figure 2.3(e) (maximum f_ϕ is ∼4.5 when G=20 nm, L=30 nm). The net enhancement (NE) in Figure 2.3(f) is the product of f_I and f_ϕ, and reaches maximum values of ∼27 at both the first (L=20 nm, G=20 nm) and second (L=120 nm, G=20 nm) resonance, where QY enhancement is greater for the shorter antenna. It should be noted again that only the radiative enhancement into the substrate is used to calculate f_ϕ and NE, but due to the finite thickness of the antenna, some radiation escapes into the upper half-space.

In the above analysis, the radiation pattern was not considered (i.e., $f_\kappa = 1$). The far-field radiation patterns of structures corresponding to the first (L=20 nm, G=20 nm) and second (L=120 nm, G=20 nm) peak NE, calculated for an x-polarized electric dipole in the active region, are shown in Figure 2.4(a). The patterns are indicative of dipole and quadrupole resonances, because the two structures are close to the corresponding order of emission resonance. The radiation of the first resonance has a prominent main lobe along the z direction (270°) with a divergence angle of ±55°, while radiation from the second resonance has two strong side lobes around ±50° with respect to the z direction, each side lobe with divergence angle around ±15°. The spatial cross-section distributions of $|E|^2$ for the two resonance modes are also shown in Figure 2.4(b) and 2.4(c), respectively. A logarithmic scale is used to allow a greater dynamic range of field intensity to be displayed. The two distinct resonance modes are clearly seen by inspecting the number of nodes in the antenna arms.

2.2.3 Bullseye Antenna Design

The bullseye antenna has more a complicated structure compared to the dipole antenna, which involves six geometrical parameters shown in Figure 2.2. Fortunately, most of the parameters can be approximately related to the groove pitch P through design criteria [129]. In addition, the hole diameter (D) defines the environment around the fluorophore, and has an influence on emission enhancement somewhat independent from the other parameters. The depth (S) and width (W) of the grooves can further modify the optical response

through groove modes [130], but these do not change the working mechanism of the bullseye structure, which relies on constructive interference at the central hole of standing waves emitted by the independent grooves [131]. Therefore, we fix the depth and width as S =20 nm and W =60 nm to remove the effect of the groove mode for simplicity. The thickness of the structure (T) is set to 100 nm. The number of grooves is set as 3 to reduce memory and computational time requirements.

Maps of the different figures of merit are generated by changing the hole size ($40\leq D \leq 100$ nm) and pitch ($100\leq P \leq 320$ nm), as shown in Figure 2.5. These maps have similar features to those of the dipole antenna: peaks in both excitation and emission enhancements occur under resonant conditions, determined by the pitch (P), while the hole size (D) affects the level of enhancement. The map of f_I in Figure 2.5(a) has first, second and third resonance peaks at P=140 nm, 200 nm and 300 nm. The larger pitch produces the higher enhancement due to the greater area for light collection. The maximum excitation enhancement is ∼61 at the third resonance with D=50 nm. The maps of emission enhancement in Figure 2.5(b), 2.5(c), 2.5(d) and 2.5(e) show the first and second peak values around P=180 nm and 280 nm, which are also shifted due to the difference in wavelengths between emission and excitation. The map of NE under unsaturated condition in Figure 2.5(f) also exhibits three peaks, with values of ∼91, 118 and 188 at P=140 nm, 200 nm and 300 nm, respectively (at D=50 nm), which follows exactly the resonances of f_I because of the dominate effect of f_I over f_ϕ.

The far-field radiation patterns are also considered, as shown in Figure 2.6(a). Three patterns corresponding to the three peak values of NE are plotted. The pattern of the first peak ($P140D50$) has two comparatively small side lobes, each with divergence angle of $\pm 15^\circ$, because the pitch corresponds to the excitation resonance rather than the emission resonance. By contrast, the other two patterns are from structures that are close to emission resonance, and show the features of first order (a main lobe along z with a divergence angle of $\pm 5^\circ$) and second order (two strong side lobes with divergence angles of $\pm 5^\circ$) of resonance, respectively. The spatial distribution of $|E|^2$ for the three cases in cross-section at the glass interface is also shown in Figure 2.6(b), 2.6(c) and 2.6(d), respectively. The resonance and off-resonance features can be clearly seen from the corresponding images.

It is worth comparing the bullseye and dipole antennas. The bullseye is an extended planar structure with much greater interaction cross-section, thus the excitation enhancement f_I is much higher for roughly the same active area. The round aperture in the bullseye has an optimal size for the excitation and emission processes - about 50 nm for excitation and 70 nm

for emission, which agree with previous studies [79] - whereas, enhancement will generally increase for the dipole antenna with decreasing gap. For the bullseye, the peak values of f_{rad} into the substrate (Figure 2.5(d)) are much larger than the total f_{rad} (Figure 2.5(c)), because the thicker aperture strongly attenuates radiation into the upper half-plane. Furthermore, the bullseye exhibits more directionality in emission due to constructive interference with scattering by the concentric grooves, an effect sometimes called "beaming" [132].

2.2.4 Aperture Array Design

If a fluorophore could be placed inside a specific aperture, an aperture array can be treated as a variation from the bullseye with one central aperture surrounding by a square lattice of apertures instead of concentric grooves. Therefore, similar performance should be expected in terms of fluorescence excitation and emission. Again our analysis will be focused on period P and aperture size D as parameters. The thickness of the structure (T) is fixed at 100 nm. The total number of periods is set as 6 due to the limitation of memory and speed of FDTD simulation.

Maps of the figures of merit are generated by changing the aperture size ($40 \leq D \leq 100$ nm) and period ($100 \leq P \leq 320$ nm), and are shown in Figure 2.7. Excitation enhancement shows resonance peaks near the same regions as the bullseye, but with much smaller enhancement values (maximum $f_I \sim 23$). A more obvious difference can be seen from emission enhancement in Figure 2.7(b), 2.7(c), 2.7(d) and 2.7(e). The influence of the period is less distinct, which implies that there is a weaker interaction between the central and nearby apertures than there is between a central aperture and concentric grooves. Therefore, the emission enhancement of the aperture array is closer to that of a single aperture, where the aperture size D is the dominant factor. The emission figures of merit $f_{Purcell}$, f_{rad} and f_{ϕ} have similar features, with maximum enhancements $\sim$4, for $D \sim$80 nm. These results are very close to those from a single aperture reported before [79] and obtained from a different simulation method, which further validates our analysis. The map of NE under unsaturated conditions exhibits three peaks, with values $\sim$41, 37 and 40 at P=120 nm, 200 nm and 300 nm, respectively, for D=50 nm, which follow the dominant excitation resonance. The stronger excitation enhancement due to the collective SPP resonance makes the NE of an aperture array stronger than that of single aperture.

The far-field angular radiation patterns from the aperture array are shown in Figure 2.8(a). The patterns for the near resonant cases ($P200D50$ and $P300D50$) have distinct directional peaks on broad nondirectional backgrounds, implying some interaction between apertures, while the off-resonance ($P120D50$) case exhibits a broad nondirectional

pattern, suggesting reduced interaperture interaction. The spatial distributions of $|E|^2$ at the glass interface for the three cases is also shown in Figure 2.8(b), 2.8(c) and 2.8(d), respectively, showing that there is no interaction between apertures in Figure 2.8 (b), while weak interaction can be found in Figure 2.8(c) and 2.8(d).

2.2.5 Performance Comparison

After the analysis of the three antenna structures, it is helpful to compare their performance. The maximum enhancement values are listed in Table 2.1. For excitation enhancement (f_I) under plane wave illumination, the bullseye gives the best performance ($\sim$61) due to its large concentrating structure. While comparing the structures based upon plane wave illumination might be appropriate for nanoantenna arrays, if single structures are to be compared, then focused illumination needs to be considered. For example, comparing the dipole and bullseye structures under the conditions of maximal f_I, one might use focused illumination of diameters 280 nm and 1.8 μm, respectively. Assuming the same power in each beam, then the intensity in the gap of the dipole antenna would be about 700$\times$ the intensity incident on the bullseye, for which the intensity within the central aperture of bullseye remains as 60.5$\times$ incident. This comparison is simply a statement that, within the diffraction limit, focusing via conventional imaging is more efficient than plasmonic focusing. The dipole antenna produces the highest emission enhancement with $f_{Purcell}$ $\sim$11, f_{rad} $\sim$7, and f_{ϕ} $\sim$4.5, due to its favorable gap structure.

The far-field angular radiation patterns of the first order of emission resonance from three structures is shown in Figure 2.9. The patterns are normalized for comparison. The bullseye antenna has the most directionality due to its extended structure with strongly interacting concentric grooves.

2.3 Polarization Multiplexed Resonances for Stokes Shift Compensation

As discussed in Section 1.3.2, UV fluorescent molecules typically present a large Stokes shift, i.e., a big difference between absorption and emission peaks. In order to fully utilize the plasmonic enhancement of metallic nanostructures, the structure is required to work under the resonant condition (matching the resonant wavelength to molecules' absorption and emission peaks). It is difficult to achieve this goal by using single resonance for such a large Stokes shift of UV molecules. In this section, we discuss a simple approach to achieving multiband response through the use of polarization multiplexing. We demonstrate this approach with the special compound bullseye structure consisting of a nanoaperture

surrounded by annular corrugations. Multiple response wavelengths are chosen based upon wavelengths commonly used in photochemical crosslinking (365 nm) and fluorescence excitation (532 nm and 635 nm). This work has been published in Plasmonics [80]. The content is presented with kind permission from Springer Science and Business Media.

2.3.1 Models

The compound bullseye structure considered here is shown in Figure 2.10, which consists of two partial bullseye structures with independent sets of parameters along two orthogonal directions. Aluminum is used in these studies because of its plasmonic response at short wavelengths [79]. We assume that this structure is supported by a semi-infinite glass (SiO_2) substrate and covered by air. Our goal is to study local field enhancement just above the glass substrate; therefore, the concentric grooves are placed on the excitation side, which is at the interface of Al and the glass substrate, and illumination is from the substrate side. The width, depth and pitch of the grooves are denoted by w, s and p, respectively, and the diameter and the depth of the nanoaperture are denoted by d and t, with $t = 200$ nm. The distance between the first groove and the nanoaperture is denoted by a, while the number of grooves is denoted by n. These parameters are varied in order to tune the resonant wavelength and optimize the field enhancement inside the nanoaperture. The area of the bullseye structure is fixed at 2.2×2.2 μm^2 in order to reduce the computation time, which means the number of grooves, n, is different for each resonant wavelength.

The size of the computational region is $3 \times 3 \times 0.8$ μm^3. Antisymmetric and symmetric boundaries are used along the x and y directions according to the symmetry of the structure and the source, which reduces the calculation and memory overhead without sacrificing resolution. Perfectly matched layers (PML) are used on the other boundaries. The grid size is $5 \times 5 \times 2$ nm^3 in the area around the metallic structure. An x-polarized or y-polarized plane wave with unit amplitude (1 V/m) is introduced inside the substrate, which normally illuminates the structure from the bottom. A 20 nm thick cylindrical monitor is placed on the bottom of the aperture in order to calculate the average intensity of the electric field within it, which is shown in the zoom-in diagram of Figure 2.10 (b). This intensity is normalized to that from the same volume without metal, which gives the E-field enhancement within the 20 nm bottom region of the aperture.

2.3.2 Optimization of the Single Bullseye Structure

In order to provide a starting point in the design of the dual polarization bullseye, we first optimize conventional bullseye structures for the three target wavelengths - 365 nm,

532 nm and 635 nm. For $\lambda = 635$ nm, design conditions are: $n = 3$, $p = 390$ nm, $a = 390$ nm, $d = 195$ nm, $w = 195$ nm and $s = 58$ nm. For $\lambda = 532$ nm: $n = 3$, $p = 320$ nm, $a = 320$ nm, $d = 160$ nm, $w = 160$ nm and $s = 48$ nm. For $\lambda = 365$ nm: $n = 6$, $p = 196$ nm, $a = 196$ nm, $d = 98$ nm, $w = 98$ nm and $s = 30$ nm. These designs also serve as references. Although the influence of bullseye's parameters are interlinked with each other, a straightforward procedure of optimization can still be performed based upon the criteria: $p \sim \lambda_{SPP}$, $d = 0.5p$, $a = p$, $w \sim 0.5p$ and $s \sim 0.4w$ [129]. Our numerical optimization follows the same procedure, but uses the field enhancement inside the nanoaperture as the target quantity, which gives the same results, except that $s \sim 0.3w$. This minor difference is due to the red-shift of the resonant transmission wavelength with increasing groove depth [133]. The period is set to correspond to the desired resonant wavelength for intensity enhancement, and the maximum intensity enhancement is obtained under conditions just below cutoff in transmission through the aperture [134]. Figure 2.11 shows the plots of normalized electric field intensity of the single bullseye structures versus wavelength. The peak enhancements for the designs at each of the three wavelengths are similar, with values around 40.

2.3.3 Partial Bullseye Structures

The compound bullseye structure is composed of two orthogonally oriented partial bullseye structures with different parameters. Therefore, the influence of the angular range of the partial bullseye structure on the resonant wavelength and the field enhancement should be clarified before considering the compound structure. Here, the central angle, θ, of a single partial bullseye is considered.

Four partial bullseye structures with central angles 60°, 90°, 120° and 180° are shown in Figure 2.12 (a). The corresponding plots of normalized intensity as a function of excitation wavelength are shown in Figure 2.12 (b). Only the results for the structure optimized for 532 nm wavelength are shown here; all structures show the same trend. It is clear that the position of the resonant peak does not change significantly, but that the intensity enhancement decreases with decreasing central angle. The reduction of enhancement is small when the central angle is larger than 90°, but becomes dramatic with further decrease.

The constancy of the resonant wavelength is due to the fact that the parameters of the structure along the polarization direction of light (x) are largely unchanged; the field enhancement under resonant conditions is due to the constructive interaction between surface plasmon polariton (SPP) waves generated at the grooved surfaces and the aperture modes [134]. However, the decrease of the central angle decreases the interaction area, which

in turn decreases the field enhancement. Note that the response for $\theta = 120°$ overlaps with that of the complete structure $\theta = 180°$, which suggests that the 60° central angle regions along the direction perpendicular to x are not utilized under illumination by x-polarized light. This implies that altering the parameters of these regions has negligible influence on the optical response.

2.3.4 Compound Bullseye Structure

According to the analysis of the previous section, the partial bullseye structure has the same resonant wavelength, but lower enhancement, compared with the complete one, which suggests that the design approach of starting with the complete bullseye structure is effective. Furthermore, the grooves in the orthogonal partial structures should have weak interaction under illumination with linearly polarized light, which makes it possible to arrange two sets of parameters along orthogonal directions to form a compound bullseye structure supporting a defined resonant wavelength for each orthogonal polarization.

Choosing the optimal parameters corresponding to the three design wavelengths, three compound bullseye structures are formed by combining two orthogonal partial structures, each with $\theta = 90°$, as shown in Figure 2.10 (a). The intensity enhancement as a function of wavelength under illumination from x and y polarized light is shown in Figure 2.13 (a) and (b) for these three combinations. The label "$XxxxYyyy$" denotes that the structure has xxx nm resonant design wavelength under x-polarized illumination and yyy nm resonant design wavelength under y-polarized illumination.

One can see that the compound bullseye structures have enhancement peaks corresponding to the designed parameters for the two orthogonal polarization states. In addition to these designed peaks, there are additional peaks which will be discussed later. The $X635Y365$ and $X532Y365$ compound structures illuminated by y-polarized light have similar profiles with prominent peaks at 365 nm, but the resonant peaks for the x polarization are at 635 nm and 532 nm, respectively. This suggests that the resonance wavelength of the compound bullseye structure for x-polarized light can be tuned by altering the parameters of the partial bullseye structure along the x direction, without modifying the y-polarized resonance.

In Figure 2.13 (a), there are additional resonant peaks on the blue side of the design wavelengths 635 nm and 532 nm. Comparing the simulated response of complete bullseye structures with the same parameters to the x-directed partial bullseye structure, as shown in Figure 2.14, the resonant peaks are the same. Further, by comparing the field distributions of the short wavelength peaks, as shown in Figure 2.15, we conclude that these peaks are the

higher-order resonance of constructively interfering SPPs propagating along the x direction. For the structure $X635Y365$, the designed peak at 635 nm is the 1st-order resonance, the peak at 380 nm is the 2nd-order resonance, and the peak at 310 nm is the 3rd-order resonance. Note that the same secondary peaks appear for the $X635Y532$ structure, but with smaller amplitudes due to the greater aperture size. For the structure $X532Y365$, the peak at 330 nm is the 2nd-order resonance.

On the other hand, in Figure 2.13 (b), there are minor resonance peaks on the red side of the design wavelength 365 nm. The positions of these peaks change based upon the parameters of the x-directed partial structures, which implies these peaks are in part the result of coupling to the pattern along the x-direction. According to the discussion in the previous section, only the area with 60° central angle perpendicular to the polarized direction has no interaction with the incident light, which means there are four regions with 15° central angles in the x-polarization bullseye portion of the compound structure that can interact with y-polarized incident light. The electric field patterns for these peaks have also been considered, and are shown in Figure 2.16, which confirm that the designed peak at 365 nm corresponds to SPP resonance in the area of the partial bullseye along the polarization direction (y), while the other peaks at 490 nm, 610 nm and 640 nm correspond to different orders of SPP resonance overlapping regions of the partial bullseye along the x direction.

The field enhancement inside the aperture is strongly influenced by the aperture size. The optimal aperture size should be $d = 0.5p$, where the cut-off condition of the aperture becomes significant and produces strong enhancement inside the aperture [134]. However, in the compound bullseye structure, there are always two periods, p_x and p_y. In Figure 2.13, for the $XxxxY365$ structures, the diameters are assigned to be half of the smallest period, $d = 0.5 \times 196 = 98$ nm. This value meets the optimal condition for the resonant design wavelength of 365 nm, so the normalized intensity of the y-polarization resonance is always higher than that of the x-polarization resonance. Therefore, every resonance, including the higher order ones, around the wavelength of 365 nm has strong enhancement. The structure of $X635Y532$ shows the same trend because the value of diameter is closer to the optimal size for the y polarization design wavelength.

2.3.5 Influence of the Nanoaperture Size: Tuning the Level of Enhancement

The aperture size can be utilized to tune the intensity enhancement. Altering the diameter of the aperture within the range $0.5p_y \leq d \leq 0.5p_x$ and fixing the other parameters,

the intensity enhancement of the compound bullseye structures with different nanoaperture sizes is calculated and shown in Figure 2.17. For the structure $X635Y365$, one can see that increasing the diameter from 98 nm to 195 nm decreases the enhancement at 365 nm, but increases the enhancement at 635 nm. When the diameter is at its optimal values of 98 nm and 195 nm, the corresponding enhancements are close to those of the complete bullseye structure. Therefore, by choosing different diameters, the relative level of enhancement for two polarization states can be tuned according to application preference. At $d = 140$ nm, the enhancement for the two design wavelengths are nearly balanced. The plots for structure $X532Y365$ also show the same trend. For the structure $X635Y532$, the case of $d = 195$ nm is not only the optimal one for 635 nm wavelength, but also the balanced one, so only two nanoaperture sizes are shown in these plots.

2.3.6 Field Localization inside the Nanoaperture

One more aspect of polarization multiplexed antennas that needs to be considered is the overlap of the electric field intensity within the aperture for the different polarizations. Using the compound bullseye structure $X635Y365$ with $d = 140$ nm as an example, the distributions of the electric field intensities in the $x - y$ plane under the two resonant conditions are shown in Figure 2.18. The measurement plane is located at the interface between Al and glass. A logarithmic scale is used to allow a greater dynamic range of field intensity to be displayed. One can see that the intensity localized on the edges of the aperture along the polarization direction, but they are not completely orthogonal.

To further characterize the overlap of the field intensity patterns along the x and y polarizations, the following equation is used:

$$O = \frac{\int_V (I_X \times I_Y) dV}{\sqrt{\int_V {I_X}^2 dV \times \int_V {I_Y}^2 dV}},$$

where I_X and I_Y are the total intensities of electric field within the 20 nm-bottom region of the aperture for the x and y incident polarizations, respectively, and V is the volume of that region. The overlap ratios for structures of $X635Y365$, $X532Y365$ and $X635Y532$ ($d = 140$ nm for $Y365$ and $d = 195$ nm $Y532$.) are 0.41, 0.40 and 0.55, respectively, which implies that it is possible to excite overlapping volumes under different polarizations by using a compound bullseye structure.

2.4 Summary

In this chapter, we developed the design method using the numerical simulation (FDTD method) based on three-level model of fluorescence emission. Two sets of calculations have

been performed for each design in order to simulate both excitation and emission procedure of fluorescence. By placing different monitors and applying two kinds of sources into the simulation model, excitation enhancement, radiative enhancement and Purcell factor can be calculated, which in turn give us the net enhancement according to Equation 1.14 and 1.15. The correct way to convert the simulated Purcell factor to the measured one is also discussed. We also introduced the averaging strategy to consider the contribution from molecules not localized in the bottom region. This method can be used to design and optimize plasmonic structures for next step of nanofabrication, and also for analysis of experimental data collected in the following experimental study.

By using our design method, three Al plasmonic structures for UV fluorescence enhancement are numerically studied by comparing five performance metrics: excitation enhancement (f_I), Purcell factor ($f_{Purcell}$), radiative enhancement (f_{rad}), QE enhancement (f_ϕ) and NE. The 2-D maps of performance metrics versus geometrical parameters are generated in order to clarify the influence of structure parameters. The far-field radiation patterns are also considered to taking into account the influence of collection efficiency. All three structures present similar features demonstrating that peak enhancement of the excitation and emission processes occurs under resonant conditions, determined by arm length for dipole antenna and pitch for the other two structures. Furthermore, distinct differences are observed across the structures. The bullseye aperture and aperture array produces higher enhancements due to their extended planar structure with much greater physical interaction cross-section with incident light. Decrease of gap size of dipole antenna will increase the enhancement of excitation and emission, while the round apertures in the bullseye and aperture array have an optimal size for the excitation ($\sim$ 50 nm) and emission ($\sim$ 70 nm) processes. Due to the favorable gap structure, the dipole antenna produces higher Purcell factor ($f_{Purcell}$ $\sim$11), radiative enhancement ($f_{rad} \sim 7$) and QE enhancement (f_ϕ $\sim$4.5). The thicker structures of bullseye and aperture array effectively suppress radiation in the direction away from the substrate, which is preferable for an epifluorescence setup. The far-field radiation of the bullseye aperture has the most directionality due to constructive interference with scattering by the concentric grooves. The aperture array has the least directionality due to the weak interaction between central and neighboring apertures.

For the purpose of compensation of large Stokes shift of UV fluorescent molecules, we have presented and analyzed a novel optical antenna structure in the form of a polarization multiplexed bullseye antenna with a central nanoaperture. By adjusting the parameters of

two, orthogonally-oriented, partial bullseye structures, the resonance response at each polarization can be tailored to a specific wavelength, independently, to match the absorption and emission peaks of molecules. In addition, the relative intra-aperture intensity enhancement can be controlled by the diameter of the nanoaperture, providing an additional degree of freedom in applying this structure to different applications. It should be noted that our design is still valid for emission enhancement even if the structure was designed based on excitation enhancement. The shifting of resonance from plane wave excitation to dipole emission is small and can be easily corrected by tuning the structural parameters.

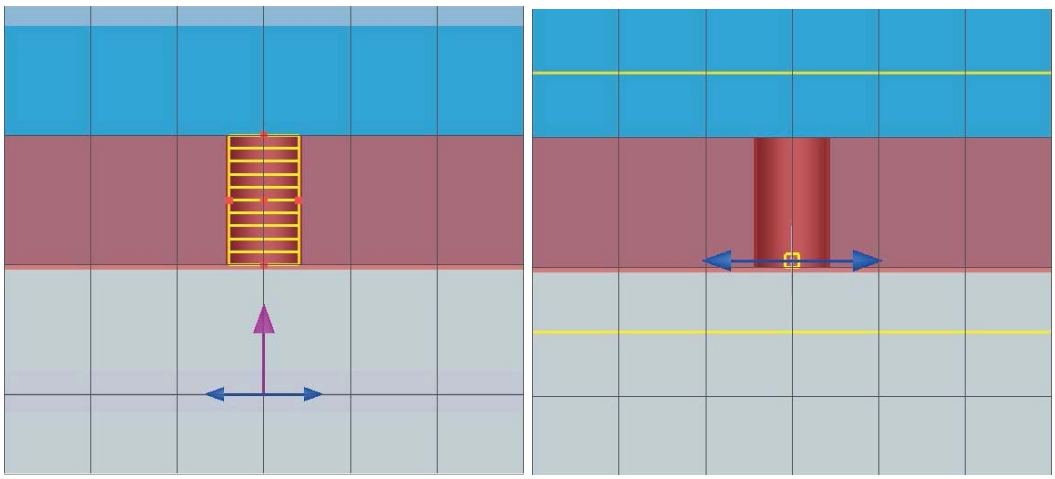

(a) (b)

Figure 2.1. Cross-section views of simulation models (nanoaperture) with sources and monitors for (a) excitation and (b) emission calculations.

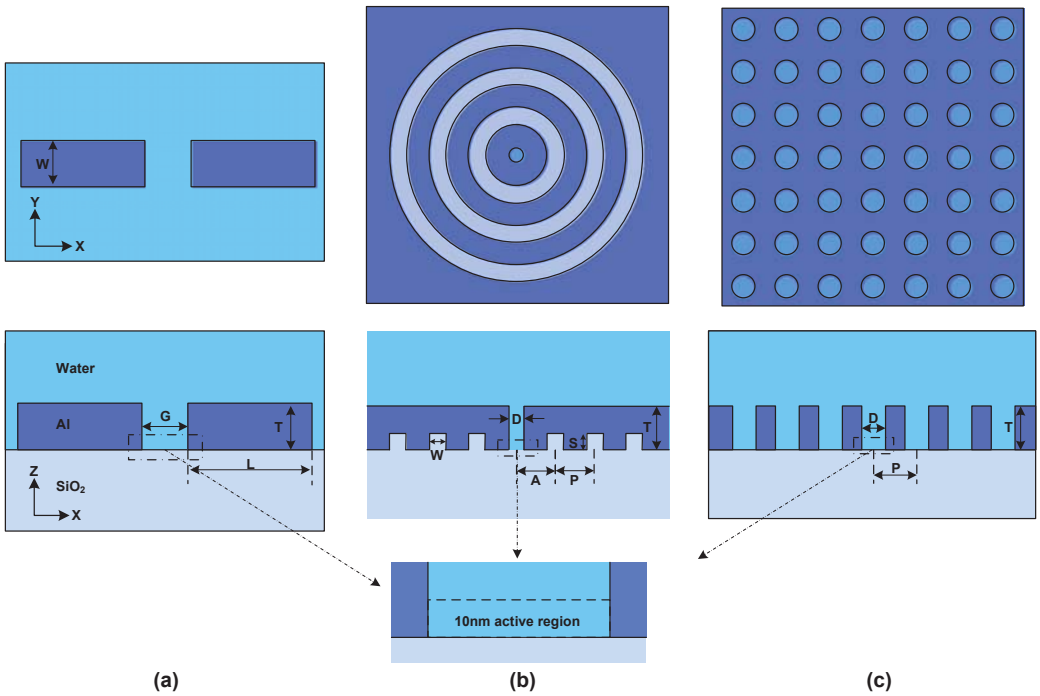

Figure 2.2. Plan view along the interface and xz cross-section of (a) dipole antenna, (b) bullseye aperture and (c) aperture array. The active region with 10 nm thickness is also shown.

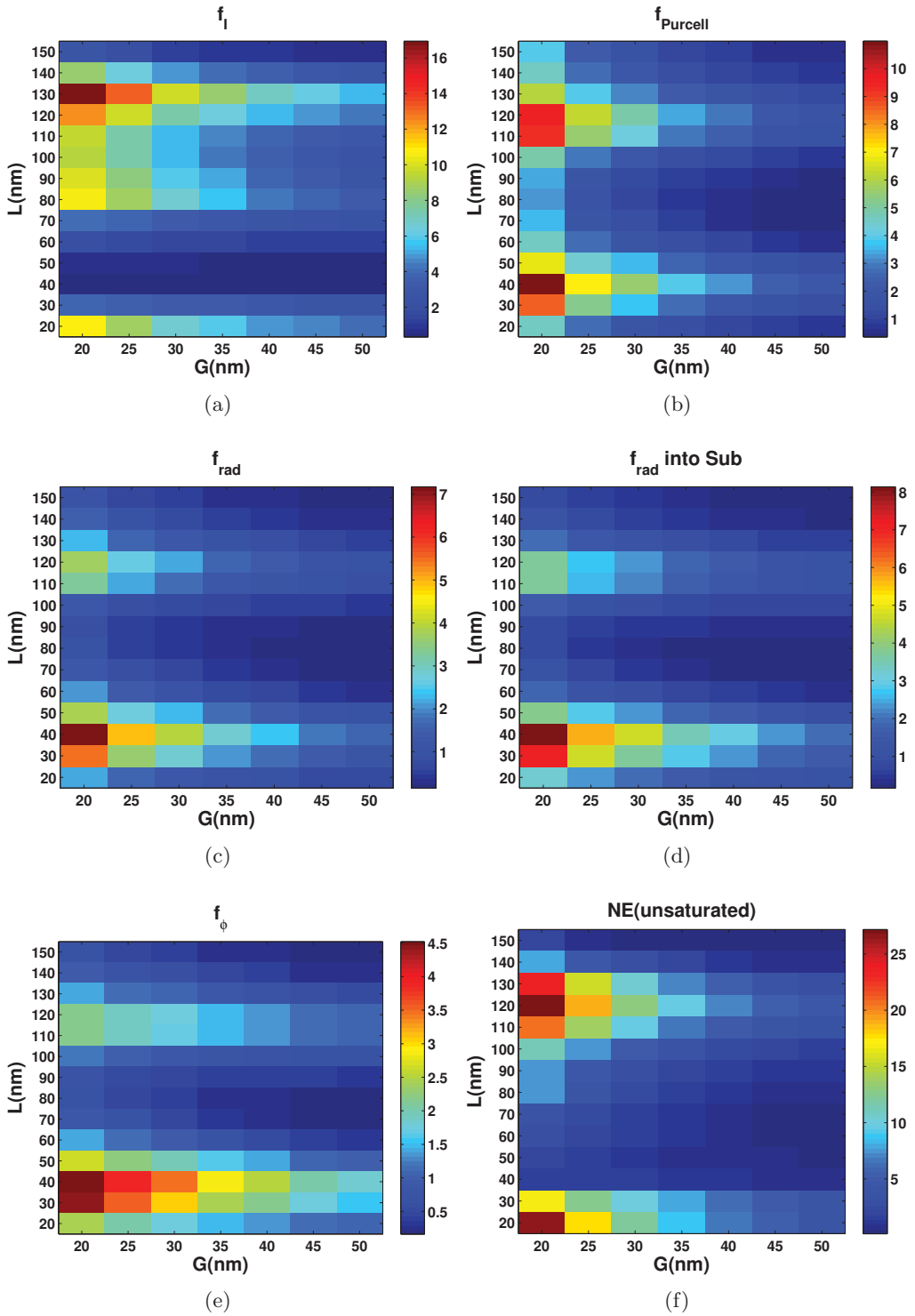

Figure 2.3. Heat maps of (a) excitation enhancement (f_I), (b) Purcell factor ($f_{Purcell}$), (c) and (d) radiative enhancement (f_{rad}), (e) QE enhancement (f_ϕ) and (f) NE (unsaturated) for an Al dipole antenna versus gap size (G) and arm length (L). (T=30 nm, W=30 nm).

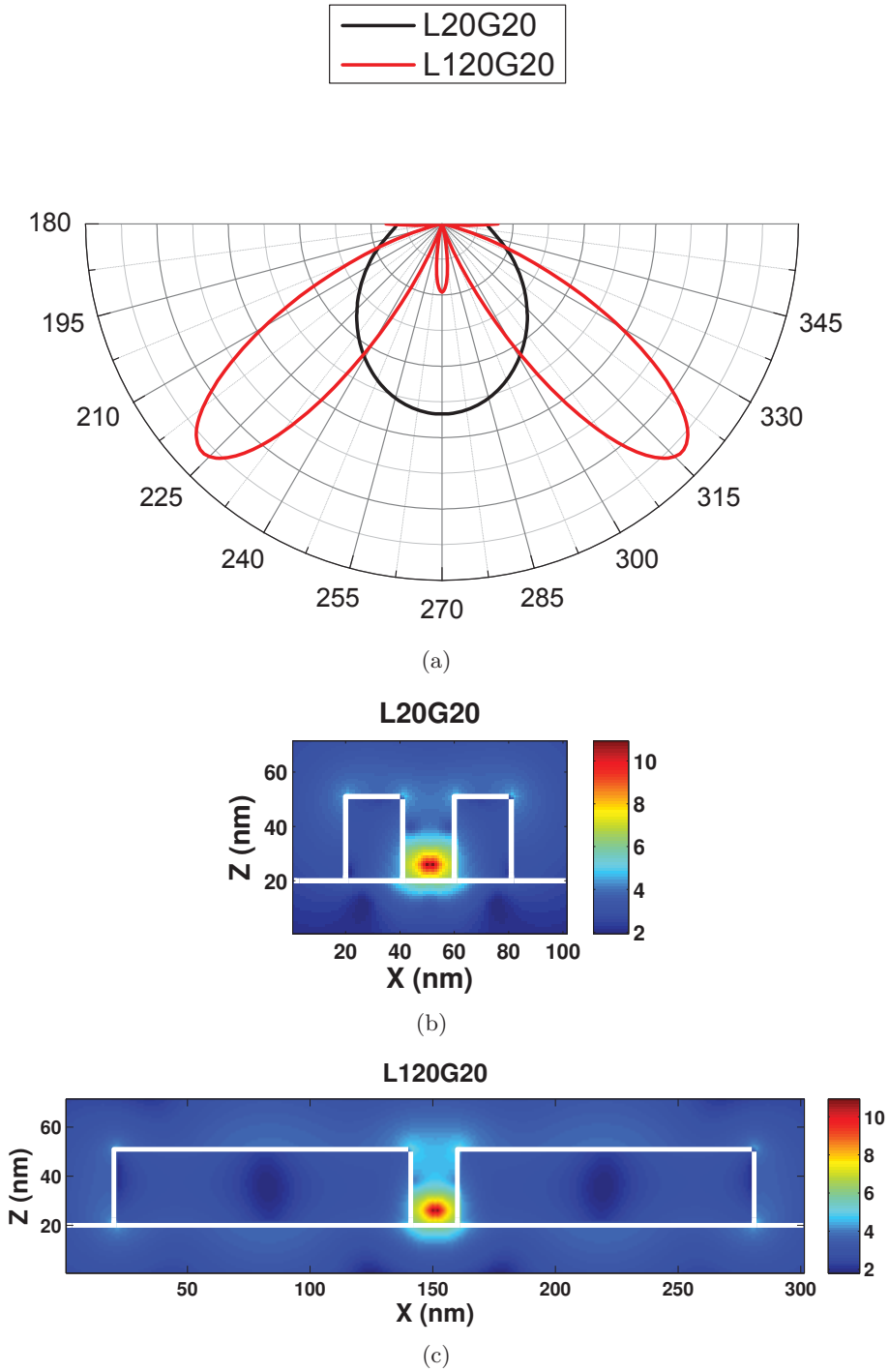

Figure 2.4. Emission of dipole antenna demonstrated by (a) far-field angular radiation patterns corresponding to the first (L=20 nm) and the second (L=120 nm) peak NE. (b) and (c) corresponding spatial distribution of $|E|^2$ in xz cross-section . An x-polarized electric dipole with 340 nm wavelength is placed in the center of the active region. (G=20 nm, W=30 nm, T=30 nm).

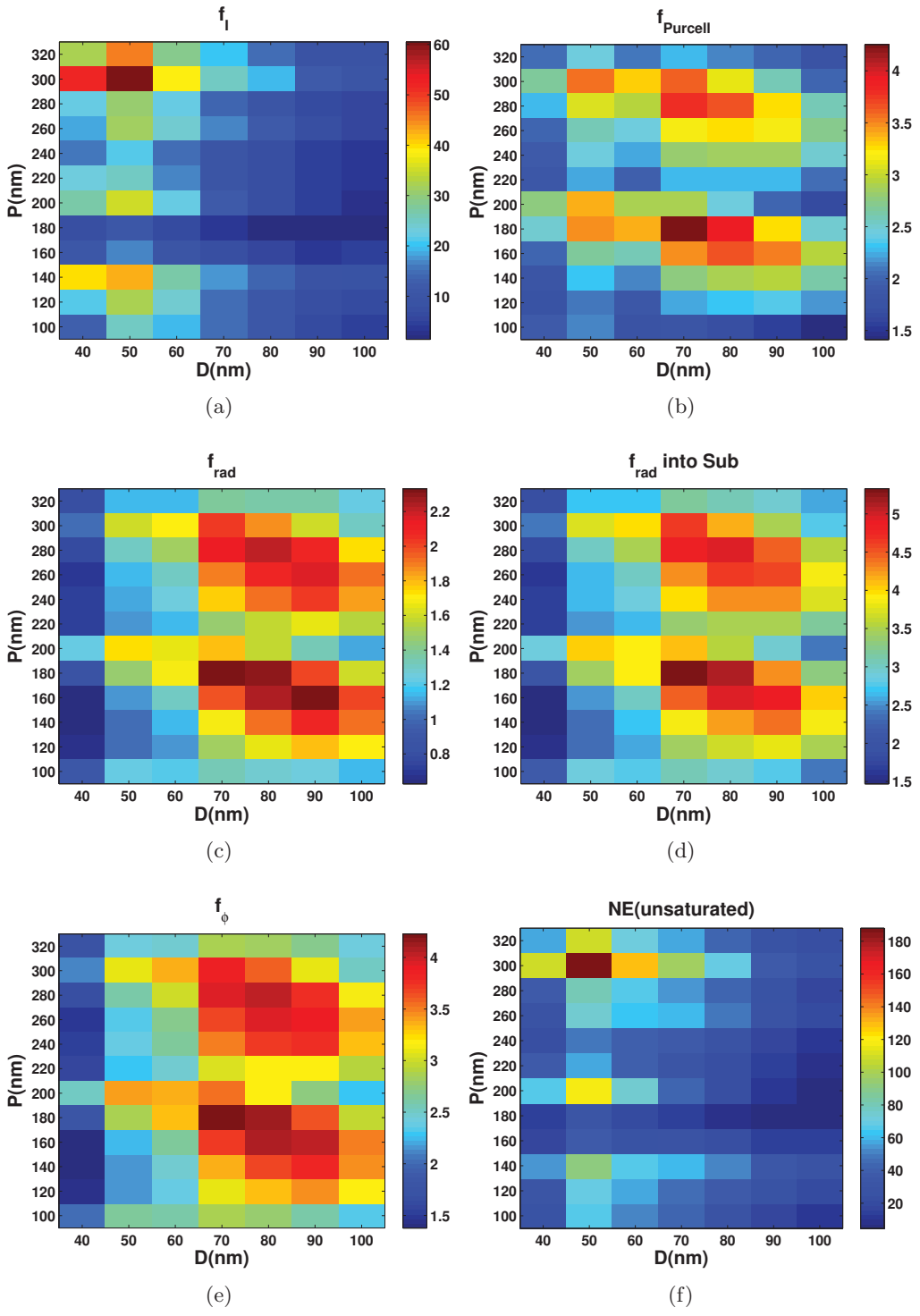

Figure 2.5. Heat maps of (a) excitation enhancement (f_I), (b) Purcell factor ($f_{Purcell}$), (c) and (d) radiative enhancement (f_{rad}), (e) QE enhancement (f_ϕ) and (f) NE (unsaturated) for the bullseye antenna versus hole size (D) and groove pitch (P). (A=P, W=60 nm, S =20 nm, T=100 nm)

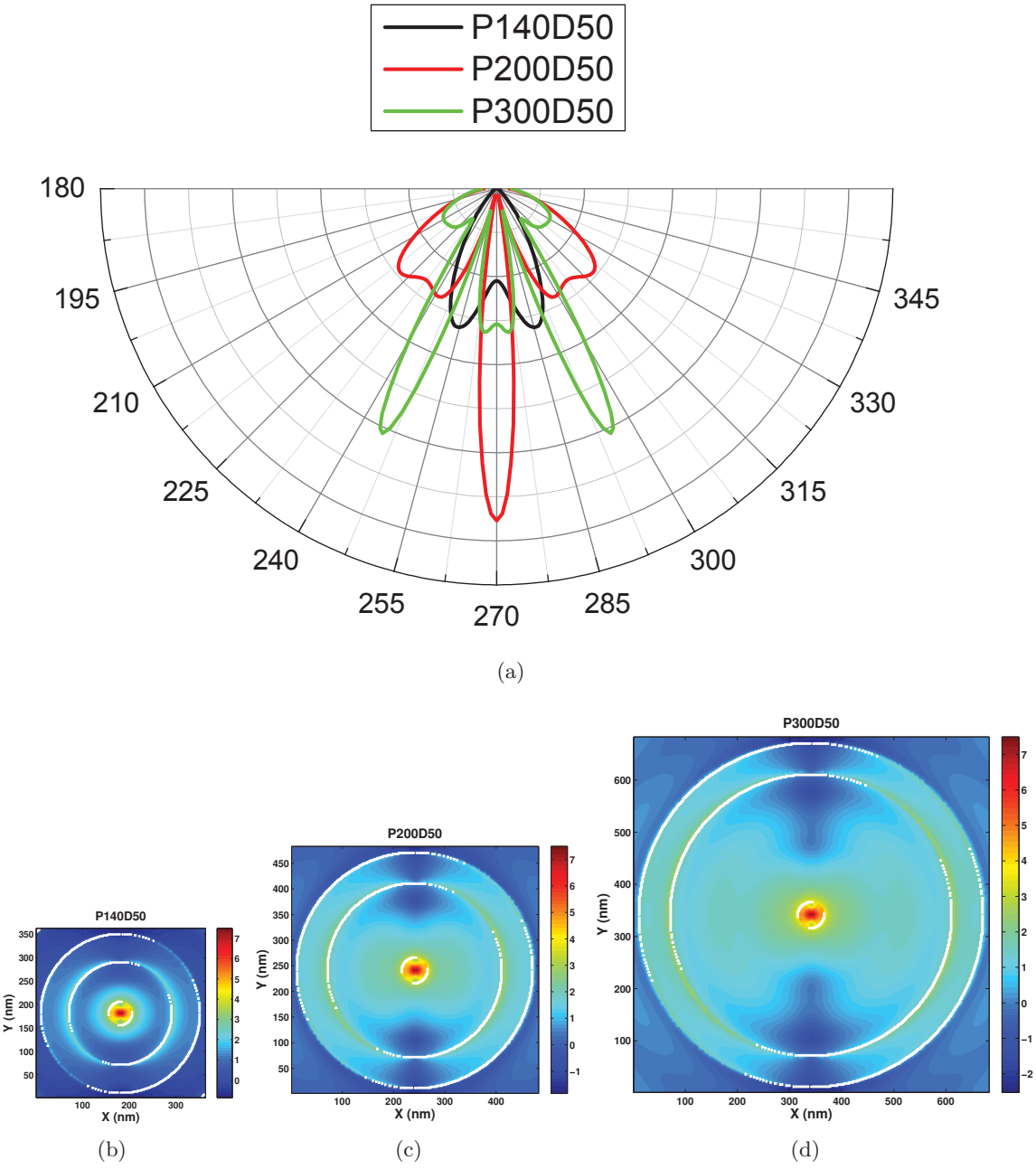

Figure 2.6. Emission of bullseye antenna demonstrated by (a) far-field angular radiation patterns of the first (P=140 nm, off-resonance), the second (P=200 nm) and the third (P=300 nm) peak NE. (b), (c) and (d) corresponding spatial distribution of $|E|^2$ in the structure/glass interface (xy surface) of bullseye. An x-polarized electric dipole with 340 nm wavelength is placed in the center of active region. (D=50 nm, A=P, W=60 nm, S=20 nm, T=100 nm)

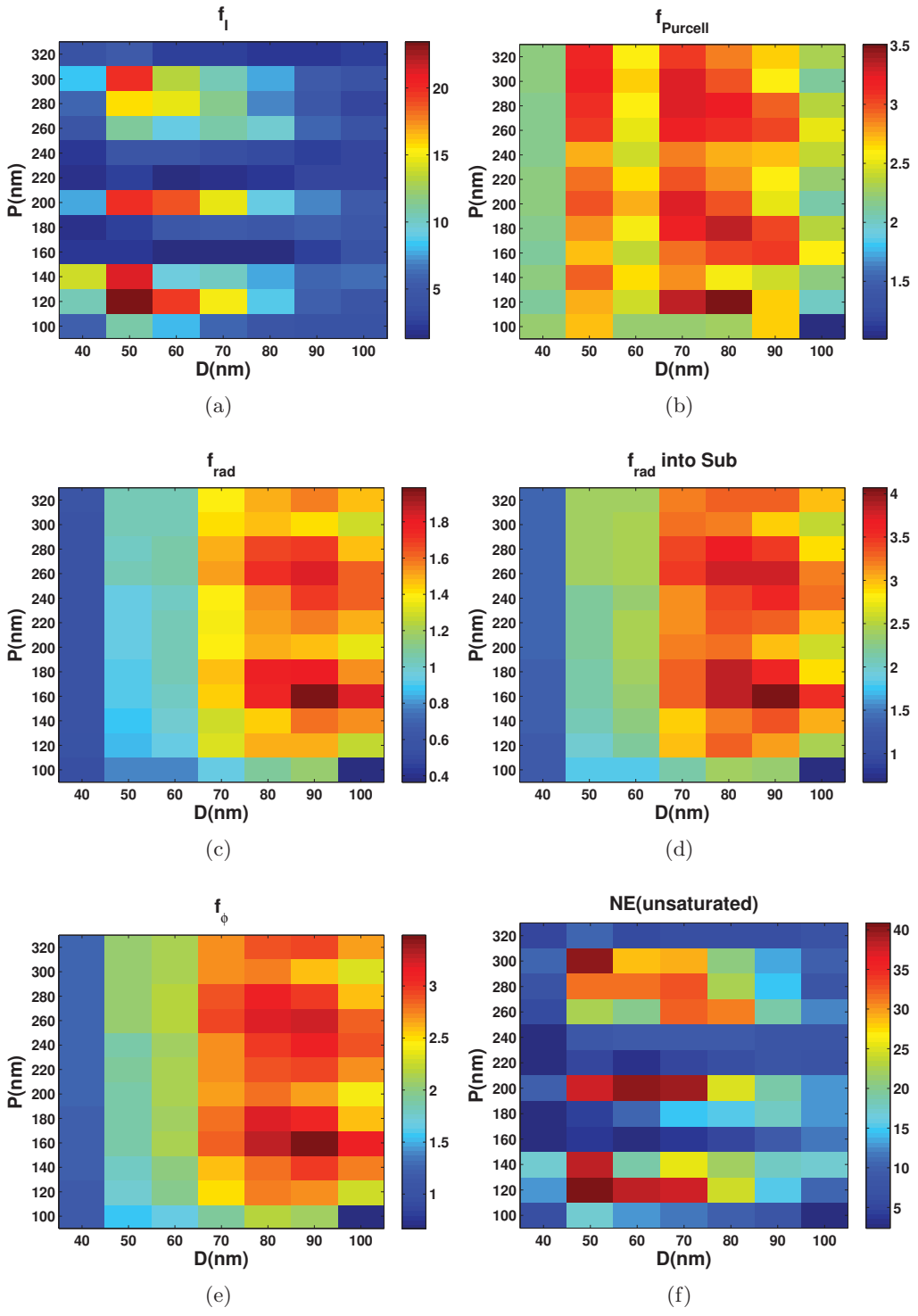

Figure 2.7. Heat maps of (a) excitation enhancement (f_I), (b) Purcell factor ($f_{Purcell}$), (c) and (d) radiative enhancement (f_{rad}), (e) QE enhancement (f_ϕ) and (f) NE (unsaturated) for an aperture array versus aperture size (D) and period (P). (T=100 nm)

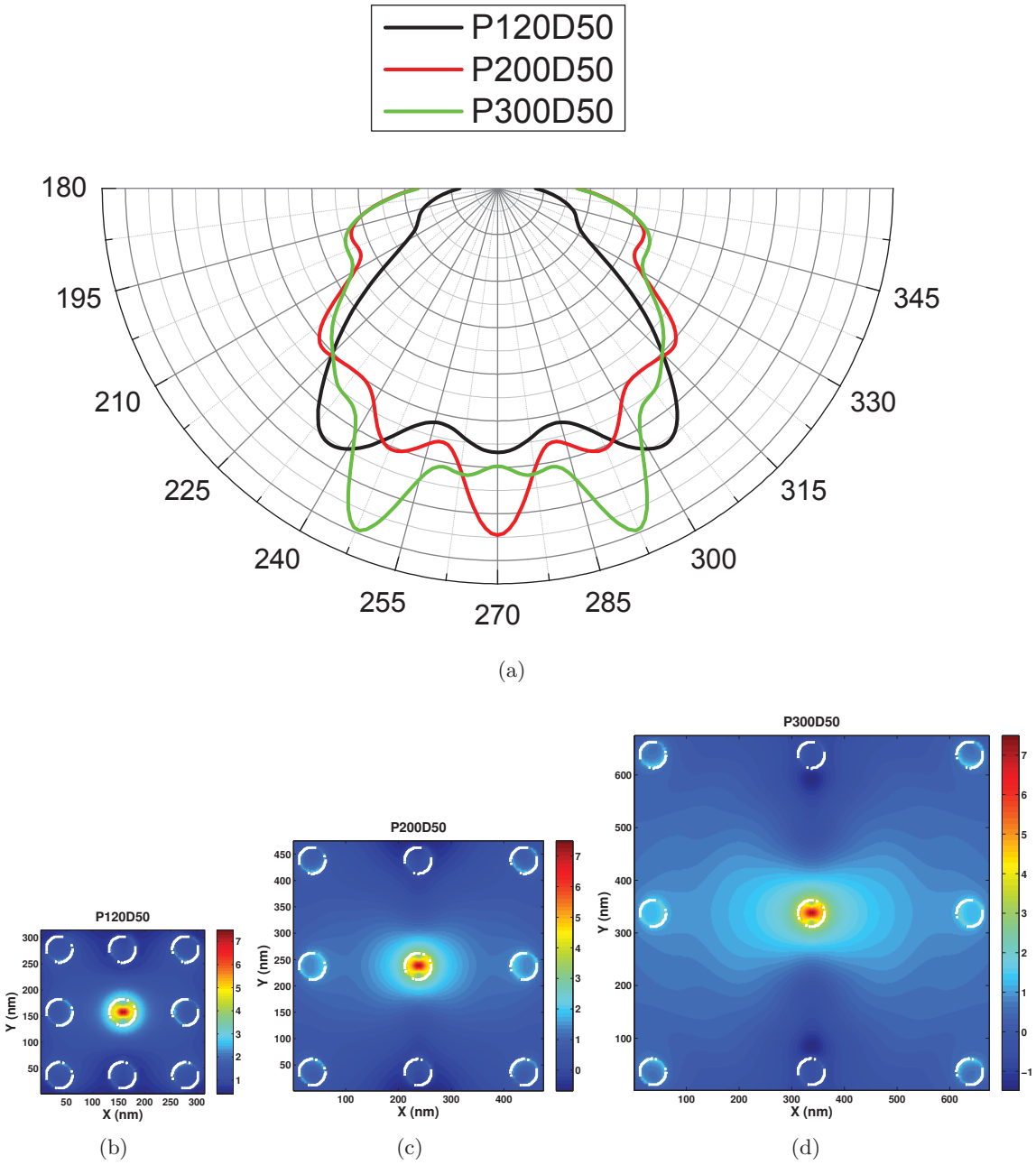

Figure 2.8. Emission of aperture array demonstrated by (a) far-field angular radiation patterns of the first (P=120 nm, off-resonance), the second (P=200 nm) and the third (P=300 nm) peak NE. (b), (c) and (d) corresponding spatial distribution of $|E|2$ in the structure/glass interface (xy surface) of aperture array. An x-polarized electric dipole with 340 nm wavelength is placed in the center of active region. (D=50 nm, T=100 nm)

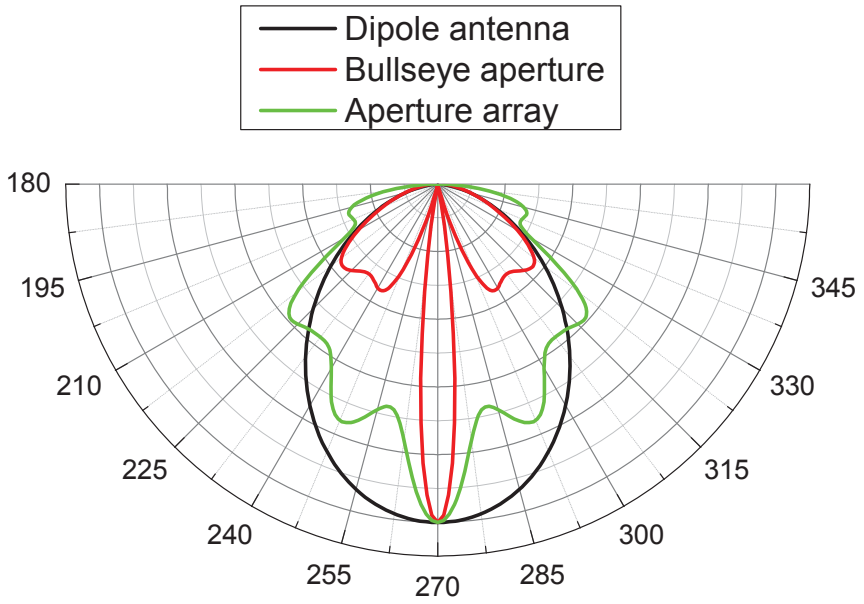

Figure 2.9. Far-field angular radiation patterns of three nanoantennas. Only the first-order emission resonances are considered and patterns are normalized. An x-polarized electric dipole with 340 nm wavelength is placed in the center of active region.

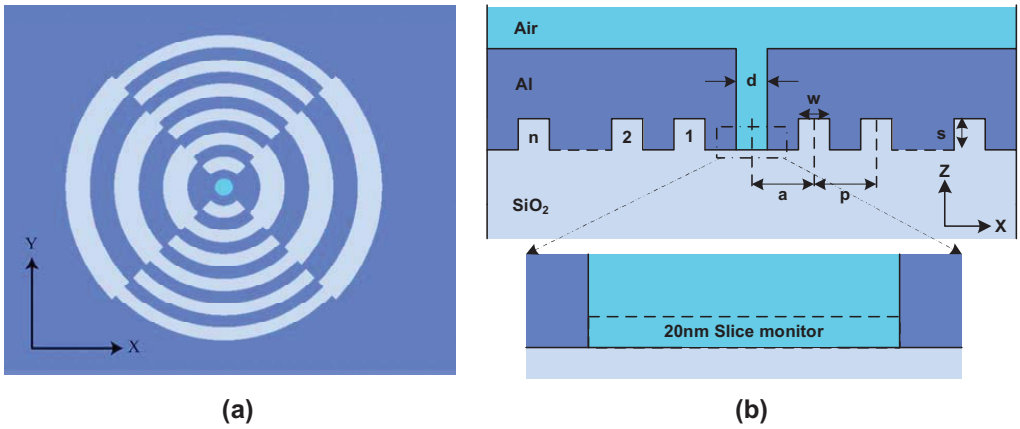

Figure 2.10. Plan view along the interface (a) and $x-z$ cross-section (b) of the compound bullseye structure, which consists of a 200 nm Al film supported by a glass substrate with n circular grooves of width w, depth s, and separated by a period p on the interface. A single nanoaperture of diameter d is milled through the film at a distance a from the center of the first groove. The corrugation has two sets of parameters along two orthogonal directions. The zoom-in diagram of region surrounded by the dash-dot lines in (b) shows a 20 nm thick slice monitor in the bottom region of the aperture used to collect the electric field in the simulations,

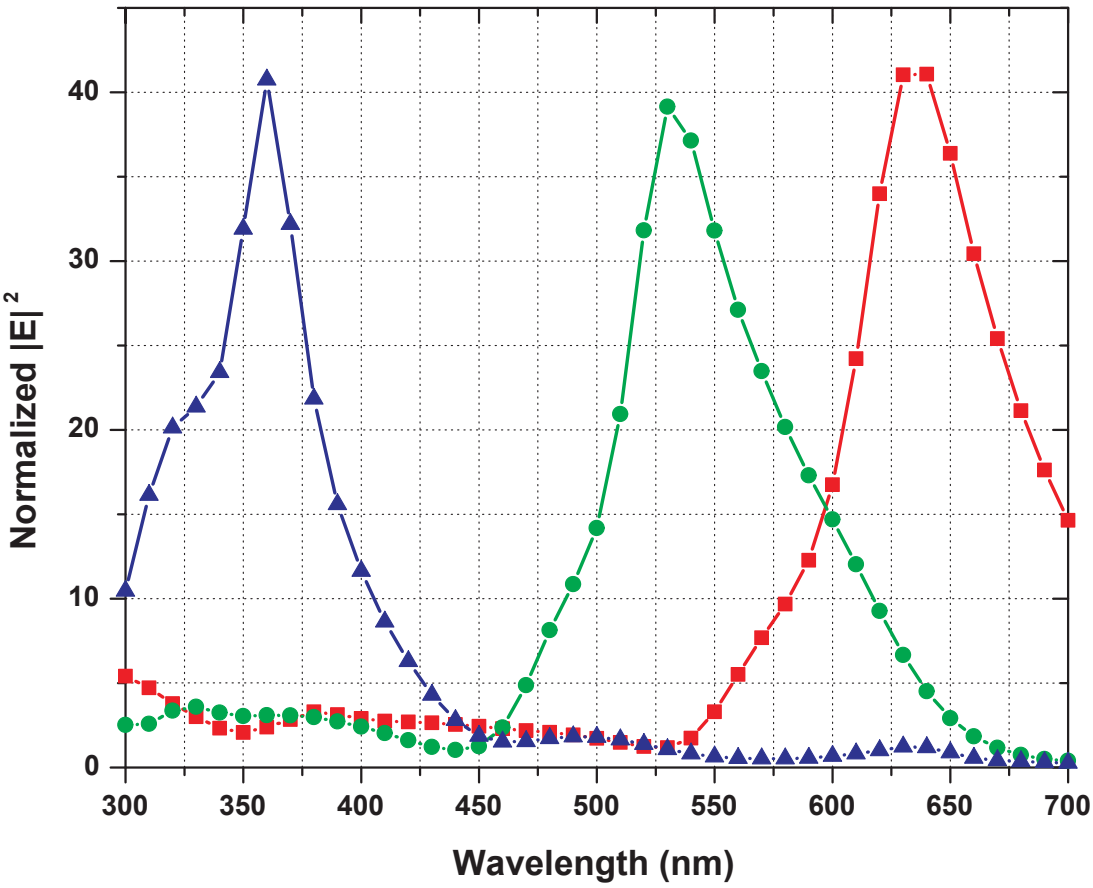

Figure 2.11. Normalized electric field intensity within the 20 nm-bottom region of the bullseye aperture versus excitation wavelength, for three different resonance wavelengths.

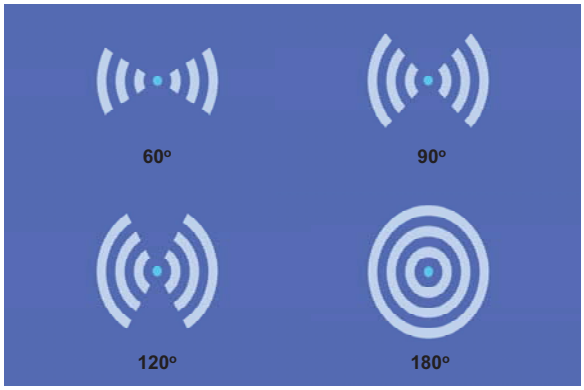

(a)

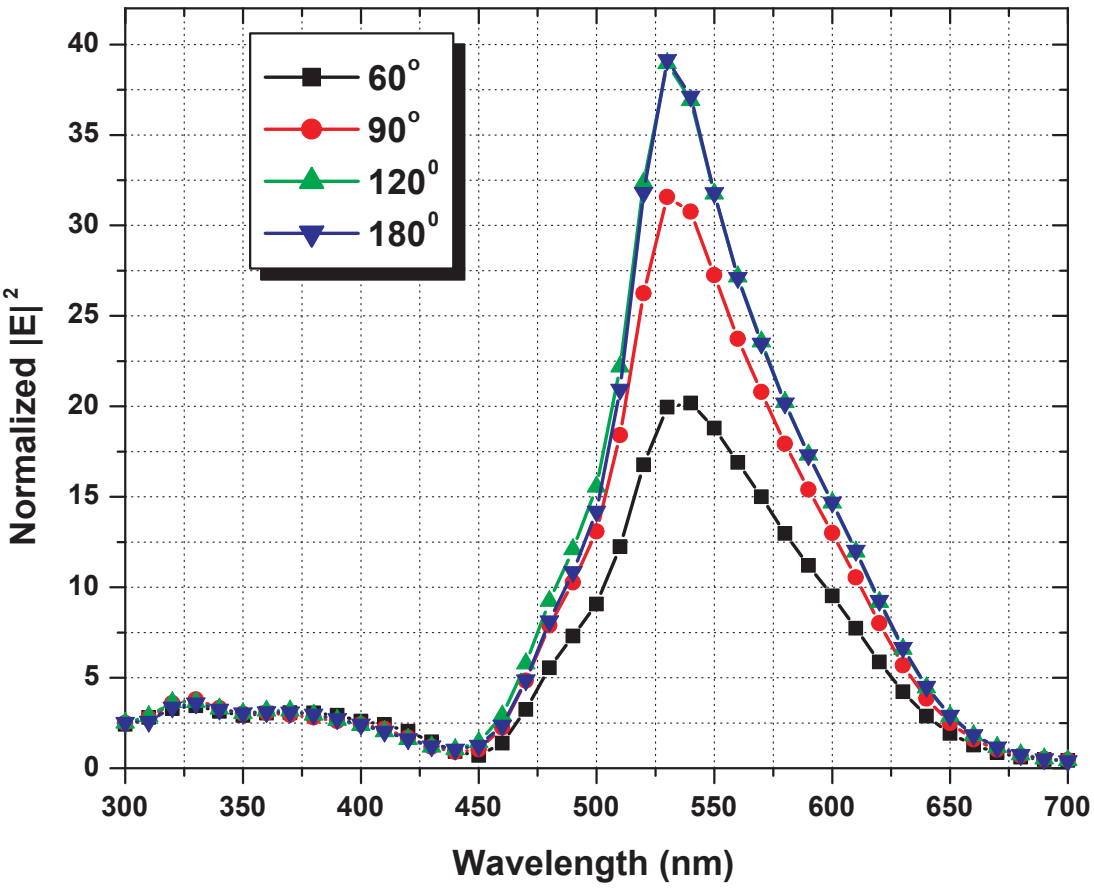

(b)

Figure 2.12. Partial bullseyes. (a) Structures with different angular openings (60°, 90°, 120° and 180°). (b) Normalized electric field intensity within the 20 nm bottom region of the aperture versus the excitation wavelength of the partial bullseye structures with different central angles ($n = 3$, $p = 320$ nm, $a = 320$ nm, $d = 160$ nm, $w = 160$ nm and $s = 48$ nm).

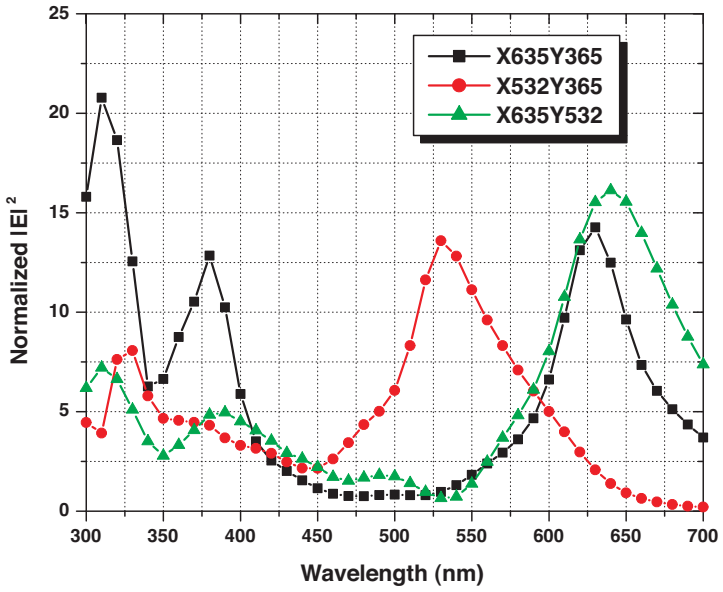

(a) x polarization

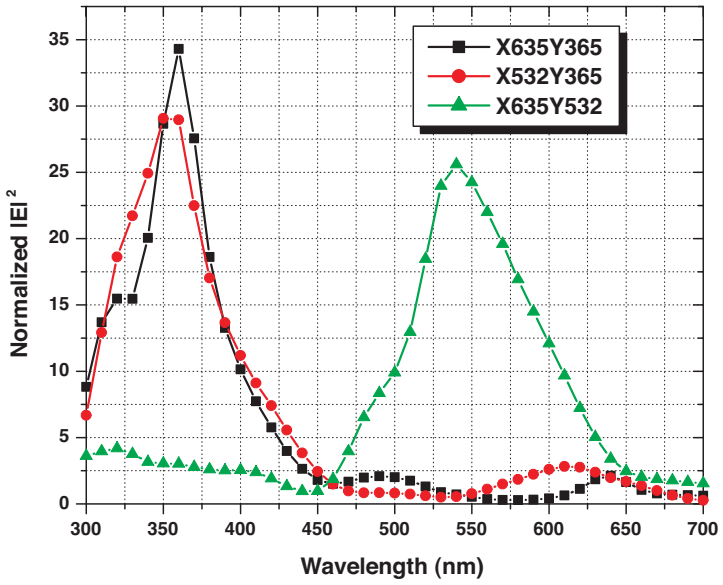

(b) y polarization

Figure 2.13. Normalized electric field intensity within the 20 nm-bottom region of the aperture versus the excitation wavelength of the compound bullseye structures ($X635Y365$, $X532Y365$ and $X635Y532$) under x-polarized (a) and y-polarized (b) illumination. The central angles of the partial bullseye structures are fixed at $\theta = 90°$, and the aperture diameter $d = 98$ nm for $Y365$ and $d = 260$ nm for $Y532$. The other parameters are the same as those of the corresponding structures in Figure 2.11.

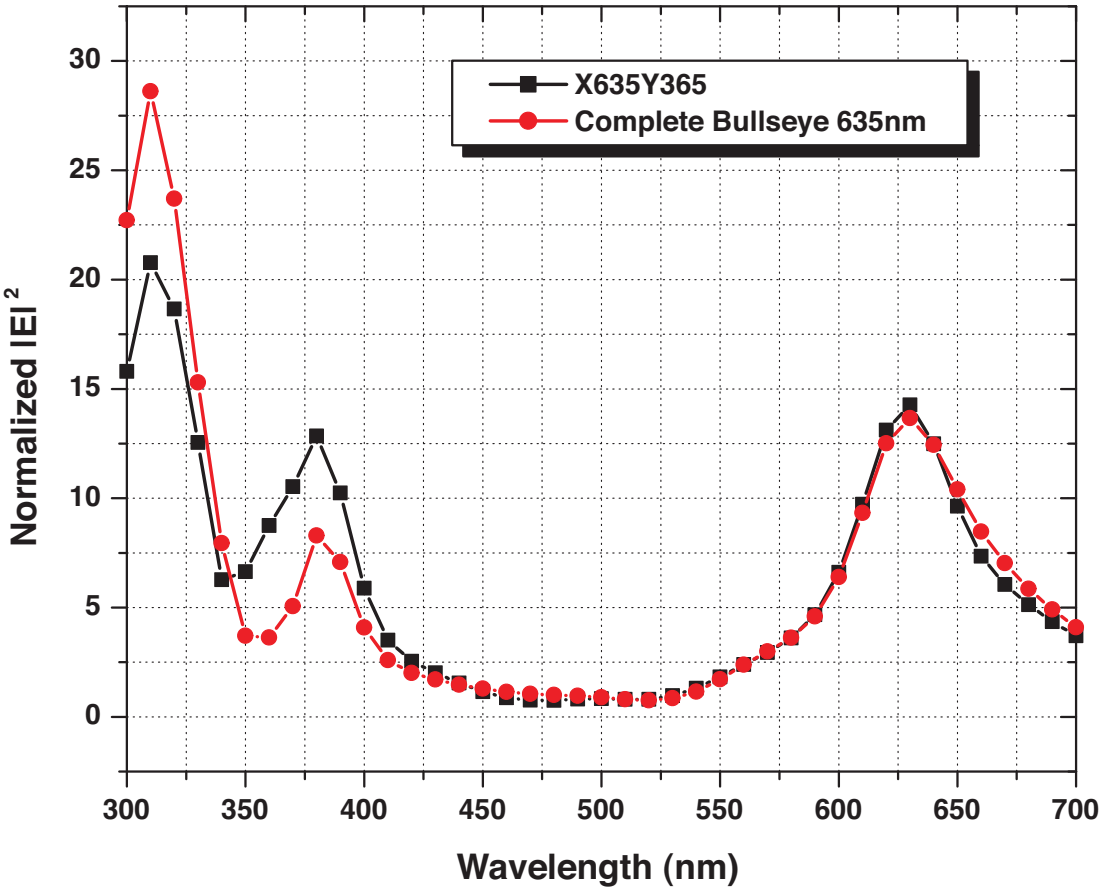

Figure 2.14. Normalized electric field intensity within the 20 nm-bottom region of the aperture versus the excitation wavelength of the compound $X635Y365$ and complete bullseye structure under x-polarized illumination. The aperture diameter $d = 98$ nm. The other parameters are the same as those of the corresponding structures in Figure 2.11.

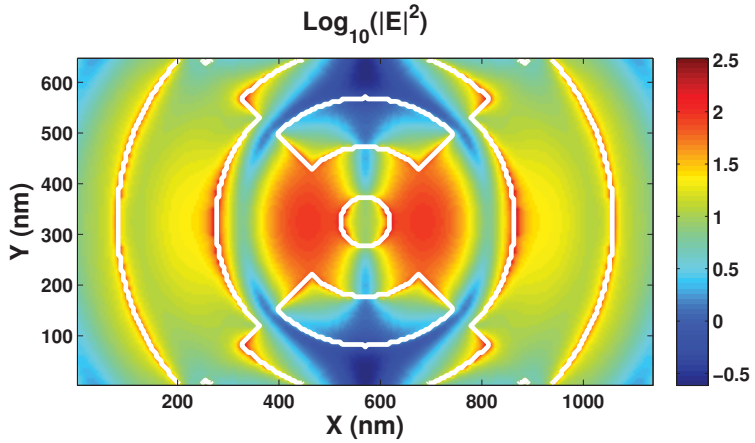

(a) 635 nm

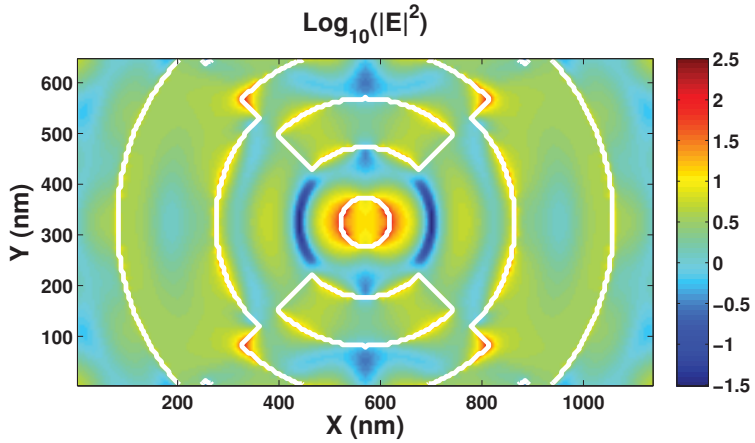

(b) 380 nm

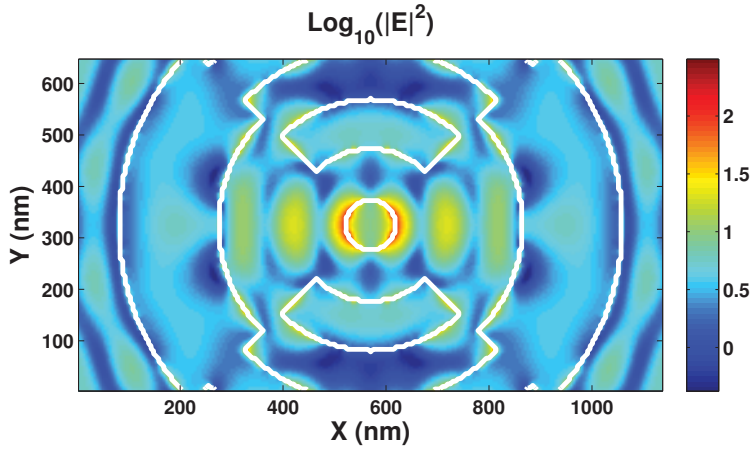

(c) 310 nm

Figure 2.15. Spatial distribution (xy surface) of electric field intensity at the bottom interface of the compound bullseye structure $X635Y365$ with $d = 98$ nm, illuminated by x-polarized light at (a) 635 nm, (b) 380 nm and (c) 310 nm wavelengths.

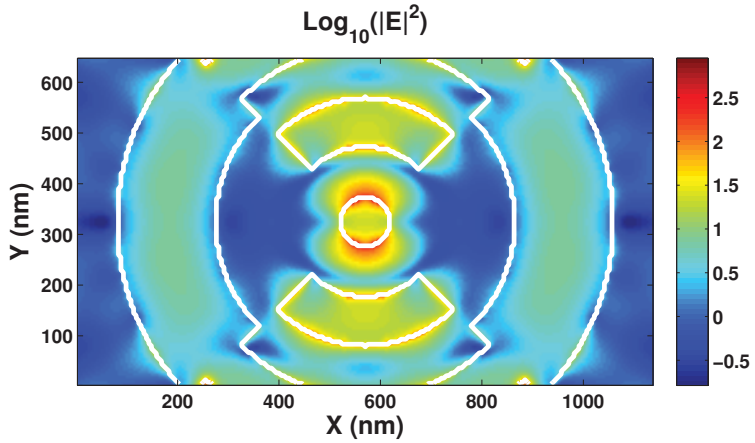

(a) 365 nm

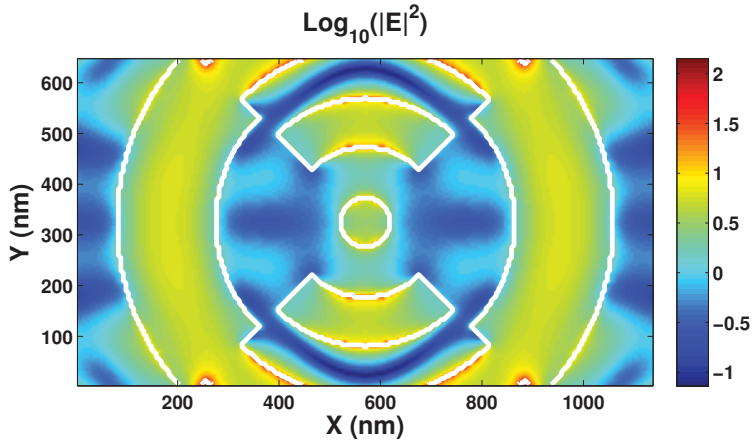

(b) 490 nm

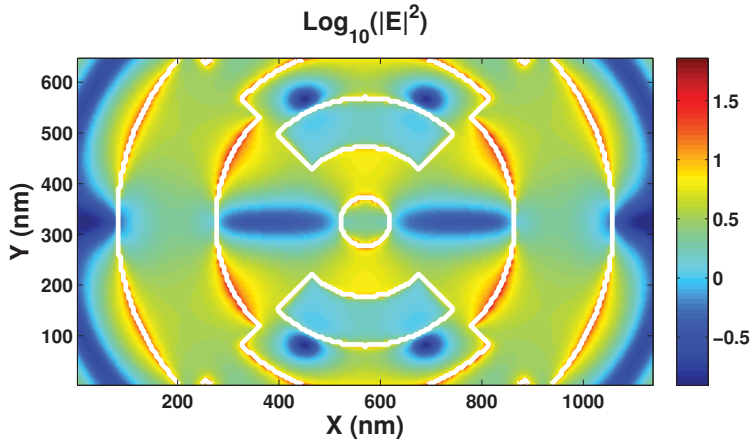

(c) 640 nm

Figure 2.16. Spatial distribution (xy surface) of electric field intensity at the bottom interface of the compound bullseye structure $X635Y365$ with $d = 98$ nm, illuminated by y-polarized light at (a) 365 nm, (b) 490 nm and (c) 640 nm wavelengths.

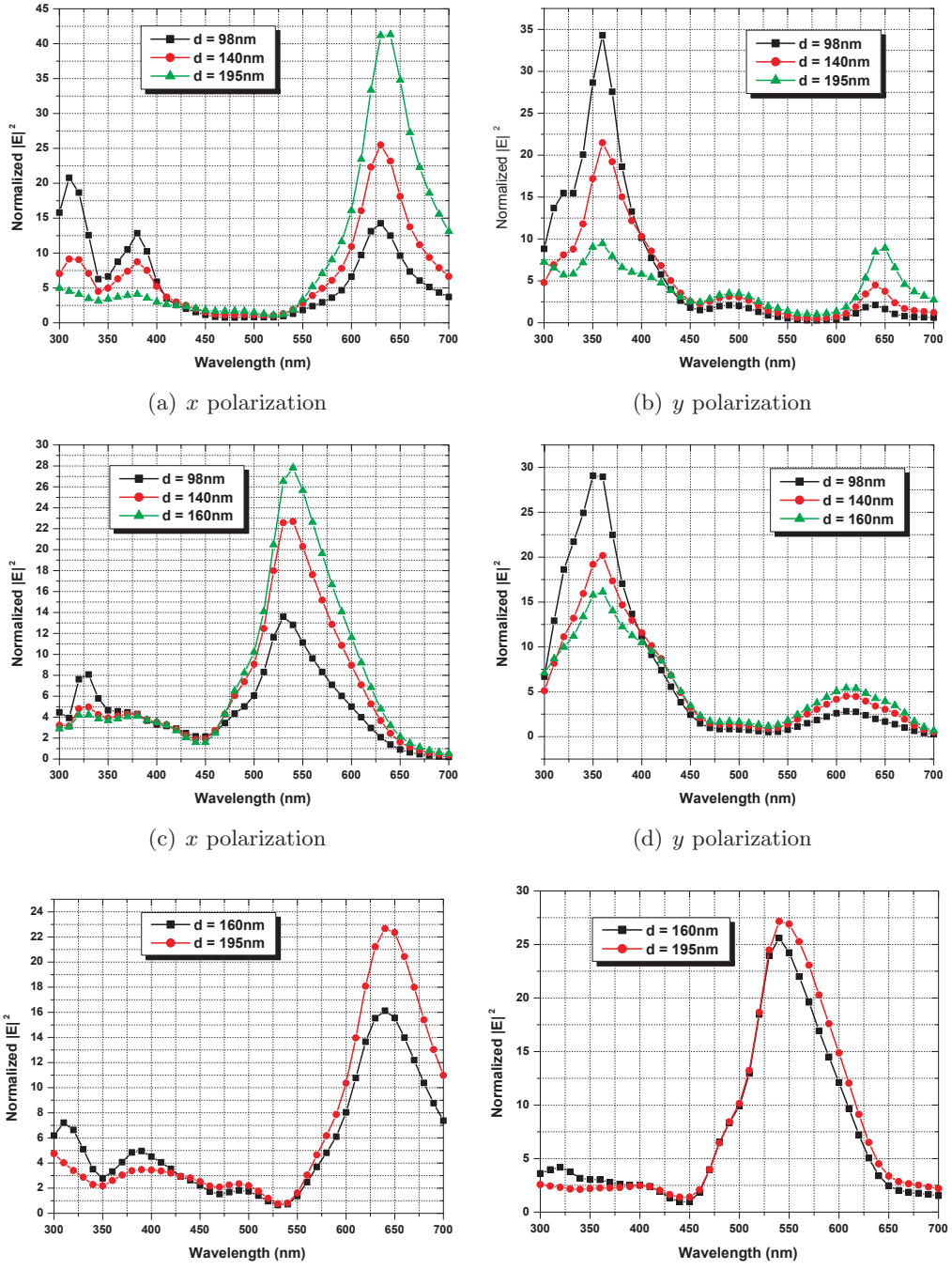

(a) x polarization (b) y polarization

(c) x polarization (d) y polarization

(e) x polarization (f) y polarization

Figure 2.17. Normalized electric field intensity within the 20 nm-bottom region of the aperture versus the excitation wavelength for the compound bullseye structures with different nanoaperture sizes: $X635Y365$ illuminated by x-polarized (a) and y-polarized (b) light; $X532Y365$ illuminated by x-polarized (c) and y-polarized (d) light; $X635Y532$ illuminated by x-polarized (e) and y-polarized (f) light. The other parameters are the same as those of the corresponding structures in Figure 2.11.

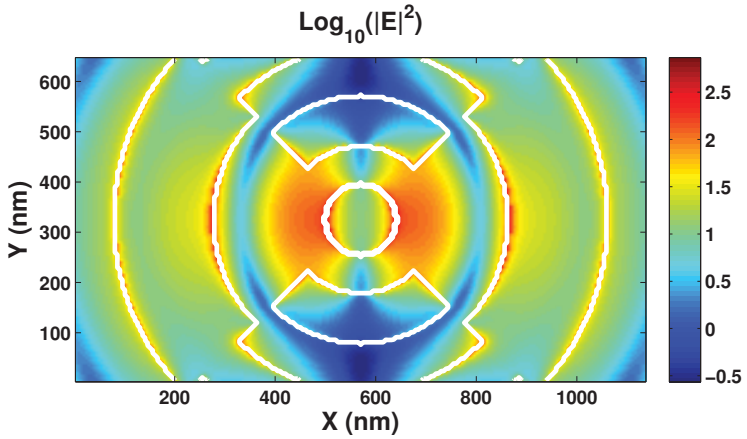

(a) x polarization

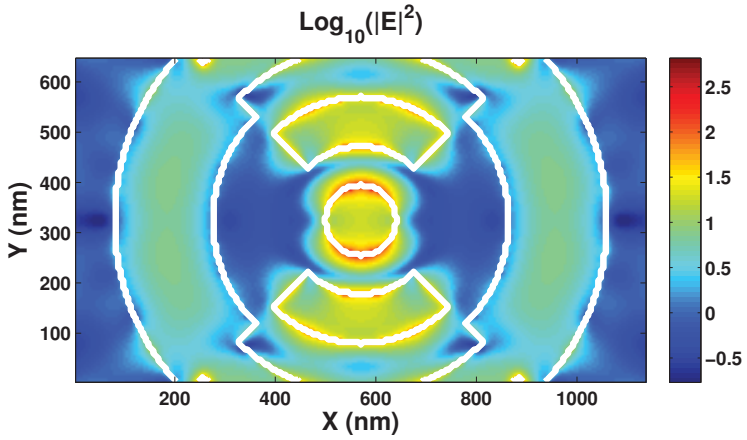

(b) y polarization

Figure 2.18. Spatial distribution ($x-y$ surface) of electric field intensity at the bottom interface of the compound bullseye structure $X635Y365$ with $d = 140$ nm, illuminated by x-polarized light at 635 nm wavelength (a) and y-polarized light at 365 nm wavelength (b).

Table 2.1. Comparison of performance metrics for the three plasmonic structures. The numerical value listed for each metric is the peak value based upon optimal geometrical parameters.

Structure	f_I	$f_{Purcell}$	f_{rad}	f_{rad} into Sub	f_ϕ	NE
Dipole	16.9	11.0	7.2	8.1	4.5	27.2
Bullseye	60.5	4.3	2.3	5.3	4.2	188.0
Aperture array	23.4	3.5	2.0	4.1	3.5	40.9

CHAPTER 3

THIN-FILM CHARACTERIZATION AND FOCUSED ION BEAM MILLING

According to the review in Chapter 1, aluminum (Al) is the dominant material used in UV Plasmonics [69–96, 96–111], due to its good plasmonic response in the UV and relative ease to work with. It is also mainly used in this dissertation work. However, Al is easily oxidized. Even if it can form a 5 nm self-protective oxide layer, the surface and bulk oxidation will still change the plasmonic resonance dramatically due to the high sensitivity of plasmonic resonance to the presence of Al oxidation [92]. Therefore, it is an important step to carefully measure the material properties and oxide thickness of Al thin-films before any further study. In addition, different film-deposition conditions will give Al thin-films with varied quality. One important parameter is the grain size. In this dissertation work, a top-down fabrication method, focused ion beam (FIB) milling, is used for all of our structure fabrication. Grain size limits the smallest features of nanostructures that can be fabricated. Thus, knowing the grain size can give us a practical guide for pattern design and structure fabrication. At last, a fabrication recipe of Al nanostructures will be developed. Several structures will be fabricated for future experimental study. Pattern quality, especially the undercut, will be carefully characterized.

3.1 Dielectric Constants and Oxidation Measurement

3.1.1 Measurement of Dielectric Constants

Ellipsometry is an optical technique for investigating the material properties (refractive index or dielectric constant) of thin films by measuring the change of the polarization states of reflected light. The polarization change is represented as an amplitude ratio, Ψ, and the phase difference, Δ. A Variable Angle Spectroscopic Ellipsometer (VASE) from J. A. Woollam is used, which is shown in Figure 3.1 (a). Two incident angles of 70 and 75° are used in the measurement. The scanning wavelength is from 260 to 1000 nm. After measurement, the measured Ψ and Δ is acquired as shown in Figure 3.1 (b). The trickiest

part is to fit those curves with a reasonable model. Because the software would fit any model the user provides, it totally depends on the user to determine if the model is reasonable. The thickness of the Al oxide layer in the fitting model will influence the dielectric constants. Figure 3.2 demonstrates the influence of Al_2O_3 thickness on the real part of the dielectric constant. One can see that the dielectric constant is different by fitting the same set of measured data with different models even if the thickness of the oxide layer only changes by several nanometers. The sensitivity of VASE is not high enough to measure such a small change of Al oxide thickness, so we need another tool to give us that information. The details will be discussed in the following part of this section.

It should be noted that the method relies on the reflection of optical light to measure the material properties, which means that only a thin-layer with thickness of skin depth can be measured. Usually, the front-side measurement is performed by shining the light on the top surface of metal film being measured shown in Figure 3.3 (a). However, our numerical and following experimental study focus on the local environment around the nanostructure at the Al/substrate interface. Due to the small skin depth of Al film in the UV ($\sim$ 12 nm), we cannot measure the interface property by doing front-side measurement. Our measurement has to be performed from the back-side of the sample, i.e., the substrate side also shown in Figure 3.3 (a). More considerations are required to correctly perform back-side measurement, because the incident light experiences two interfaces: air/glass and glass/Al. In order to eliminate the reflection from the air/substrate interface, we need to separate the beam reflected by the glass/Al interface from that reflected by the air/glass interface. Focusing probes need to be installed in the system, and several settings in the software need to change. The main steps for back-side measurement are summarized as follows:

1. Follow the SOP to initialize and calibrate the VASE system.
2. Install focusing probes to minimize the light spots.
3. Front-side measure the standard sample (25 nm SiO_2 + Si wafer).
4. Fit the standard model to get the angular offset and windows effect introduced by focused probes.
5. Back-side measure our film (align the detector probe to only collect the reflection from Al/substrate interface).

6. Add the offsets from step 4 into the model and fit it to get the optical constants. (In fitting option, set "# of Back-sides" to 1 and the "% First Reflection" to 0.)

To get the angle offset, when fitting the standard data, we need to check the box of globe offset in the model window/Angles shown in Figure 3.4 (a) before fitting. After getting the angle offset, we need to uncheck this box and fix the offset to the number acquired before. To get the windows effect, we need to check the boxes of delta offset in the model window/Option shown in Figure 3.4 (b).

Figure 3.3 (b) presents the front-side and back-side measured dielectric functions of Al films with different ages and from different sources. Here, we assume the old sample is oxidized more than the new one. The lines with black color stand for the data by in-situ measurement from the handbook [62], so those are treated as the perfect Al without oxidation. One can see that the magnitude of the real part of dielectric constant decreases with increase of oxidation. The data of back-side measurement (red lines) are the closest ones to the handbook data, since they are the properties at interface, which is protected by 100 nm Al film from oxidation. And the film from Moxtek was deposited under much higher vacuum, which means a lower level of bulk oxidation, so it is the second closest one to the handbook data. The reason why it is not the closest one is due to the surface oxidation.

As discussed previously, Al films always have native oxide layers on the top surface and the thickness influences the fitted data. Besides directly measuring the oxide thickness with other sophisticated tools, we use a simple fitting strategy to indirectly figure out how thick the native oxide layer is. This strategy is based on the reasonable assumption that fitting both front-side and back-side measurements should give the same data if the correct amount of oxide is included in the fitting model. The main steps are summarized as follows:

1. Measure the dielectric constants from both front and back sides.

2. Perform model fitting with different thickness of Al oxide of both sets of data.

3. Compare data of front-side and back-side measurements.

4. Choose the data sets which are the most close to each other.

By using this method, we figure out the thickness of Al oxide should be about 5 nm. Finally, the measured dielectric constants versus wavelength are shown in Figure 3.5. The measured data of 100 nm Mg film are also shown for comparison. The data were measured by Mr. Kanagasundar Appusamy.

3.1.2 Measurement of Oxidation

In order to accurately measure the oxidation level and oxide thickness of Al film, depth profiling with X-ray photoelectron spectroscopy (XPS) is applied. XPS is a surface-sensitive quantitative spectroscopic technique acquiring surface elemental composition by measuring the kinetic energy and number of electrons that escape from 0-10 nm thick surface due to X-ray radiation. Because it is a surface analysis tool, ion sputtering is required to collect the information of depth profile. In this measurement, argon (Ar) ions are used to mill the Al. After each step of milling, XPS is used to measure the surface elemental information. The procedure of milling and measuring is repeated until predefined thickness of Al is measured. The etching rate is roughly 10 nm per minute. Figure 3.6 shows the atomic concentrations of different elements versus depth of Al film. Depth data are plotted versus sputtering time, as precise depth calibration requires extensive calibration. The native oxide layer thickness at the metal-air interface is estimated to be about 4 nm, while the oxide layer at the metal-substrate interface (due to diffusion of oxygen from SiO_2) is also about 4 nm, although this layer is not as well defined. This is consistent with the thickness predicted by fitting our ellipsometry data. The bulk of the Al film is about 90% pure Al, and is a function of deposition conditions [92].

3.2 Grain Size

Figure 3.7 presents SEM images of Al films with the same thickness of 100 nm prepared with two different sputtering systems. One can see that the film quality in terms of grain size is quite different. Figure 3.7 (a) shows the Al film deposited with a Denton Discovery 18, using a base pressure of 10^{-6} Torr, Ar flow of 22.5 SCCM and sputtering power of 100 W. It is the film we are using for the following fabrication and experimental study due to its finer grains.

The grain size is usually estimated by manually measuring the 2D topographic image acquired by atomic force microscope (AFM). However, this method is not consistent due to the fact that it is difficult to define the boundary. In order to consistently estimate the grain size of Al thin film, a method based on power spectral density (PSD) function is applied [135]. The main steps are summarized as follows:

1. 2D topological image of Al thin film is acquired with AFM, which is shown in Figure 3.8 (a).

2. PSD is acquired by 2D Fourier transformation of the AFM image, which is shown in Figure 3.8 (b) as black dots.

3. PSD is fitted with a surface model. Here the ABC model is used, which can be described by [135]:

$$S(f) = \frac{A}{(1 + (Bf^2))^{C/2}}$$

where B is the correlation length, which is a measure of average grain size.

The correlation length of our film is fitted as ∼55 nm. It implies that to fabricate the structure with feature size of 50 nm will be a challenging and unstable procedure since it is close to the grain size of film.

3.3 Nanofabrication with FIB Milling

As discussed in Section 1.2 of Chapter 1, advanced nanofabrication techniques are the essential factors enabling the exploding development of Plasmonics. Various sophisticated methods have been developed [121]; however, fabrication of feature sizes of ≤50 nm with good enough quality for future characterization is still challenging, given the limit of film quality and fabrication capability.

In our research, fabrication is performed by using FIB milling. FIB milling is a top-down fabrication technique, which forms the nanostructure by physically sputtering away the material with a focused ion beam. Due to the massive mass of an ion compared to an electron, its de Broglie wavelength can be three orders of magnitude smaller than the electron's, so its resolution is not limited by the diffraction limit, but mainly determined by the aberration of the ion imaging system and the following developing processes. Figure 3.9 shows the SEM image of the inner chamber of our FIB system (FEI Helios NanoLab 650 Duobeam system @nanofab). This system integrates ion (at 52° with respect to normal direction of stage) and electron (in normal direction) beams for FIB and SEM functionality in one machine. This system also includes the gas injection systems for the purpose of EB/IB-induced deposition and other advanced applications. From Figure 3.9, one can see that there are three needles around the IB column, which are the needles for Pt and carbon deposition, and iodine-etch-enhanced-gas injection.

This system offers two important capabilities. One is the real-time cross-section E-beam image during FIB milling, which is demonstrated in Figure 3.10. Figure 3.10 (a) shows a tilted SEM image of a partial bullseye fabricated with FIB. Figure 3.10 (b) presents the SEM image of the cross-section of the same pattern fabricated also with FIB immediately following the pattern fabrication. By utilizing this feature, we can easily achieve in-situ optimization and control of feature definition.

Another important feature is the capability of iodine enhanced etch. Iodine enhanced etch removes material faster than normal FIB milling. It injects a halogen gas compound (iodine) directed toward the surface of the sample during milling with a gas-injected needle. Sputtered material chemically reacts with the assisting gas to form a volatile compound that can be pumped away for faster etching. This method can effectively increase etching rates, improve the selectivity between some materials (such as Al and glass) and prevent the redeposition. Figure 3.11 compares two Al hole arrays fabricated with and without iodine enhanced etch. One can see that some apertures are blocked due to the redeposition for the case without iodine, while all apertures are milled through with iodine. The improvement is obvious.

The sputtering rate of FIB milling (R) is described as function of sputtering yield (Y), which is defined as follows [136]:

$$Y = \frac{numbers\ of\ target\ atoms\ removed}{numbers\ of\ incident\ ions} \quad (atoms/ions)$$
$$R = \frac{Ym}{96.4\rho} \quad (\mu m^3/nC) \qquad for\ 30kV\ Ga\ ion$$

where m is the atomic mass in the unit of AMU, and ρ is the density in the unit of g/cm^3. We can see that the sputtering rate (R) is a function of atomic mass and material density. Based on the expression, we calculated the sputtering rate of different materials shown in Table 3.1. The iodine-enhanced factors are also included. All data are extracted from the FEI FIB manual except for Mg, which is taken from [136]. From the table, we can see that the sputtering rate of Al and Al_2O_3 is much slower compared to gold. Fortunately, the sputtering rate of Al can enhanced by 7 to 20 times, which implies that use of iodine-enhanced etching is essential for Al fabrications. However, the sputtering rate of Al_2O_3 is still small even applying iodine gas. From Section 3.1, we know there are always ∼4 nm oxide layers presenting on both top surfaces and the Al/quartz interface due to the oxidation. Therefore, it is challenging to fabricate Al nanostructures with FIB milling. Longer dwell time is usually required to ensure the etching goes through the oxide layers. The sputtering rate of Mg is similar to Al, but it is easier to be fabricated due to the absence of sputtering-resist oxide layers.

From the previous discussion, we know that large beam current gives the faster etching rate. However, small beam current is required to achieve fabrication with higher resolution. So we have to take into account both etching speed and etching resolution to determine the proper beam current. We choose accelerating voltage of 30 kV, beam current of 24 pA (corresponds to beam spot size ∼40 nm) for most of Al fabrication with feature size down

to 40 nm. The dwell time at each point is controlled by setting dwell time and passes. We are using 8–38 μs times 60 passes, which means 480–2280 μs at each point. To remove the same thickness of material, the dwell time is longer for smaller features due to redeposition. The overlap between adjacent spots can be also controlled. In order for good fabrication quality, the rule of thumb is positive overlap for milling (without enhanced gas), zero overlap for etching (with gas) and negative overlap for deposition. The main steps involved in the fabrication are shown as follows:

1. Generate Bitmap files in gray scale with Matalb code. Different gray scale corresponds to different dwell time.

2. Load the sample, and optimize the beam by adjusting the astigmatism.

3. Carefully adjust the focus. The pattern quality is very sensitive to the focus, especially when the pattern is very small ($\sim$50 nm).

4. Load the Bitmap file and perform the milling.

After developing the fabrication recipe, three nanostructures designed and analyzed in Chapter 2 are fabricated in 100 nm Al film with FIB milling, which is shown in Figure 3.12.

The pattern quality near the interface is crucial for our future experimental study. In addition, we have to apply longer dwell time in order to etch through the oxide layers on the surface of the Al structure, which inevitably introduces the undercut into the substrate. Figure 3.13 shows a typical SEM image of cross-section of a round Mg nanoaperture with 80 nm diameter, which is fabricated with beam current of 24 pA and dwell time of 2.04 and 1.92 ms. The undercuts are as large as 200 nm. With/without undercut strongly influences the numerical simulation, experimental results and data analysis. Therefore, it is necessary and important to carefully characterize the cross-section of nanostructures, especially the region around the interface. Fortunately, with duo-beam FIB system, we can acquire the cross-section image immediately after the pattern is fabricated. However, due to the small feature of our patterns, it is impossible to accurately define the cross-section region of the interesting pattern by manually placing the etching region. Additional steps need to be applied for this purpose. Our FIB system provides a software called “Auto slicer and viewer” meant for this kind of application. The basic idea of the software is simple, which mainly includes two steps —making a fiducial pattern for drifting compensation and accurately locating of etching region, and a loop of slice cross-sectioning and image acquisition. However, this software is not stable, and frequently loses the communication

with the main software, especially when switching from protection layer deposition to milling. We develop a procedure, which combines several manually operating steps and part of the automatic functions provided by this software, to acquire the cross-section of our nanostructures. It is summarized as follows:

1. Make a fiducial pattern for stage drifting compensation.

2. Define a region to be investigated by depositing a 300 nm Pt protection layer on top of it. It is noted that the deposition needs to be achieved by E-beam deposition instead of ion beam. By using E-beam, we can avoid damage of the top surface, even though the deposition rate is much slower compared to ion beam.

3. Run the software (Auto slicer and viewer). Define the region in the software and make sure to overlap it with the protection layer deposited in the previous step.

4. Following the steps of software to finish the slicing and imaging.

By doing the automatic slicing and imaging, we can collect series of slice views across the structure, so that we can always find the right cross-section corresponding to the cutting through the center of the nanoaperture.

3.4 Summary

In this chapter, the dielectric constants and oxidation of Al thin-film have been carefully measured in order to accurately design the UV plasmonic structures, and to analyze the experimental data acquired in the following steps. The dielectric constant of a 100 nm thick Al film was measured with VASE through both front-side and back-side measurements. The procedure of back-side measurement with VASE, which is required for our simulation and experiment, has been developed. Using the simple fitting strategy by adjusting the thickness of the Al oxide layer inside the fitting model, we have indirectly estimated the thickness of the native oxide layer of our Al film, which is about 5 nm. In addition, the oxide thickness and oxidation percentage have been directly measured by XPS. Through the measurement, we know that the thickness of the oxide layer is about 4 nm, which is consistent with the value estimated from ellipsometry measurement. Furthermore, there is another 4 nm thick oxide layer found at the Al/glass interface formed by the diffusion of oxygen. The bulk oxidation percentage of our Al film is about 10%.

We have explored a way to consistently measure the grain size by fitting the PSD function, which is the Fourier transform of the AFM image, with a surface model. The grain size has been estimated as ~ 55 nm.

The recipe of making Al nanostructure with FIB milling has been developed. The typical milling parameters are found to be dwell time of 2.28 ms with accelerating voltage of 30kV and beam current of 24pA for milling 100 nm Al with feature size of 60 nm. The operation procedure of automatically cross-sectioning and imaging has also been developed by combining manual operation and partial functions provided by system software. This is important for characterization of geometric properties of nanostructures at the Al/glass interface.

3.5 Acknowledgements

The author thanks Dr. Paolo Perez for performing the XPS measurement, Dr. Jianing Sun for discussion about back-side measurement with VASE and Dr. Randy Polson for FIB training and discussion of fabrication.

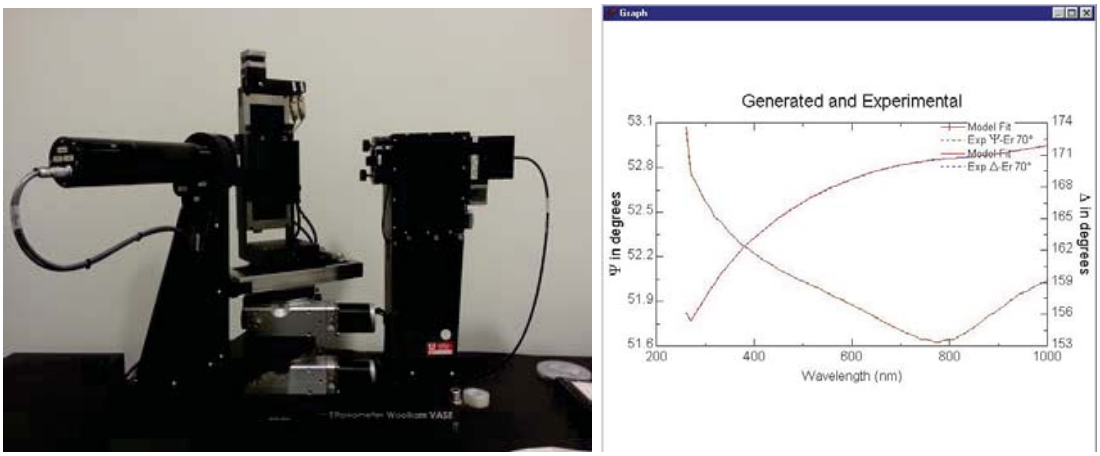

(a) (b)

Figure 3.1. Variable angle spectroscopic ellipsometer (VASE) in nanofab. (a) Picture of VASE. (b) Typical curves of Ψ and Δ from 100 nm Al thin-film measured with VASE.

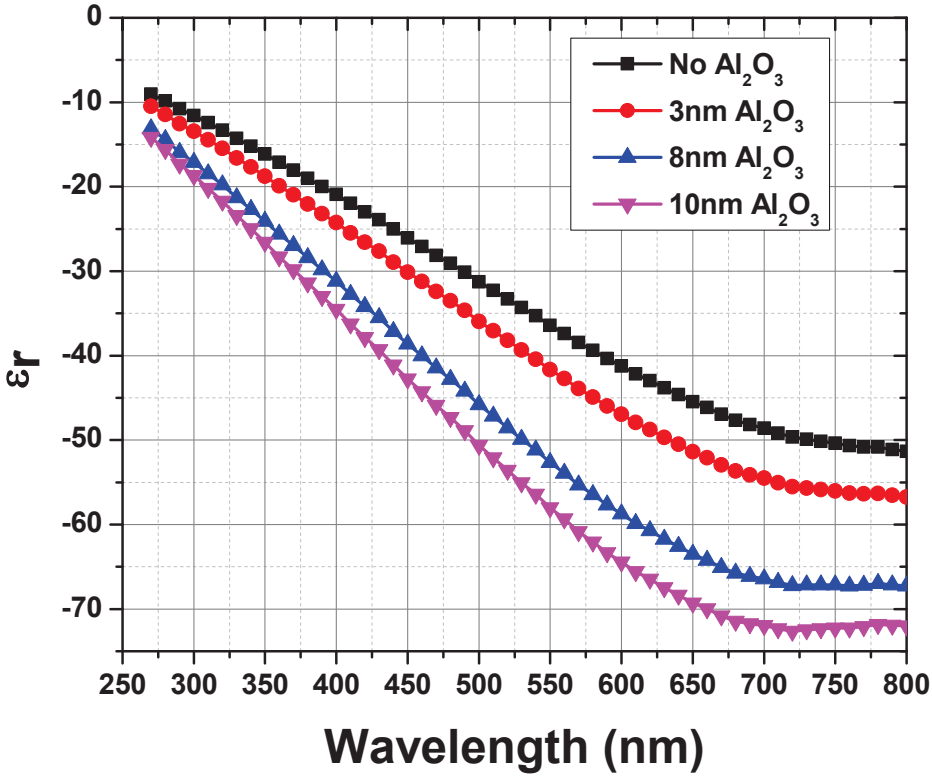

Figure 3.2. Real part of dielectric constant of 100 nm Al thin-film calculated by fitting the same measured data with different models including Al oxide layers with different thicknesses.

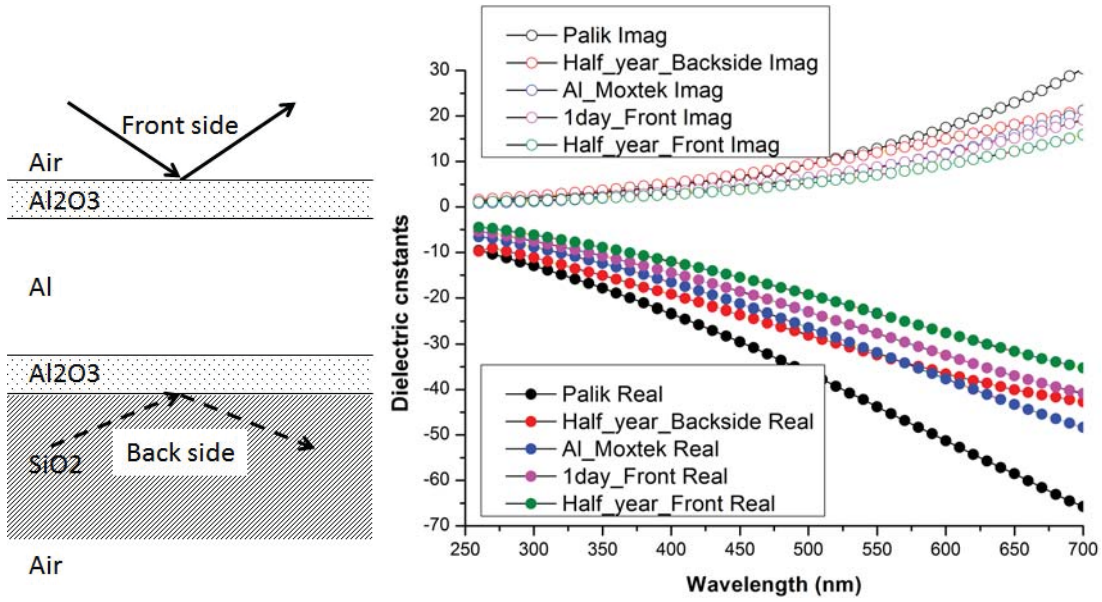

(a) (b)

Figure 3.3. VASE measurement. (a) Diagram of front-side and back-side measurement with VASE. (b) Real and imaginary parts of dielectric constants of Al films from different sources with different ages.

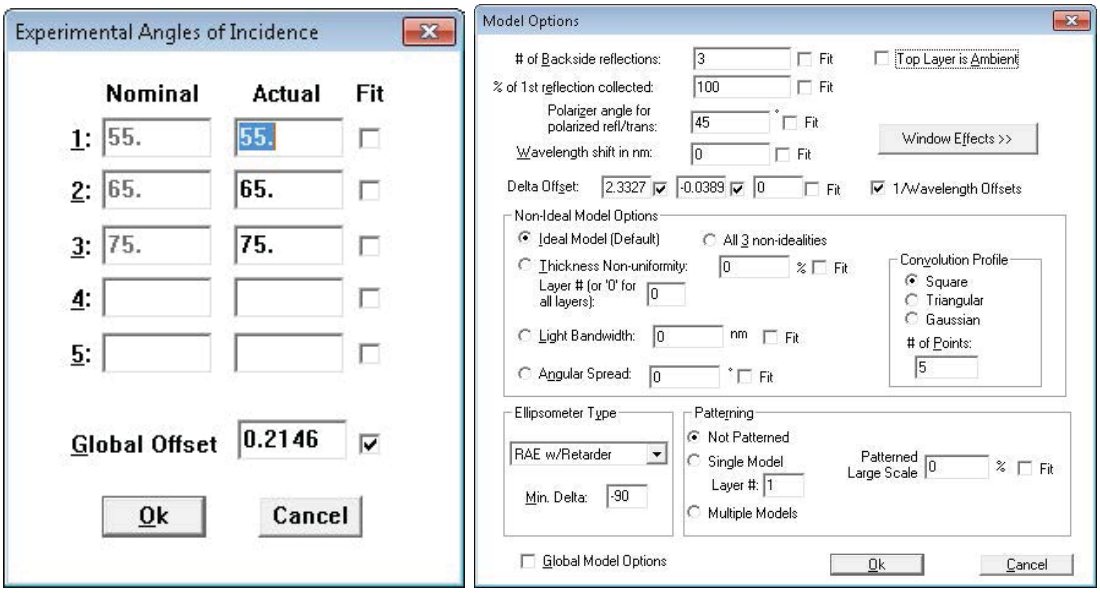

(a) (b)

Figure 3.4. The screenshots of software windows for (a) angle offset and (b) windows effect fittings. Credit to Dr. Jianing Sun from J. A. Woollam.

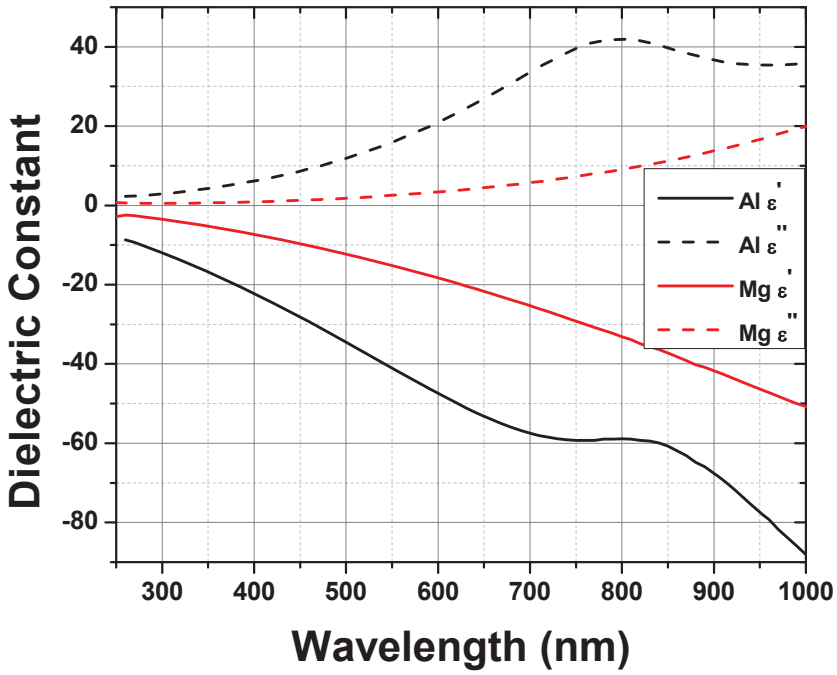

Figure 3.5. Real (ϵ') and imaginary (ϵ'') parts of dielectric constants of 100 nm Al film and 100 nm Mg film versus wavelength. Mg data were measured by Mr. Kanagasundar Appusamy.

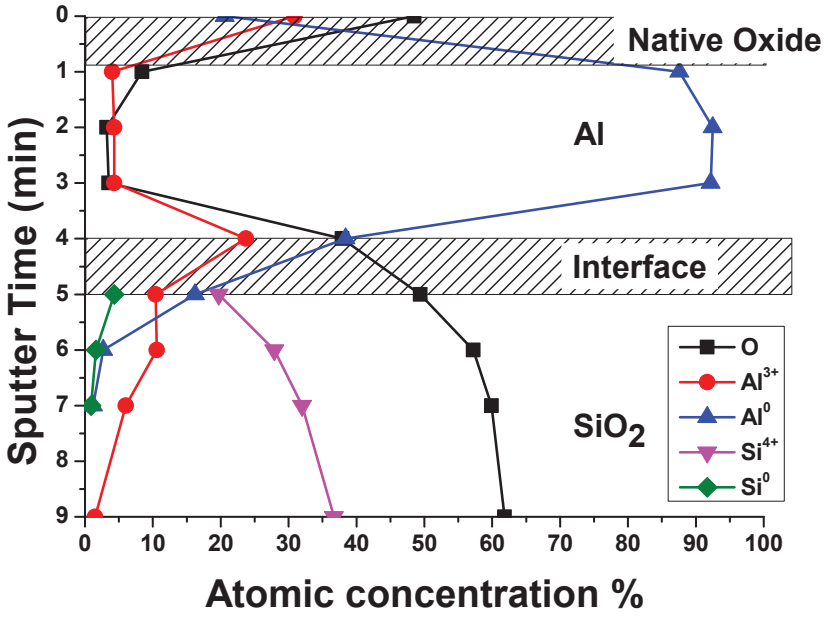

Figure 3.6. Atomic concentrations of elements of an Al thin-film obtained by XPS depth profiling. To reduce profiling time, a film with 50 nm thickness was measured.

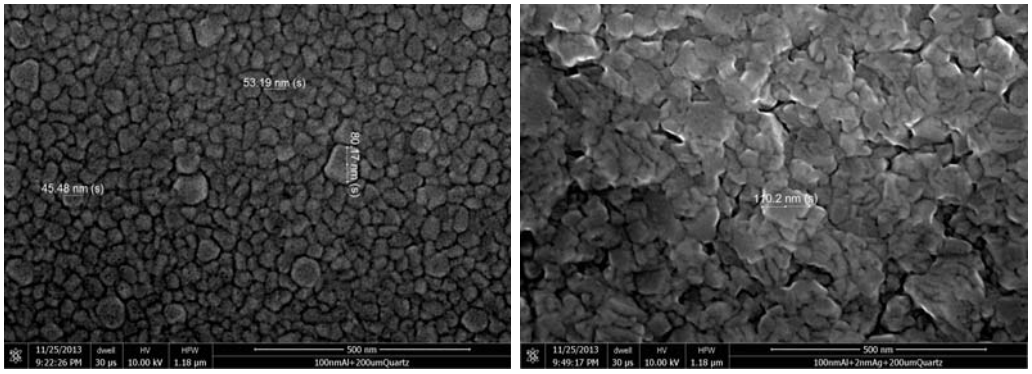

(a) (b)

Figure 3.7. SEM images of (a) 100 nm Al + 200 μm quartz and (b) 100 nm Al + 2 nm Ag seed layer + 200 μm quartz.

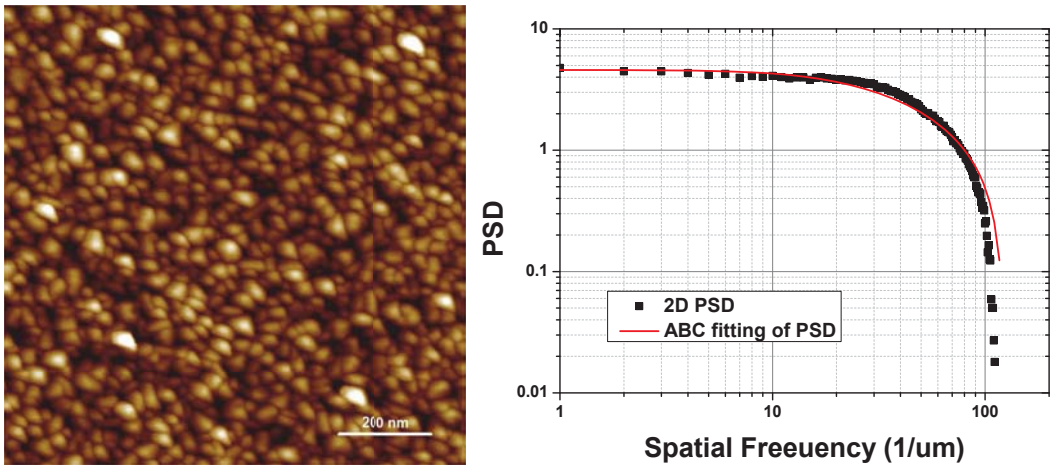

(a) (b)

Figure 3.8. Grain-size measurement. (a) AFM image of a 100 nm-thick Al film on a quartz substrate. (b) Power spectral density (PSD) function of AFM image (black dots) is fitted with ABC model [135] (red line).

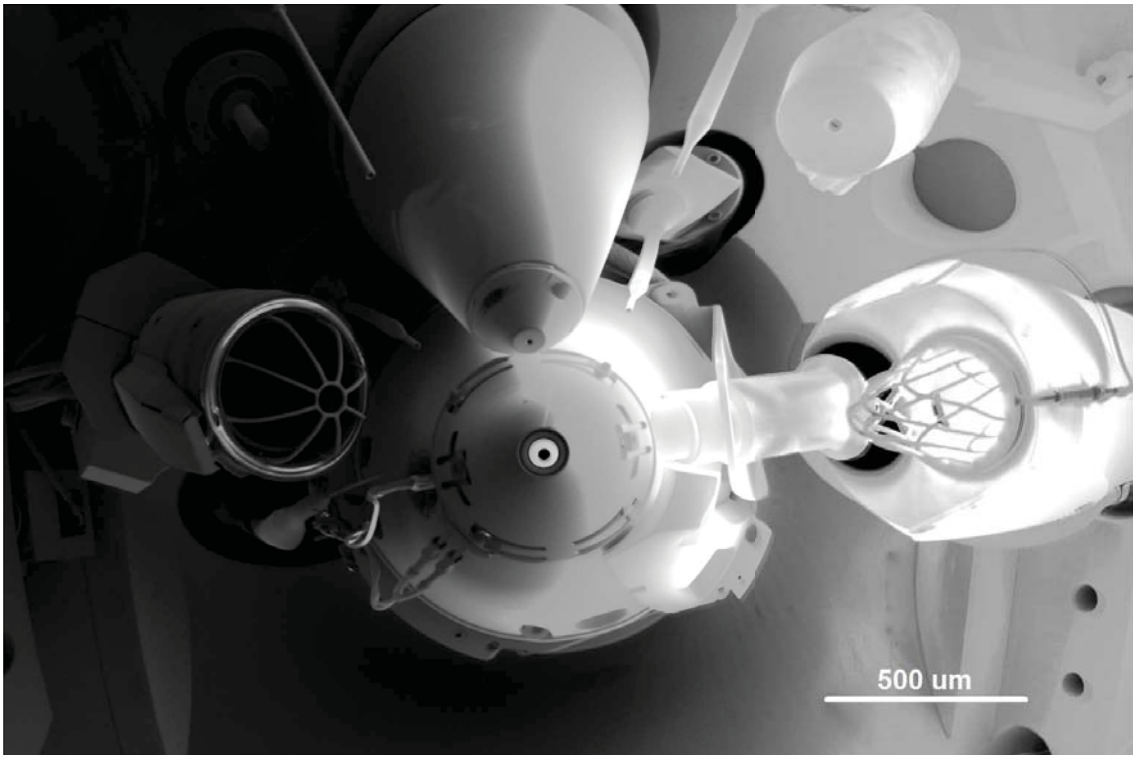

Figure 3.9. SEM image of inner chamber of FIB system formed with sapphire mirror. Credit to Dr. Randy Polson @ Nanofab

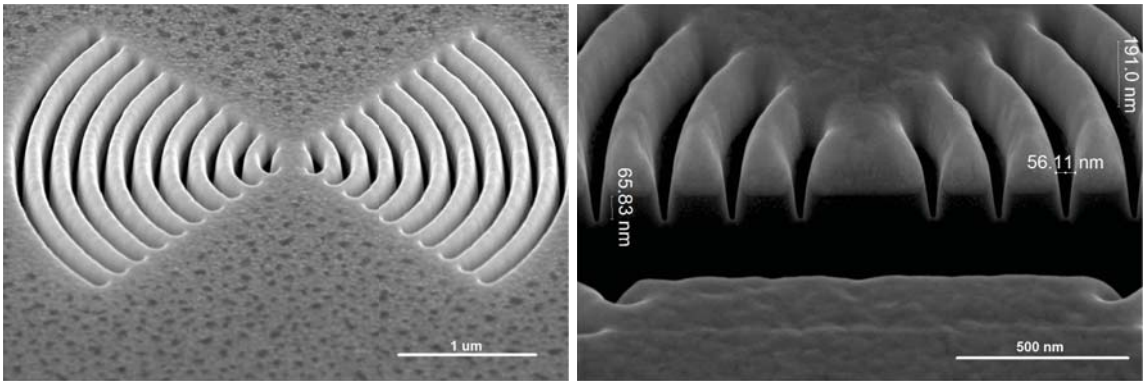

(a) (b)

Figure 3.10. SEM images of (a) tilted partial bullseye and (b) cross-section of the same pattern.

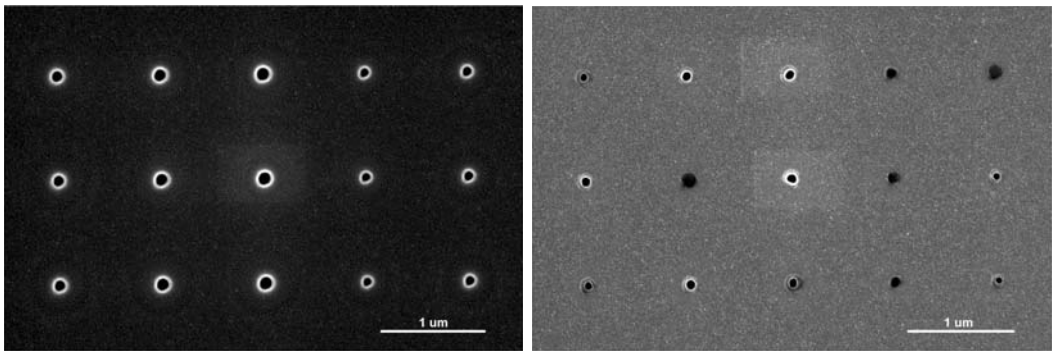

(a) (b)

Figure 3.11. SEM images of Al hole arrays fabricated (a) with and (b) without iodine enhanced etching.

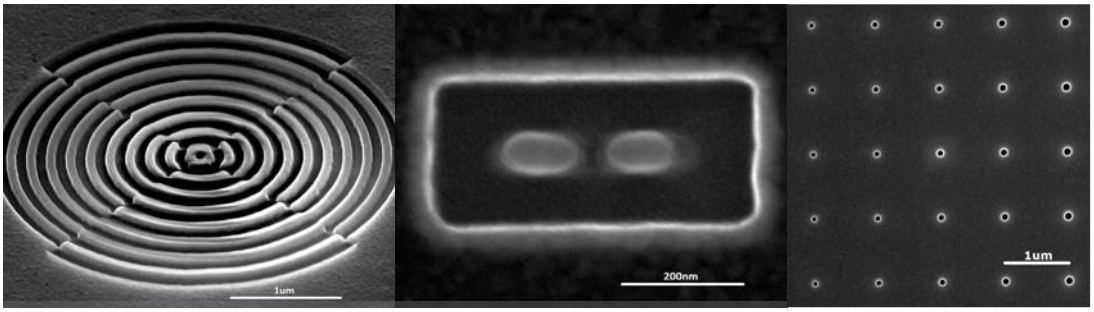

Figure 3.12. SEM images of plasmonic nanostructures fabricated by FIB in 100 nm-thick Al film: (from left to right) combined bullseye, trenched dipole antenna and hole arrays.

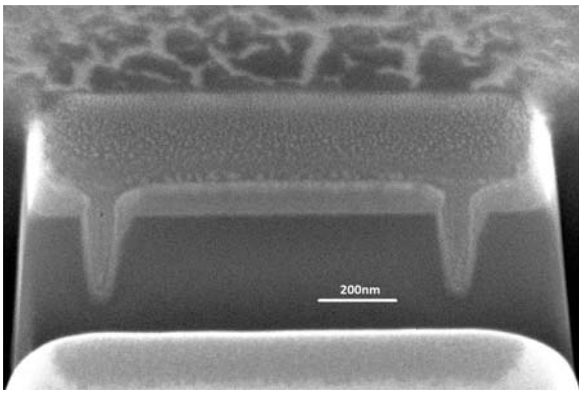

Figure 3.13. SEM image of cross-section of round Mg nanoaperture with 80 nm diameter milled with beam current of 24 pA and dwell time of 2.04 and 1.92 ms.

Table 3.1. Summary of sputtering rates and iodine-enhanced factors of different materials. All data are extracted from the FEI FIB manual except for Mg, which is from [136].

Material	Atomic mass (AMU)	Density (g/cm^3)	Sputtering yield (atoms/ions)	Sputtering rate ($\mu m^3/nC$)	Iodine Enhancement
Au	196.97	19.3	5.67–15.12	0.6–1.6	1–2
Si	28.09	2.33	1.60	0.2	5–15
SiO_2	60.08	2.65	0.85	0.2	1–1.5
$\mathbf{Al_2O_3}$	101.96	3.95	0.37	**0.1**	1–1.5
Al	26.98	2.7	4.83	**0.5**	7–20
Mg	24.31	1.738	4.91	**0.7**	

CHAPTER 4

UV FLUORESCENCE ENHANCEMENT BY ALUMINIUM NANOAPERTURES

After development of the design method, characterization of thin-film properties and nanofabrication of plasmonic structures, we reach the most important step of this dissertation work: study of plasmonic enhancement of UV fluorescence. Nanoapertures are very promising structures for the application of fluorescence enhancement due to the fact that they are relatively easy to be fabricated, and their physical structure is efficient for elimination of unwanted background signal. Al is the dominant material so far [69–96, 96–111]. So Al nanoaperture is the plasmonic structure studied in this chapter. Fluorescence lifetime is the intrinsic property of fluorescent molecules. The change of lifetime, i.e., Purcell factor, is one of the three factors influencing the final net enhancement according to Equation 1.15. Therefore, as the first step of UV fluorescence study, we will experimentally investigate the excited-state lifetime modification of diffusing molecules by Al nanoapertures in the UV. We will measure the lifetime reductions of two molecules (laser dye p-terphenyl with high quantum yield (QY) and one kind of amino acid tryptophan with low QY) inside the Al nanoaperture with different diameters and undercuts. The influence of diameter and undercut will be investigated. The QY-dependency of lifetime reduction will be experimentally demonstrated for the first time. We will validate our design method by examining the agreement of calculated and experimental data. Then, UV fluorescence enhanced by Al nanoapertures will be numerically studied. The enhancement of excitation, radiative and total emission versus dipole position will be calculated. The influence of native QY of molecule and undercut will be finally discussed.

4.1 Experimental Study of UV Lifetime Reduction

4.1.1 Sample Fabrication

Round nanoaperture samples were fabricated with FIB milling on 1"-diameter quartz coverslips (200 μm thickness). 100 nm Al deposition was performed by sputtering. Dielectric

properties and composition versus depth of the Al films have been obtained by ellipsometry and XPS measurement discussed in Chapter 3. As shown in Figure 4.1 (a), arrays of isolated apertures were produced with aperture size varying along the horizontal direction and milling dose varying along the vertical direction, so that the influence of both diameter and undercut can be studied within the same pattern. Two different patterns with the same design parameters were used in the experiments. Although the size is designed to be constant along the vertical direction, the varied dose can introduce the difference. In order to characterize the difference between fabricated and designed apertures, a topographic image of holes was acquired with AFM scanning. Then the diameters of 8 apertures with the same designed size and different milling dose were measured for each column. The plot of averaged measured diameters versus designed ones is shown in Figure 4.1 (b). The standard error is also included. One can see that the milled apertures are about 10 nm larger than designed. The variation increases up to 15 nm with apertures.

Furthermore, in order to study the influence of undercut, we need to measure the undercut versus dose for these patterns by duo-beam cross-section analysis. The detail of measurement can be found in Chapter 3. Fluorescence lifetime measurements for p-terphenyl and tryptophan were performed using two different nanoaperture patterns (both patterns for p-terphenyl and one pattern for tryptophan), so cross-section analysis was performed for each. Figure 4.2 shows the fitted undercut height versus FIB milling dose, which is used to convert milling dose to undercut depth for the lifetime measurements. Y error bars represent the regular residuals of linear fitting,

4.1.2 UV Fluorescent Molecules

In these experiments, we investigate two fluorescing molecules with different native QYs. The high QY dye is p-terphenyl, which is a UV laser dye with measured $\phi_0 = 0.88$ and $\tau = 0.98$ ns in 1-octanol (measured at 266 nm). Measured absorption and emission spectrum are shown in Figure 4.3, whose peaks are near 276 nm and 340 nm, respectively. We also investigate tryptophan, an aromatic amino acid, which is less photochemically stable than p-terphenyl. Tryptophan has $\phi_0 = 0.13$ in Tris buffer [124], with measured $\tau = 2.95$ ns, maximum absorption near 278 nm and peak emission near 340 nm. The solutions of 100 μM p-terphenyl in 1-octanol and 1 mM tryptophan in 5 mM Tris (pH=7.4) were prepared and characterized by Dr. Eric Peterson.

4.1.3 Fluorescence Lifetime Measurement

The measurement setup is depicted in Figure 4.4 (a). The laser source is a Coherent Chameleon Vision II Ti:Sapphire laser (not shown) with wavelength tunable range from 680 to 1080 nm, which is frequency-tripled using an A·P·E HarmoniXX unit. The UV light at 26 nm is guided by interconnecting optics built by ourself, which consist of a beam expander and a variable attenuator. Then it reaches the input of a Picoquant MT-200 system designed specifically for UV operation. A dichroic mirror reflects the input to an Olympus IX 71 inverted microscope with 40× 0.6 NA Ultrafluar UV objective and nanopositioning stage. Fluorescence collected through the objective passes the dichroic, is confocally imaged onto a 30 μm pinhole, then passes through a spectral emission filter (357±22 nm) placed before the UV-sensitive PMT (PMA-C 175-M Ultra). Note that the system has two detection paths, only one of which is used for lifetime measurements. The PMT output is connected to the PicoHarp 300 which records photon arrival time relative to the initial laser pulse. Time correlated single photon counting (TCSPC) is performed in the PicoHarp 300 to get the final histogram of fluorescence. The sync signal is generated from a photodiode collecting the fundamental output at 800 nm from the harmonic unit. Figure 4.4 (b) presents the zoom-in diagram of molecules diffusing in and out of single nanoapertures. Molecules at the bottom region of the aperture can be excited by UV light and emit UV fluorescence.

By using a confocal microscope and a nanopositioning stage, this system can generate a 2D scanning fluorescence image. Figure 4.5 (a) shows the SEM image of Al hole arrays; the 2D scanning image of the same area is shown in Figure 4.5 (b), which is usually used in the experiment to locate a different aperture for lifetime measurement.

Figure 4.6 (a) shows the instrument response function (IRF) and "free-solution" photon arrival histograms for p-terphenyl and tryptophan emission. The IRF was measured by using the reflection of the incident light pulses from an unpatterned region of the samples, and replacing the bandpass filter with a neutral density filter. The FWHM is about 156 ps. For the free-solution reference, fluorescence histograms were generated using a 500 nm diameter aperture placed on the same sample as the experimental aperture patterns, and adjusting focus slightly into solution; the 500 nm aperture is larger than the focal spot diameter. With the experimental nanoaperture patterns, backscattered excitation light was used to adjust focus onto the metal-substrate interface. Figure 4.6 (b) shows an example decay curve measured with a 60 nm nanoaperture. The SymPhoTime 64 software uses a multi-exponential reconvolution model to fit the TCSPC histograms. We use a single time constant for the fitting.

4.1.4 Experimental Results and Discussion

Figure 4.6 (b) also compares the fluorescence histograms of p-terphenyl in free solution (500 nm aperture) and in a 60 nm diameter Al nanoaperture. It is clear that lifetime is effectively reduced by the nanoaperture. Lifetime reduction is calculated as the ratio of lifetime in free solution and in nanoaperture. For Figure 4.6 (b), lifetime reduction is about 3.8. To further investigate the influence of geometric parameters of nanoaperture (diameter and undercut) on lifetime reduction, the lifetime is measured from the p-terphenyl solution inside each aperture with different diameter and undercut shown in Figure 4.1 (a). The measured fluorescence lifetime reduction for p-terphenyl versus undercut and diameter for two different patterns with the same design parameters are shown in Figure 4.7 (a) and (b), respectively. Y error bars represent the standard deviation of two sets of measurement, and X error bars count for the variation of undercut, which is deduced from Figure 4.2. Both figures show that the lifetime reduction increases with decreasing aperture size, and decreases with increasing undercut. The maximum lifetime reduction is ~ 3.8 for diameter of 60 nm with 50 nm undercut into the substrate. The reason for measuring lifetime from these two patterns is that they were fabricated before and after a big adjustment of the FIB system. One can see the big difference between two sets of data for smaller apertures (60 and 70 nm), because stronger plasmonic interaction inside smaller aperture make lifetime reduction more sensitive to the change of the local environment.

Lifetime measurement of tryptophan is more difficult, because tryptophan has low QY and less photostability. Low QY requires higher incident power to improve the signal. On the other hand, less photostability requires lower incident power to prevent photopolymerization. The fine point of incident power is hard to be found, especially taking into account the different plasmonic enhancement of apertures with different diameter. Figure 4.8 (a) shows the SEM image of pattern surface after lifetime measurement. One can see that some apertures are totally blocked by the photopolymerization. This unknown polymer is hard to be removed. Regular organic solvent and plasma cleaning do not work. Fortunately, we found that 1-octanol can dissolve it during the experiment. Figure 4.8 (b) presents the measured lifetime reduction for tryptophan inside the Al nanoaperture versus undercut. The trend is the same as that of p-Terphenyl: lifetime reduction decreases with increase of undercut and diameter. But the amplitude is smaller than p-Terphenyl, and the maximum lifetime reduction is ~ 1.7 for diameter of 60 nm with 50 nm undercut. One can also see that the error bar, i.e., the standard deviation, is much larger for the case of tryptophan, which is due to the weak signal and less photostability.

In order to compare the responses of the two molecules, we extracted the lifetime reduction from ∼50 nm undercut for each aperture size for both p-terphenyl and tryptophan. These values are plotted in Figure 4.9. The curves of linear fitting are also shown. One can see that the lifetime reduction is inversely proportional to the diameter for both molecules, but with different slopes. As shown, the lifetime reduction for tryptophan is significantly lower, even though both molecules experience the same photonic environment. The slope of curve of tryptophan is also smaller than that of p-Terphenyl. At 100 μM concentration, we estimate that about 10 p-terphenyl molecules contribute to the fluorescence measured from the 60 nm aperture, and about 60 molecules contribute to fluorescence from the 110 nm aperture. At 1 mM concentration, the number of tryptophan molecules contributing to the fluorescence measurements is 10× higher.

The difference of lifetime reduction for two molecules reflects the fact that the lifetime reduction is a function of native QY ϕ_0. To our knowledge, this relationship is not widely appreciated, but the implications are straightforward. In order to achieve an appreciable Purcell effect (e.g., $f_{Purcell} \geq 10$), the photonic structure must produce

$$\zeta \geq 1 + \frac{9}{\phi_0}$$

according to Equation 1.12, which can be difficult to achieve for poor emitters. More importantly for fluorescence detection, however, achieving a large Purcell factor is not a prerequisite for increased effective QY. QY can only be increased when $f_{rad} > f_{Purcell}$ (Equation 1.13); f_ϕ will always be greater for a poor emitter compared to a good emitter. In contrast, in the photobleaching limit, the total number of detected photons increases by a factor f_{rad} [137, 138], independent of ϕ_0. Nevertheless, for a good emitter, a large Purcell factor, even without increased QY, can lead to increased fluorescence count rate in the linear regime through an increased saturation intensity, which may be necessary for excitation enhancement to be fully utilized (but a photobleaching limit still applies). It is also clear that applications requiring large Purcell factors [139] benefit from the use of high ϕ_0 emitters.

To further analyze the fluorescence enhancement, we need to clarify whether the excitation is in saturated or unsaturated region. The total count rate and lifetime versus normalized input power were measured for p-terphenyl in 500 nm and 60 nm apertures, which is shown in Figure 4.10 (a) and (b). Similar results were obtained for other aperture sizes (not shown here). Saturation shown in this plot is primarily due to the 80 MHz repetition rate of the laser, not due to the internal cycle time of molecule, which is ≥1 GHz for p-terphenyl. The variation of measured lifetime is negligible below/above the saturation.

Reported lifetime measurements of p-terphenyl and tryptophan were made at 200 a.u, which lies in the unsaturated region. The measured power before objective versus normalized power is shown in Figure 4.10 (c). One can see that 200 a.u. corresponds to about 86 mW. We also found that tryptophan underwent photochemical reaction (photopolymerization shown in Figure 4.8 (a)) at powers above 500 a.u. due to its less photochemical stability.

4.2 Numerical Study of UV Fluorescence Enhancement

Lifetime reduction is indeed the Purcell factor ($f_{Purcell}$) discussed in Section 1.3.1 of Chapter 1. Based on the design method introduced in Section 2.1, we can calculate excitation enhancement, radiative enhancement and Purcell factor. In this section, the calculated and measured lifetime reduction will be compared. Whether they agree with each other or not will examine the validity of our design method. After validation of our design method, we will calculate the excitation (f_I) and radiative enhancement (f_{rad}), and ultimately analyze the influence of diameter and undercut on net enhancement (NE) of UV fluorescence.

4.2.1 Simulation Model

The round nanoaperture structures considered in this chapter are depicted in Figure 4.11 in cross-section. The nanoapertures are assumed to be supported by a semi-infinite quartz (SiO_2) substrate and covered by water. The refractive index of water is 1.3835 at 266 nm and 1.3603 at 340 nm [62], whereas 1-octanol, the other solvent used in our experiments, has a somewhat higher index of 1.46, measured at 325 nm [140]; all simulations used water refractive indices. Based on the characterization of the fabricated nanoaperture structure, the model of Figure 4.11 (a) has a 50 nm undercut into the substrate, while an idealized model is shown in Figure 4.11 (b) with no undercut for the purpose of comparison. The thicknesses of the native oxide layer along the exposed surfaces and the interfacial oxide layer at the substrate are assumed to be 4 nm according to XPS measurement discussed in Chapter 3. The dielectric function of Al is incorporated from measurements and dielectric data for other materials are obtained from the handbook data [62].

Three-dimensional electromagnetic simulation is performed using Lumerical FDTD Solutions. Symmetric boundaries are used along the x and y directions according to the symmetry of the structure. Perfectly matched layers (PML) are used on the other boundaries. The grid size is $2\times2\times2$ nm^3. The detail of calculation of excitation and emission enhancement can be found in Chapter 2. It should be noted that emission calculations are

performed for the x dipole orientation only due to the symmetry of the aperture, and to the fact that the z orientation makes a negligible contribution to far-field emission [141], which is demonstrated in Figure 4.12.

4.2.2 Validation of Design Method

Using the design method introduced in Section 2.1, we simulate round Al nanoapertures with oxide layers and 50 nm undercut shown in Figure 4.11 (a). The comparison of calculated and measured lifetime reduction versus diameter for p-terphenyl and tryptophan is shown in Figure 4.13. One can see that the calculation agrees with the measurement very well for the case of p-terphenyl. For tryptophan, the deviation is larger, and the measured numbers are higher than calculated ones. It implies that there are other decay channels in the experiment not taken into account in the simulation. We believe that one additional channel is introduced by molecular interaction due to the high concentration of tryptophan solution.

4.2.3 Position Dependency of Excitation and Emission Enhancement

With good agreement between the experiment and calculations established for the fluorescence lifetime reduction, further characterization of the fluorescence procedure can be fulfilled numerically. Figure 4.14 shows excitation enhancement (f_I at 270 nm), radiative enhancement (f_{rad}) and Purcell factor ($f_{Purcell}$) when $\phi_0 = 1$, versus vertical position within Al nanoapertures of different diameters. A 50 nm undercut into the substrate is assumed, and the position z=0 nm is at the interface between Al and the underlying interfacial oxide. Emission quantities are averaged over the 330 nm to 380 nm passband of the emission filter used in the experiments.

As expected, the maximum excitation enhancement occurs near the metal-substrate interface, with decay towards the top surface; a smaller secondary peak also exists near the metal top surface. The enhancement peaks are closer to the metal-substrate interface for the smaller aperture diameters due to the localized surface plasmon resonance (LSPR), which decreases in strength as the diameter increases. Shoulders in the enhancement curves beneath the interface are due to standing waves inside the undercut region, formed by reflections at the substrate-liquid and aperture interfaces [122]. The propagating mode cutoff condition is approached for the larger aperture diameters, giving rise to peak enhancement shifted to lie within the aperture [142]. Similarly, radiative enhancement (emission into the substrate) will decay for dipole positions towards the metal-solution interface. Due

to the large Stokes shift between excitation (λ ~270 nm) and emission (λ ~340 nm), the larger apertures are well below cutoff for the emitted light, so the radiative enhancement is largely due to the LSPR. The Purcell factor peaks at both the metal-substrate interface and metal top surface due to the LSPRs at these locations. Nevertheless, lifetime reduction at the top interface would be difficult to realize with our experimental setup of bottom-side excitation/collection due to the fact that both excitation and collected emission are strongly attenuated.

Real fluorescent molecules have native QY that are less than unity; Figure 4.15 plots lifetime reduction, QY enhancement and net enhancement (in the weak excitation regime) for $\phi_0 = 0.88$, which corresponds to p-terphenyl in our experiments. The lifetime reduction is rescaled from the situation of a perfect dipole according to Equation 1.12, with maximum local value of about 5.7. Measured lifetimes will be smaller than the peak values due to the fact that fluorescence will be detected from molecules distributed throughout the depth of the nanoaperture. This has been taken into account by performing a weighted-average of the lifetime with the net fluorescence enhancement calculated versus depth in the previous section. Net enhancement is the product of f_I and f_ϕ , and is greatest throughout the undercut region and within 10 to 20 nm above the aperture entrance due to the combination of both excitation enhancement and slight enhancement in effective QY near the interface. The maximum lifetime reduction occurs within about 20 nm of the aperture entrance; the rapid decay in lifetime reduction into the undercut region is responsible for the increase in f_ϕ and net enhancement beneath the aperture entrance, where $f_{rad} \gtrapprox f_{Purcell}$. As a result, a 50 nm undercut would lead to a reduced measured lifetime change, but increased net enhancement, as compared to no undercut. An undercut greater than 50 nm would reduce both the measured lifetime change, and, due to rapidly decreasing f_I , the net enhancement as well.

The same enhancement factors for tryptophan ($\phi_0 = 0.13$) are also shown in Figure 4.16. As expected, the local lifetime reduction is significantly smaller for tryptophan (compare to Figure 4.15 (a) for p-terphenyl), which leads to a significant increase in QY enhancement (Figure 4.16 (b)). There is an additional qualitative difference in the net enhancement. For tryptophan, the enhancement is predicted to be greatest near $z = 0$, due to the spatial overlap of greatest QY enhancement with excitation enhancement, compared to the maximum enhancement occurring deeper into the undercut region for p-terphenyl ($z \sim -35$ nm). This leads to a rather remarkable conclusion that with an undercut nanoaperture, the observation volume of the measurement is also determined by ϕ_0.

It is also interesting to further explore the effect of aperture undercut. Radiative rate enhancement, Purcell factor and excitation enhancement for the two cases (with 50 nm undercut and no undercut) are calculated for varying dipole locations along the depth of the aperture, which is shown in Figure 4.17. Despite the difference in undercut, the results are nearly identical, with the nonundercut case being truncated at z =4 nm. Experimentally, the difference between the undercut and nonundercut apertures would manifest in a lifetime reduction. Predicted lifetime reductions for the two molecules are shown in Figure 4.18, where the lifetime reductions are the weighted-average with net fluorescence enhancement versus depth. Because of the truncation of net fluorescence enhancement for the nonundercut case, the averaged lifetimes are weighted towards z ~10 nm where the local lifetime reductions are the greatest, whereas for the 50 nm undercut case, weighting is biased towards $z < 0$, where local lifetime reductions are rapidly decaying. Nevertheless, in terms of net fluorescence enhancement, a 50 nm undercut is advantageous.

A more efficient antenna structure could be used to increase net enhancement. From a previous numerical study of antenna structures in the UV discussed in Chapter 2 [81], which assumed the ideal case of pure Al and no surface oxidation, a dipole antenna will lead to a greater QY enhancement for low QY molecules. The bullseye aperture structure will also lead to increased effective QY due to high directionality in emission. These two structures can further lead to significant increase in excitation enhancement, but a complicating factor in their design is the large Stokes shift of many molecules of interest, which requires optimization of the structures at one or both of two wavelength regions, based upon measurement requirements [80].

4.3 Summary

In this chapter, we have demonstrated lifetime reductions for UV chromophores in free solution using two molecules with high and low native quantum yields for the first time. The lifetime reduction decreases with increase of diameter and undercut into substrate. Lifetime reduction and aperture diameter has a inversely linear relation, and the change slope is higher for molecules with higher quantum yield. Furthermore, the QY-dependence of lifetime reduction has been experimentally demonstrated. Molecules with higher native quantum yield experience larger lifetime reduction compared to those with lower quantum yield under the same plasmonic environment. The measured lifetime reduction as function of diameter can be predicted with simulation, which validates our design method. Based on simulation, we further analyzed the excitation and emission enhancement versus dipole

position, and found that the observation volume of the measurement can be determined by native quantum yield of molecule for a nanoaperture with undercut. We also demonstrated that undercut of the nanoapertures into the substrate is detrimental for lifetime reduction, but simulations show that undercut can be beneficial for net fluorescence enhancement.

These results further illustrate the applicability of engineered photonic structures to different regimes of fluorescence emission modification based upon the native quantum yield of the emitter. A poor emitter can experience a large quantum yield enhancement, but with small lifetime reduction, as compared to a good emitter, which can experience a large lifetime reduction and small quantum yield enhancement (or even quantum yield reduction). A strong motivation for investigating UV Plasmonics is the fact that many UV chromophores are poor emitters.

4.4 Acknowledgements

The experimental work presented in this chapter is a collaboration between Dr. Blair's and Dr. Harris' groups, which mainly involves Dr. Eric Peterson from Dr. Harris' group and the author. Dr. Peterson has devoted his knowledge, experience and time to the early stage of fluorescence experiment, which is essential for the research starting from scratch. He has helped to choose and prepare the fluorescence solutions, and also participated in part of the experiment. The author thanks him for his important guide to start the fluorescence experiment, and for his inspiring suggestions and tremendous help to solve many experimental issues.

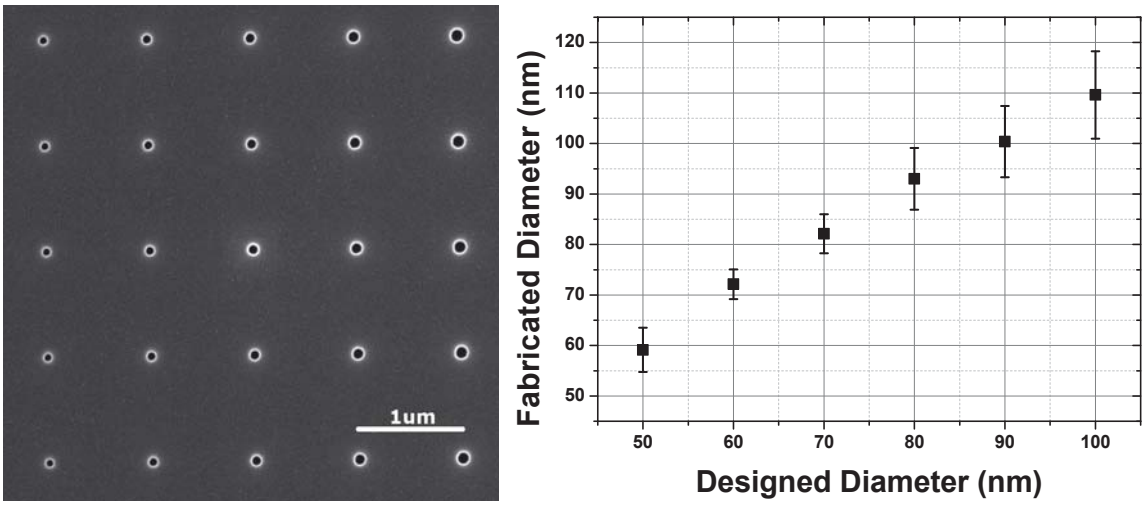

(a) (b)

Figure 4.1. Al nanoapertures fabricated with FIB milling. (a) SEM image of Al nanoapertures. Aperture size varies along the horizontal direction from 60 nm to 110 nm diameter. Milling dose varies along the vertical direction from 2280 μs to 480 μs.(b) AFM measured versus designed aperture diameter. Each data point represents 8 measured diameters (at different doses) for the same designed size.

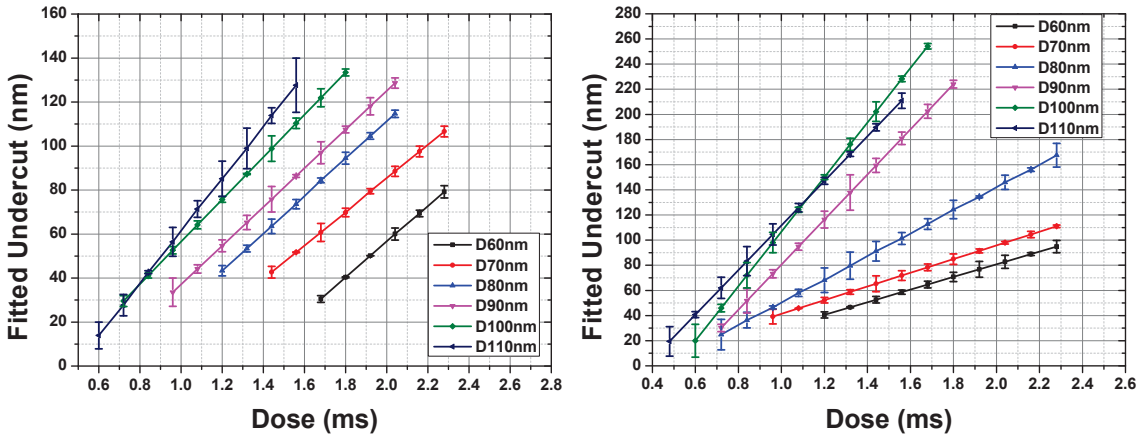

(a) (b)

Figure 4.2. Fitted undercut height versus FIB milling dose for nanoaperture patterns used for fluorescence lifetime measurements for (a) p-terphenyl and (b) p-terphenyl and tryptophan.

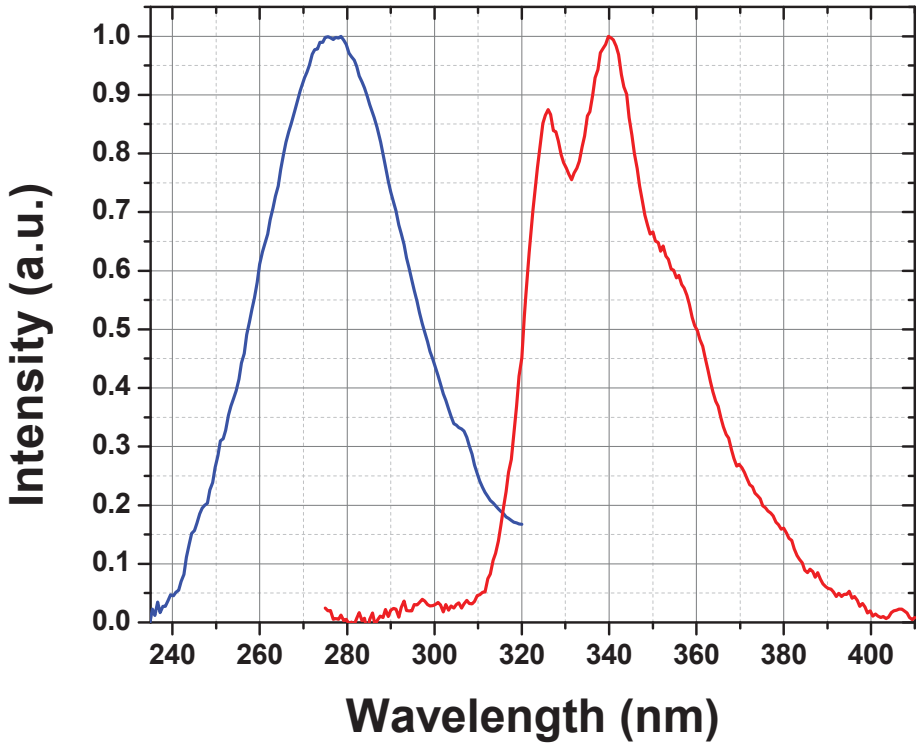

Figure 4.3. Fluorescence excitation and emission spectrums for p-terphenyl in 1-octanol. Fluorescence excitation is performed at 274 nm. Credit to Dr. Eric Peterson.

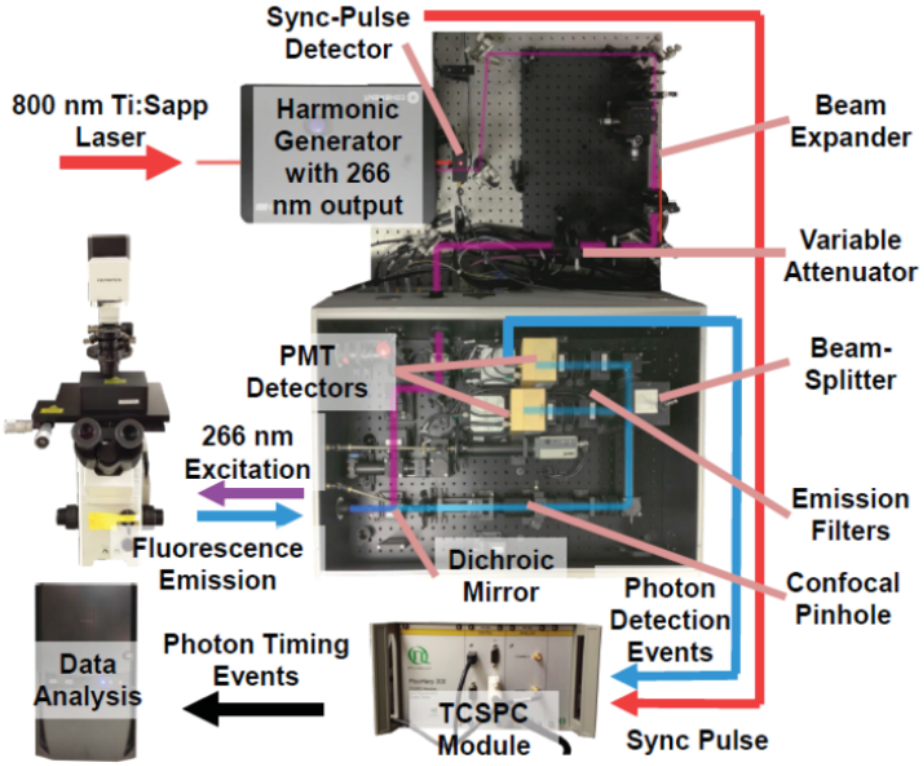

(a)

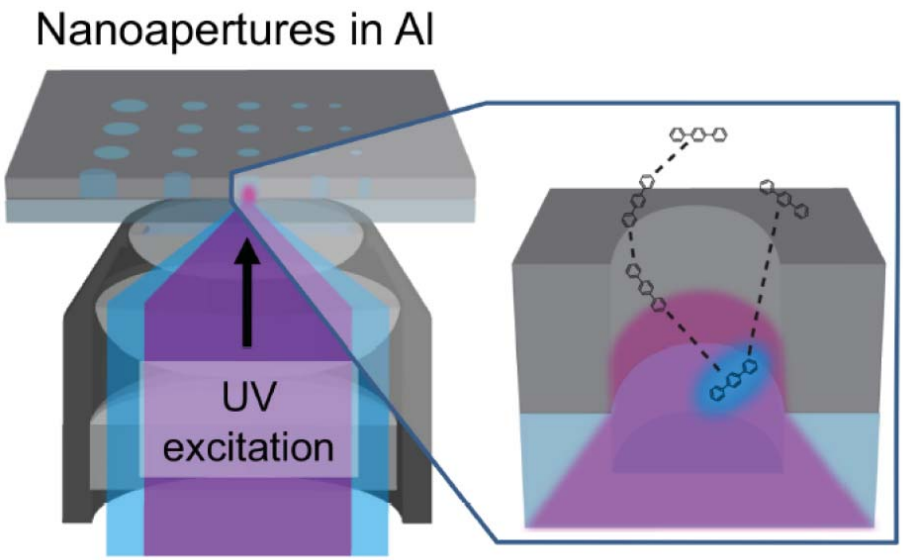

(b)

Figure 4.4. Diagrams of (a) experimental setup for lifetime measurements and (b) molecules diffusing in and out of nanoapertures

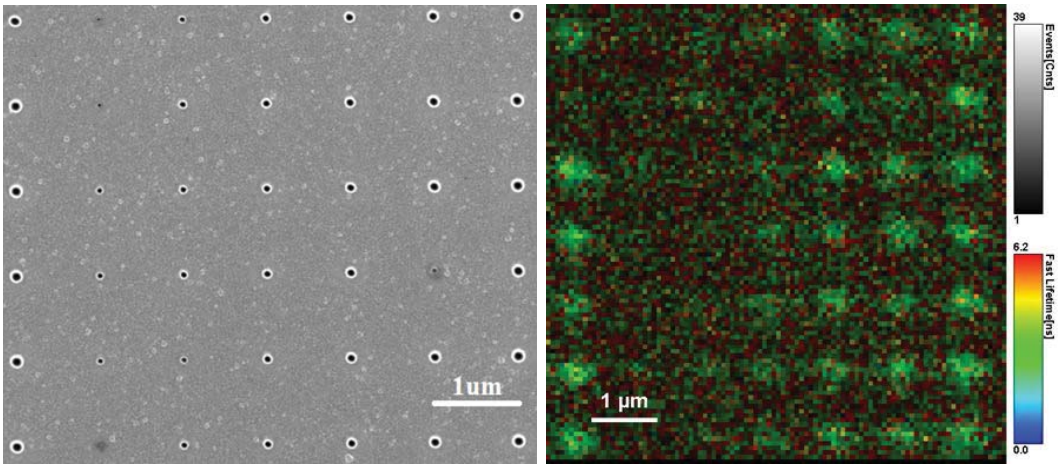

(a) (b)

Figure 4.5. Al hole arrays covered with fluorescent molecules. (a) SEM image of Al hole arrays. (b) 2D scanning fluorescence image of the same area.

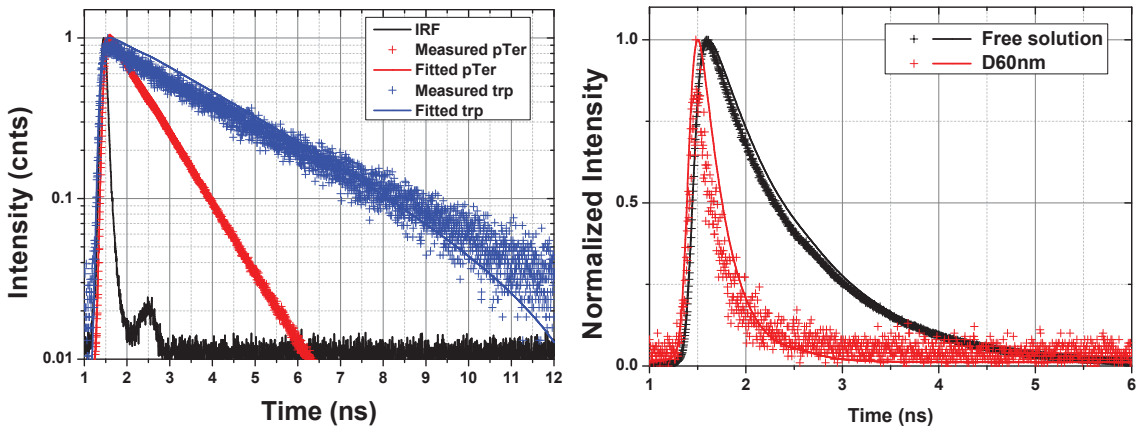

(a) (b)

Figure 4.6. Fluorescence histograms of (a) p-terphenyl (red symbols) and tryptophan (blue symbols) in free solution (500 nm aperture) compared to the instrument response function and (b) p-terphenyl in free solution (500 nm aperture) compared to a 60 nm diameter nanoaperture. The lifetimes of p-terphenyl and tryptophan are 0.98 ns and 2.95 ns in free solution, respectively.

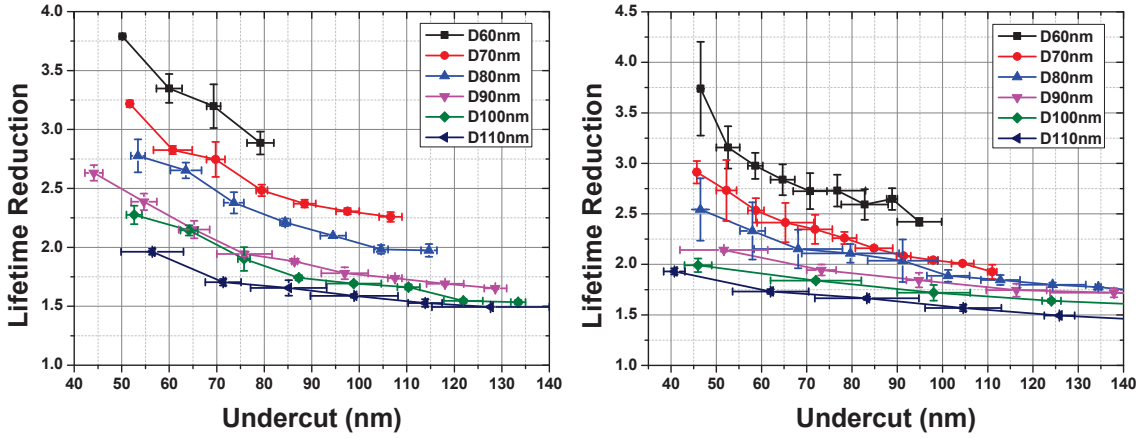

Figure 4.7. Measured lifetime reduction versus undercut for p-terphenyl with different aperture sizes. Two different nanoaperture patterns were used. Each panel represents two sets of measurements from one pattern. Y error bars are standard deviations of two measurements. Uncertainty in undercut is shown as X error bars. p-Terphenyl concentration is 100 μM in 1-octanol.

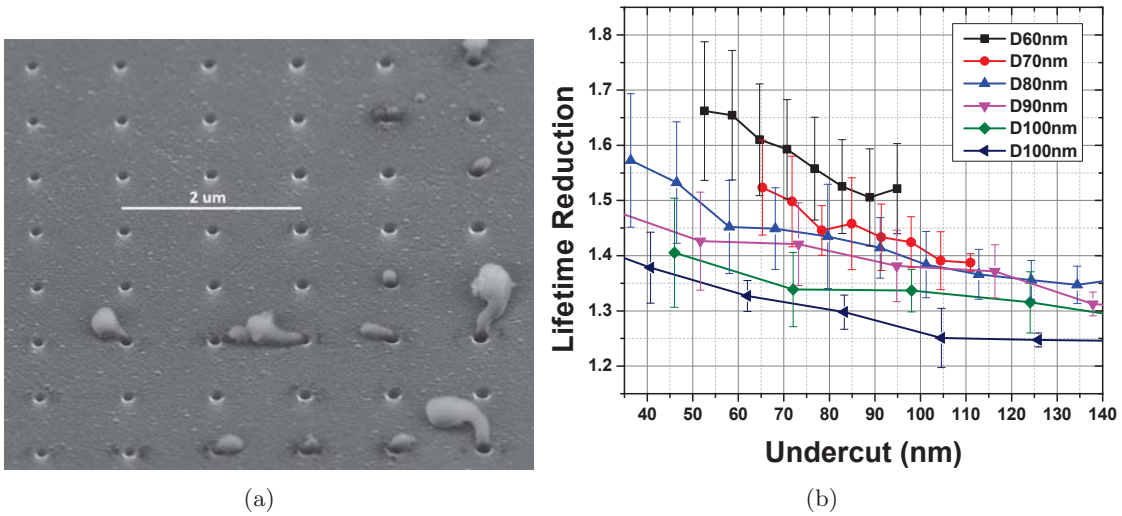

Figure 4.8. Al hole arrays covered with the tryptophan solution. (a) SEM image of pattern surface with photopolymerized tryptophan. (b)Measured lifetime reduction versus undercut for tryptophan with different aperture sizes. Two sets of measurements are averaged. Y error bars are standard deviations of two measurements. Tryptophan concentration is 1 mM in in 5 mM Tris (pH=7.4).

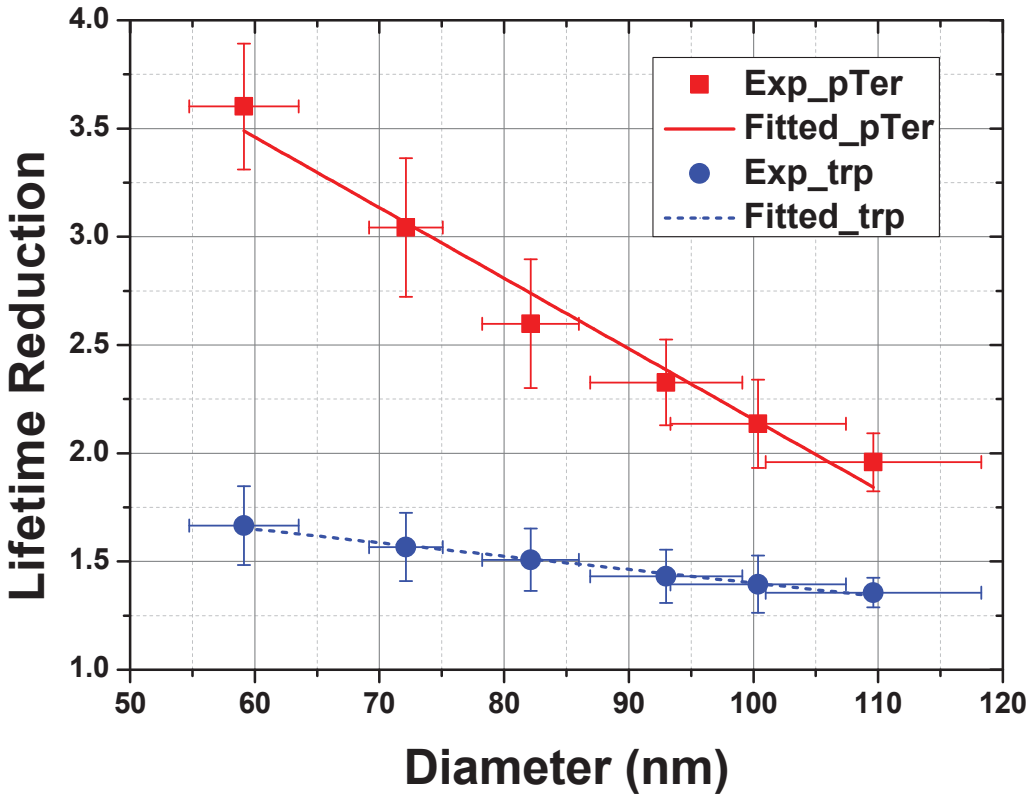

Figure 4.9. Measured lifetime reduction versus aperture diameter for p-terphenyl (100 μM in 1-octanol, red square) and tryptophan (1 mM in 5 mM Tris pH 7.4, blue circle). Data points for p-terphenyl are based on average and standard deviation of four independent measurements (two sets on each of two patterns), while data points for tryptophan are based on the same for two independent measurements (one pattern). Y error bars stand for the standard deviation of measured lifetime reduction, and X error bars count for the uncertainty in aperture size deduced from Figure 4.1 (b). Linear fits are also shown for the data.

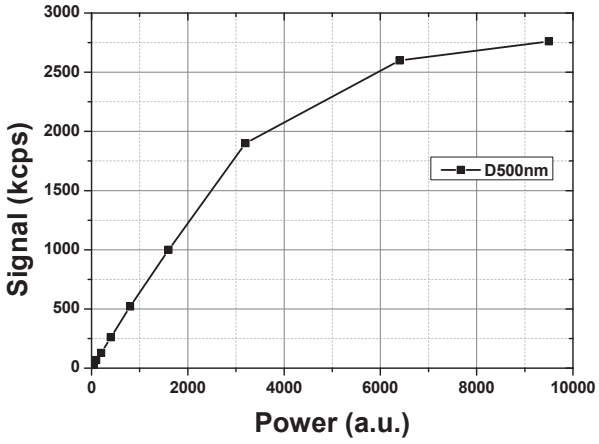

(a)

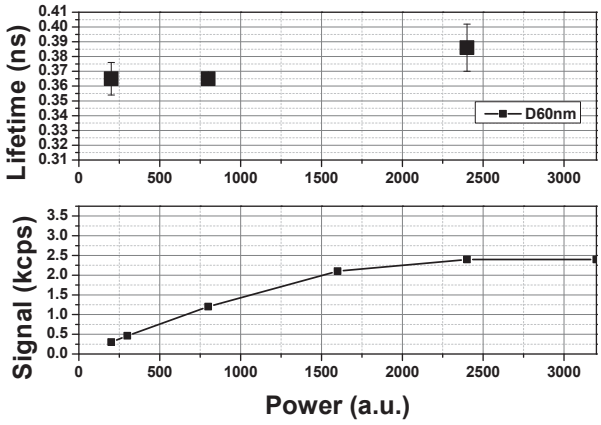

(b)

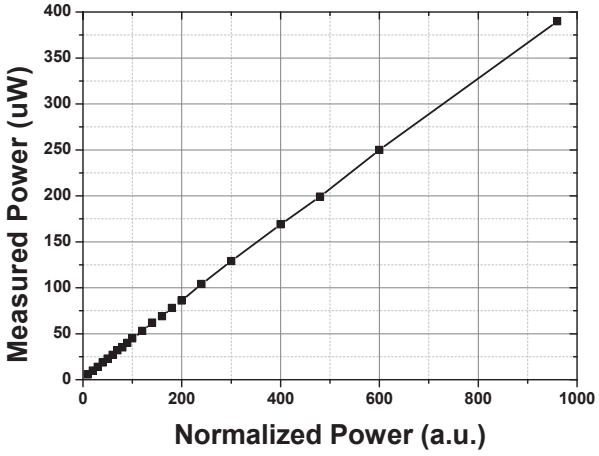

(c)

Figure 4.10. Fluorescence count rate versus normalized laser excitation power for 100 μM pterphenyl in 1-octanol measured in a (a) 500 nm aperture as a free solution reference and in a (b) 60 nm aperture with about 70 nm undercut. Lifetime is also shown for the 60 nm aperture versus laser power. (c) Power measured before objective versus normalized laser excitation power.

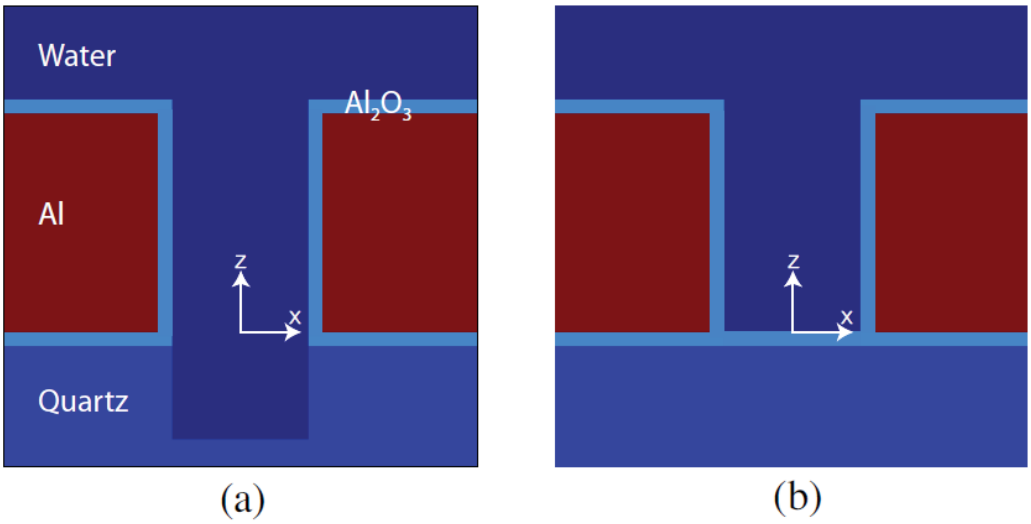

Figure 4.11. Cross-section views of the nanoaperture structure with (a) 50 nm undercut into the substrate and (b) no undercut. Oxide layer thicknesses are 4 nm.

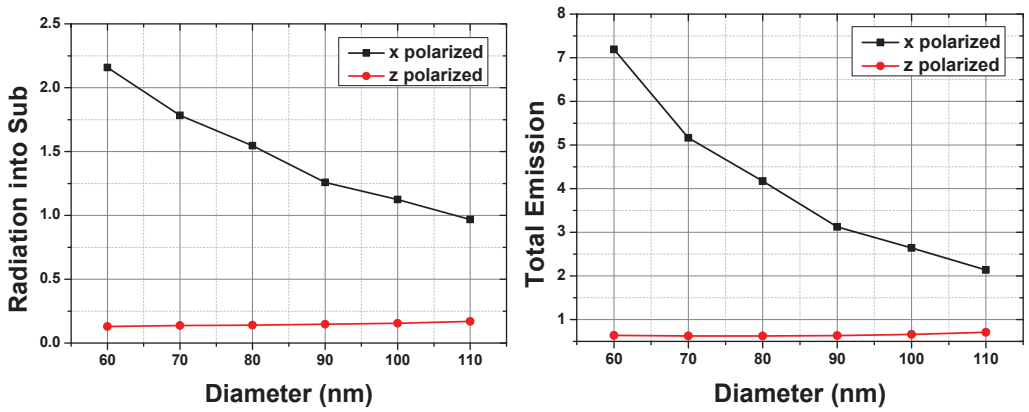

(a) (b)

Figure 4.12. Influence of polarization. (a) Radiative emission into substrate and (b) total emission of x-polarized and z-polarized dipole inside a 60 nm aperture.

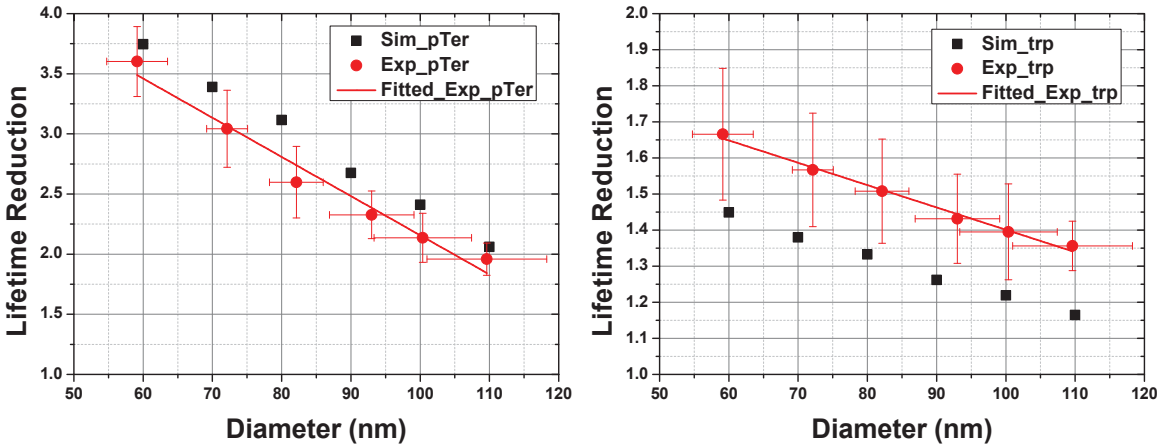

(a) (b)

Figure 4.13. Measured (red circle) and calculated (black square) lifetime reduction versus aperture diameter for (a) p-terphenyl (100 μM in 1-octanol) and (b) tryptophan (1 mM in 5 mM Tris pH 7.4). Experimental data points for p-terphenyl are based on average and standard deviation of four independent measurements (two sets on each of two patterns), while data points for tryptophan are based on the same for two independent measurements (one pattern). Uncertainty in aperture size is based on Figure 4.1 (b). Linear fits are shown for the experimental data points.

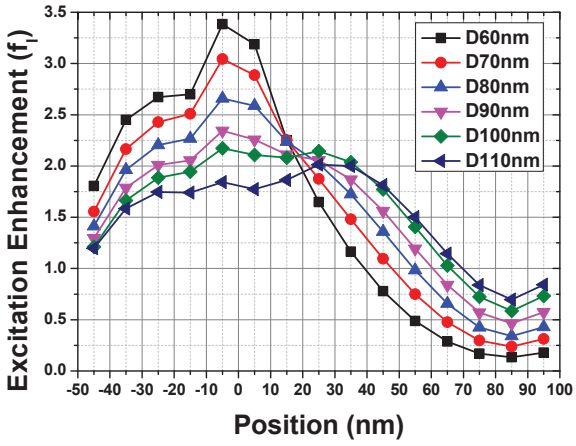

(a)

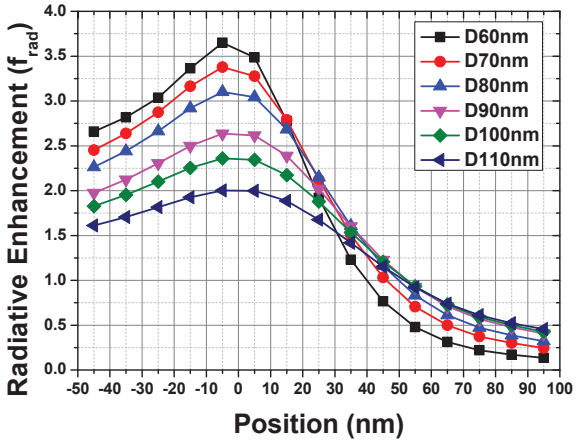

(b)

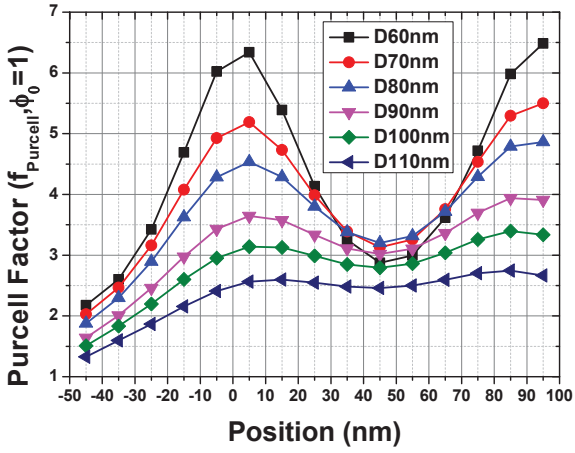

(c)

Figure 4.14. Calculated enhancement factors versus vertical position within the nanoaperture with a 50 nm undercut, versus aperture diameter: (a) excitation enhancement, (b) radiative enhancement into substrate and (c) Purcell factor ($\phi_0 = 1$).

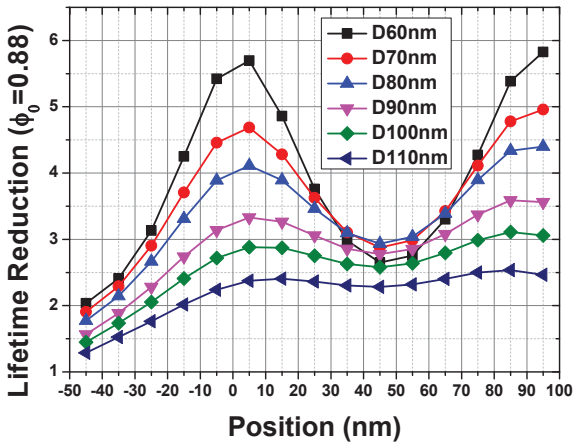

(a)

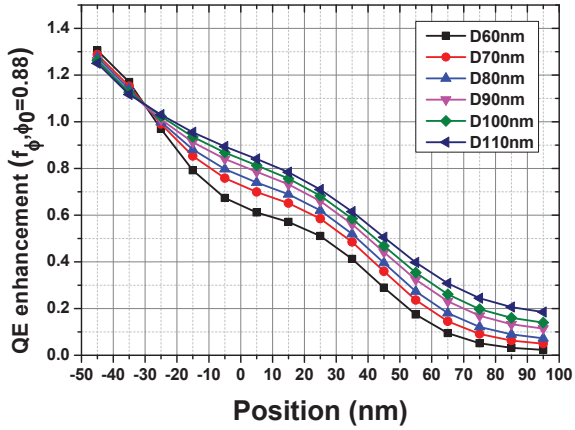

(b)

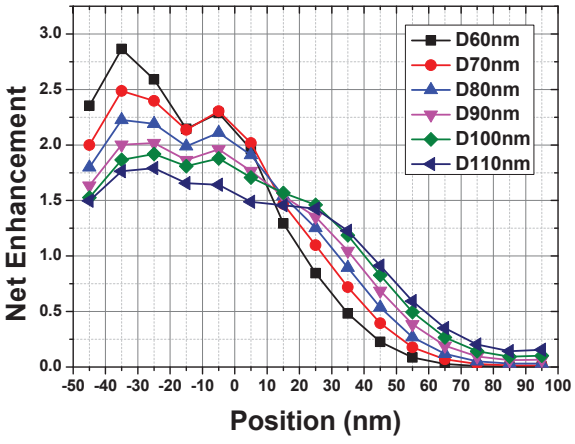

(c)

Figure 4.15. Calculated enhancement factors for p-terphenyl ($\phi_0 = 0.88$) versus vertical position within a nanoaperture with a 50 nm undercut, versus aperture diameter: (a) lifetime reduction, (b) QY enhancement and (c) net enhancement in the regime $I_e \ll I_s$.

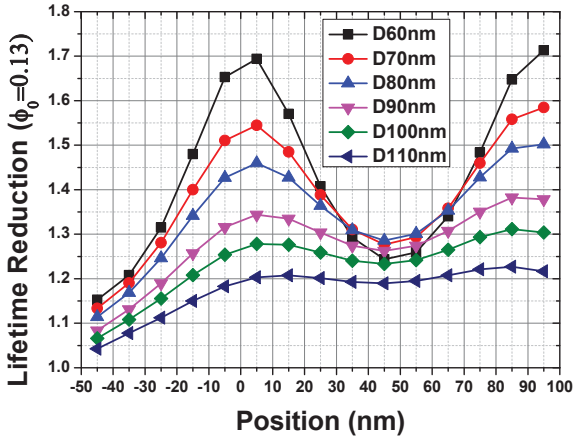

(a)

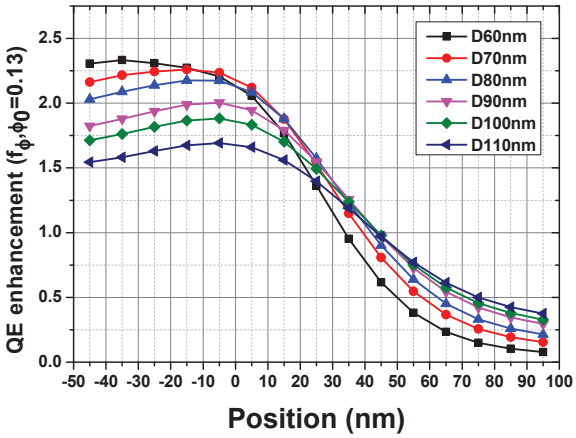

(b)

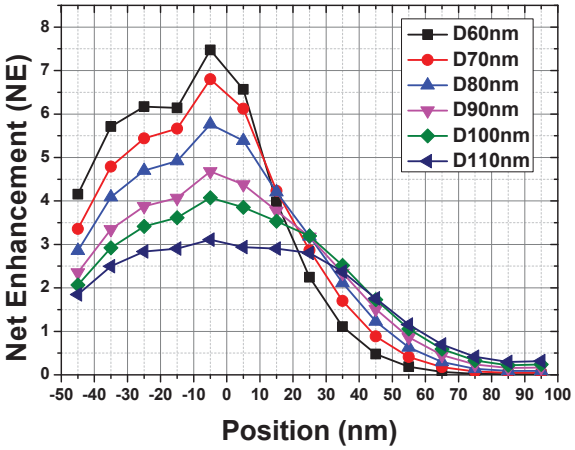

(c)

Figure 4.16. Calculated enhancement factors for tryptophan ($\phi_0 = 0.13$) versus vertical position within a nanoaperture with a 50 nm undercut, versus aperture diameter: (a) lifetime reduction, (b) QY enhancement and (c) net enhancement in the regime $I_e \ll I_s$.

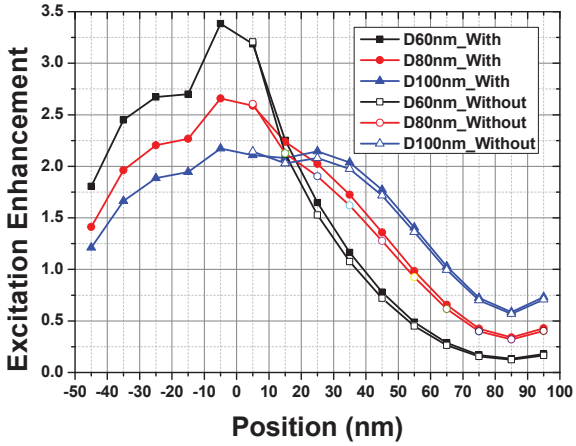

(a)

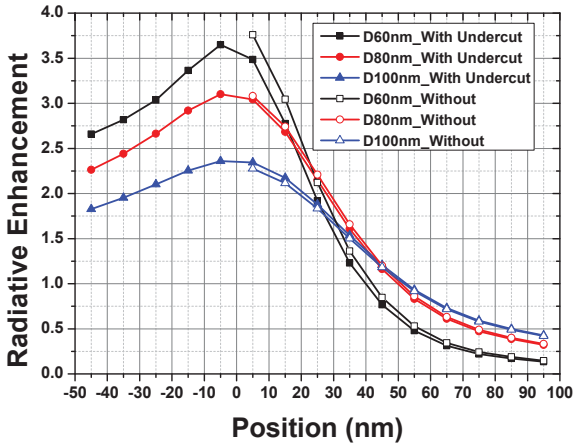

(b)

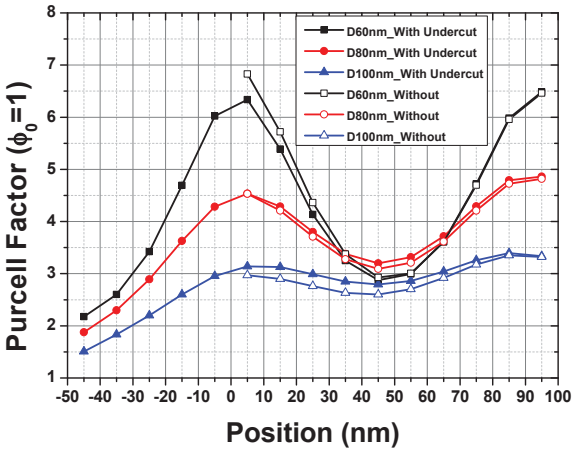

(c)

Figure 4.17. Calculated (a) excitation enhancement, (b) radiative rate enhancement and (c) Purcell factor ($\phi_0 = 1$) versus dipole position within nanoapertures with 50 nm undercut (solid symbols, ref. Figure 4.11 (a)) and without undercut (open symbols, ref. Figure 4.11 (b)).

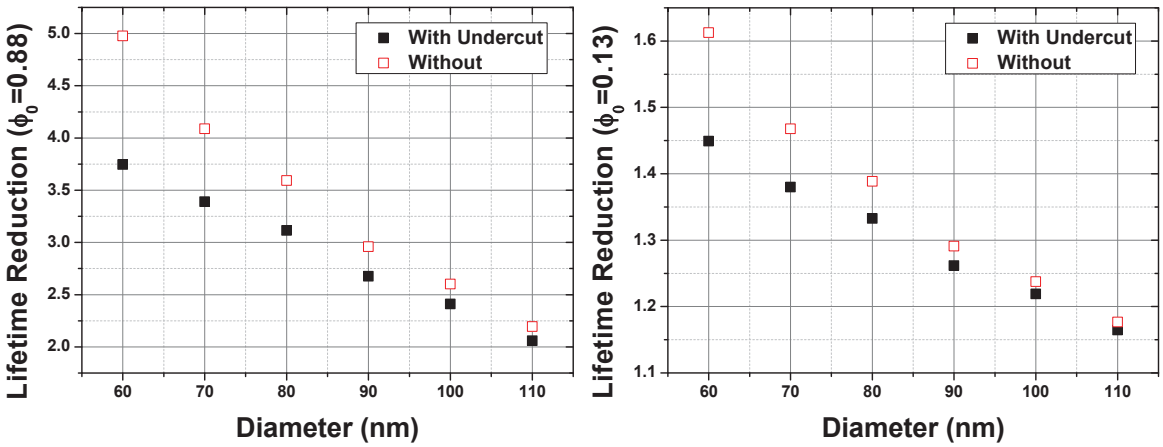

(a) (b)

Figure 4.18. Calculated lifetime reduction for (a) p-terphenyl and (b) tryptophan in nanoapertures with 50 nm undercut (ref. Figure 4.11 (a)) and without undercut (ref. Figure 4.11 (b)) versus diameter.

CHAPTER 5

ANOTHER POSSIBLE UV PLASMONIC MATERIAL: MAGNESIUM

So far, Al is the dominant material used for UV Plasmonics [69–96, 96–111]. Besides, several other materials have been studied as reviewed in Chapter 1, such as Zn [114], Ga [112, 115], Pt [113], In [96, 108] and Mg [64, 96, 115]. Among them, Magnesium (Mg) has similar material properties to Al. Both of them do not have d-shell electrons, so that interband transitions in these metals do not affect UV plasmonic response. Furthermore, Mg has better performance than Al for application based on localized surface plasmons (LSPs), such as UV fluorescence enhancement, suggested by the LSP figure of merit (FOM_{LSP}) in the UV. Therefore, it is worth exploring the possibility of applying Mg in the application of UV Plasmonics. At the beginning of this chapter, plasmonic response of Mg will be analyzed and compared numerically with Al for the application of UV fluorescence enhancement. Because both metals are easily oxidized, the effect of bulk and surface oxidation will also be considered. In addition, experimental study of lifetime reduction by Mg nanoapertures will be performed. The influence of diameters and undercuts will be investigated as well. At last, another plasmonic phenomenon, extraordinary optical transmission (EOT), of Mg and Al nanohole arrays will be studied, which is related to the resonance of surface plasmon polaritons (SPPs). The performance of Mg and Al in terms of transmission will be compared as well.

5.1 Comparison of Al and Mg for UV Fluorescence Enhancement

5.1.1 Comparison of Material Properties

Before starting the numerical comparison, it is helpful to compare the material properties of Mg and Al. Figure 5.1 (a) and (b) show the dielectric constants of Mg and Al versus wavelength from the handbook [62]. Curve fitting with the Drude model is performed to generate more data points in the UV range, especially for Mg. Those interpolated data will

be used for the following simulation. One can see that the amplitudes of both the real and imaginary parts of dielectric constants of Mg are smaller than those of Al. LSP figure of merit (FOM_{LSP}) (Equation 1.6) is also compared in Figure 5.1 (c). Mg has higher value than that of Al in the whole range from 250 to 600 nm, which implies that Mg should perform better in the LSP-based applications, such as fluorescence enhancement by nanoapertures. SPP figure of merit (FOM_{SPP}) for both metals is also compared in Figure 5.1 (d). Al's FOM_{SPP} is higher in most of the UV range ($\lambda \lesssim 360$ nm), and lower in the small part of UV ($360 \lesssim \lambda < 400$ nm) and all of the visible. The skin depths of both metals are smaller than 22 nm. The film thickness is chosen to be 100 nm in our experiment, which ensures there is no couple between top and bottom surfaces.

5.1.2 Simulation Model

The cross-sections of a round nanoaperture considered are depicted in Figure 5.2. The nanoapertures with thickness of 100 nm are assumed to be supported by a semi-infinite quartz (SiO_2) substrate and covered by solution (either water or a nonaqueous solution such as 1-octanol). The diameter is be changed from 30 nm to 100 nm. Wavelength range from 250nm to 400 nm is considered. The refractive index of water is 1.3835 at 266 nm and 1.3603 at 340 nm [62], whereas 1-octanol has a somewhat higher index of 1.46, measured at 325 nm [140]; all simulations used water refractive indices for simplicity. Even though experimentally, water cannot be used with Mg structures due to the oxidation issue, there are still other nonaqueous solvents with a refractive index close to water's [143]. Both models with and without native oxide layers are shown . Both models include an interfacial oxide layer between the metal and substrate. The thicknesses of the native oxide layer along the exposed surfaces and the interfacial oxide layer at the substrate are assumed to be 4 nm according to the characterization in Section 3.1 of Chapter 3. The position z =0 nm is defined at the interface between metal and the underlying interfacial oxide. The parameters of FDTD simulation are the same as those used in Chapter 4.

5.1.3 Enhancement Analysis of Ideal and Non-ideal Emitters

The ideal emitter is a perfect dipole source with native QY $\phi_0 = 1$. Figure 5.3 shows excitation enhancement, radiative enhancement, Purcell factor and QY enhancement versus wavelength for Al nanoapertures of different diameters with an ideal emitter. According to Equation 1.12, Purcell factor $f_{Purcell} = \zeta$ actually describes the pure effect of structure. As expected, there is a red shift in these enhancement factors with increasing aperture diameter, consistent with the size-tunability of these structures [43]. However, there is a

trend of increasing maximum enhancement with decreasing aperture size, which is likely due to the fact that the FOM of LSP for Al increases with decreasing wavelength shown in Figure 5.1 (c), with near order-of-magnitude enhancement in local intensity and lifetime reduction. The maximum radiative enhancement shows less variation. Figure 5.1 (d) shows that there is no QY enhancement over the considered wavelength due to the fact that QY is already maximal as 1 for the ideal emitter. Here, QY enhancement $f_\phi = f_{rad}/\zeta$ represents an effective quantum yield of the aperture itself, and decreases with decreasing aperture size due to increasing ohmic losses.

For comparison, Figure 5.4 shows the same quantities calculated for Mg apertures. The most significant qualitative difference is that, over the range of aperture sizes plotted, the resonance positions for Mg apertures are red-shifted from the positions for corresponding Al apertures by more than 50 nm. It is due to the difference of dielectric constants of two metals. Nevertheless, the maximum enhancements for Mg apertures are greater than for Al apertures at the same resonance wavelengths. This again correlates with the FOM_{LSP} for Mg, which peaks in the near-UV range with values greater than that for Al, as shown in Figure 5.1. We therefore expect that greater enhancements may be obtained throughout the near-UV range using Mg apertures. But Mg nanoapertures need to be even smaller to move the resonance back to the interesting region. It should be noted that QY enhancement of Mg shown in Figure 5.4 (d) is lower than for Al over the same range due to the higher Purcell factor.

The non-ideal emitter or real fluorescent molecules have native quantum yields that are less than unity. We also know that the Purcell factor is QY-dependent, as demonstrated in Chapter 4. So we will compare high and low quantum yield molecules. For the purposes of calculations, we assume that the molecules of interest absorb near 270 nm excitation wavelength and emit near 340 nm. We first plot excitation enhancement for both Al and Mg nanoapertures versus vertical position within the apertures, as shown in Figure 5.5. The results are qualitatively very different. For the smaller Al aperture sizes, the primary enhancement mechanism is the plasmonic resonance near the bottom interface, whereas at the larger sizes, enhancement is due to the excitation wavelength being below the mode cutoff condition [142]. In the case of Mg nanoapertures, there is negligible plasmonic enhancement at this wavelength, and excitation enhancement is due to the Fabry-Perot interference of the aperture modes; the peak enhancement lies about 25 to 45 nm above the interfacial oxide interface, depending upon aperture size.

Figure 5.6 plots lifetime reduction, change in quantum yield and net enhancement along

the depth of Al nanoapertures for $\phi_0 = 0.88$, which corresponds to the high quantum yield laser dye p-terphenyl. The lifetime reduction is rescaled from the situation of an ideal dipole (Equation 1.12), with maximum local values of about 9 near the aperture-interfacial oxide and about 8 near the aperture-solution interface. Net enhancement is the result of f_I, as the effective quantum yield of the molecule is reduced within the aperture, and rapidly decays due to the decreasing quantum yield (and intensity enhancement) away from the substrate interface.

Figure 5.7 presents the same plots but for tryptophan with smaller QY $\phi_0 = 0.13$. As expected, the local lifetime reduction is significantly smaller for tryptophan, which leads to a significant *increase* in quantum yield, Figure 5.7 (b), and net enhancement, Figure 5.7 (c), due to the *reduction in lifetime*. Furthermore, the optimal aperture diameter changes with native QY, which implies that the optimal structure can be different for different molecules.

Calculated enhancements in the case of Mg nanoapertures are shown in Figure 5.8 and Figure 5.9 for p-terphenyl and tryptophan, respectively. Comparing first the results for p-terphenyl, there are some differences between Mg and Al nanoapertures. First, the lifetime reduction factors are greater for Mg apertures, but the QY enhancement is lower. Nevertheless, there is a region within the Mg aperture, $z = 25$ to 30 nm, where the net enhancement is *greater*; the shift away from the lower interface is due to the excitation enhancement, which is dominated by FP resonance of waveguide mode instead of LSP resonance. It also means that the molecules inside the aperture will give the main contribution for the final fluorescence signal if Mg nanoapertures are used in the experiment. This need to be considered in the simulation and data analysis. The same trends appear in the comparison between Mg and Al apertures for the case of tryptophan. The lifetime reduction is greater for Mg, whereas the quantum yield enhancement is reduced, such that the maximum net enhancement in the region $z = 20$ to 25 nm is less than Al. It should be noted that Mg nanoapertures considered here are far away from the resonance condition, especially for excitation procedure shown in Figure 5.4 (a). The net enhancement shown in Figure 5.8 (c) and Figure 5.9 (c) is mainly due to the FP resonance of waveguide modes, which implies that the enhancement performance of Mg nanoapertures is still underestimated.

5.1.4 Effects of Bulk and Surface Oxidation

It is well-established that Al surface oxidation [74,75] and bulk Al purity [92] can strongly influence the plasmonic response. We expect the same to be true for Mg, but are not aware of any previous studies to this effect. Figure 5.10 and 5.11 plots predicted enhancement

factors of Al and Mg nanoapertures versus diameter for different combinations of bulk metal oxidation and surface oxidation. No surface oxidation means that the interior walls of the nanoapertures are not oxidized, shown in Figure 5.2 (b), as might be accomplished experimentally through surface passivation methods [144–146] or careful sample handling to minimize exposure to atmosphere or aqueous environments. The partially-oxidized bulk Al and Mg dielectric properties are calculated using the Bruggeman model [92].

For Al nanoapertures shown in Figure 5.10, excitation enhancement follows the expected trend in that the case of pure metal with no surface oxide produces the greatest enhancements, followed by pure metal with native surface oxide. As the percentage of bulk oxide increases, excitation enhancement further decreases; the FOM_{LSP} is known to decrease with increasing bulk oxidation [92]. For radiation enhancement, however, the trends are different. The case of pure metal without surface oxide has a lower maximum value than with native oxide, and lower than the 10% bulk oxide case. The maxima with native surface oxide are shifted towards smaller aperture diameters to account for the red shift of the resonance due to the interior oxide layer. The lifetime reduction trend is nearly opposite to the excitation enhancement trend in that the most highly oxidized case produces the highest Purcell factor. This is because that increase of oxidation moves the plasmonic resonance away from excitation peak, but close to the emission peak. In comparing to the radiative enhancement, it is clear that these large Purcell factors are due to nonradiative mechanisms.

For Mg nanoapertures shown in Figure 5.11, the trends are quite different. Excitation enhancement for the highly oxidized cases is relatively flat with aperture size, because 270 nm is far away from the resonance according to Figure 5.4 (a). But we can still see a clear downward trend for the smaller apertures comprised of pure Mg bulk due to operation deeper into the mode cutoff regime. The radiative enhancement is maximized with pure Mg films with or without the native oxide, since 340 nm is much closer to the resonance condition according to Figure 5.4 (b). But the presence of bulk oxide results in a significant reduction. These trends also hold for the lifetime reduction factor, in opposition to the trends in lifetime reduction for Al apertures. In situations where the largest radiative enhancement is desired, despite the lower quantum yield, Mg would be preferable over Al.

The predicted effect of Al oxidation on the net fluorescence enhancement for p-terphenyl and tryptophan is shown in Figure 5.12. As expected, the results for both molecules are similar, with the trends dominated by the excitation enhancement component. On the other hand, the case of Mg is similar, as shown in Figure 5.13, except that the net enhancement

is calculated within the 10 nm thick cylindrical volume centered at $z = 25$ nm, which is the approximate position of maximum excitation enhancement at 270 nm for all aperture sizes. Mg appears to be slightly better than Al for high quantum yield molecules such as p-terphenyl, and would have some advantages for low quantum yield molecules as well. For example, even though Al apertures show higher net enhancement for tryptophan, these enhancements occur for sizes below 70 nm. For aperture sizes 70 nm and above, Mg apertures are comparable to or better than Al for the case of pure bulk metals, and more specifically, for the case of native surface oxide.

5.2 UV Lifetime Reduction with Mg Nanoapertures

The previous simulation suggests that Mg nanoapertures perform better in application of UV fluorescence compared with Al in terms of Purcell factor or lifetime reduction. The experimental study of lifetime is performed in order to further confirm it.

5.2.1 Sample Preparation

Mg films are prepared by Mr. Kanagasundar Appusamy. Their research has demonstrated that the inclusion of a 10 nm-thick Al seed layer can give Mg film the best quality in terms of FOM_{LSP} [65]. Therefore, 100 nm Mg films plus 10 nm Al seed layers are deposited by them on 0.2 mm quartz coverslips with DC/RF magnetron sputtering. Mg nanoapertures with varied diameters from 40 to 100 nm and varied doses from 480 to 2280 μs are fabricated with FIB milling. The fabrication parameters and the pattern arrangement are the same as those of Al nanoapertures shown in Figure 4.1 (a). According to Table 3.1, Mg's sputtering rate is different from Al's, which means that the plot of undercut depth versus milling dose is different and needs to be remeasured.

Figure 5.14 presents the fitted undercut depth versus FIB milling dose. Y error bars represent the regular residues of linear fitting. This figure is used to map the dwell time to undercut depth for the following analysis of lifetime measurement. Compared with the case of Al, undercuts of Mg nanoapertures are more than double at the same doses due to the larger sputtering rate of Mg.

Mg can form a protective oxide layer of 20 to 50 nm thickness, but the oxide layer consisting of MgOH can be formed and keep growing if the film is placed in the aqueous solution or humid environment [63]. In order to protect Mg nanoapertures, a nonaqueous solvent, 1-octanol, is used in the lifetime experiment. Before the experiment, the film is kept inside a sealed container filled with argon gas. During the experiment, a coverslip is placed on top of the surface after the solution is dropped, which further protects the surface

from water penetration. After the experiment, the sample continues to be protected by the coverslip and is stored inside the refrigerator. The protection with 1-octanol can keep the sample for about 48 hours, after which the water gradually oxidizes the surface. A picture of an oxidized surface around nanoaperture arrays under microscope is shown in Figure 5.15. The straight line is a scratch on the surface, but the transparent regions with unregular shapes are formed with oxidation.

5.2.2 Experimental Results and Discussion

We only investigate one of two molecules studied in Chapter 4, which is p-terphenyl with higher QY $\phi_0 = 0.88$ and $\tau = 0.98$ ns in free solution, because only p-terphenyl can be dissolved in 1-octanol, a nonaqueous solvent. Its absorption and emission spectrums have been shown in Figure 4.3. The concentration is 100 μM. The same experimental setup introduced in Chapter 4 is used. Figure 5.16 presents the first sets of data we acquired of measured lifetime reduction versus undercut for different aperture diameter. One can see that lifetime reduction decreases with increase of diameter and undercut, which is the same as the case of Al nanoapertures shown in Figure 4.7. Furthermore, the magnitude of lifetime reduction for Mg is close to or higher than Al, even though the undercuts are more than doubled. It implies that lifetime reduction with Mg nanoaperture is larger, which is consistent with the simulation results shown in Figure 5.10 and 5.11.

The issue with lifetime measurement for Mg nanoapertures is that its signal is too weak to be collected consistently. As suggested by simulation in Figure 5.12 and Figure 5.13, the net enhancement of fluorescence signal from Mg aperture is lower than Al one. The curves in Figure 5.16 are not smooth, and there are some outliers. It is due to the inconsistency of our data collection. For this set of data and all date collected from Al nanoapertures, our data collection relied on manually locating the apertures from a two-dimensional scanning image of fluorescence, which is shown in Figure 5.17.

The pattern is arranged in the same order as Figure 4.1 (a). The diameter is the same in the same column and decreases from right to left (100 to 40 nm). The milling dose is the same in the same row and decreases from top down. One can see that the signal is very weak for the apertures with diameter smaller than 70 nm. Based on this image, we could only effectively measure the apertures with signal higher than background. For apertures smaller than 70 nm, we had to manually place the collecting point for several times around the aperture until the signal was found, which introduced the inconsistency. In Figure 5.16, there is no curve of diameter of 50 nm, because we could not find the signal. However, lifetime can be measured from the signal lower than the background with long

enough collection time as long as the aperture is found. In order to improve the consistency of data collection for smaller apertures, Dr. Yunshan Wang has developed a simple but effective method. A grid pattern is drawn with the same size as the image, and printed on a transparent sheet. Then this sheet is overlain on the top of the image, so that we can use it as a reference to locate the apertures even if we can not see them. With this method, the fluorescence lifetime is successfully measured by increasing the collection time when the signal is lower than the background. Figure 5.18 presents the measured lifetime reduction versus undercut of Mg nanoapertures by using the new data collection method. One can see that curves become much smoother, and more data points from an aperture of 50 nm are collected. The maximal lifetime reduction is about 11 for a diameter of 50 nm.

Figure 5.19 presents a detailed comparison of Mg and Al nanoapertures with the same diameters. The measured lifetime is presented this time. Only three diameters (50, 80 and 100 nm) are selected since others give the same trend. For all aperture diameters, lifetime measured from Mg nanoapertures with larger undercuts is still smaller than that from Al nanoapertures. For the case of a 50 nm diameter with 125 nm undercut, the minimal lifetime of Mg nanoapertures ($\sim$0.07) is more than three times smaller than that of Al aperture with the same diameter but only 50 nm undercut (0.25). With increase of aperture diameter, the measured lifetime from Mg nanoapertures becomes closer to that from Al. The comparison clearly demonstrates that lifetime reduction of Mg nanoapertures is stronger than that of Al for a smaller aperture ($< 80\ nm$), while they are similar for larger ones. This is due to the fact that Mg nanoaperture with a smaller diameter is closer to the resonant condition, which has been numerically discussed in Section 5.1.3. Our experimental results are consistent with the simulations shown in Figure 5.10 and Figure 5.11, which suggests that Mg nanoapertures are preferred for applications requiring shorter lifetime [139].

5.3 UV Extraordinary Optical Transmission (EOT) of Nanohole Arrays

The numerical and experimental studies performed in the two previous sections are focused on the LSP-related application: UV fluorescence enhancement. Another interesting plasmonic phenomenon is SPP-related extraordinary optical transmission (EOT) of nanohole arrays. The motivation to study EOT of Mg nanohole arrays is 2-fold: there is still no published report on EOT of Mg nanohole arrays, plus no experimental evaluation of Mg performance in SPP-related applications.

5.3.1 Samples

Mg and Al nanohole arrays with area size of 50×50 μm^2 are fabricated from 100 nm thick film on quartz coverslip with FIB milling. Four periods, 280 nm, 300 nm, 330 nm and 350 nm, are chosen in order to place the dips of EOT spectrum in the wavelength range from 250 to 400 nm. Only SEM images of Mg nanohole arrays with two periods (300 and 330 nm) are shown in Figure 5.20. It should be noted that the aperture is treated as a single pixel in the designed image in order to save the fabrication time. So aperture size is controlled by beam current and dwell time. To fabricate a 100 nm aperture diameter, beam current of 0.23 nA and dwell time of 16 s are required for a 100 nm Mg milling, while 0.43 nA and 16 s are required for a 100 nm Al milling. Iodine-enhanced etching is applied for both cases. The figure also shows that the hole shape is not a perfect circle, which may be one reason resulting in the difference between experimental and simulation data.

5.3.2 Experimental Setup

The picture of the experimental setup for UV transmission measurement is shown in Figure 5.21. It consists of a laser-driven light source (Model EQ-99-FC from Energetiq), optical iris, UV ND filter (OD3, NDUV530A from Thorlabs), UV polarizer (Al grating from Moxtek), UV focusing lens (focal length $f = 25$ mm), sample stage and detector connected to spectrometer (Maya 2000pro from Ocean Optics). White light generated from our light source has a wide and flat spectrum from 170 to 900 nm. However, due to the absorption of optical fiber and following optics (ND filter and polarizer), the measured spectrum of our light source has a broad peak around 340 nm instead of a flat spectrum, and rapidly decays at a wavelength smaller than 300 nm, which is shown in Figure 5.22 (a).

The biggest challenge of this experiment is how to find the fabricated patterns and focus the light right on it. There are three efforts required to solve this issue. The first one is to generate a small enough beam spot on the surface of sample. Our pattern size is 50×50 μm^2. Most of the incident power could be reflected by the metal surface if the beam size is too big compared with the pattern size. The small focus spot is achieved by arranging the setup into a $4f$ imaging system. The distance between the light source and the focusing lens is as the same as the distance between the focusing lens and the sample, which is equal to $2f$. In this arrangement, the image of a light source with the same size is formed on the sample surface. The collimated lens on the optical fiber emitting the light has to be removed, so that the light is converted from parallel to diverging. The fiber has the diameter of ~ 100 μm, which means our light source becomes a point source with size of 100 μm. Under the perfect condition, the spot size on the sample surface should be ~ 100 μm. However, the practical

size is larger than that due to the size limitation of entrance pupils of optics before sample. The second effort is to make an alignment mark with bigger size of $100 \times 100\ \mu m^2$ and a predefined distance away from the measured pattern. Since real patterns are too small to be seen with eyes, we will find the alignment mark first, then translate the sample stage to move the beam onto the real pattern. The diffraction pattern of the alignment mark can also be used as the means to align the pattern horizontally. The third effort is to build a sample stage with the capability of accurately translating the sample, which is achieved by stacking two translating stages and one rotation stage. Through these three efforts, we can finally locate the focused beam onto the measured pattern.

It should be noted that UV ND filter is only used when the reference spectrum without sample, i.e., the spectrum of 100% transmission, is measured. Without sample, the detector can be totally saturated due to the high intensity of our white light, so the ND filter is required to attenuate the light. UV polarizer is used to convert the unpolarized light to linear-polarized light, which can clean up the transmission spectrum and make it easier to analyze the data. At last, the transmission is calculated based on the following expression:

$$T = \frac{I_{sig} - I_{dark}}{I_{ref} - I_{dark}} T_{ND} \kappa_{area}$$

where I_{sig} is the transmitted intensity, I_{ref} (Figure 5.22 (a)) and I_{dark} the reference and dark intensity, and T_{ND} the transmission of ND filter shown in Figure 5.22 (b). κ_{area} is a correction factor taking into account the difference of beam size and pattern area, which is the ratio of beam and pattern areas. In our experiment, we assume κ_{area} as 16 by the discussion of comparison of experimental and simulated data in the following section. It means that beam diameter is roughly four times as big as the pattern size, which is about 200 μm.

In the experiment, the incident light is always in the normal direction, and the data are collected by using an integration time of 800 ms, an average times of 10 and data smoothed over 20 pixels.

5.3.3 Results and Discussions

Figure 5.23 presents the transmission versus wavelength for (a) Mg and (b) Al nanohole arrays with different period. All curves present peak-dip-peak features. With increase of spacing, those features are moving to the longer wavelength. It should be noted that only the transmission at wavelength longer than period is studied, since we will only consider the lowest order of SPP resonance (1,0). The LSP of a single nanohole also contributes to the EOT; however, its peak appears in the shorter wavelength out of our measured range.

And its position does not change with the period. Using this criterion, we can easily tell that the first peak on the left-hand side of the dip is not due to LSP, but due to the higher order of SPP resonance. As expected, the EOT phenomenon is presented for both Mg and Al nanohole arrays. For transmission of Mg nanohole arrays in Figure 5.23 (a), the peak amplitude decreases with increase of period, while for the case of Al nanohole arrays in Figure 5.23 (b), the dependence of peak magnitude on period is not monotonous, which might be due to the deviation of fabricated structures from the designed ones.

In order to further discuss the difference of Mg and Al hole arrays, Figure 5.24 presents the detailed comparison of transmission spectrums for Mg and Al structures. It clearly demonstrates that the transmission amplitudes of Al nanohole arrays are always higher than those of Mg, which is consistent with the comparison of FOM_{SPP} shown in Figure 5.1 (d). The maximal transmission of Al nanohole arrays is $\sim$ 10%, while only $\sim$ 5% for Mg nanohole arrays. Furthermore, the dip positions of Mg hole arrays are always at a longer wavelength than those of Al, which can be explained by the difference of dielectric constants of Mg and Al. It is well known that the dip position can be predicted by the following analytical expression:

$$\lambda = \frac{p}{\sqrt{i^2 + j^2}} \sqrt{\frac{\epsilon_m \epsilon_d}{\epsilon_m + \epsilon_d}} \tag{5.1}$$

where p is the period of hole arrays, ϵ_m and ϵ_d the dielectric constants of metal and dielectric, and i and j the order of resonance. Here, we only consider the normal incidence and the lowest order of resonance (1,0). From this expression, we can see that the wavelength increases with decrease of the real part of dielectric constant (ϵ) when ignoring the imaginary part of ϵ. Mg has smaller amplitudes of both the real and imaginary parts of ϵ compared with Al, which is why the wavelength red-shift is larger for Mg structures. Using this expression, we can also accurately calculate the dip positions. The comparison of calculated and experimental values of dip positions is shown in Table 5.1. One can see that the agreement between experiment and theory is pretty good. As expected, the predicted shifting of dip position for Mg is always larger than Al, which is consistent with our experimental results. The difference between measured and predicted values is about 10 nm for Mg nanohole arrays, and about 5 nm for Al. The dip positions are always slightly larger than the period and move to longer wavelength with larger period, which implies that the period can be directly used to simply predict the resonance peak.

Equation 5.1 can only predict the dip position. In order to further understanding the mechanism behind the transmission spectrum, full wave simulation with FDTD is performed. In simulation, the structure is sitting on the quartz substrate and covered

with air. The aperture diameter is set to be 120 nm, 4 nm oxide layers are included on the surface of the structure and at the metal/quartz interface. A plane wave with unit amplitude is placed on the air side. The measured dielectric constants of Mg and Al are used. Figure 5.25 and Figure 5.26 represent the comparison of experimental and simulated transmission spectra for Mg and Al nanohole arrays with different periods. One can see that the experimental spectra have similar features to the simulated ones. The dip positions are matched pretty well. The difference of dip positions and of the amplitudes are believed to be due to the difference of simulation model from the practical structures, and also the difference of real beam size from the predicted one. There is a large divergence only found for Mg nanohole arrays at wavelengths shorter than 280 nm. The simulation predicts a peak around 260 nm, while measurement does not show it. We notice that this peak position does not change with the period, and further simulation with a larger period (1000 nm) confirms that this peak is always on 260 nm. To figure out where this peak is coming from, the E-field intensity distributions along the cross-section corresponding to this peak (260nm) of Mg nanohole arrays with period of 300 nm are calculated. Furthermore, the field patterns of another peak (400 nm) and dips (300 and 360 nm) are calculated as well. All patterns are shown in Figure 5.27. The intensity distribution of first peak at 260 nm in Figure 5.27 (a) shows field enhancement inside the aperture, which implies that it is not formed by LSP, but by Fabry-Perot (FP) resonance of propagating waveguide mode inside the aperture. The peak position does not change with the period since the FP resonance is only influenced by thickness. The LSP peak should be at the even shorter wavelengths out of our measured range. Figure 5.27 (b) and (c) presents the field pattern at the first (300 nm) and the second (360 nm) dips. They present two different modes exited at the oxide layer. It is interesting that the wavelength difference between two dips is as large as 60 nm even if the thickness of the oxide layer is only 4 nm. This feature implies that we can characterize the oxide layer thickness by monitoring the wavelength difference between dips. Figure 5.27 (d) presents a typical filed pattern when EOT happens. The field is localized and enhanced on both surfaces of the structure, and there is a coupling between them, which gives the transmission peak at 400 nm.

In our measured spectrums, the first peak at 260 nm does not show up. We believe there are two reasons. The first one is due to the limitation of our reference spectrum shown in Figure 5.22 (a). One can see that the intensity of wavelength shorter than 300 nm decreases dramatically, because of which the transmission at shorter wavelengths is too weak to be measured. Another reason is that our fabricated apertures are not perfectly round apertures

with diameter of 120 nm as demonstrated in Figure 5.20. Since this peak is due to the FP resonance of waveguide mode, its position should be sensitive to the aperture shape and size. It is possible that the peak drifts out. For the case of Al, there is no peak showing up at shorter wavelengths because the LSP and waveguide peaks for the Al nanohole are at wavelengths shorter than 250 nm.

One issue about Mg that always concerns us is the fact that the oxide layer consisting of MgOH on the Mg surface keeps growing in the humid environment [63], which eventually destroys the Mg structures. In order to characterize the period of validity of our Mg structures in the lab environment, we repeat the transmission measurement of Mg nanohole arrays over time. Figure 5.28 shows the transmitted intensity of Mg holes with 350 nm period measured at different times over the time period of a week. One can see that no obvious degradation is found according to the transmitted signal. There is a drop between two sets of data, which is believed to be due to the fluctuation of the light source. This experiment suggests that Mg sample stored in a lab environment can be valid for at least a week, which dramatically increases its feasibility for UV plasmonic applications.

5.4 Summary

In this chapter, a possible candidate of UV plasmonic material, Magnesium (Mg), has been extensively studied both numerically and experimentally. Since Al has been the dominant material in this area, the comparison of Mg and Al has been performed in order to evaluate Mg's potential by using Al as a reference.

At the first, we numerically studied fluorescence enhancement in Al and Mg nanoapertures using high and low QY UV emitters and further considered the effects of bulk and surface metal oxidation. Generally, smaller aperture sizes are needed with Mg in order to maximize emission enhancement. Within the considered diameter range (30–100 nm), Mg nanoapertures are far away from the resonance, especially for excitation procedure, which makes the FP resonance of waveguide mode inside aperture dominant over the LSP resonance. So the maximal enhancement happens inside the aperture instead of at the interface for the case of Al. However, Mg nanoapertures still give higher lifetime reduction. Furthermore, in terms of net enhancement of fluorescence, Al gives the higher signal when aperture size is smaller than 70 nm, while with the larger aperture, Mg apertures are comparable to or better than Al for the case of pure bulk metals, and more specifically, for the case of native surface oxide. In order to improve fluorescence enhancement, avoiding bulk oxidation during film deposition is important. However, bulk and surface oxidations

are not always detrimental for different enhancement factors. It is possible to use oxidation as an optimization parameter for some enhancement mechanisms.

After the extensive study of Mg and Al nanoapertures for UV fluorescence enhancement, the experimental study of lifetime reduction has been performed. The methodology of the whole experiment is the same as the study of Al nanoapertures introduced in Chapter 4, except that more attention needs to be paid on sample handling and data collection due to different material and plasmonic properties of Mg. Same as the case of Al nanoapertures, the lifetime reduction with Mg nanoapertures decreases with increase of diameter and undercut. But the magnitude of lifetime reduction is much higher compared with Al. The maximal lifetime reduction of p-terphenyl in Mg nanoaperture with 50 nm diameter and 125 nm undercut is ~ 13, which is more than three times higher than Al. Our experimental study further confirms that Mg nanoapertures are preferred structures for applications requiring shorter lifetime [139].

At last, SPP-related EOT of both Mg and Al nanohole arrays have been experimentally studied. As expected from FOM comparison, Al nanohole arrays give the higher transmission with maximum of 10%, while Mg nanohole arrays only give maximal transmission of 5%. The red-shifting of resonant dip-peaks of both structures with increase of periods has been experimentally demonstrated. Further simulation and analysis have been performed. The agreement between experimental and simulation results help us understand the forming mechanism of peaks. Through this experiment, we evaluate the performance of Mg nanohole arrays in SPP-related phenomenon. Even though it is worse than Al, it still gives the decent transmission, which implies Mg can be another candidate material for SPP-related applications in the UV.

5.5 Acknowledgements

The experimental work presented in this chapter is a collaboration between Dr. Blair's and Dr. Guruswanmy's groups, which mainly involve Dr. Yunshan Wang, Mr. Kanagasundar Appusamy and the author. Dr. Wang improved the lifetime data collection method as mentioned in this chapter. She also participated in every step of the study presented in this chapter, including pattern fabrication, lifetime experiment, setup installation, transmission measurement and simulation. Mr. Appusamy prepared the Mg thin-film, and characterized the material properties. He also contributed to the steps of fabrication and transmission measurement. The author thanks them for their tremendous efforts devoted to this research.

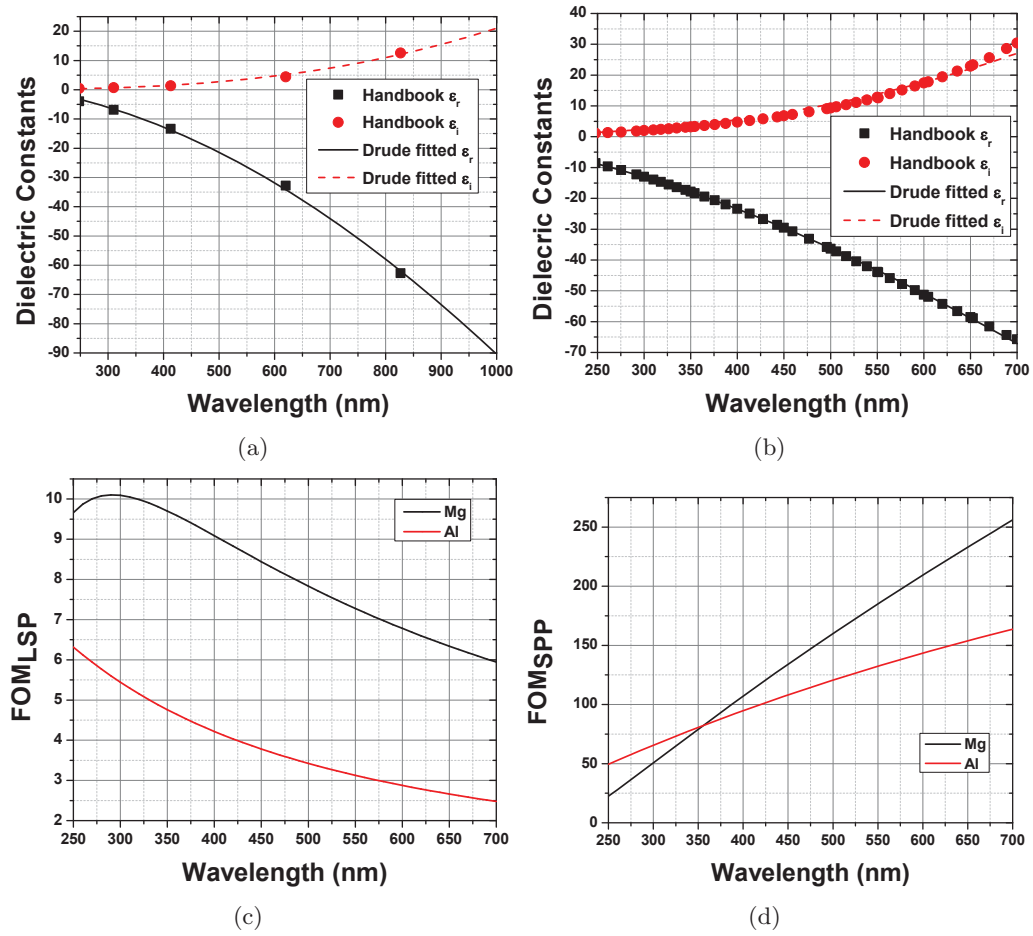

Figure 5.1. Real (black square) and imaginary (red circle) parts of dielectric constants of (a) Mg and (b) Al as function of wavelength [62]. The Drude fitted curves are also shown. (c) FOM_{LSP} and (d) FOM_{SPP} for Mg and Al versus wavelength.

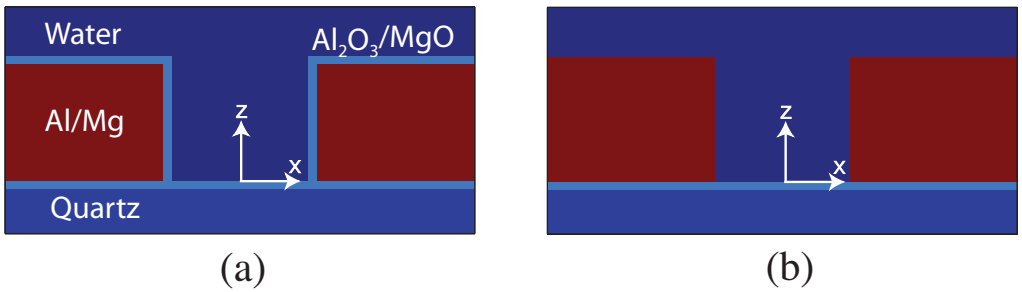

Figure 5.2. Cross-section views of the nanoaperture structure with (a) oxidized surfaces and (b) an idealized case with no surface oxide, except at the substrate interface. All oxide layer thicknesses are 4 nm.

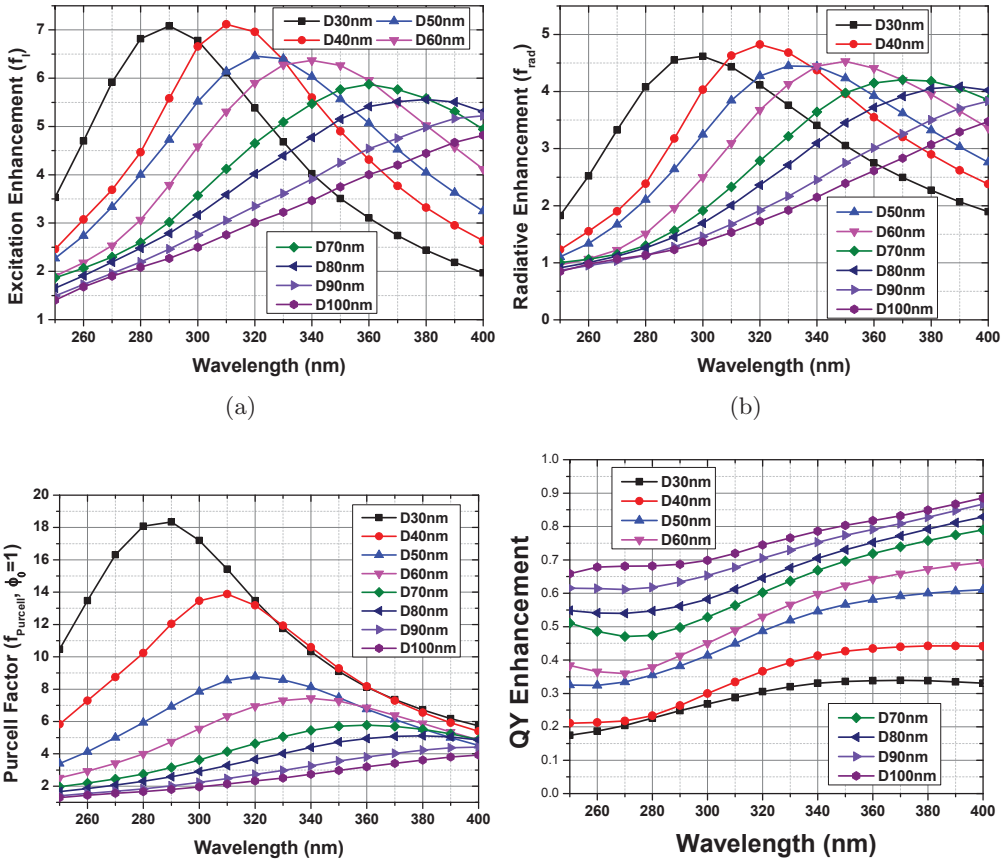

Figure 5.3. Calculated (a) excitation enhancement f_I, (b) radiative enhancement f_{rad}, (c) Purcell factor $f_{Purcell}, \phi_0 = 1$ and (d) QY enhancement f_ϕ versus wavelength for Al nanoapertures of diameters ranging from 30 to 100 nm. A 4 nm oxide layer is assumed.

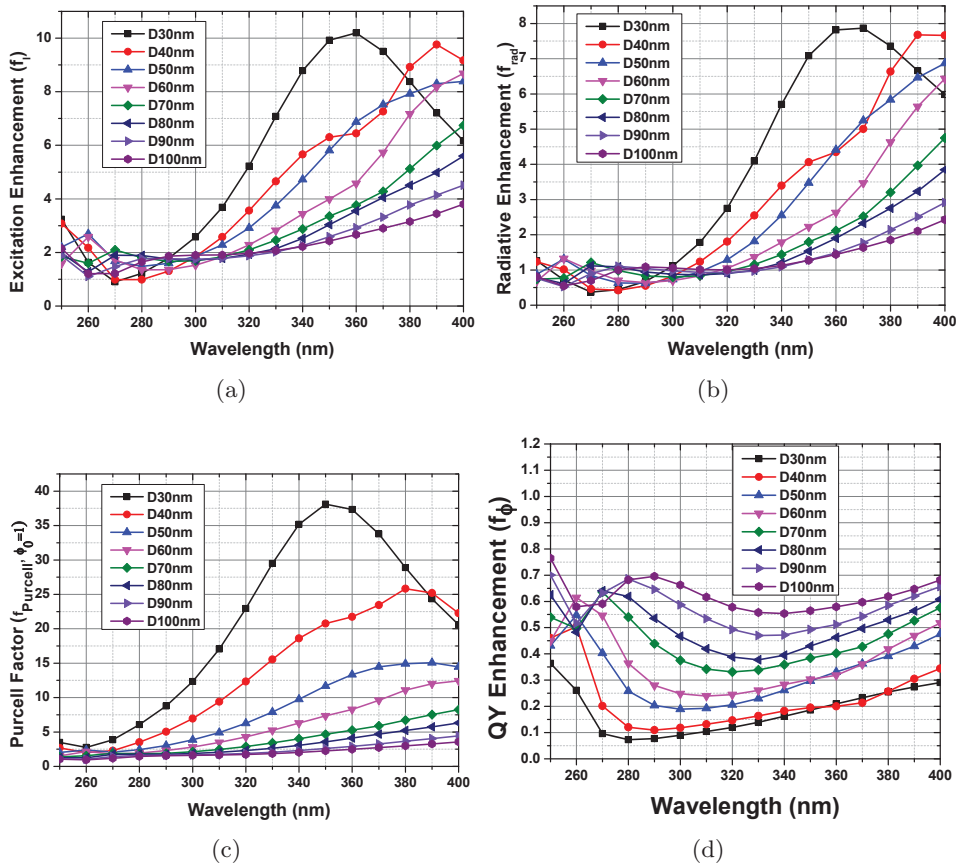

Figure 5.4. Calculated (a) excitation enhancement f_I, (b) radiative enhancement f_{rad}, (c) Purcell factor $f_{Purcell}, \phi_0 = 1$ and (d) QY enhancement f_ϕ versus wavelength for Mg nanoapertures of diameters ranging from 30 to 100 nm. A 4 nm oxide layer is assumed.

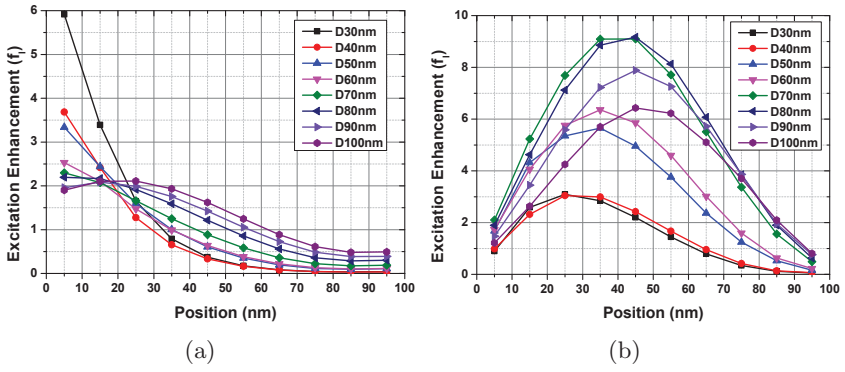

Figure 5.5. Calculated excitation enhancement factors versus vertical position within (a) Al nanoapertures and (b) Mg nanoapertures, versus aperture diameter. Excitation is at 270 nm.

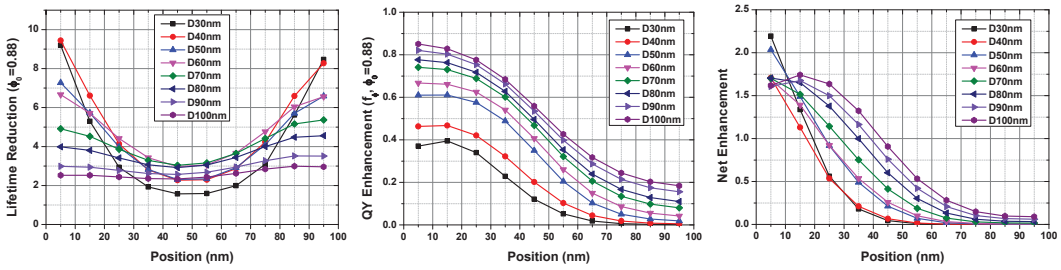

(a) (b) (c)

Figure 5.6. Calculated enhancement factors for p-terphenyl ($\phi_0 = 0.88$) versus vertical position within Al nanoapertures, versus aperture diameter: (a) lifetime reduction, (b) QY enhancement and (c) net fluorescence enhancement in the regime $I_e \ll I_s$.

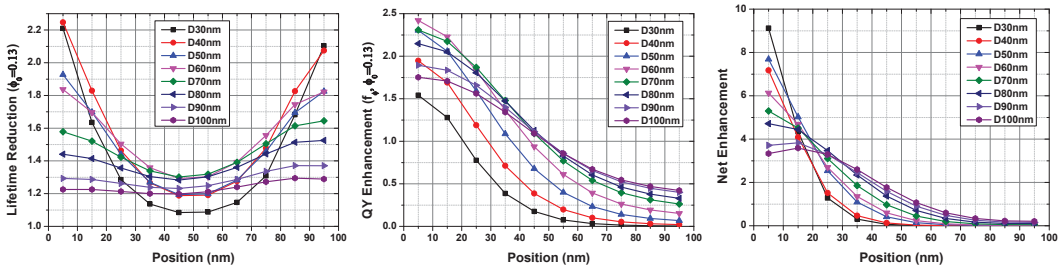

(a) (b) (c)

Figure 5.7. Calculated enhancement factors for tryptophan ($\phi_0 = 0.13$) versus vertical position within Al nanoapertures, versus aperture diameter: (a) lifetime reduction, (b) QY enhancement and (c) net fluorescence enhancement in the regime $I_e \ll I_s$.

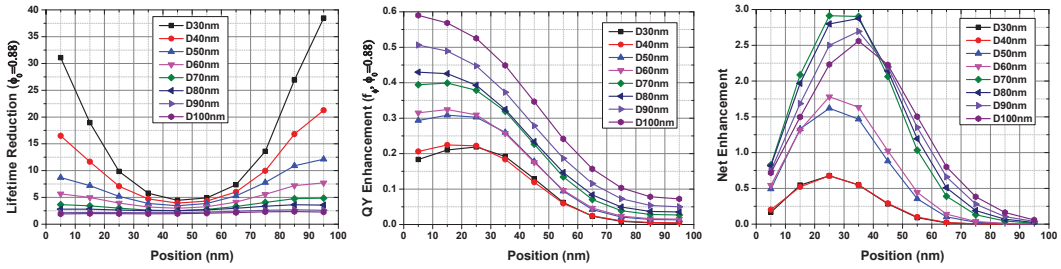

(a) (b) (c)

Figure 5.8. Calculated enhancement factors for p-terphenyl ($\phi_0 = 0.88$) versus vertical position within Mg nanoapertures, versus aperture diameter: (a) lifetime reduction, (b) QY enhancement and (c) net fluorescence enhancement in the regime $I_e \ll I_s$.

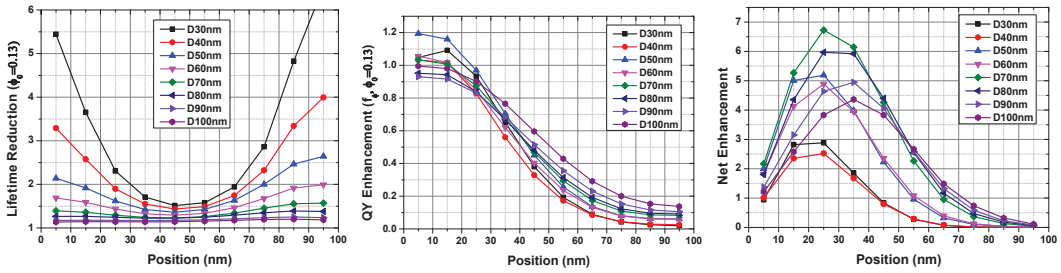

(a) (b) (c)

Figure 5.9. Calculated enhancement factors for tryptophan ($\phi_0 = 0.13$) versus vertical position within Mg nanoapertures, versus aperture diameter: (a) lifetime reduction, (b) QY enhancement and (c) net fluorescence enhancement in the regime $I_e \ll I_s$.

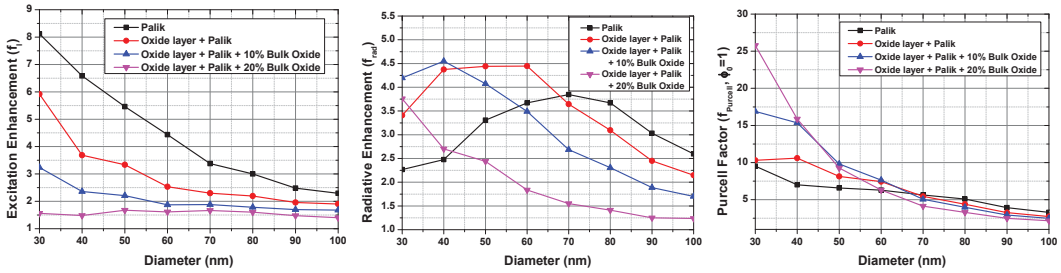

(a) (b) (c)

Figure 5.10. Calculated (a) excitation enhancement, (b) radiative enhancement and (c) Purcell factor for Al nanoapertures comprised of different oxidation states versus diameter. 4 nm surface oxide, excitation at 270 nm and emission at 340 nm. An ideal dipole emitter is assumed.

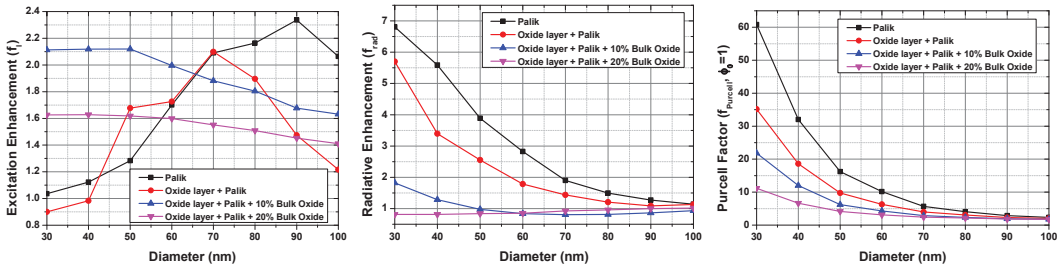

(a) (b) (c)

Figure 5.11. Calculated (a) excitation enhancement, (b) radiative enhancement and (c) Purcell factor for Mg nanoapertures comprised of different oxidation states versus diameter.

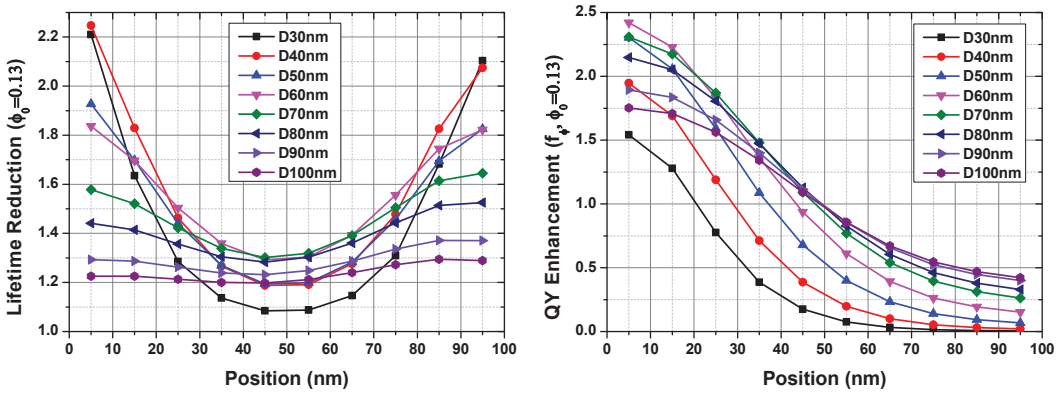

(a) (b)

Figure 5.12. Predicted net enhancement for (a) p-terphenyl and (b) tryptophan for Al nanoapertures comprised of different combinations of surface and bulk oxidation state. Surface oxide is taken to be 4 nm, and diameter refers to the inner nanoaperture diameter. Excitation is at 270 nm and emission is at 340 nm. The dipole is placed at z= 5nm.

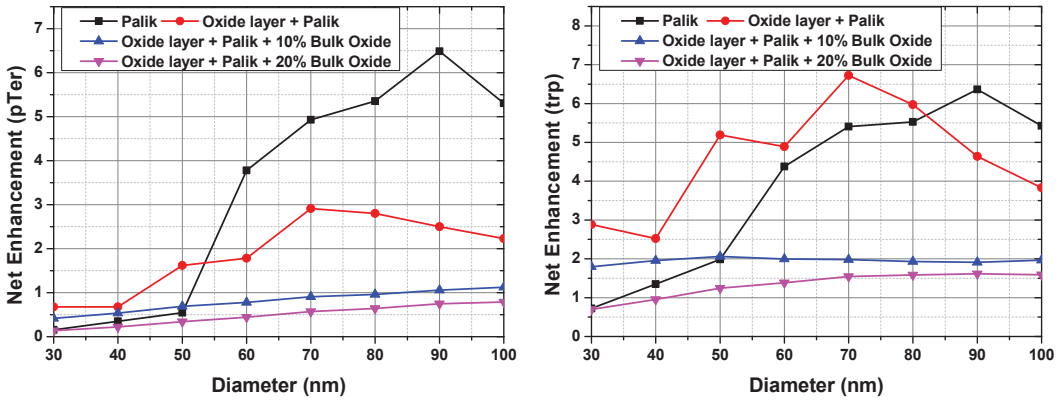

(a) (b)

Figure 5.13. Predicted net enhancement for (a) p-terphenyl and (b) tryptophan for Mg nanoapertures comprised of different combinations of surface and bulk oxidation state. Surface oxide is taken to be 4 nm, and diameter refers to the inner nanoaperture diameter. Excitation is at 270 nm and emission is at 340 nm. The dipole is placed at z= 5nm.

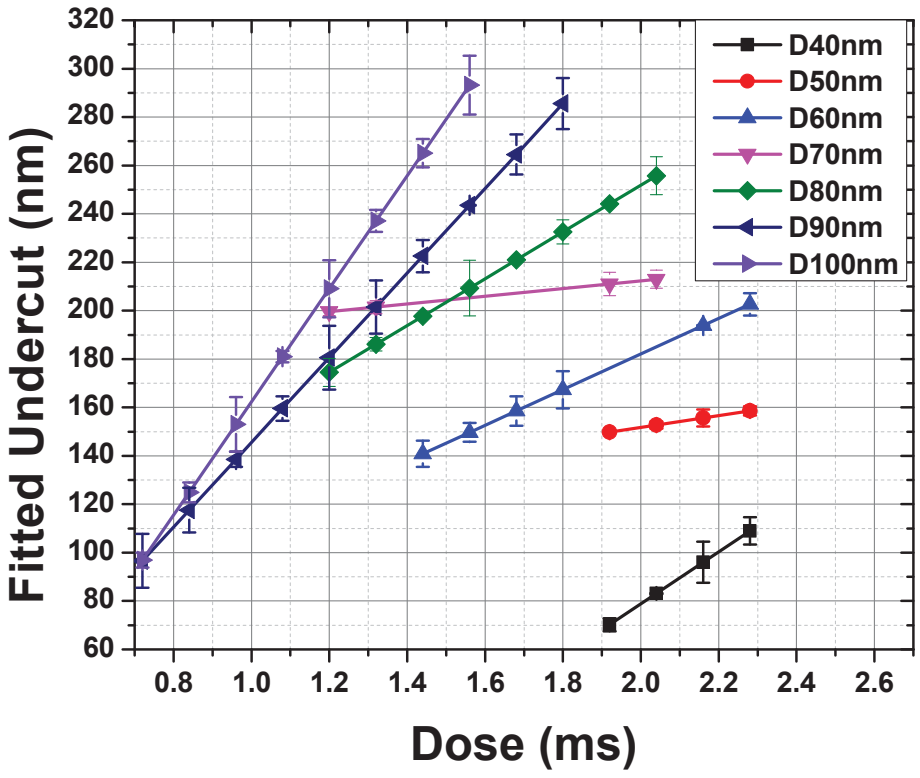

Figure 5.14. Fitted undercut height versus FIB milling dose for Mg nanoaperture used in the following lifetime measurements.

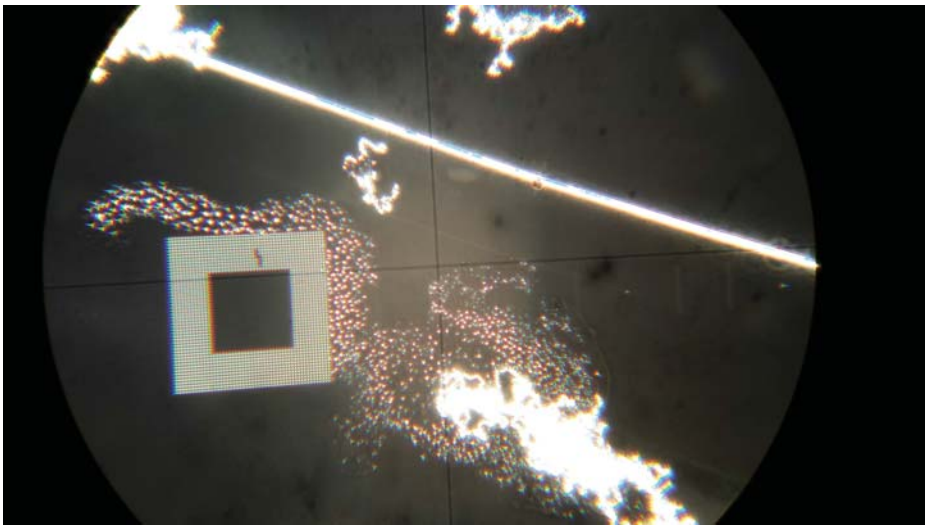

Figure 5.15. Microscope image of oxidized Mg surface around the pattern.

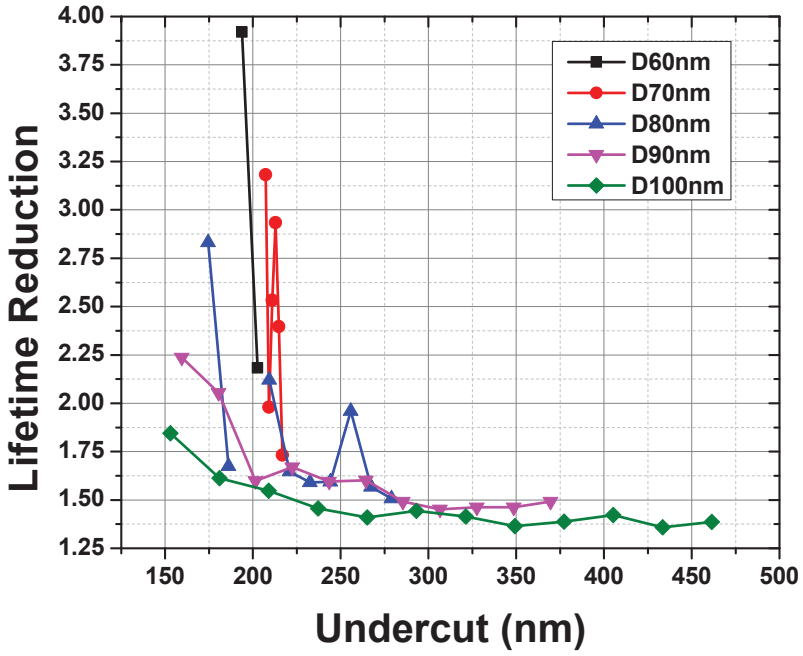

Figure 5.16. The first set of data of lifetime reduction versus undercut for p-terphenyl inside Mg nanoapertures with different aperture sizes. p-Terphenyl concentration is 100 μM in 1-octanol.

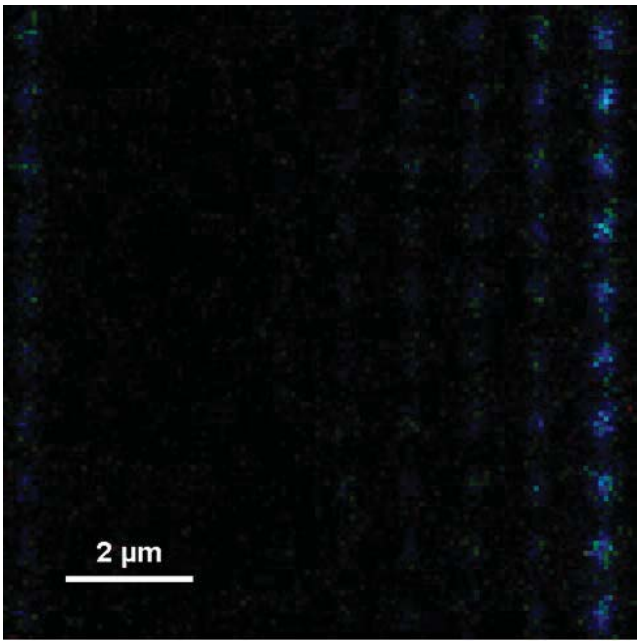

Figure 5.17. Fluorescence image of Mg nanoapertures covered with p-terphenyl solution. The size is $10 \times 10 \mu m^2$. The apertures are arranged in the same order as Figure 4.1 (a).

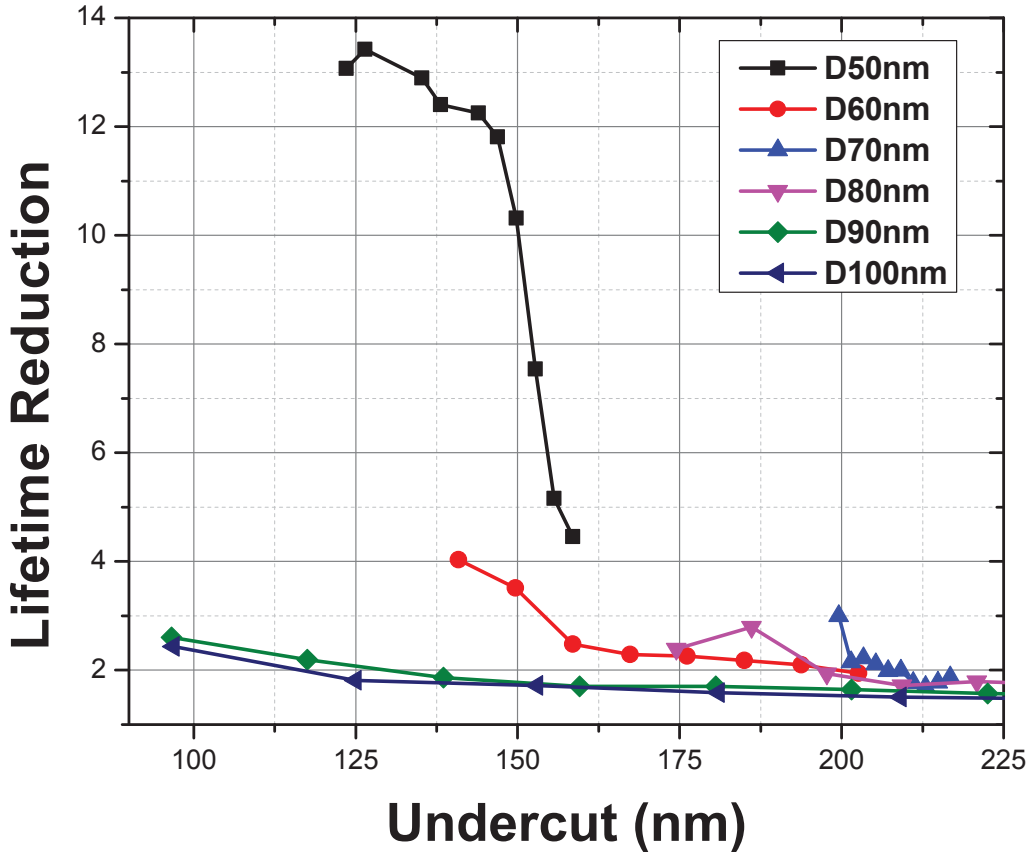

Figure 5.18. Measured lifetime reduction versus undercut for p-terphenyl inside Mg nanoapertures with different aperture sizes. p-Terphenyl concentration is 100 μM in 1-octanol. The data are collected with improved consistency by applying a grid pattern as reference.

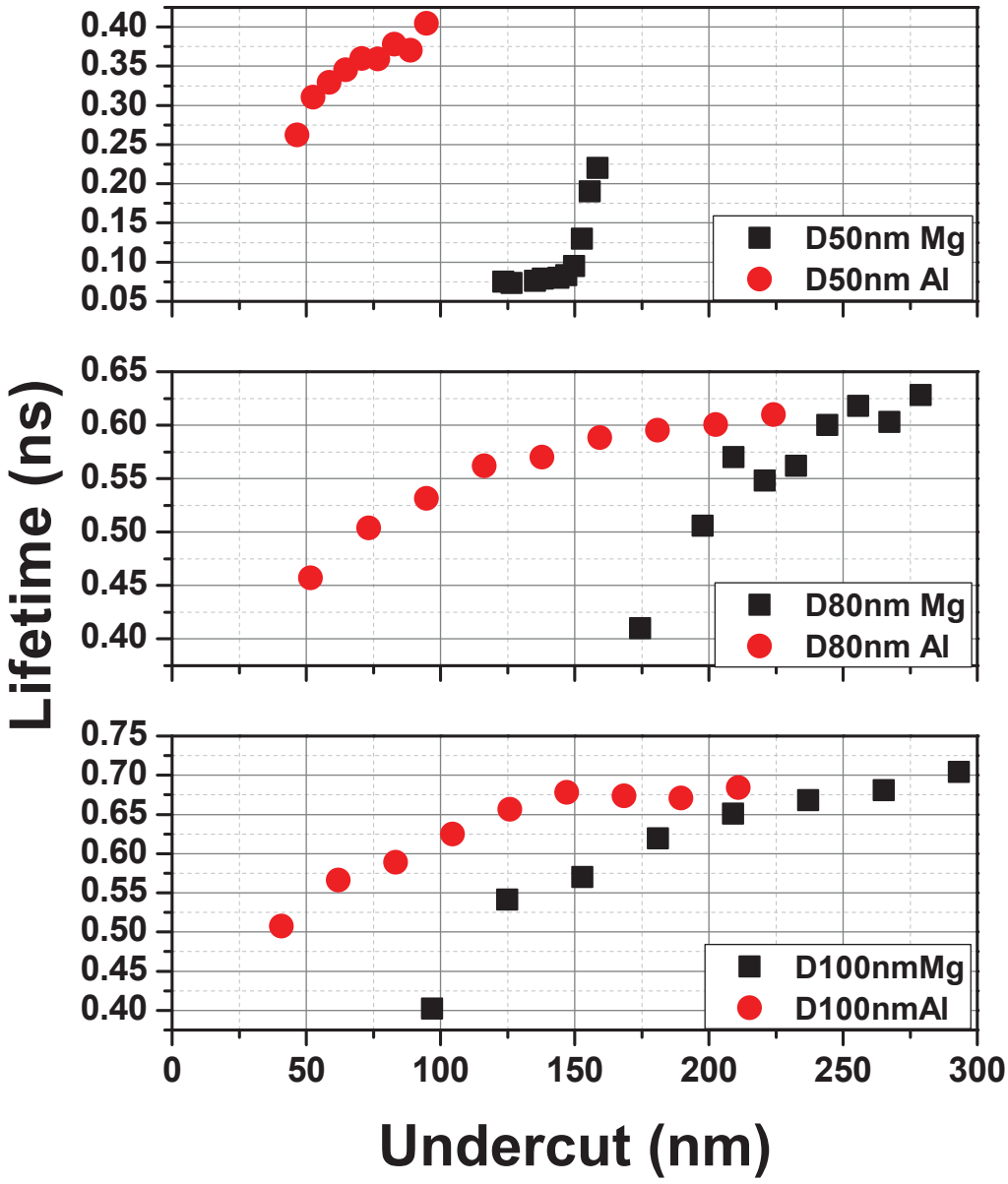

Figure 5.19. Comparison of lifetime of Mg and Al nanoapertures versus undercut. The results of three diameters (50 nm, 80 nm and 100 nm) are presented.

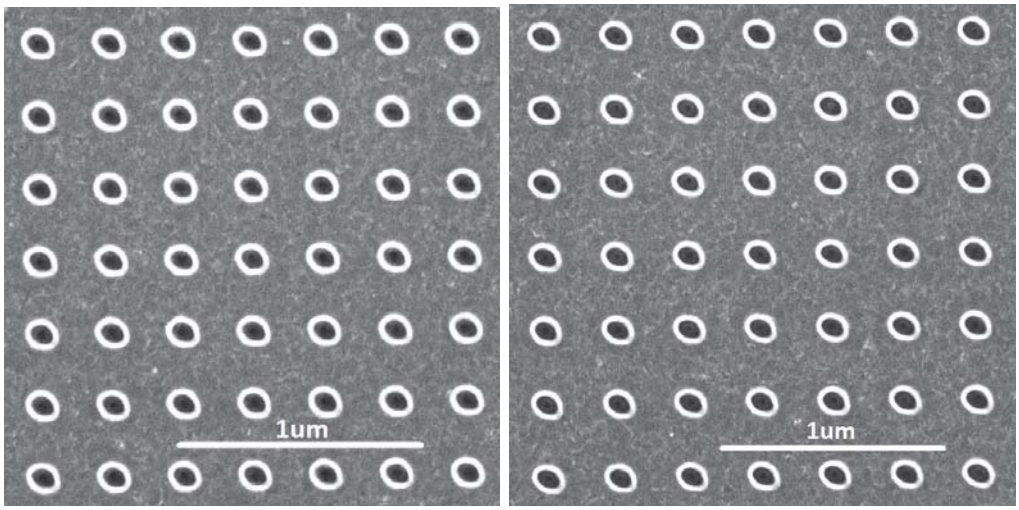

(a) (b)

Figure 5.20. SEM images of Mg nanohole arrays with (a) 300 nm period and (b) 330 nm period.

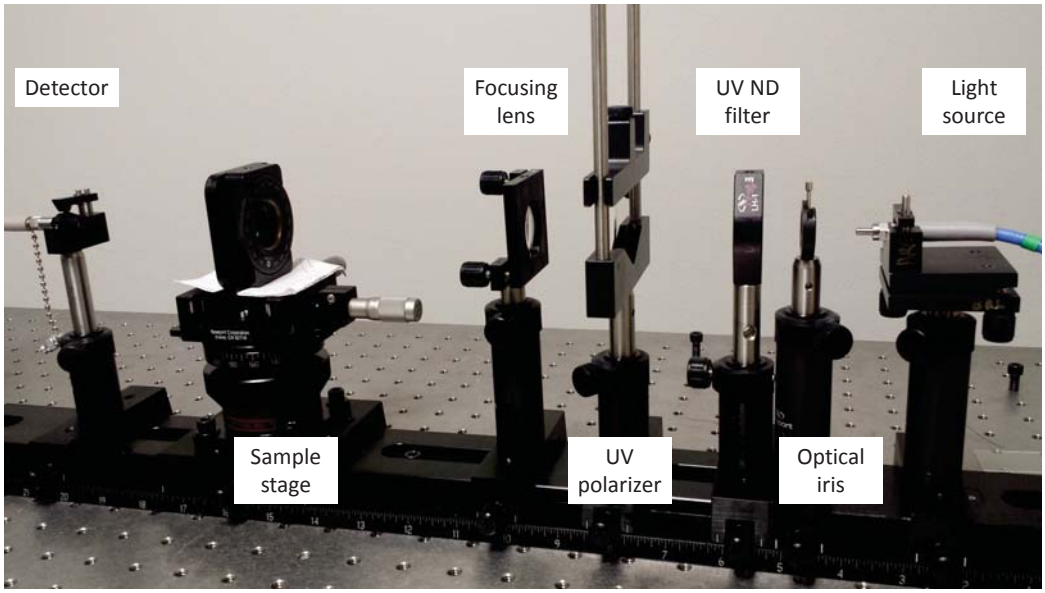

Figure 5.21. Picture of optical setup for UV transmission measurement.

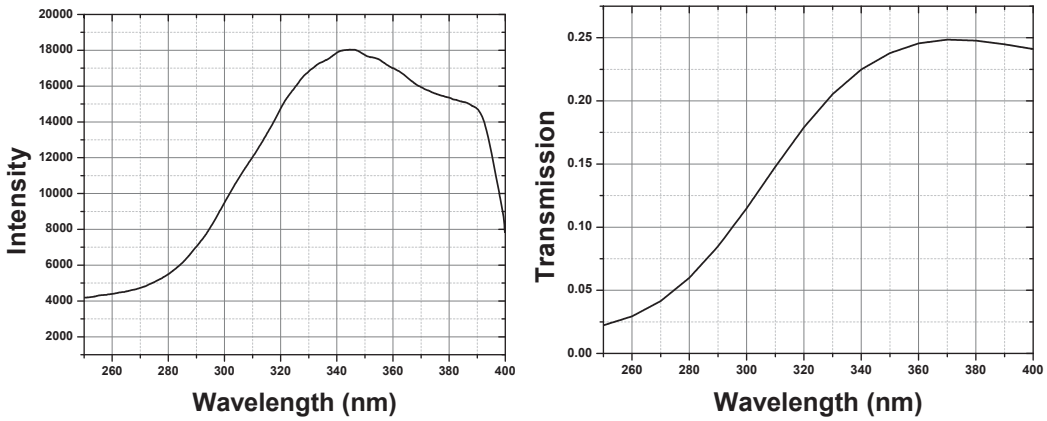

(a) (b)

Figure 5.22. Measured spectra of (a) intensity light source after UV ND filter and polarizer and (b) transmission of UV ND filter.

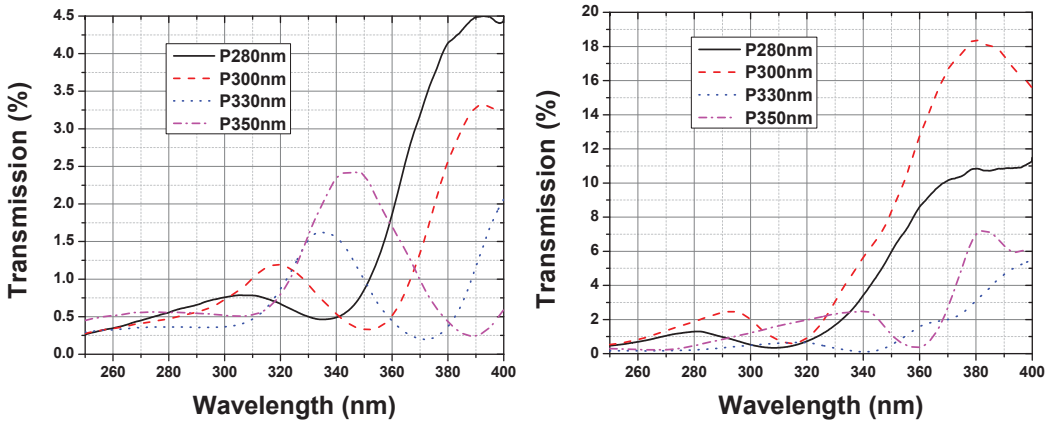

(a) (b)

Figure 5.23. Transmission spectra of (a) Mg and (b) Al nanohole arrays with different periods.

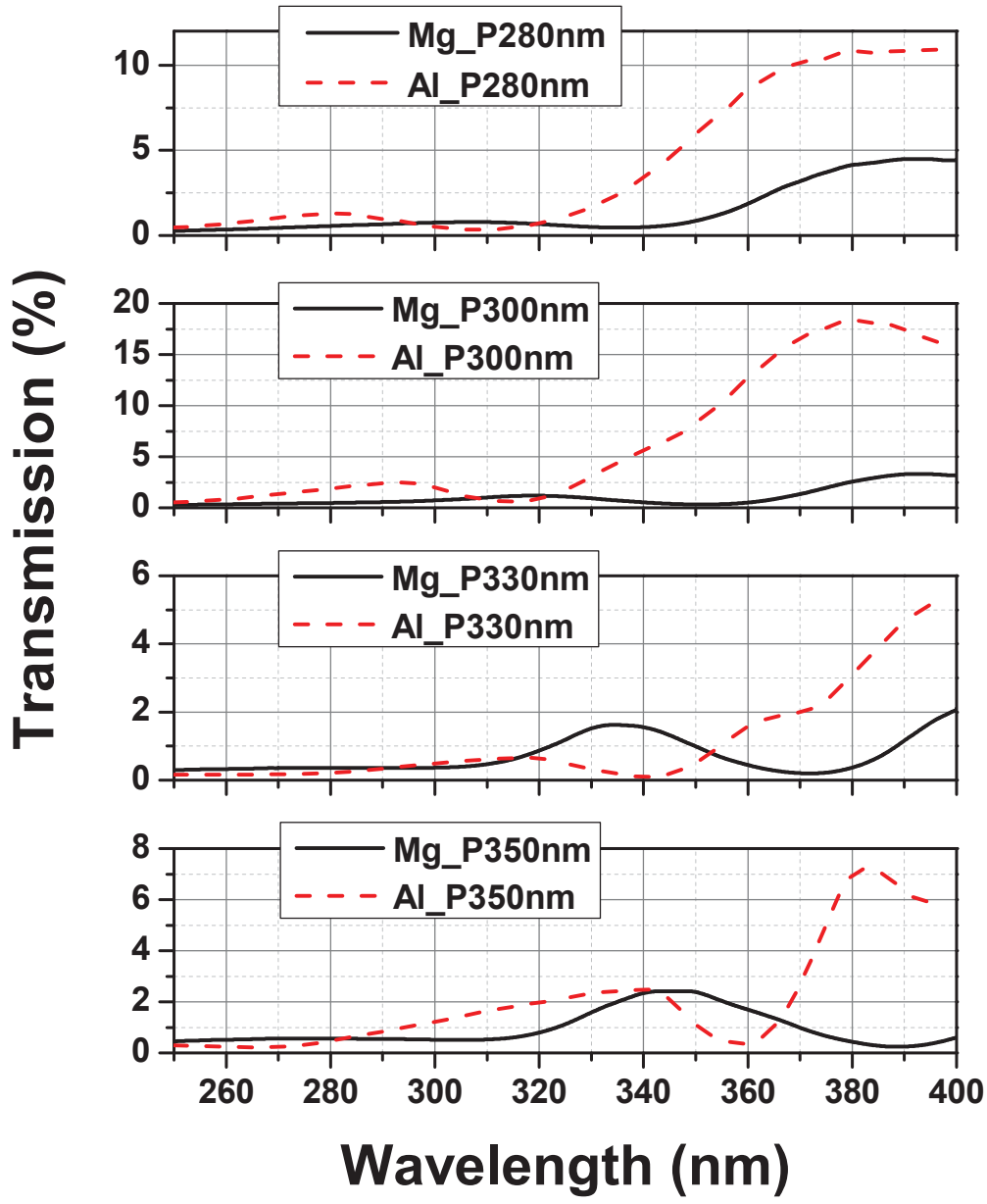

Figure 5.24. Comparison of transmission spectra of Mg and Al nanohole arrays with different periods.

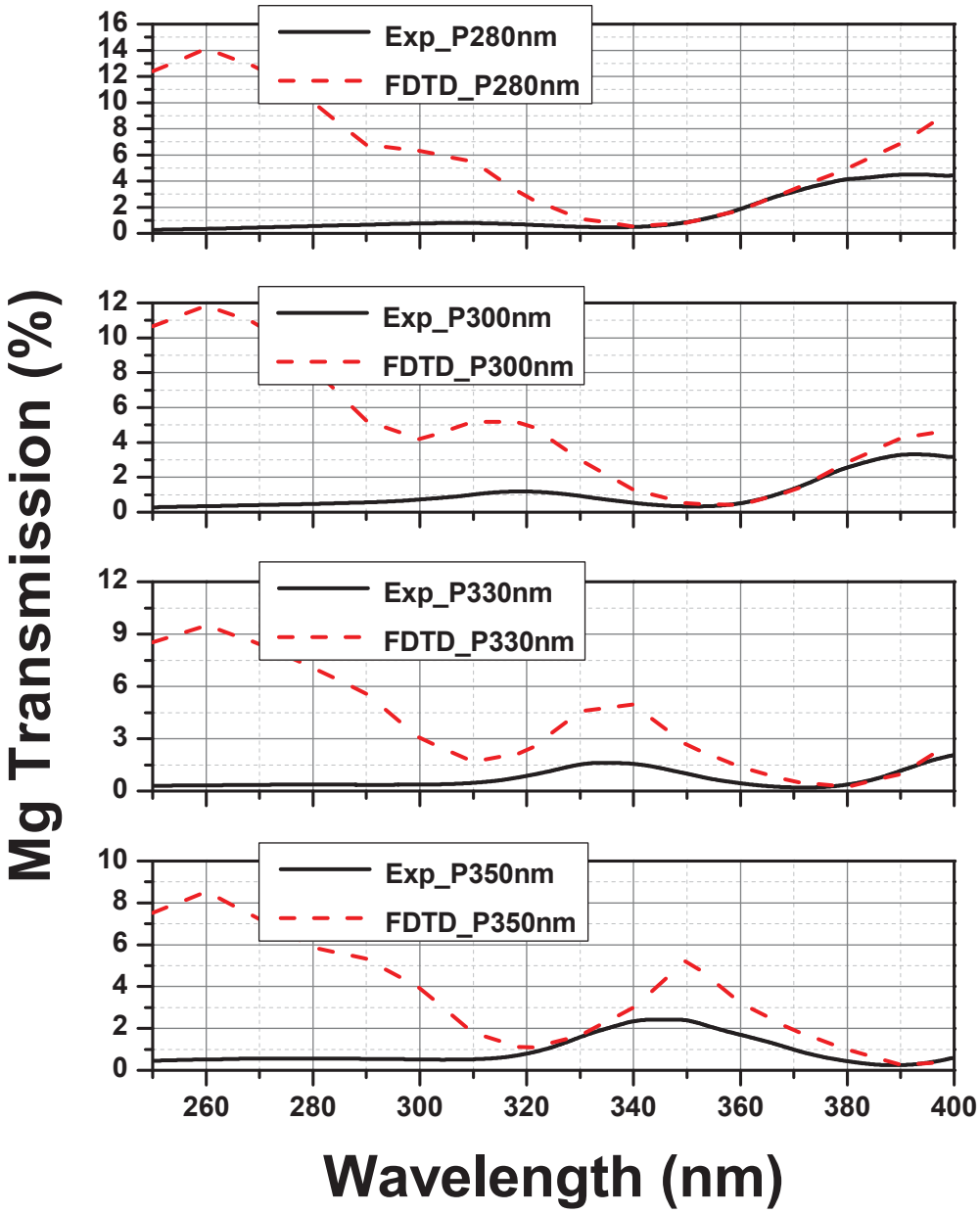

Figure 5.25. Comparison of measured and calculated transmission spectra of Mg nanohole arrays with different periods.

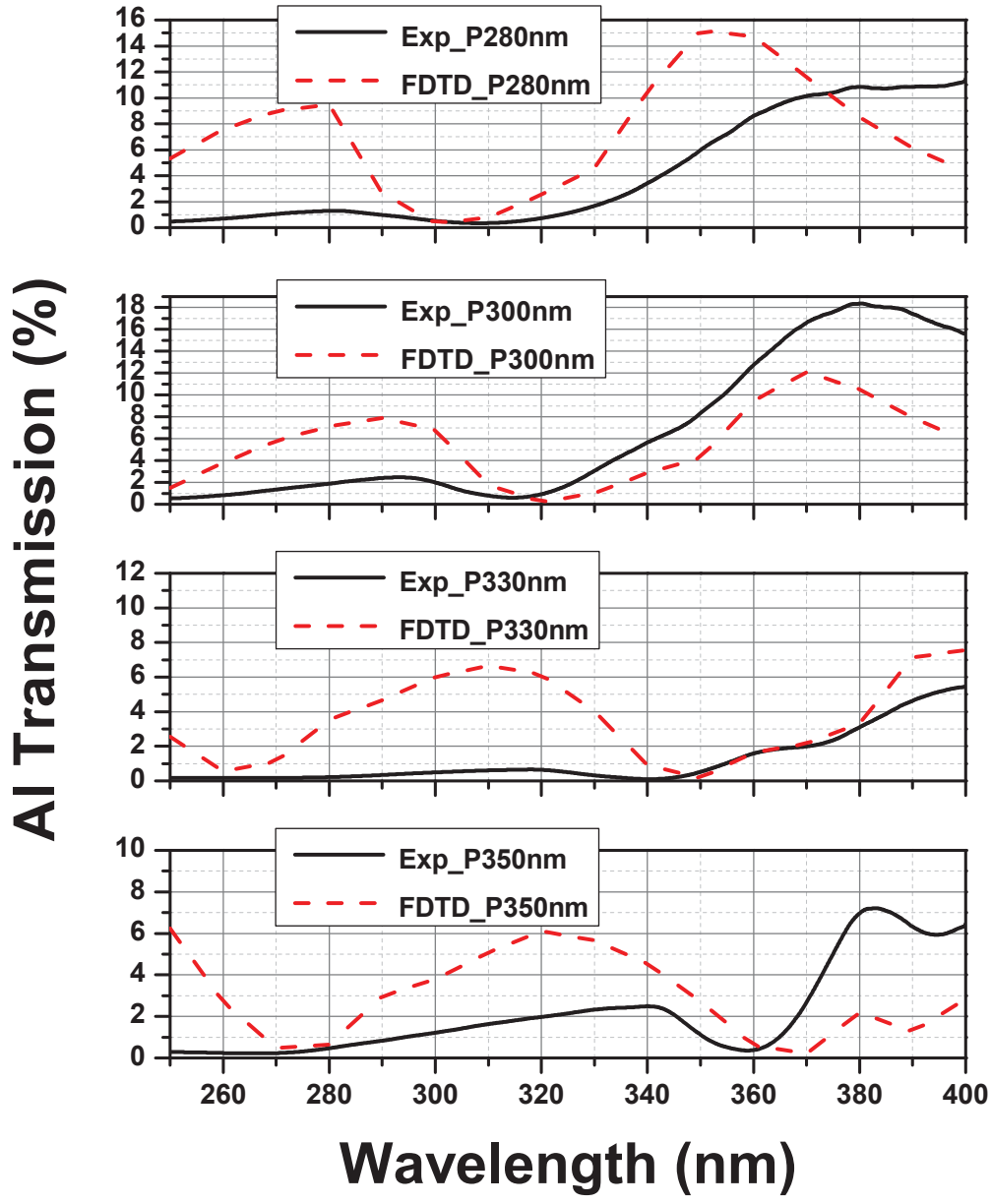

Figure 5.26. Comparison of measured and calculated transmission spectra of Al nanohole arrays with different periods.

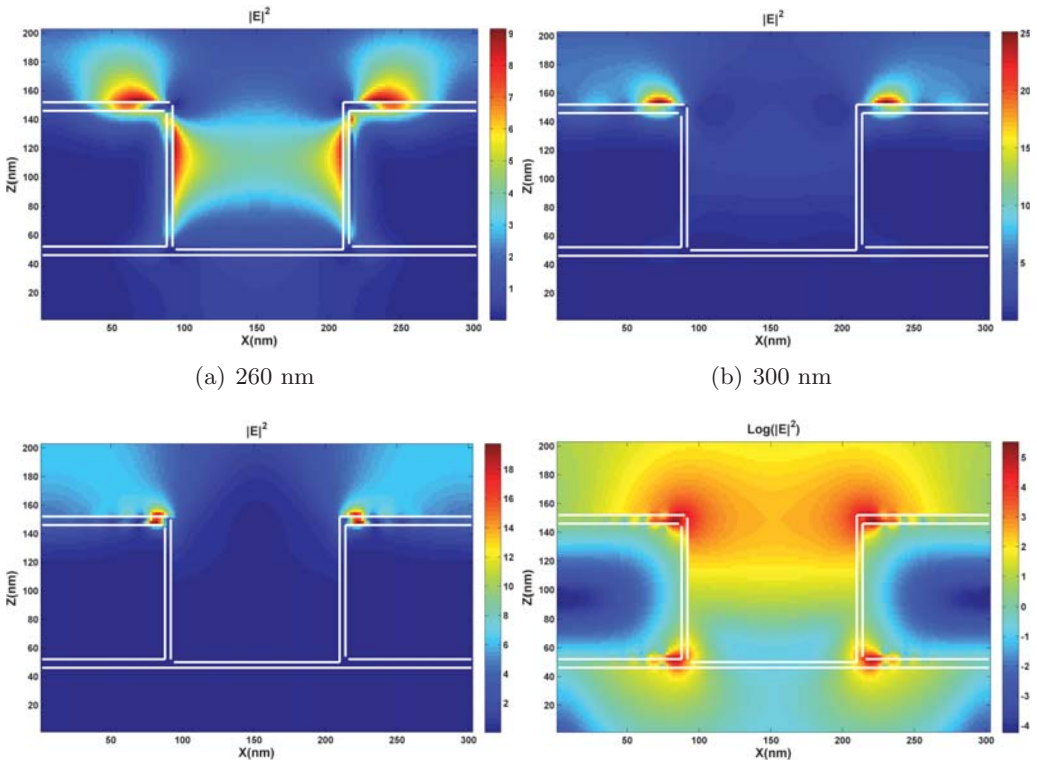

(a) 260 nm (b) 300 nm

(c) 360 nm (d) 400 nm

Figure 5.27. Distribution of electric field intensity in the cross-section of Mg nanohole arrays with period of 300 nm and diameter of 120 nm illuminated by the plane wave with wavelength of (a) 260 nm, (b) 300 nm, (c) 360 nm and (d) 400 nm. The thickness is 100 nm. Only one period is plotted.

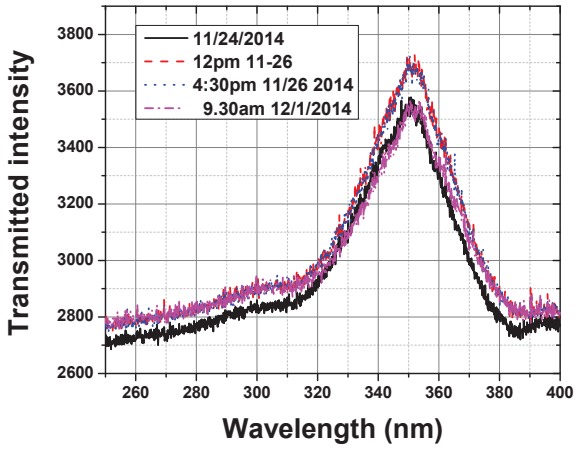

Figure 5.28. Measured transmitted intensity of Mg nanohole arrays with 350 nm period. This experiment is repeated over time period of one week.

Table 5.1. Comparison of predicted (Equation 5.1) and measured values of dip positions corresponding to (1,0) resonance for Mg and Al nanohole arrays with different period. Credit to Dr. Yunshan Wang.

Material	Mg				Al			
Period (nm)	280	300	330	350	280	300	330	350
(1,0) Predicted (nm)	322	338	363	380	293	312	341	360
(1,0) Measured (nm)	334	352	370	387	306	315	338	357

CHAPTER 6

SUMMARY AND FUTURE WORK

In this chapter, a brief summary of the dissertation work is provided. This whole project has been an exploration and learning experience for me. With enriching experience and knowledge obtained along with advancing our research, I start to realize that there are still more things to be further studied. However, due to the time limitation, I will propose those ideas here for future research.

6.1 Summary of Dissertation Work

This dissertation work is proudly supported by the NSF materials research science and engineering center (MRSEC) grant DMR-1121252, which is a collaborative research center with aims for investigating new materials for Plasmonics and Spintronics. The main goal of this dissertation is to fill the gap of Plasmonics in the UV with efforts of design, fabrication and characterization of metallic nanostructures by exploring the application of label-free bimolecular detection via native UV fluorescence. Figure 6.1 presents the work flow of the whole research project and also summarizes the contributions of this dissertation to the whole research project and to this area of study.

The first step of this dissertation work is to address the numerical design of metallic nanostructures in the context of UV fluorescence enhancement, which is introduced in Chapter 2. A design method that combines analytical analysis with numerical simulation has been developed. By using this method, performance of three canonical plasmonic structures - the dipole antenna, bullseye nanoaperture and nanoaperture array - has been compared. The optimal geometrical parameters have been determined. A novel design of a compound bullseye structure has been proposed and numerically analyzed for the purpose of compensating for the large Stokes shift typical of UV fluorescence.

The second step of this dissertation work is thin-film characterization and nanofabrication, which is discussed in Chapter 3. Here, the characterization includes two efforts: one is to characterize Al thin-film properties including dielectric constants, grain size and oxide

layer thickness; another is to examine the quality of nanostructures fabricated from the films. The standard operation procedure (SOP) of back-side measurement with a varied angle spectroscopic ellipsometer (VASE) has been developed, and the dielectric properties of Al films near the Al/quartz interface have been measured. Through depth profiling with X-ray photoelectron spectroscopy (XPS), we have found about 4 nm-thick oxide layers not only on the top surface, but also at the Al/quartz interface. All of this information helps to refine the numerical models for design and analysis of later experiments. Plasmonic structures discussed in Chapter 2 have been fabricated with FIB milling. The recipe of nanofabrication of Al film has been developed. The structural quality, especially the undercut into the substrate, has been carefully measured for the later experimental study. SOP of auto slicing and viewing with duo-beam analysis has been developed.

The third step of this dissertation work is to study plasmonic enhancement of UV fluorescence by using nanoapertures, which is presented in Chapter 4 and Chapter 5. In Chapter 4, UV lifetime modification of diffusing molecules by Al nanoapertures has been experimentally demonstrated for the first time to our knowledge. Furthermore, quantum-yield-dependence of lifetime reduction has been experimentally demonstrated. Lifetime reduction is higher ($\sim 3.5\times$) for high QY laser dye, while it is smaller ($\sim 1.7\times$) for the low QY molecule. Lifetime reduction as a function of aperture size, undercut and native quantum yield has been experimentally investigated, and accurately predicted by simulation. The comparison of experimental and simulation data further validate our design method. And then, detailed study of UV fluorescence enhancement has been performed with FDTD simulation. We found that observation volume of the measurement can be determined by native quantum yield of molecules for a nanoaperture with undercut. We have also demonstrated that undercut of the nanoapertures into the substrate is detrimental for lifetime reduction, but simulations show that undercut can be beneficial for net fluorescence enhancement.

Chapter 5 presents our efforts of exploring and evaluating another possible UV plasmonic material, Mg, for UV Plasmonics. Through extensive numerical simulation, we have found that smaller aperture sizes are required with Mg in order to maximize the emission enhancement due to the fact that it is further away from the resonant condition compared with Al. But Mg nanoapertures still give higher lifetime reduction in the diameter range that has been studied. Furthermore, in terms of net enhancement of fluorescence, Mg apertures give fluorescence signal comparable to or better than Al with larger apertures for the case of pure bulk metals, and more specifically, for the case of native surface oxide. The influence of oxidation has been examined. In general, avoiding bulk oxidation is important, but bulk

and surface oxidation can also be used as an optimization factor for different enhancement mechanisms. After numerical study, the experimental study of lifetime reduction has been repeated for Mg nanoapertures. Lifetime reduction is higher compared to the case of Al even if the Mg apertures have deeper undercut. The maximal lifetime reduction is ~ 13 for a diameter of 50 nm with 125 nm undercut, which further confirms that Mg nanoapertures are the preferred structures for applications requiring shorter lifetime [139].

In addition, we have examined the potential of Mg for SPP-related applications by measuring the extraordinary optical transmission (EOT) of Mg nanohole arrays. EOT of Al nanohole arrays has also been measured for the purpose of comparison. As expected from FOM comparison, Al nanohole arrays give the higher transmission with a maximum of 10%, while Mg nanohole arrays only give a maximal transmission of 5%. We have observed the red-shifting of resonant dip-peak of both structures with increase of periods. Through further simulation, the difference of transmission spectra of Mg and Al nanohole arrays has been discussed. We have found that Mg nanohole arrays can still give decent transmission even if it is worse than Al, which implies that Mg can be another candidate material for SPP-related applications in the UV.

At last, this work has established a methodology for the study of plasmonic enhancement of UV fluorescence including simulation, characterization, fabrication and measurement. It has paved the way for more extensive research on UV fluorescence enhancement.

6.2 Future Work

The proposed ideas for future work are categorized into follow-up research of this dissertation work and new directions.

6.2.1 Follow Up Research

6.2.1.1 Native-QY-Dependency of Lifetime Reduction

The UV lifetime study discussed in Chapter 4 and Chapter 5 demonstrates the native-QY-dependency of lifetime reduction by using two molecules with high and low QYs. However, more data points need to be added for molecules with different native QY and measurable lifetime in order to fully characterize the dependency. The repetition rate of our light source (80 MHz) determines the upper limit of measurable lifetime, 12.5 ns; on the other hand, the instrument response function of the system gives the lower limit, 156 ps. Dr. Eric Peterson compiled the list of potential UV dyes that covers a range of quantum yield and fluorescence lifetime, which is shown in Figure 6.2. Based on this plot, several UV dyes can be selected for the QY dependency study.

6.2.1.2 Other Plasmonic Structures

Only round nanoapertures have been considered in this dissertation work. However, the simulation in Chapter 2 and Chapter 5 also demonstrates that other plasmonic structures should be used for different purposes of applications. For excitation enhancement under plane wave illumination, the bullseye gives the best performance due to its large concentrating structure, while the dipole antenna produces the highest emission enhancement due to its favorable gap structure. Besides, the double-nanohole [147] can be a promising extension of single nanohole. The fabrication recipes for most structures should be straightforward with the developed recipe of Al fabrication. Making the bullseye structure at the Al/glass interface requires more steps. At first, 10 nm thick metal deposition is followed by the FIB milling to fabricate the concentric rings on the glass substrate. Then thin-film deposition will be performed again to make a thicker metal film. At last, the central nanoaperture will be milled with FIB.

6.2.1.3 Extensive Study of EOT in the UV

In this dissertation work, the EOT of Mg and Al hole arrays has been preliminarily studied. In order to fully characterize the influence of geometric parameters on EOT of Mg hole arrays, more structures with different period, different diameter and different thickness should be prepared and measured. Furthermore, more complicated patterns including variation of hole shape and lattice symmetry can be studied. In addition, our setup has the capability of varying the incident angle, which gives a new control freedom for future study. At last, more materials can be explored such as Al/Mg alloy.

6.2.1.4 Fluorescence Correlation Spectroscopy (FCS)

According to the discussion in Chapter 1, FCS analysis is necessary for the single molecule analysis. Combined with lifetime measurement, FCS can distinguish the contribution from excitation and from emission, so it is an important follow-up study. FCS is a useful method to observe molecular behaviors by correlation analysis of intensity fluctuation that are the result of some dynamic process, such as Brownian motion of molecules [31]. The autocorrelation of temporal fluctuations $F(t)$ of fluorescence signal can be computed

$$G(\tau) = \frac{< F(t) \cdot F(t+\tau) >}{< F(t) >^2} = 1 + \frac{< \delta F(0) \delta F(\tau) >}{< F >^2}$$

where <> stands for time averaging. The experimental data will be numerically fitted based on a three-dimensional Brownian diffusion model [43]:

$$G(\tau) = 1 + \frac{1}{N}(1 - \frac{< B >}{< F >})^2[1 + n_T \exp(-\frac{\tau}{\tau_{b_T}})] \times \frac{1}{(1+\tau/\tau_d)\sqrt{1+\kappa^2\tau/\tau_d}} \tag{6.1}$$

where N is the total number of molecules, $< F >$ the total signal, $< B >$ the background noise, n_T the amplitude of the dark state population, τ_{b_T} the dark state blinking time, τ_d the mean diffusion time and $kappa = s/z$ the ratio of transversal to axial dimensions of the analysis volume. It should be noted that a free three-dimensional diffusion model is not strictly fulfilled within an aperture. Fortunately, it has been demonstrated that this discrepancy can be taken into account by setting the aspect ratio s as a fitting parameter [43]. From equation 6.1, one can see that

$$N = \frac{(1 - \frac{<B>}{<F>})^2[1 + n_T)}{G(0) - 1}$$

when $< F > \ll < B >$ and without considering triplet state, $n_T \sim 0$, we can get $N = 1/(G(0) - 1)$. Knowing the average number of molecules inside the observed volume, measured signal $< F >$ and background $< B >$, the count rates per molecule can be estimated by $CRM = (< F > - < B >)/N$. FCS is a sensitive analytical tool because it observes molecules in a small volume confined by a focused laser beam and a confocal aperture. It also implies that the quality of FCS data is strongly dependent on that of confocal volume, which is determined by the optical alignment and required to be carefully characterized. Figure 6.3 shows a typical auto-correlation curve measured from 110 nm polystyrene nanoparticles in free solution.The diffusion coefficient of a nanosphere with known radius, r, can be calculated based on the Stokes-Einstein equation [31]:

$$D = \frac{k_B T}{6\pi\eta r}$$

where k_B is the Boltzmann's constant, η the viscosity of the solvent ($\eta = 0.00089$ Pa·s at 25 °C for water). The detection radius (s) can be calculated from $s^2 = 4D\tau_d$. By fitting the curve with equation 6.1, the diffusion time is 10 ± 2 ms, which corresponds to $\sim$0.4 μm radius detection region.

Furthermore, the signal-to-noise ratio, SNR, can be expressed as [45]

$$SNR = \frac{CRM\sqrt{T_{tot}\Delta\tau}}{(1 + 1/N)^{1/2}} \tag{6.2}$$

where T_{tot} is the total acquisition time, $\Delta\tau$ correlator channel minimum width. One can see that CRM has the dominate impact on the SNR. This is also one reason to use plasmonic structures as the platform for FCS in the UV.

The proposed working plan mainly includes two steps. First, a standard sample (solution of polystyrene nanospheres) will be used to calibrate the detection volume. Second, the FCS experiment will be carried out on the same nanospheres inside nanoapertures. Photostable

specimens with intense emission will be preferred, such as nanospheres or quantum dots. After acquiring valid data from those samples, we will gain the basic knowledge such as concentration and signal level required for successful FCS. Then FCS will be performed on the molecules used in lifetime measurement. The experimental procedures have to be properly designed based on equation 6.2 to achieve comparable SNR. More complicated structures, such as double-hole, may be required for this purpose.

6.2.2 UV Optical Trapping

Conventional optical trapping or optical tweezers by the diffraction-limited focus of a laser beam have become a powerful and flexible tool for manipulating micrometer-sized objects [148,149]. However, extending optical trapping down to the nanometer scale can be challenging due to the decreasing of both restoring force (following an R^3 law) and damping with particle size [150], which will increase the delocalization and allow the specimen to escape from the trap. To compensate this delocalization, plasmon-enhanced optical trapping has been proposed, which has been proven to be particularly efficient in controlling light down at the nano-scale [14]. The first experimental implementation of SP-based trapping was demonstrated using a glass surface decorated by micrometer-sized gold disks [151,152]. Gap antennas can give even higher control of the plasmonic field, which make it possible to achieve optical trapping of nanoparticles [153, 154]. A new trapping scheme named self-induced back-action (SIBA) trapping was also demonstrated using a nanoaperture in a metallic film [155], which relies on the high sensitivity of the aperture transmission to its dielectric environment. The illuminating laser wavelength was red-detuned to match the resonance of the nanoaperture with the presence of the nanoparticle. This resonance provides the automatic back action which prevents the nanoparticles from escaping.

Many other structures have been proposed, such as gold strip [156], gold dipole antenna [157], gold double-nanohole [147,158–160], bowtie antenna array [161], bowtie aperture [162], silver coaxial aperture [163], SPP virtual probe excited by radially polarized light [164], 2D plasmonic lattice [165] and gold nanoblock pair [166]. Optical trapping of dielectric particles of 10-50 nm has been experimentally shown [147, 155, 157, 158], and a protein with a hydrodynamic radius of 3.4 nm was successfully trapped by double-nanohole. The thermal effects associated with intense fields has gained attention recently. >micrometer per second fluid convection induced by local heating of plasmonic nanostructures was experimentally demonstrated, which opens up a new avenue for plasmonic optical trapping and particle assembly [167].

Since trapping events cannot be directly observed for extremely small nanosized objects,

it is necessary to track them by indirect measurements. Linear optical properties such as transmission [147,158–160] and Rayleigh scattering [157] have been used. Second harmonic generation has been demonstrated as a promising alternative [168]. Fluorescence is another efficient way to monitor the optical trapping [156]. However, additional tag and light source complicate the whole experimental system. Utilizing the native UV fluorescence of some biomolecules may be a promising strategy to perform and monitor the trapping events at the same time. UV light with a shorter wavelength will make optical trapping at the nano-scale more efficient. Furthermore, its higher energy will introduce stronger trapping interaction, which also induces convection by local heating. In addition, UV plasmon-enhanced trapping could seamlessly integrated with label-free detection with plasmon-enhanced UV fluorescence, and improve its efficiency by transferring and confining more interested molecules to the working area.

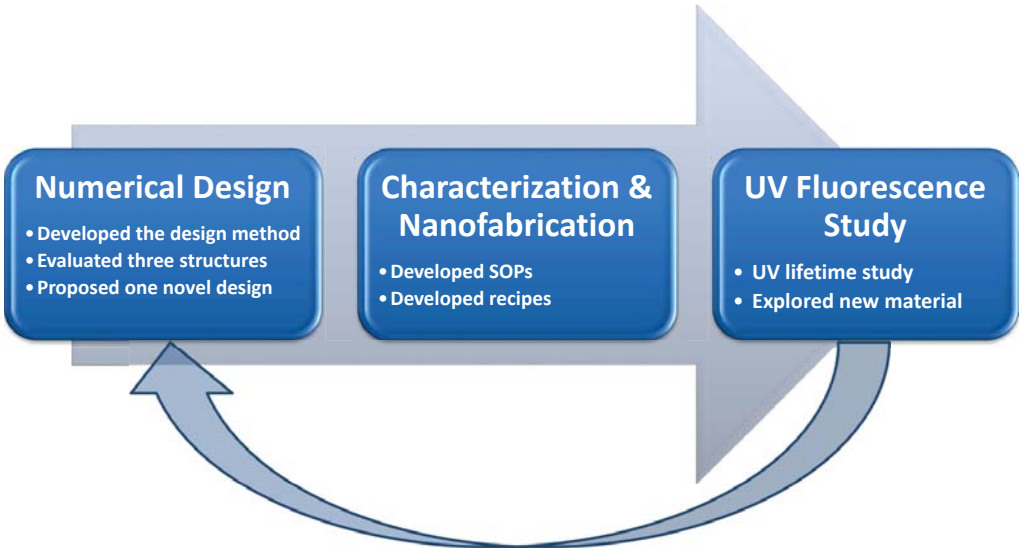

Figure 6.1. Work flow of dissertation work with summary of contribution to the whole research project and to this area.

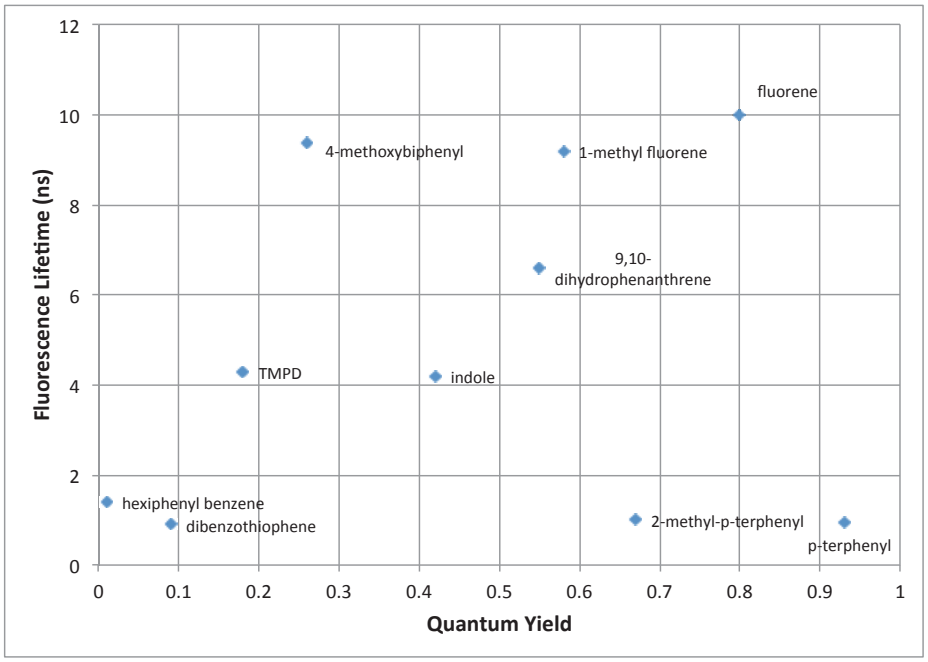

Figure 6.2. UV dyes with decent absorption around 266 nm listed in the 2D map of lifetime an native QY. Credit to Dr. Eric Peterson.

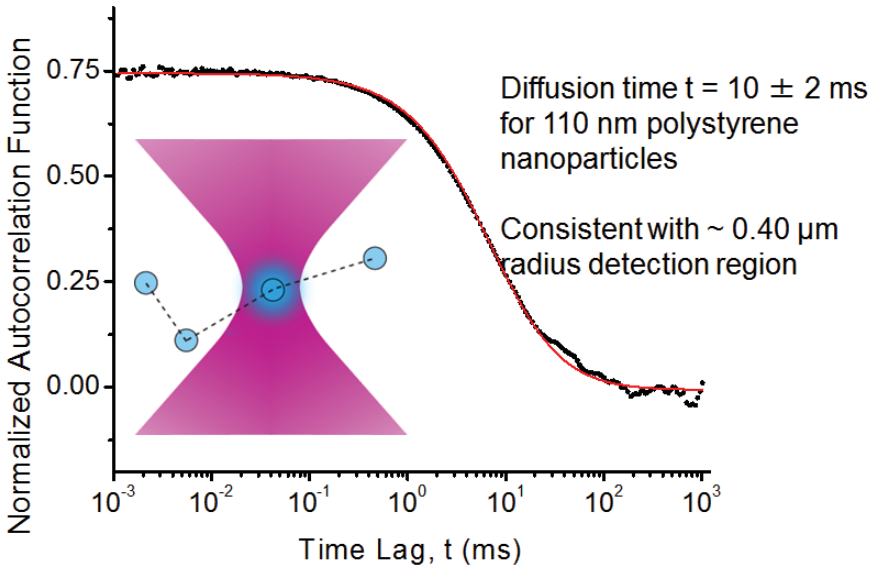

Figure 6.3. Auto-correlation curve of 110 nm polystyrene nanoparticles in free solution measured with FCS. Credit to Dr. Eric Peterson.

REFERENCES

[1] S. Maier, *Plasmonics: fundamentals and applications*. Berlin: Springer, 2007.

[2] R. F. Aroca, "Plasmon enhanced spectroscopy," *Physical Chemistry Chemical Physics: PCCP*, vol. 15, no. 15, pp. 5355–63, Apr. 2013.

[3] J. N. Anker, W. P. Hall, O. Lyandres, N. C. Shah, J. Zhao, and R. P. Van Duyne, "Biosensing with plasmonic nanosensors,," *Nature Materials*, vol. 7, no. 6, pp. 442–53, Jun. 2008.

[4] A. G. Brolo, "Plasmonics for future biosensors," *Nature Photonics*, vol. 6, no. 11, pp. 709–713, Nov. 2012.

[5] H. Raether, *Surface plasmons on smooth and rough surfaces and on gratings*. Berlin: Springer, 1988.

[6] D. Sarid and W. Challener, *Modern introduction to surface plasmons: theory, mathematica modeling, and applications*. Cambridge: Cambridge University Press, 2010.

[7] G. Mie, "Beiträge zur optik trüber medien, speziell kolloidaler metallösungen," *Annalen der Physik*, vol. 330, no. 3, pp. 377–445, 1908.

[8] T. Ebbesen, H. Lezec, H. Ghaemi, T. Thio, and P. Wolff, "Extraordinary optical transmission through sub-wavelength hole arrays,," *Nature*, vol. 391, pp. 667–669, Feb. 1998.

[9] R. Gordon, A. G. Brolo, D. Sinton, and K. L. Kavanagh, "Resonant optical transmission through hole-arrays in metal films: physics and applications," *Laser & Photonics Reviews*, vol. 4, no. 2, pp. 311–335, May 2009.

[10] F. J. Garcia-Vidal, T. W. Ebbesen, and L. Kuipers, "Light passing through subwavelength apertures," *Reviews of Modern Physics*, vol. 82, no. 1, pp. 729–787, Mar. 2010.

[11] S. A. Maier, M. L. Brongersma, P. G. Kik, S. Meltzer, A. A. G. Requicha, and H. A. Atwater, "Plasmonics–a route to nanoscale optical devices," *Advanced Materials*, vol. 13, no. 19, pp. 1501–1505, Sep. 2001.

[12] H. A. Atwater and A. Polman, "Plasmonics for improved photovoltaic devices," *Nature Materials*, vol. 9, no. 3, pp. 205–13, Mar. 2010.

[13] Z. Han and S. I. Bozhevolnyi, "Radiation guiding with surface plasmon polaritons," *Reports on Progress in Physics*, vol. 76, no. 1, p. 016402, Jan. 2013.

[14] J. A. Schuller, E. S. Barnard, W. Cai, Y. C. Jun, J. S. White, and M. L. Brongersma, "Plasmonics for extreme light concentration and manipulation," *Nature Materials*, vol. 9, no. 3, pp. 193–204, Mar. 2010.

[15] M. I. Stockman, "Nanoplasmonics: past, present, and glimpse into future," *Optics Express*, vol. 19, no. 22, p. 22029, Oct. 2011.

[16] E. Ozbay, "Plasmonics: merging photonics and electronics at nanoscale dimensions," *Science*, vol. 311, no. 5758, pp. 189–93, Jan. 2006.

[17] S. Kawata, Y. Inouye, and P. Verma, "Plasmonics for near-field nano-imaging and superlensing," *Nature Photonics*, vol. 3, no. 7, pp. 388–394, Jul. 2009.

[18] D. K. Gramotnev and S. I. Bozhevolnyi, "Plasmonics beyond the diffraction limit," *Nature Photonics*, vol. 4, no. 2, pp. 83–91, Jan. 2010.

[19] Z. Xie, W. Yu, T. Wang, H. Zhang, Y. Fu, H. Liu, F. Li, Z. Lu, and Q. Sun, "Plasmonic nanolithography: a review," *Plasmonics*, vol. 6, no. 3, pp. 565–580, May 2011.

[20] M. G. Blaber, M. D. Arnold, and M. J. Ford, "A review of the optical properties of alloys and intermetallics for plasmonics," *Journal of Physics: Condensed Matter*, vol. 22, no. 14, p. 143201, Apr. 2010.

[21] P. West, S. Ishii, G. Naik, N. Emani, V. Shalaev, and A. Boltasseva, "Searching for better plasmonic materials," *Laser & Photonics Reviews*, vol. 4, no. 6, pp. 795–808, Nov. 2010.

[22] A. Boltasseva and H. A. Atwater, "Low-loss plasmonic metamaterials," *Science*, vol. 331, no. 6015, pp. 290–1, Jan. 2011.

[23] G. V. Naik, J. Kim, and A. Boltasseva, "Oxides and nitrides as alternative plasmonic materials in the optical range," *Optical Materials Express*, vol. 1, no. 6, p. 1090, Sep. 2011.

[24] P. Tassin, T. Koschny, M. Kafesaki, and C. M. Soukoulis, "A comparison of graphene, superconductors and metals as conductors for metamaterials and plasmonics," *Nature Photonics*, vol. 6, no. 4, pp. 259–264, Mar. 2012.

[25] G. V. Naik, V. M. Shalaev, and A. Boltasseva, "Alternative plasmonic materials: beyond gold and silver." *Advanced Materials*, vol. 25, no. 24, pp. 3264–94, Jun. 2013.

[26] J. D. Jackson, *Classical electrodynamics*, 3rd ed. New York, NY: John Wiley & Sons, Inc., 1999.

[27] A. N. Grigorenko, M. Polini, and K. S. Novoselov, "Graphene plasmonics," *Nature Photonics*, vol. 6, no. 11, pp. 749–758, Nov. 2012.

[28] V. G. Kravets, R. Jalil, Y.-J. Kim, D. Ansell, D. E. Aznakayeva, B. Thackray, L. Britnell, B. D. Belle, F. Withers, I. P. Radko, Z. Han, S. I. Bozhevolnyi, K. S. Novoselov, a. K. Geim, and a. N. Grigorenko, "Graphene-protected copper and silver plasmonics," *Scientific Reports*, vol. 4, p. 5517, Jan. 2014.

[29] U. Guler, A. Boltasseva, and V. M. Shalaev, "Applied physics. Refractory plasmonics," *Science*, vol. 344, no. 6181, pp. 263–4, Apr. 2014.

[30] U. Guler, V. M. Shalaev, and A. Boltasseva, "Nanoparticle plasmonics: going practical with transition metal nitrides," *Materials Today*, Nov. 2014 (Available online).

[31] J. R. Lakowicz, *Principles of fluorescence spectroscopy*, 3rd ed. Springer: New York, 2006.

[32] E. M. Purcell, "Spontaneous emission probabilities at radio frequencies," in *Physical Review*, vol. 69, 1946, p. 681.

[33] K. Drexhage, "Influence of a dielectric interface on fluorescence decay time," *Journal of Luminescence*, vol. 1-2, pp. 693–701, 1970.

[34] W. L. Barnes, "Fluorescence near interfaces: the role of photonic mode density," *Journal of Modern Optics*, vol. 45, no. 4, pp. 661–699, Apr. 1998.

[35] J. R. Lakowicz, "Radiative decay engineering 5: metal-enhanced fluorescence and plasmon emission," *Analytical Biochemistry*, vol. 337, no. 2, pp. 171–194, Feb. 2005.

[36] C. Geddes and J. Lakowicz, "Editorial: metal-enhanced fluorescence," *Journal of Fluorescence*, vol. 12, no. 2, pp. 121–129, 2002.

[37] Chris D. Geddes, Ed., *Metal-enhanced fluorescence*. New Jersey: John Wiley & Sons, 2010.

[38] E. Sánchez, L. Novotny, and X. Xie, "Near-field fluorescence microscopy based on two-photon excitation with metal tips," *Physical Review Letters*, vol. 82, no. 20, pp. 4014–4017, May 1999.

[39] S. Nie, "Probing single molecules and single nanoparticles by surface-enhanced raman scattering," *Science*, vol. 275, no. 5303, pp. 1102–1106, Feb. 1997.

[40] M. J. Levene, J. Korlach, S. W. Turner, M. Foquet, H. G. Craighead, and W. W. Webb, "Zero-mode waveguides for single-molecule analysis at high concentrations," *Science*, vol. 299, no. 5607, pp. 682–6, Jan. 2003.

[41] H. Rigneault, J. Capoulade, J. Dintinger, J. Wenger, N. Bonod, E. Popov, T. Ebbesen, and P.-F. Lenne, "Enhancement of single-molecule fluorescence detection in subwavelength apertures," *Physical Review Letters*, vol. 95, no. 11, p. 117401, Sep. 2005.

[42] S. Kühn, U. Hå kanson, L. Rogobete, and V. Sandoghdar, "Enhancement of single-molecule fluorescence using a gold nanoparticle as an optical nanoantenna," *Physical Review Letters*, vol. 97, no. 1, pp. 1–4, Jul. 2006.

[43] D. Gérard, J. Wenger, N. Bonod, E. Popov, H. Rigneault, F. Mahdavi, S. Blair, J. Dintinger, and T. Ebbesen, "Nanoaperture-enhanced fluorescence: towards higher detection rates with plasmonic metals," *Physical Review B*, vol. 77, no. 4, p. 045413, Jan. 2008.

[44] J. Wenger, D. Gérard, and J. Dintinger, "Emission and excitation contributions to enhanced single molecule fluorescence by gold nanometric apertures," *Optics Express*, vol. 16, no. 5, pp. 8855–8865, Mar. 2008.

[45] J. Wenger, D. Gérard, and H. Aouani, "Nanoaperture-enhanced signal-to-noise ratio in fluorescence correlation spectroscopy," *Analytical Chemistry*, vol. 81, no. 2, pp. 834–839, Dec. 2008.

[46] H. Aouani, J. Wenger, D. Gérard, H. Rigneault, E. Devaux, T. W. Ebbesen, F. Mahdavi, T. Xu, and S. Blair, "Crucial role of the adhesion layer on the plasmonic fluorescence enhancement," *ACS Nano*, vol. 3, no. 7, pp. 2043–2048, Jul. 2009.

[47] J. Wenger, H. Aouani, D. Gérard, S. Blair, T. W. Ebbesen, and H. Rigneault, "Enhanced fluorescence from metal nanoapertures: physical characterizations and biophotonic applications," in *Proc. SPIE 7577, Plasmonics in Biology and Medicine VII*, T. Vo-Dinh and J. R. Lakowicz, Eds., no. 2, Feb. 2010, pp. 75 770J1–75 770J8.

[48] S. Blair and J. Wenger, "Enhancing fluorescence with sub-wavelength metallic apertures," in *Metal-enhanced fluorescence*, C. D. Geddes, Ed. John Wiley & Sons, 2010, ch. 17, p. 489.

[49] P. Zhu and H. G. Craighead, "Zero-mode waveguides for single-molecule analysis," *Annual Review of Biophysics*, vol. 41, pp. 269–93, Jan. 2012.

[50] H. Aouani, O. Mahboub, T. W. Ebbesen, E. Devaux, H. Rigneault, and J. Wenger, "Large molecular fluorescence enhancement by a nanoaperture with plasmonic corrugations," *Optics Express*, vol. 19, no. 14, pp. 13 056–13 062, Jul. 2011.

[51] H. Aouani, O. Mahboub, N. Bonod, E. Devaux, E. Popov, H. Rigneault, T. W. Ebbesen, and J. Wenger, "Bright unidirectional fluorescence emission of molecules in a nanoaperture with plasmonic corrugations," *Nano Letters*, vol. 11, no. 2, pp. 637–44, Feb. 2011.

[52] A. Kinkhabwala, Z. Yu, S. Fan, Y. Avlasevich, K. Müllen, and W. E. Moerner, "Large single-molecule fluorescence enhancements produced by a bowtie nanoantenna," *Nature Photonics*, vol. 3, no. 11, pp. 654–657, Oct. 2009.

[53] G. Lu, W. Li, T. Zhang, S. Yue, J. Liu, L. Hou, Z. Li, and Q. Gong, "Plasmonic-enhanced molecular fluorescence within isolated bowtie nano-apertures," *ACS Nano*, no. 2, pp. 1438–1448, Jan. 2012.

[54] Y. Fu, J. Zhang, and J. Lakowicz, "Large enhancement of single molecule fluorescence by coupling to hollow silver nanoshells," *Chemical Communications*, vol. 48, no. 78, pp. 9726–9728, Aug. 2012.

[55] G. P. Acuna, F. M. Möller, P. Holzmeister, S. Beater, B. Lalkens, and P. Tinnefeld, "Fluorescence enhancement at docking sites of DNA-directed self-assembled nanoantennas," *Science*, vol. 338, no. 6106, pp. 506–10, Oct. 2012.

[56] L. Zhou, F. Ding, H. Chen, W. Ding, W. Zhang, and S. Y. Chou, "Enhancement of immunoassay's fluorescence and detection sensitivity using three-dimensional plasmonic nano-antenna-dots array," *Analytical Chemistry*, vol. 84, no. 10, pp. 4489–95, May 2012.

[57] K. J. Russell, T.-l. Liu, S. Cui, and E. L. Hu, "Large spontaneous emission enhancement in plasmonic nanocavities," *Nature Photonics*, vol. 6, no. July, May 2012.

[58] X.-W. Chen, M. Agio, and V. Sandoghdar, "Metallodielectric hybrid antennas for ultrastrong enhancement of spontaneous emission," *Physical Review Letters*, vol. 108, no. 23, pp. 1–5, Jun. 2012.

[59] G. D. Fasman, Ed., *Practical handbook of biochemistry and molecular biology.* CRC Press, 1989.

[60] N. B. Colthup, L. H. Daly, and S. E. Wiberley, *Introduction to infrared and Raman spectroscopy.* Academic Press, 1990.

[61] C. R. Johnson, M. Ludwig, S. O'Donnell, and S. a. Asher, "UV resonance Raman spectroscopy of the aromatic amino acids and myoglobin," *Journal of the American Chemical Society*, vol. 106, no. 17, pp. 5008–5010, Aug. 1984.

[62] E. D. Palik, Ed., *Handbook of optical constants of solids*. London: Academic Press, 1985.

[63] Y. Song, D. Shan, R. Chen, and E.-H. Han, "Investigation of surface oxide film on magnesium lithium alloy," *Journal of Alloys and Compounds*, vol. 484, no. 1-2, pp. 585–590, Sep. 2009.

[64] K. Appusamy, S. Blair, A. Nahata, and S. Guruswamy, "Low-loss magnesium films for plasmonics," *Materials Science and Engineering: B*, vol. 181, no. d, pp. 77–85, Feb. 2014.

[65] K. Appusamy, X. Jiao, S. Blair, and A. Nahata, "Mg thin films with Al seed layers for UV plasmonics," *Submitted*.

[66] J. R. Lakowicz, B. Shen, Z. Gryczynski, S. D'Auria, and I. Gryczynski, "Intrinsic fluorescence from DNA can be enhanced by metallic particles," *Biochemical and Biophysical Research Communications*, vol. 286, no. 5, pp. 875–9, Sep. 2001.

[67] H. Szmacinski, K. Ray, and J. R. Lakowicz, "Metal-enhanced fluorescence of tryptophan residues in proteins: application toward label-free bioassays," *Analytical Biochemistry*, vol. 385, no. 2, pp. 358–64, Feb. 2009.

[68] Y. Kumamoto, A. Taguchi, M. Honda, K. Watanabe, Y. Saito, and S. Kawata, "Indium for deep-ultraviolet surface-enhanced resonance Raman scattering," *ACS Photonics*, vol. 1, no. 7, pp. 598–603, Jul. 2014.

[69] I. Gryczynski, J. Malicka, Z. Gryczynski, K. Nowaczyk, and J. R. Lakowicz, "Ultraviolet surface plasmon-coupled emission using thin aluminum films," *Analytical Chemistry*, vol. 76, no. 14, pp. 4076–81, Jul. 2004.

[70] Y. Ekinci, H. H. Solak, and C. David, "Extraordinary optical transmission in the ultraviolet region through aluminum hole arrays," *Optics Letters*, vol. 32, no. 2, p. 172, 2007.

[71] K. Ray, M. H. Chowdhury, and J. R. Lakowicz, "Aluminum nanostructured films as substrates for enhanced fluorescence in the ultraviolet-blue spectral region," *Analytical Chemistry*, vol. 79, no. 17, pp. 6480–7, Sep. 2007.

[72] K. Ray, H. Szmacinski, and J. R. Lakowicz, "Enhanced fluorescence of proteins and label-free bioassays using aluminum nanostructures," *Analytical Chemistry*, vol. 81, no. 15, pp. 6049–54, Aug. 2009.

[73] T. Dörfer, M. Schmitt, and J. Popp, "Deep-UV surface-enhanced Raman scattering," *Journal of Raman Spectroscopy*, vol. 38, no. 11, pp. 1379–1382, Nov. 2007.

[74] C. Langhammer, M. Schwind, B. Kasemo, and I. Zorić, "Localized surface plasmon resonances in aluminum nanodisks," *Nano Letters*, vol. 8, no. 5, pp. 1461–71, May 2008.

[75] G. H. Chan, J. Zhao, G. C. Schatz, and R. P. V. Duyne, "Localized surface plasmon resonance spectroscopy of triangular aluminum nanoparticles," *Journal of Physical Chemistry C*, vol. 112, no. 36, pp. 13 958–13 963, Sep. 2008.

[76] A. Taguchi, N. Hayazawa, K. Furusawa, H. Ishitobi, and S. Kawata, "Deep-UV tip-enhanced Raman scattering," *Journal of Raman Spectroscopy*, vol. 40, no. 9, pp. 1324–1330, Sep. 2009.

[77] M. H. Chowdhury, K. Ray, S. K. Gray, J. Pond, and J. R. Lakowicz, "Aluminum nanoparticles as substrates for metal-enhanced fluorescence in the ultraviolet for the label-free detection of biomolecules," *Analytical Chemistry*, vol. 81, no. 4, pp. 1397–403, Feb. 2009.

[78] M. H. Chowdhury, S. Chakraborty, J. R. Lakowicz, and K. Ray, "Feasibility of using bimetallic plasmonic nanostructures to enhance the intrinsic emission of biomolecules," *The journal of physical chemistry. C*, vol. 115, no. 34, pp. 16 879–16 891, Sep. 2011.

[79] F. Mahdavi and S. Blair, "Nanoaperture fluorescence enhancement in the ultraviolet," *Plasmonics*, vol. 5, no. 2, pp. 169–174, Mar. 2010.

[80] X. Jiao and S. Blair, "Polarization multiplexed optical bullseye antennas," *Plasmonics*, vol. 7, no. 1, pp. 39–46, Aug. 2011.

[81] ——, "Optical antenna design for fluorescence enhancement in the ultraviolet," *Optics Express*, vol. 20, no. 28, p. 29909, Dec. 2012.

[82] X. Jiao, E. M. Peterson, J. M. Harris, and S. Blair, "UV fluorescence lifetime modification by aluminum nanoapertures," *ACS Photonics*, vol. 1, no. 12, pp. 1270–1277, Dec. 2014.

[83] G. Ding, J. Deng, L. Zhou, Q. Gan, J. C. M. Hwang, V. Dierolf, F. J. Bartoli, C. Mazuir, and W. V. Schoenfeld, "Al nanogrid electrode for ultraviolet detectors," *Optics Letters*, vol. 36, no. 18, pp. 3663–5, Sep. 2011.

[84] Y. Watanabe, W. Inami, and Y. Kawata, "Deep-ultraviolet light excites surface plasmon for the enhancement of photoelectron emission," *Journal of Applied Physics*, vol. 109, no. 2, p. 023112, Jan. 2011.

[85] S. Attavar, M. Diwekar, and S. Blair, "Photoactivated capture molecule immobilization in plasmonic nanoapertures in the ultraviolet," *Lab on a Chip*, vol. 11, no. 5, pp. 841–4, Mar. 2011.

[86] Z.-L. Yang, Q.-H. Li, B. Ren, and Z.-Q. Tian, "Tunable SERS from aluminium nanohole arrays in the ultraviolet region." *Chemical Communications*, vol. 47, no. 13, pp. 3909–11, Apr. 2011.

[87] S. Butun, N. a. Cinel, and E. Ozbay, "LSPR enhanced MSM UV photodetectors," *Nanotechnology*, vol. 23, no. 44, p. 444010, Oct. 2012.

[88] S. Crosbie and D. Zerulla, "Long range surface plasmon resonance and enhanced fluorescence near the ultra-violet vacuum cutoff limit," *Journal of Applied Physics*, vol. 111, no. 8, p. 084702, Jul. 2012.

[89] L. Li, S. Fang Lim, A. a. Puretzky, R. Riehn, and H. D. Hallen, "Near-field enhanced ultraviolet resonance Raman spectroscopy using aluminum bow-tie nano-antenna," *Applied Physics Letters*, vol. 101, no. 11, p. 113116, Sep. 2012.

[90] J. Hu, L. Chen, Z. Lian, M. Cao, H. Li, W. Sun, N. Tong, and H. Zeng, "Deep-ultravioletblue-light surface plasmon resonance of Al and Al core/Al_2O_3 shell in spherical and cylindrical nanostructures," *The Journal of Physical Chemistry C*, vol. 116, no. 29, pp. 15 584–15 590, Jul. 2012.

[91] M. W. Knight, L. Liu, Y. Wang, L. Brown, S. Mukherjee, N. S. King, H. O. Everitt, P. Nordlander, and N. J. Halas, "Aluminum plasmonic nanoantennas," *Nano Letters*, vol. 12, no. 11, pp. 6000–4, Nov. 2012.

[92] M. W. Knight, N. S. King, L. Liu, H. O. Everitt, P. Nordlander, and N. J. Halas, "Aluminum for plasmonics," *ACS Nano*, vol. 8, no. 1, pp. 834–40, Jan. 2014.

[93] K.-D. Park, Y. H. Kim, J.-H. Park, J. S. Park, H. S. Lee, S.-Y. Yim, Y. H. Lee, and M. S. Jeong, "Ultraviolet tip-enhanced nanoscale Raman imaging," *Journal of Raman Spectroscopy*, vol. 43, no. 12, pp. 1931–1934, Dec. 2012.

[94] S. K. Jha, Z. Ahmed, M. Agio, Y. Ekinci, and J. F. Löffler, "Deep-UV surface-enhanced resonance Raman scattering of adenine on aluminum nanoparticle arrays," *Journal of the American Chemical Society*, vol. 134, no. 4, pp. 1966–9, Feb. 2012.

[95] N. Gao, K. Huang, J. Li, S. Li, X. Yang, and J. Kang, "Surface-plasmon-enhanced deep-UV light emitting diodes based on AlGaN multi-quantum wells," *Scientific Reports*, vol. 2, p. 816, Jan. 2012.

[96] J. M. McMahon, G. C. Schatz, and S. K. Gray, "Plasmonics in the ultraviolet with the poor metals Al, Ga, In, Sn, Tl, Pb, and Bi," *Physical Chemistry Chemical Physics: PCCP*, vol. 15, no. 15, pp. 5415–23, Apr. 2013.

[97] J. E. Abboud, X. Chong, M. Zhang, Z. Zhang, N. Jiang, S. Roy, and J. R. Gord, "Photothermally activated motion and ignition using aluminum nanoparticles," *Applied Physics Letters*, vol. 102, no. 2, p. 023905, Jan. 2013.

[98] A. Ono, M. Kikawada, R. Akimoto, W. Inami, and Y. Kawata, "Fluorescence enhancement with deep-ultraviolet surface plasmon excitation," *Optics Express*, vol. 21, no. 15, pp. 17 447–17 453, Jul. 2013.

[99] A. Ono, N. Shiroshita, M. Kikawada, W. Inami, and Y. Kawata, "Enhanced photoelectron emission from aluminum thin film by surface plasmon resonance under deep-ultraviolet excitation," *Journal of Physics D: Applied Physics*, vol. 48, no. 18, p. 184005, May 2015.

[100] D. O. Sigle, E. Perkins, J. J. Baumberg, and S. Mahajan, "Reproducible deep-UV SERS on aluminum nanovoids," *The Journal of Physical Chemistry Letters*, vol. 4, no. 9, pp. 1449–1452, May 2013.

[101] J. M. Sanz, D. Ortiz, R. Alcaraz de la Osa, J. M. Saiz, F. González, A. S. Brown, M. Losurdo, H. O. Everitt, and F. Moreno, "UV plasmonic behavior of various metal nanoparticles in the near- and far-field regimes: geometry and substrate effects," *The Journal of Physical Chemistry C*, vol. 117, pp. 19 606–19 615, Sep. 2013.

[102] G. Maidecchi, G. Gonella, R. Proietti Zaccaria, R. Moroni, L. Anghinolfi, A. Giglia, S. Nannarone, L. Mattera, H.-L. Dai, M. Canepa, and F. Bisio, "Deep ultraviolet plasmon resonance in aluminum nanoparticle arrays," *ACS Nano*, vol. 7, no. 7, pp. 5834–41, Jul. 2013.

[103] J. Martin, J. Proust, D. Gérard, and J. Plain, "Localized surface plasmon resonances in the ultraviolet from large scale nanostructured aluminum films," *Optical Materials Express*, vol. 3, no. 7, p. 954, Jun. 2013.

[104] T. M. Schmidt, V. E. Bochenkov, J. D. A. Espinoza, E. C. P. Smits, A. M. Muzafarov, Y. N. Kononevich, and D. S. Sutherland, "Plasmonic fluorescence enhancement of $DBMBF_2$ monomers and $DBMBF_2$-Toluene exciplexes using Al-hole arrays," *The Journal of Physical Chemistry C*, vol. 118, no. 4, pp. 2138–2145, Jan. 2014.

[105] M. Honda, Y. Kumamoto, A. Taguchi, Y. Saito, and S. Kawata, "Plasmon-enhanced UV photocatalysis," *Applied Physics Letters*, vol. 104, no. 6, p. 061108, Feb. 2014.

[106] ——, "Efficient UV photocatalysis assisted by densely distributed aluminum nanoparticles," *Journal of Physics D: Applied Physics*, vol. 48, no. 18, p. 184006, May 2015.

[107] F. Bisio, R. Proietti Zaccaria, R. Moroni, G. Maidecchi, A. Alabastri, G. Gonella, A. Giglia, L. Andolfi, S. Nannarone, L. Mattera, and M. Canepa, "Pushing the high-energy limit of plasmonics," *ACS Nano*, vol. 8, no. 9, pp. 9239–47, Sep. 2014.

[108] M. B. Ross and G. C. Schatz, "Aluminum and indium plasmonic nanoantennas in the ultraviolet," *The Journal of Physical Chemistry C*, vol. 118, no. 23, pp. 12 506–12 514, Jun. 2014.

[109] M. Rodriguez, C. Furse, J. S. Shumaker-Parry, and S. Blair, "Scaling the response of nanocrescent antennas into the ultraviolet," *ACS Photonics*, vol. 1, no. 6, pp. 496–506, Jun. 2014.

[110] D. Gérard and S. K. Gray, "Aluminium plasmonics," *Journal of Physics D: Applied Physics*, vol. 48, no. 18, p. 184001, May 2015.

[111] J. Martin and J. Plain, "Fabrication of aluminium nanostructures for plasmonics," *Journal of Physics D: Applied Physics*, vol. 48, no. 18, p. 184002, May 2015.

[112] Y. Yang, J. M. Callahan, T.-H. Kim, A. S. Brown, and H. O. Everitt, "Ultraviolet nanoplasmonics: a demonstration of surface-enhanced Raman spectroscopy, fluorescence, and photodegradation using gallium nanoparticles," *Nano Letters*, vol. 13, no. 6, pp. 2837–41, Jun. 2013.

[113] N. Akbay, F. Mahdavi, J. R. Lakowicz, and K. Ray, "Metal-enhanced intrinsic fluorescence of nucleic acids using platinum nanostructured substrates," *Chemical Physics Letters*, vol. 548, pp. 45–50, Oct. 2012.

[114] K. Aslan, M. J. R. Previte, Y. Zhang, and C. D. Geddes, "Metal-enhanced fluorescence from nanoparticulate zinc films," *The Journal of Physical Chemistry. C*, vol. 112, no. 47, pp. 18 368–18 375, Nov. 2008.

[115] P. C. Wu, T.-H. Kim, A. Suvorova, M. Giangregorio, M. Saunders, G. Bruno, A. S. Brown, and M. Losurdo, "GaMg alloy nanoparticles for broadly tunable plasmonics," *Small*, vol. 7, no. 6, pp. 751–6, Mar. 2011.

[116] J.-Y. Ou, J.-K. So, G. Adamo, A. Sulaev, L. Wang, and N. I. Zheludev, "Ultraviolet and visible range plasmonics in the topological insulator $Bi_{1.5}Sb_{0.5}Te_{1.8}Se_{1.2}$," *Nature Communications*, vol. 5, p. 5139, Jan. 2014.

[117] J. Henzie, J. Lee, M. H. Lee, W. Hasan, and T. W. Odom, "Nanofabrication of plasmonic structures," *Annual Review of Physical Chemistry*, vol. 60, pp. 147–65, Jan. 2009.

[118] X. Zhang, A. V. Whitney, J. Zhao, E. M. Hicks, and R. P. Van Duyne, "Advances in contemporary nanosphere lithographic techniques," *Journal of Nanoscience and Nanotechnology*, vol. 6, no. 7, pp. 1920–1934, Jul. 2006.

[119] S. Yang and Y. Lei, "Recent progress on surface pattern fabrications based on monolayer colloidal crystal templates and related applications," *Nanoscale*, vol. 3, no. 7, pp. 2768–82, Jul. 2011.

[120] B. H. Kim, M. J. Hackett, J. Park, and T. Hyeon, "Synthesis, characterization, and application of ultrasmall nanoparticles," *Chemistry of Materials*, vol. 26, no. 1, pp. 59–71, Jan. 2014.

[121] N. C. Lindquist, P. Nagpal, K. M. McPeak, D. J. Norris, and S.-H. Oh, "Engineering metallic nanostructures for plasmonics and nanophotonics." *Reports on Progress in Physics*, vol. 75, no. 3, p. 036501, Mar. 2012.

[122] T. Tanii, R. Akahori, S. Higano, K. Okubo, H. Yamamoto, T. Ueno, and T. Funatsu, "Improving zero-mode waveguide structure for enhancing signal-to-noise ratio of real-time single-molecule fluorescence imaging: A computational study," *Physical Review E*, vol. 88, no. 1, p. 012727, Jul. 2013.

[123] B. Ren, X.-F. Lin, Z.-L. Yang, G.-K. Liu, R. F. Aroca, B.-W. Mao, and Z.-Q. Tian, "Surface-enhanced Raman scattering in the ultraviolet spectral region: UV-SERS on rhodium and ruthenium electrodes," *Journal of the American Chemical Society*, vol. 125, no. 32, pp. 9598–9, Aug. 2003.

[124] R. F. Chen, "Fluorescence quantum yields of tryptophan and tyrosine," *Analytical Letters*, vol. 1, pp. 35–42, 1967.

[125] J. R. Lakowicz, J. Malicka, I. Gryczynski, Z. Gryczynski, and C. D. Geddes, "Radiative decay engineering: the role of photonic mode density in biotechnology," *Journal of physics D: Applied physics*, vol. 36, pp. R240–R249, Jul. 2003.

[126] A. ZAYATS, I. SMOLYANINOV, and A. MARADUDIN, "Nano-optics of surface plasmon polaritons," *Physics Reports*, vol. 408, no. 3-4, pp. 131–314, Mar. 2005.

[127] L. Novotny and B. Hecht, *Principles of nano-optics*. Cambridge University Press, 2006.

[128] H. Fischer and O. J. F. Martin, "Engineering the optical response of plasmonic nanoantennas," *Optics Express*, vol. 16, no. 12, pp. 9144–54, Jun. 2008.

[129] O. Mahboub, S. C. Palacios, C. Genet, F. J. Garcia-Vidal, S. G. Rodrigo, L. Martin-Moreno, and T. W. Ebbesen, "Optimization of bulls eye structures for transmission enhancement," *Optics Express*, vol. 18, no. 11, p. 11292, May 2010.

[130] M. Kuttge, F. J. García de Abajo, and A. Polman, "How grooves reflect and confine surface plasmon polaritons," *Optics Express*, vol. 17, no. 12, p. 10385, Jun. 2009.

[131] S. Carretero-Palacios, O. Mahboub, F. J. Garcia-Vidal, L. Martin-Moreno, S. G. Rodrigo, C. Genet, and T. W. Ebbesen, "Mechanisms for extraordinary optical transmission through bulls eye structures," *Optics Express*, vol. 19, no. 11, p. 10429, May 2011.

[132] H. J. Lezec, A. Degiron, E. Devaux, R. a. Linke, L. Martin-Moreno, F. J. Garcia-Vidal, and T. W. Ebbesen, "Beaming light from a subwavelength aperture," *Science*, vol. 297, no. 5582, pp. 820–2, Aug. 2002.

[133] K. Shuford, M. Ratner, S. Gray, and G. Schatz, "Finite-difference time-domain studies of light transmission through nanohole structures," *Applied Physics B*, vol. 84, no. 1-2, pp. 11–18, Apr. 2006.

[134] N. Bonod, E. Popov, D. Gérard, J. Wenger, and H. Rigneault, "Field enhancement in a circular aperture surrounded by a single channel groove," *Optics Express*, vol. 16, no. 3, pp. 2276–87, Feb. 2008.

[135] R. Gavrila, A. Dinescu, and D. Mardare, "A power spectral density study of thin films morphology based on AFM profiling," *Romanian Journal of Information Science and Technology*, vol. 10, no. 3, pp. 291–300, 2007.

[136] L. A. Giannuzzi and F. A. Stevie, *Introduction to focused ion beams: instrumentation, theory, techniques and practice*. Springer US, 2005.

[137] T. Hirschfeld, "Quantum efficiency independence of the time integrated emission from a fluorescent molecule," *Applied Optics*, vol. 15, no. 12, pp. 3135–9, Dec. 1976.

[138] H. Cang, Y. Liu, Y. Wang, X. Yin, and X. Zhang, "Giant suppression of photobleaching for single molecule detection via the Purcell effect," *Nano Letters*, vol. 13, no. 12, pp. 5949–53, Jan. 2013.

[139] E. Yablonovitch, "Metal optics, optical antennas, and spontaneous hyper-emission," in *10th IEEE International Conference on Nanotechnology*. IEEE, Aug. 2010, pp. 13–14.

[140] F. T. Rabouw, S. A. den Hartog, T. Senden, and A. Meijerink, "Photonic effects on the Förster resonance energy transfer efficiency." *Nature Communications*, vol. 5, p. 3610, Jan. 2014.

[141] Y. Liu, F. Mahdavi, and S. Blair, "Enhanced fluorescence transduction properties of metallic nanocavity arrays," *IEEE Journal of Selected Topics in Quantum Electronics*, vol. 11, no. 4, pp. 778–784, Jul. 2005.

[142] E. Popov, M. Nevière, J. Wenger, P.-F. Lenne, H. Rigneault, P. Chaumet, N. Bonod, J. Dintinger, and T. Ebbesen, "Field enhancement in single subwavelength apertures," *Journal of the Optical Society of America. A*, vol. 23, no. 9, pp. 2342–8, Sep. 2006.

[143] K.-l. Liu, Y.-T. Chen, H.-h. Lin, C.-s. Hsu, H.-w. Chang, and I.-c. Chen, "Dynamics of the excited states of p-terphenyl and tetracene: solute-solvent interaction," *The Journal of Physical Chemistry C*, vol. 115, no. 45, pp. 22 578–22 586, Nov. 2011.

[144] M. J. Meziani, C. E. Bunker, F. Lu, H. Li, W. Wang, E. a. Guliants, R. a. Quinn, and Y.-P. Sun, "Formation and properties of stabilized aluminum nanoparticles," *ACS Applied Materials & Interfaces*, vol. 1, no. 3, pp. 703–9, Mar. 2009.

[145] S. W. Chung, E. A. Guliants, C. E. Bunker, D. W. Hammerstroem, Y. Deng, M. A. Burgers, P. A. Jelliss, and S. W. Buckner, "Capping and passivation of aluminum nanoparticles using alkyl-substituted epoxides." *Langmuir*, vol. 25, no. 16, pp. 8883–7, Aug. 2009.

[146] H. M. Lee and J.-Y. Yun, "Preparation of aluminum-oleic acid nano-composite for application to electrode for Si solar cells," *Materials Transactions*, vol. 52, no. 6, pp. 1222–1227, Jun. 2011.

[147] Y. Pang and R. Gordon, "Optical trapping of 12 nm dielectric spheres using double-nanoholes in a gold film," *Nano Letters*, vol. 11, no. 9, pp. 3763–7, Sep. 2011.

[148] A. Ashkin, J. M. Dziedzic, J. E. Bjorkholm, and S. Chu, "Observation of a single-beam gradient force optical trap for dielectric particles," *Optics Letters*, vol. 11, no. 5, pp. 288–290, May 1986.

[149] D. G. Grier, "A revolution in optical manipulation," *Nature*, vol. 424, no. 6950, pp. 810–6, Aug. 2003.

[150] M. L. Juan, M. Righini, and R. Quidant, "Plasmon nano-optical tweezers," *Nature Photonics*, vol. 5, no. 6, pp. 349–356, Jun. 2011.

[151] M. Righini, A. S. Zelenina, C. Girard, and R. Quidant, "Parallel and selective trapping in a patterned plasmonic landscape," *Nature Physics*, vol. 3, no. 7, pp. 477–480, May 2007.

[152] M. Righini, G. Volpe, C. Girard, D. Petrov, and R. Quidant, "Surface plasmon optical tweezers: tunable optical manipulation in the femtonewton range," *Physical Review Letters*, vol. 100, no. 18, p. 186804, May 2008.

[153] a. N. Grigorenko, N. W. Roberts, M. R. Dickinson, and Y. Zhang, "Nanometric optical tweezers based on nanostructured substrates," *Nature Photonics*, vol. 2, no. 6, pp. 365–370, May 2008.

[154] M. Righini, P. Ghenuche, S. Cherukulappurath, V. Myroshnychenko, F. J. García de Abajo, and R. Quidant, "Nano-optical trapping of Rayleigh particles and Escherichia coli bacteria with resonant optical antennas," *Nano Letters*, vol. 9, no. 10, pp. 3387–91, Oct. 2009.

[155] M. L. Juan, R. Gordon, Y. Pang, F. Eftekhari, and R. Quidant, "Self-induced back-action optical trapping of dielectric nanoparticles," *Nature Physics*, vol. 5, no. 12, pp. 915–919, Oct. 2009.

[156] K. Wang, E. Schonbrun, P. Steinvurzel, and K. B. Crozier, "Scannable plasmonic trapping using a gold stripe," *Nano Letters*, vol. 10, no. 9, pp. 3506–11, Sep. 2010.

[157] W. Zhang, L. Huang, C. Santschi, and O. J. F. Martin, "Trapping and sensing 10 nm metal nanoparticles using plasmonic dipole antennas," *Nano Letters*, vol. 10, no. 3, pp. 1006–11, Mar. 2010.

[158] Y. Pang and R. Gordon, "Optical trapping of a single protein," *Nano Letters*, vol. 12, no. 1, pp. 402–6, Jan. 2012.

[159] A. Zehtabi-Oskuie, H. Jiang, B. R. Cyr, D. W. Rennehan, A. A. Al-Balushi, and R. Gordon, "Double nanohole optical trapping: dynamics and protein-antibody co-trapping," *Lab on a Chip*, vol. 13, no. 13, pp. 2563–8, Jul. 2013.

[160] A. Kotnala, D. DePaoli, and R. Gordon, "Sensing nanoparticles using a double nanohole optical trap," *Lab on a Chip*, vol. 13, no. 20, pp. 4142–6, Oct. 2013.

[161] B. J. Roxworthy, K. D. Ko, A. Kumar, K. H. Fung, E. K. C. Chow, G. L. Liu, N. X. Fang, and K. C. Toussaint, "Application of plasmonic bowtie nanoantenna arrays for optical trapping, stacking, and sorting," *Nano Letters*, vol. 12, no. 2, pp. 796–801, Feb. 2012.

[162] J. Berthelot, S. S. Aćimović, M. L. Juan, M. P. Kreuzer, J. Renger, and R. Quidant, "Three-dimensional manipulation with scanning near-field optical nanotweezers," *Nature Nanotechnology*, vol. 9, pp. 295–299, Mar. 2014.

[163] A. A. E. Saleh and J. A. Dionne, "Toward efficient optical trapping of sub-10-nm particles with coaxial plasmonic apertures," *Nano Letters*, vol. 12, no. 11, pp. 5581–6, Nov. 2012.

[164] C. Min, Z. Shen, J. Shen, Y. Zhang, H. Fang, G. Yuan, L. Du, S. Zhu, T. Lei, and X. Yuan, "Focused plasmonic trapping of metallic particles," *Nature Communications*, vol. 4, p. 2891, Jan. 2013.

[165] K.-Y. Chen, A.-T. Lee, C.-C. Hung, J.-S. Huang, and Y.-T. Yang, "Transport and trapping in two-dimensional nanoscale plasmonic optical lattice," *Nano Letters*, vol. 13, no. 9, pp. 4118–22, Sep. 2013.

[166] Y. Tanaka, S. Kaneda, and K. Sasaki, "Nanostructured potential of optical trapping using a plasmonic nanoblock pair," *Nano Letters*, vol. 13, no. 5, pp. 2146–50, May 2013.

[167] B. J. Roxworthy, A. M. Bhuiya, S. P. Vanka, and K. C. Toussaint Jr, "Understanding and controlling plasmon-induced convection," *Nature Communications*, vol. 5, Jan. 2014.

[168] J. Butet, A. Lovera, and O. Martin, "Detecting the trapping of small metal nanoparticles in the gap of nanoantennas with optical second harmonic generation," *Optics Express*, vol. 21, no. 23, pp. 256–264, 2013.